THE ENHANCED PERFORMANCE OF AN INTEGRATED NAVIGATION SYSTEM IN A HIGHLY DYNAMIC ENVIRONMENT

THESIS

Brian J. Bohenek
Second Lieutenant, USAF

AFIT/GE/ENG/94D-01

DEPARTMENT OF THE AIR FORCE
AIR UNIVERSITY
AIR FORCE INSTITUTE OF TECHNOLOGY

Wright-Patterson Air Force Base, Ohio

AFIT/GE/ENG/94D-01

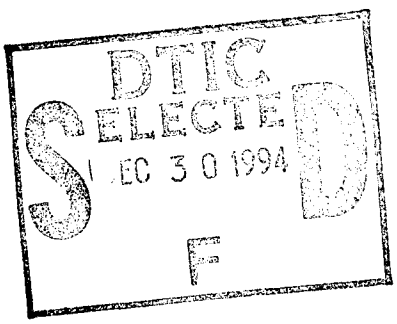

THE ENHANCED PERFORMANCE OF AN INTEGRATED NAVIGATION SYSTEM IN A HIGHLY DYNAMIC ENVIRONMENT

THESIS

Brian J. Bohenek
Second Lieutenant, USAF

AFIT/GE/ENG/94D-01

Approved for public release; distribution unlimited

The views expressed in this thesis are those of the author and do not reflect the official policy or position of the Department of Defense or the U. S. Government.

AFIT/GE/ENG/94D-01

THE ENHANCED PERFORMANCE OF AN INTEGRATED NAVIGATION SYSTEM IN A HIGHLY DYNAMIC ENVIRONMENT

THESIS

Presented to the Faculty of the Graduate School of Engineering

of the Air Force Institute of Technology

Air University

In Partial Fulfillment of the

Requirements for the Degree of

Master of Science in Electrical Engineering

Brian J. Bohenek, B.S. Electrical Engineering

Second Lieutenant, USAF

December 1994

Preface

The completion of this thesis is not the work of just one person but of several people who either directly or indirectly helped make this thesis a reality. First of all, my sponsoring organization, the Central Inertial Guidance Test Facility (CIGTF) of the 46th Test Group, Holloman AFB, NM. This thesis was completed in support of their mission to test and evaluate the accuracy and reliability of integrated navigation systems.

The efforts of Captain Neil Hansen, CN Air Force, in development of the PNRS models in MSOFE which were vital in the successful completion of this thesis. I would also like to thank 1Lt William "Chip" Mosle of CIGTF who on many occasions helped me to understand the inner workings of MSOFE which proved to be most helpful.

I would also like to thank the members of my thesis committee for their help and guidance throughout this thesis effort. A special thanks must go out to Lt Col Robert Riggins, my thesis advisor. His constant support and encouragement always kept me focused on where I was going with my thesis especially when it seemed like I ran into a brick wall. I would also like to thank Dr. Peter Maybeck for his diligence and "eagle eye" when proof-reading and evaluating my written work. Also, thanks must go out to Captain Ron Delap for his time and effort in proof-reading and evaluating my work along with words of encouragement.

Thanks must go out to the Guidance and Control Class of GE-94D. Their guidance and support with class work proved to be most valuable when needed. Also to the "Tuesday and Thursday Basketball Crew," thanks for well needed stress reliefs throughout this thesis effort. I would especially like to thank Captain Pete Eide whose support, SEGA stress relief games, and assistance with class work proved to invaluable for me to make it to graduation.

My family deserves a special thanks for their constant support in all that I have accomplished. Mom, Dad, and Jason thanks for all the love and support over the years, I would not be where I am today without you behind me.

Finally, the deepest expression of my thanks has to go to my fiancé, Linda. Her constant support, strength, love, and encouragement throughout the last year and a half always helped me to maintain a proper perspective and focus on my thesis. She was able to put up with all of the stress associated with medical school and would always find time for me and for this I am most thankful.

Brian J. Bohenek

Table of Contents

List of Figures

Figure Page

List of Tables

Abstract

For the U. S. Air Force to maintain an accurate and reliable Navigation Reference System (NRS) with Carrier-Phase Global Positioning System (CPGPS) measurements, it must develop an accurate and robust NRS in the face of cycle slips caused by highly dynamic maneuvers. This research investigates the implementation of a double differencing between receivers/satellites scheme to improve the accuracy of current NRS models. The removal of the "perfect Doppler velocity aiding measurements" (a very poor assumption of past research) was completed with stable and accurate results. The double differencing implemented showed improvement in the accuracy of the NRS. An investigation of two Failure Detection, Isolation, and Recovery (FDIR) algorithms for large cycle slip failures is conducted. The two FDIR techniques are the Chi-Square test and a Multiple Model Adaptive Estimator (MMAE). The FDIR results show that a Chi-Square test as a stand-alone algorithm can work accurately for detection and isolation of failures with an accurate and reliable recovery algorithm. The MMAE algorithm as conjectured seems to be the best FDIR technique to handle single and multiple cycle slips accurately and reliably.

THE ENHANCED PERFORMANCE OF AN INTEGRATED NAVIGATION SYSTEM IN A HIGHLY DYNAMIC ENVIRONMENT

I. Introduction

The Central Inertial Guidance Test Facility (CIGTF), of the 46th Test Group, located at Holloman AFB in New Mexico, is currently in the process of upgrading their Navigation Reference System (NRS) to incorporate highly accurate Carrier-Phase measurements of the Global Positioning System (GPS). The addition of Carrier-Phase GPS measurements is expected to improve the accuracy of the NRS to ensure that the NRS keeps an order of magnitude or better accuracy advantage over the navigation system under test. This accuracy advantage is necessary for CIGTF to provide the Air Force with an accurate and reliable benchmark upon which to analyze the performance of navigation systems under test.

The upgraded NRS will be composed of three different navigation systems: a Litton LN-93 Inertial Navigation System (INS), Carrier-Phase Global Positioning System (CPGPS), and the Range/Range-Rate System (RRS) of ground transponders. The NRS is an airborne system which optimally calculates the position and velocity errors of the test system through the use of an Extended Kalman Filter (EKF) to correct the INS-indicated position of the aircraft. Figure 1.1 depicts the configuration of the NRS with the incorporation of CPGPS measurements.

The system under test is flown by CIGTF over the test range and measurements from the RRS transponders, GPS receiver, and NRS INS, along with the navigation solution of the test system, are recorded to magnetic storage devices for post-flight processing. The post-flight processing of the data provides the NRS EKF solution, which is used in comparison with the navigation solution of the test item.

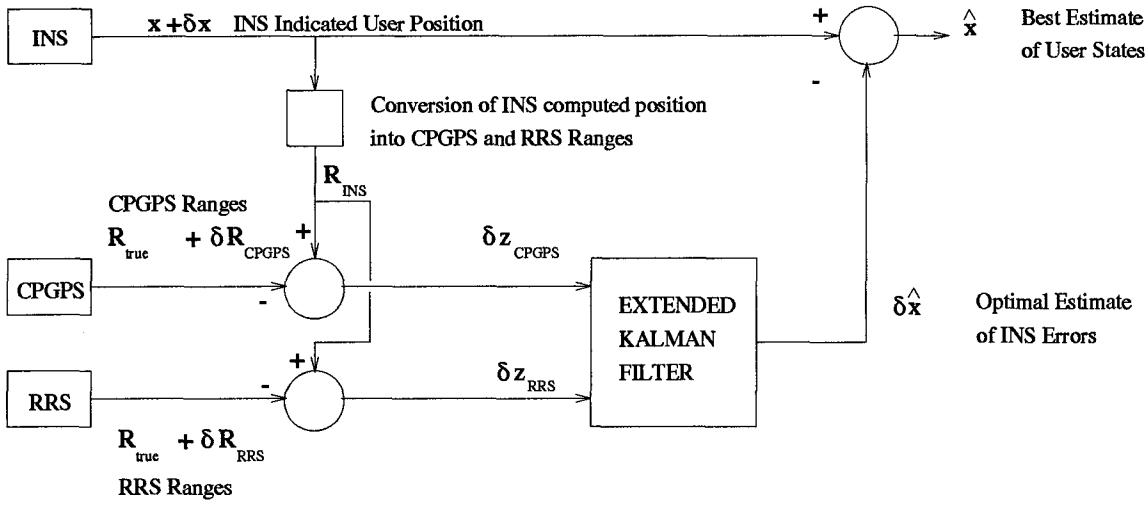

Figure 1.1 Block Diagram of CIGTF's NRS with CPGPS

1.1 Background

The current incorporation of Differential GPS (DGPS) and RRS measurements in the NRS has provided CIGTF with an adequate benchmark for inertial navigation system testing. Due to the current advances in technology and the emergence of the embedded GPS/INS systems, the accuracy levels of these new and upcoming navigation systems are beginning to approach and possibly exceed the accuracy level of the NRS. For the NRS to continue to be considered a reliable reference system, CIGTF must continue to upgrade the equipment and algorithms of the NRS to improve its accuracy. The incorporation of CPGPS measurements into the NRS is the way CIGTF has chosen to keep the accuracy of the NRS ahead of the new and upcoming systems.

The masters thesis and temporary duty assignment to CIGTF of Captain Neil Hansen of the Canadian Forces (Air) is currently being used in the development and testing of the CIGTF High-Accuracy Positioning System (CHAPS) which incorporates CPGPS measurements into its navigation solution. See Figure 1.1 for a block diagram depiction of CIGTF's NRS. The goals of this CHAPS project is to create the Sub-meter Accuracy Reference System (SARS) which will provide overall sub-meter accuracy over 2-3 hour flight profiles with baselines of up to 300 miles

from the NRS (8). The acronym NRS will be used throughout the rest of this thesis to refer to CHAPS and SARS, the reference system currently being used and tested by CIGTF.

To ensure the NRS can accurately evaluate an Integrated Navigation System's performance, reducing the errors caused by high dynamics on the reference system and the implementing of a CPGPS measurement differencing method, such as the double differencing method to be implemented in this research, is the next logical step in the development of the upgraded NRS. With an understanding of how to detect and compensate for errors associated with high dynamics, CIGTF will continue to provide the Air Force with an accurate and reliable navigation reference system.

1.2 Problem Statement

Through the introduction of CPGPS measurements into the NRS, the overall accuracy in the navigation solution of the reference system should be improved. In order to maintain this high level of accuracy in all possible flight profiles, especially profiles involving highly dynamic maneuvers, the system should be able to operate without any significant loss of accuracy in the navigation solution. A significant cause of error in the navigation solution using CPGPS would be "cycle slips" (For a better explanation of cycle slips, see Section 1.3 of this chapter and Chapter II, Section 2.3.4). The capabilities of today's fighter aircraft to complete highly dynamic maneuvers present the problem of such maneuvers causing multiple cycle slips, which over time can severely degrade the accuracy of a navigation system such as CIGTF's NRS with CPGPS. This research will explore the implementation of a CPGPS double differencing measurement technique to reduce further the errors inherent in the system. Also to be covered will be the problem of cycle slips and the development of ways to detect, isolate, and recover from the occurrence of cycle slips.

1.3 Summary of Previous Knowledge

The NRS models to be implemented in this thesis effort have come from the thesis research of several AFIT graduate students. The thesis work of Britt Snodgrass (26), Joseph Solomon (28), Richard Stacey (29), William Negast (23), William Mosle (20), and Neil Hansen (9) have developed the current NRS models which are to be used in this thesis.

Neil Hansen(9) has completed the initial work in the integration of CPGPS into the current NRS to develop the Precision Navigation Reference System (PNRS). Through a thorough investigation of CPGPS characteristics, Hansen was able to construct the equations and models necessary for implementation of CPGS into the current NRS filter. His research has shown an improvement over the Enhanced Navigation Reference System (ENRS) results of Negast(23), who used DGPS and not CPGPS. Although this improvement was not on the scale of an order of magnitude from the ENRS, this improvement validates that incorporation of CPGPS into the NRS should increase the accuracy of the system, as expected. Hansen also investigated the effects of small and large cycle slips (loss of phase lock between receiver and satellite) on the filter. These two types of cycle slips were used because, through experience, it was found that these are the most realistic types of cycle slips (9). The results from these tests showed that the effects of small cycle slips can become "lost in the noise" and never become observable in the navigation solution (9). For large cycle slips, the filter was able to estimate the phase ambiguity term (to be explained in Chapter II, Section 2.3.2 and apply corrections to the navigation solution with nominal errors, but the several minutes needed for recovery is unacceptable for accurate navigation in a highly dynamic environment. Also, Hansen did not implement any measurement differencing techniques, nor did he develop any detection, isolation or recovery algorithms in his evaluation of cycle slips. His research concentrated on the effects of cycle slips on the estimated variables.

The desire of CIGTF to operate an airborne sub-meter accuracy reference system over large baselines of up to 300 miles (8) with various amounts of dynamics motivates the need to investigate

the accuracy of CPGPS systems in this type of environment. Lachapelle and his colleagues have conducted dynamic land experiments to investigate the use of DGPS over a baseline of 600 miles using both pseudorange and carrier-phase measurements (7). The conditions of the tests conducted by Lachapelle et. al are similar to those experienced in a CIGTF flight test, therefore validating its use in this research. The authors used a series of static and dynamic experiments to establish the validity of the claim that the use of CPGPS measurements will increase the overall accuracy of the system through the reduction of inherent errors in the system by using the more accurate CPGPS measurements. The comparison of results of the static and dynamic experiments shows that CPGPS measurement incorporation does increase the accuracy of the system by a margin of one to eight meters with the use of CPGPS.

The method in which CPGPS measurements are taken has a profound effect on the overall improvement of the accuracy of the navigation solution. Through the use of various methods of single, double, or triple differencing between the different measurements, several significant inherent errors of GPS can be eliminated or reduced significantly. Lachapelle, Gerard, and Casey have investigated the use of single and double differencing techniques in high precision GPS navigation (6). The effect each differencing technique has on inherent GPS errors was also covered in (6). An in-depth discussion on the differencing techniques mentioned above and their effects on GPS errors is given in Chapter II, Section 2.3.3.

The accurate estimation of the carrier-phase ambiguity term, the integer quantity from which the CPGPS phase-range measurement is obtained, is important to the overall accuracy of the CPGPS navigation solution in the presence of cycle slips. Because the phase ambiguities remain unchanged until a cycle slip occurs, the phase ambiguities can, in principle, be held fixed for that sequence once initially found (7). Interruptions of the receiver's phase monitoring, caused by highly dynamic maneuvers or satellite shadowing due to surrounding terrain, cause the phase cycle count to stop and cause phase cycles to be "slipped" and go uncounted. Once the receiver regains satellite

lock, the cycle slip terminates, and the receiver will begin counting cycles again as if the cycle slip had never occurred, creating a navigation solution containing unacceptable errors. To correct for this problem, the appropriate number of slipped cycles must be determined through estimation using other measurements and added to all of the phase ambiguity terms affected by the cycle slip to reestablish the original phase ambiguity (13). For more information into carrier-phase ambiguity estimation and cycle slip occurrence, see Chapter II, Sections 2.3.2 and 2.3.4, respectively.

If a cycle slip does occur, it must be compensated, as stated previously, otherwise the CPGPS receiver will provide inaccurate position readings which is unacceptable for CIGTF's upgraded NRS. To accomplish this task, a cycle slip must first be detected, then the satellite or satellites which have lost lock on the receiver must be determined. Once the cycle slip is detected and successfully isolated, an algorithm to estimate the phase ambiguity term must be implemented to allow for recovery from the cycle slip without significant degradation of the navigation solution's accuracy. The thesis research of William Mosle (20) investigated ways of implementing failure detection, isolation, and recovery algorithms into the NRS. Using statistical tests such as Chi-Squared and Generalized Likelihood Ratios, Mosle was able to detect a series of different failures in the RRS transponders and with code-phase GPS measurements successfully and recover from them. Wong et. al in (32) discuss the importance of cycle slip removal in a GPS-INS system for high accuracy positioning. They suggest using a Kalman filter to estimate the number of cycles slipped by keeping track of the rate of change of the carrier phase (32). Another method of cycle slip removal can be accomplished by using INS aiding to provide position and velocity data to the receiver to maintain accuracy of the CPGPS measurements over the cycle slip period (11, 32).

1.4 Assumptions

This section list the assumptions to be used in this thesis research. These assumptions are clearly defined to aid the reader in making a proper evaluation of the work presented in this thesis.

1. The results presented in this thesis come from computer simulations. The truth models used in this research are to represent the "real world." For a clear definition of all truth and filter models implemented in this research, see Chapter III and Appendix A for a tabular listing of the specific states.

2. The truth models developed for the Multimode Simulation for Optimal Filter Evaluation (MSOFE)(3) used by Hansen (9) will be taken as accurate and sufficient representations of the "real world."

3. The filter model to be used will be the reduced-order filter model of Mosle's research (20) with the addition of four phase ambiguity states necessary for the implementation of CPGPS measurements.

4. The one-state baro-altimeter model used in Hansen's research (9) will be assumed to be an accurate representation of a real barometric altimeter. The use of a baro-altimeter as an outside source of stabilization for the INS is necessary to compensate for the inherent instability of the INS in the vertical channel (1). A description of the baro-altimeter model can be found in Chapter II, Section 3.7.1.

5. The CPGPS antenna to be used will be placed on the top of the test aircraft's body to permit maximum exposure of the antenna to the GPS satellite constellation. The RRS transponder antenna will be placed on the belly of the test aircraft, again to maximize the exposure of the antenna to the ground transponders. The two antennas will be assumed collocated at the aircraft's center of gravity with the INS. This assumption is made to eliminate the need for moment arm compensation in the measurements. Extensions to this research to include non-collocated units can easily be made. Figure 1.2 depicts the locations of the INS and antennas on a model of a typical aircraft. The locations of the antenna on the top and bottom of the aircraft's fuselage are consistent with the locations on the test aircraft used by CIGTF. The

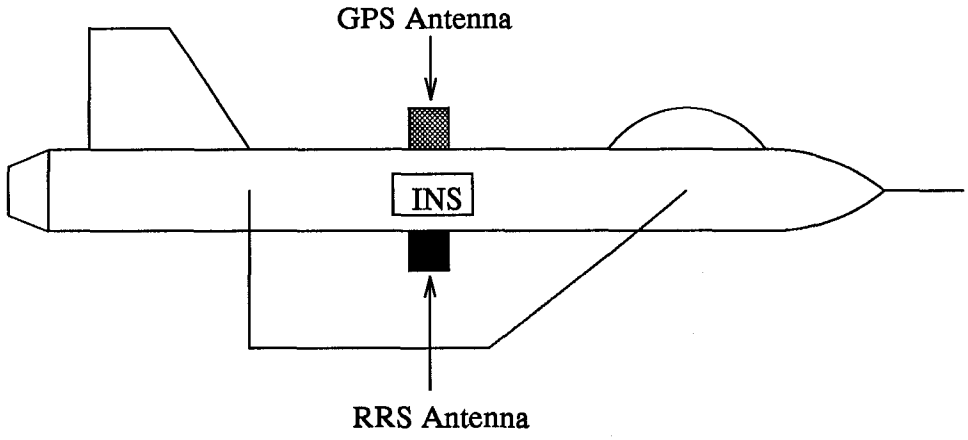

Figure 1.2 GPS, RRS Antenna and INS Locations on Model Test Aircraft

assumption of collocation of the INS and antennas does not hold true for CIGTF test aircraft and is for simulation purposes only.

6. The CPGPS measurements used as inputs to the EKF implemented in MSOFE are assumed to be differentially corrected upon entering the simulation. The noise levels associated with the measurements are determined by the simulation's operator for implementation into MSOFE. These adjustable noise levels allow for the simulation to represent not only one receiver but many different receivers through proper alterations made to the input data.

7. The simulation runs to be conducted on MSOFE will be the results of 15-run Monte Carlo analyses. Although a larger number of Monte Carlo runs would produce sample statistics that more closely reflect the true underlying error statistics, with an infinite number of runs producing truly optimal results, fifteen was decided upon to keep the computational burden and time of each simulation run within reasonable limits to maximize the amount of time devoted to true research.

8. The flight profiles and GPS satellite data used in this thesis effort will come from one of two sources. The first source is PROFGEN and the MSOFE user subroutines ORBITS and CALDOP. PROFGEN (22) is a software package which generates flight profile data based on user inputs for implementation in MSOFE. The user subroutines ORBITS and CALDOP

are the results of the thesis work of Hansen and Mosle (9, 20). ORBITS calculates the GPS satellites positions based upon GPS almanac data which is an input to the subroutine. CALDOP determines which satellites are in view of the GPS antenna and receiver and also calculates the Position Dilution of Precision (PDOP) for a given set of satellites which are in view. The calculated PDOP is then compared to an operator-set maximum MAXDOP, and if the calculated PDOP is less than MAXDOP the set of satellites is taken into the simulation. If the PDOP is greater than MAXDOP, then CALDOP chooses another set of satellites in view and tests the calculated PDOP until it is less than MAXDOP. The orbital trajectories calculated by ORBITS are assumed to be correct through extensive testing and verification completed during their development (21).

9. The Kalman filter simulation package to be used will be the established software package MSOFE (3). All filter simulations will be run on MSOFE. All Failure Detection, Isolation, and Recovery (FDIR) algorithms will be run on the commercial software package MATLAB (14).

10. The differencing method to be used by CIGTF is tentatively to be a true double differencing method between receivers and satellites (10, 27). After discussion with Captain Britt Snodgrass of CIGTF (27), it was decided to implement the double differencing method with differentially corrected CPGPS measurements, or Method I from (8). This decision was made because it would take a lesser amount of MSOFE recoding to be fully implemented. The time saved in the use of this method allows for more time to be devoted to MSOFE debugging, research, and simulation runs. Insofar as error reduction capabilities of the two different methods mentioned, they are considered to be equivalent (25).

11. The configuration of the NRS in simulation is of a feedforward design. This configuration does not allow for any real-time corrections to be fed back to the INS, as can be found in a feedback configuration.

12. The double differencing method implemented will use the following satellite (SV) combinations: $SV1 - SV4$, $SV2 - SV4$, and $SV3 - SV4$ with satellite four, SV4, being arbitrarily chosen as the base satellite. All satellite measurements are assumed independent of each other. This allows for all process and measurement noise matrices to be diagonal (30). Appendix M contains the proof of the lack of independence of the four satellite measurements. The independence assumption is made with full knowledge of the actual dependence of the satellite measurements, which totally neglects the correlation between the satellites measurements. To compensate for this dependence would involve significant recoding of MSOFE and is beyond the scope of this thesis.

1.5 Scope

This thesis will concentrate on investigating the effect highly dynamic maneuvers have on the CPGPS measurements of the NRS, and on the detection, isolation, and recovery from poor performance. Cycle slips caused by such maneuvers will be the focus of this investigation. Of the possible different problems faced by an integrated navigation system using CPGPS in a highly dynamic environment, cycle slips have been determined to be the most significant. This decision corresponds with CIGTF's main concern in highly dynamic environments.

Once the problem of cycle slip detection is conquered, the task of developing cycle slip isolation and recovery algorithms must be completed. These algorithms are necessary to ensure that the accuracy of the NRS stays within established tolerances during the entire flight profile, regardless of the level of dynamics of the maneuvers of the test aircraft.

The inclusion of another CPGPS measurement technique will also be explored. The use of a double differencing method between receivers and satellites will be implemented to improve the accuracy of the simulated system. A double differencing technique has not been implemented at

AFIT nor CIGTF before, but is necessary to reduce/eliminate inherent errors such as the user and satellite clock biases, atmospheric delays, and the integer phase ambiguity term.

1.6 Approach/Methodology

This research will generate accurate and reliable truth and filter error state models for an Integrated Navigation System in a highly dynamic environments. The phenomenon of cycles slips in the CPGPS measurements will be the concentration of this research. The study of cycle slips will include the development of failure detection, isolation, and recovery algorithms to ensure the accuracy of the Integrated Navigation System will not be significantly degraded during cycle slip occurrences. The following steps will be taken to complete the stated task:

1. Hansen's 71-state filter model (9) will be reduced to 19-states (the first 15 states being Mosle's reduced order filter (20) and the remaining four being the four CPGPS phase ambiguity states). This filter order reduction is being accomplished to reduce the time necessary to complete a simulation run from over two days experienced by Hansen (9) to approximately eight hours for a full two-hour flight profile simulation run. This step will mean that retuning of the filter will have to be completed to ensure that the accuracy of this filter will be comparable to Hansen's filter. It is understood that the implementation of a reduced order filter will never exactly reproduce the results of Hansen's work, but the retuning to be accomplished will be to compensate for the order reduction and accuracy improvement.
2. The double differencing between receivers and satellites technique described in (8) will be implemented. This technique is expected to increase the accuracies of the reduced order filter through exploitation of the high accuracies attainable in CPGPS usage. This step will further reduce the order of the filter to 17 states and reduce the order of the truth model to 89 states. This will eliminate one of the most dominant GPS errors, the user clock bias. For a more

detailed description of the differencing techniques of CPGPS and the method to be used in this research, see Chapter II, Section 2.3.3, Chapter III, Section 3.4.2 or (8).

3. Begin development and implementation of Cycle Slip Failure Detection, Isolation, and Recovery (FDIR) algorithms. After tuning and cycle slip induction into the simulation is working accurately and reliably, the feasibility of proposed FDIR algorithms will be studied for their accuracy and reliability.

The NRS configuration implemented in MSOFE is depicted in Figure 1.3. When compared to Figure 1.1, the differences between the real system and simulated system of this figure are evident through the additions of the PROFGEN and ORBIT data blocks for flight and satellite trajectories. Also, the real components of the NRS, the INS, GPS and RRS receivers, are replaced by models of each component which add the modeled errors of each component to the true position or range provided by PROFGEN or ORBITS. As can be seen in the block diagram, most of the data

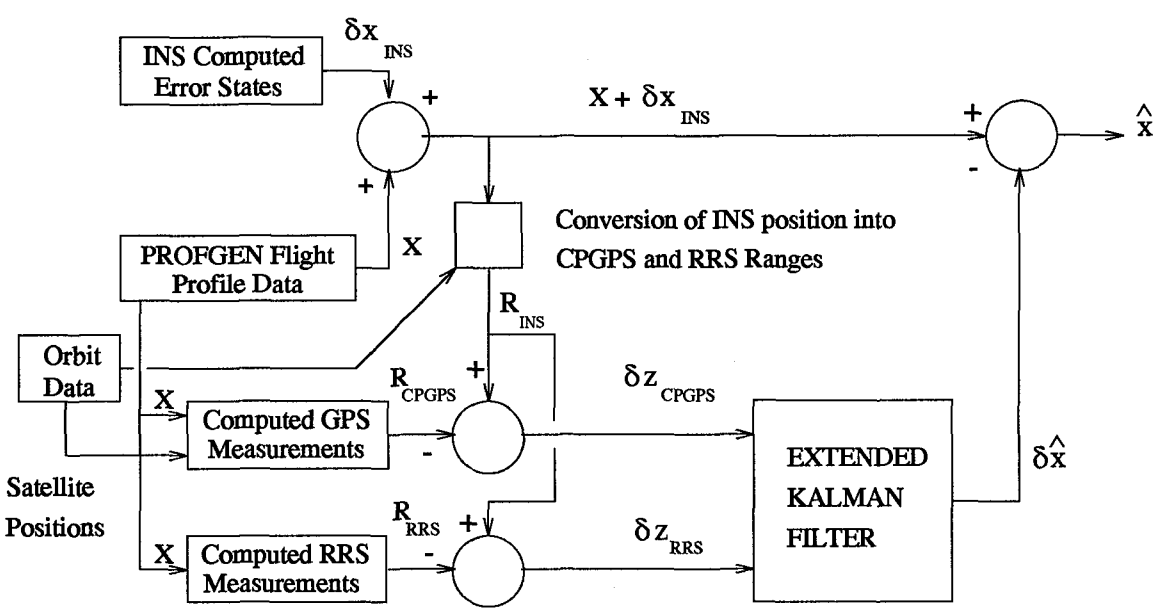

Figure 1.3 Block Diagram of CIGTFs NRS as Implemented in MSOFE

processing is completed outside of the Extended Kalman Filter (EKF). Before any measurements are input into the EKF, the differences between the INS-computed ranges to the GPS satellites

and RRS transponders must be subtracted from the GPS satellite and RRS transponder-computed ranges to produce the proper error measurement for the EKF. All computations of satellite and transponder positions and ranges are internally computed in MSOFE, while the user position comes from the flight profile generated by PROFGEN. The outputs of the EKF are the filter's best estimate of the INS and GPS error states.

When the double differencing technique is introduced into MSOFE, some changes must be made to Figure 1.3. These changes are depicted in Figure 1.4. The major difference in the two

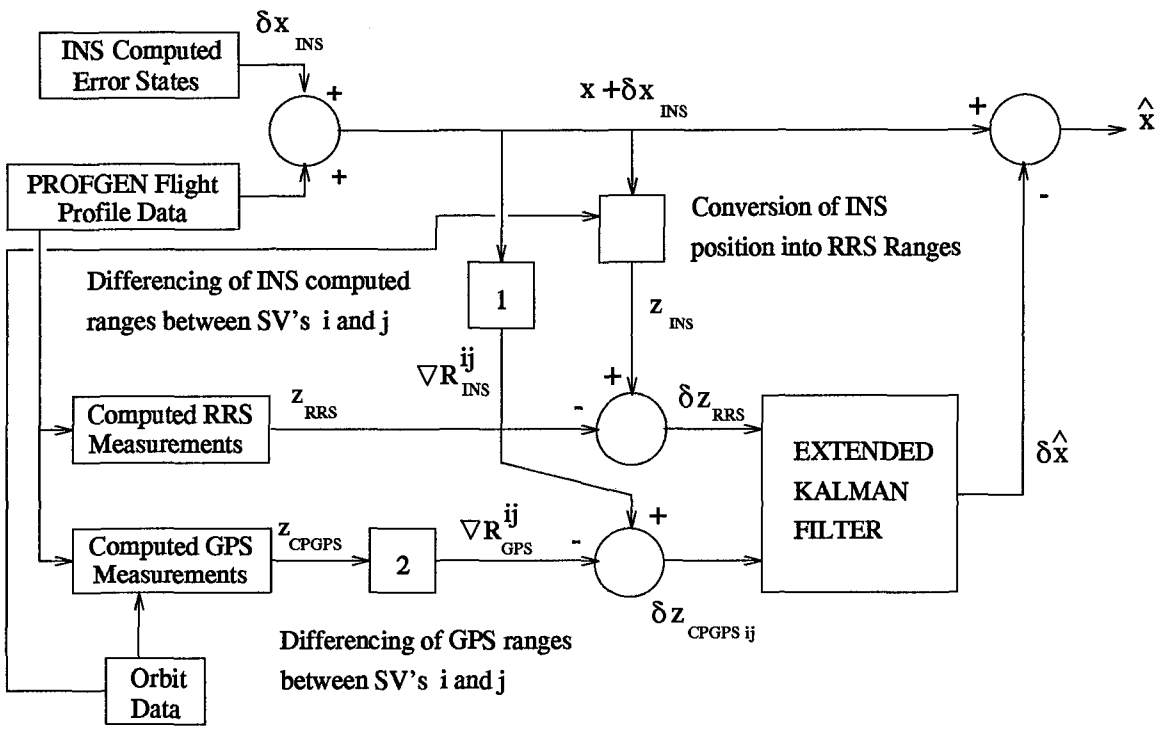

Figure 1.4 NRS Implementation in MSOFE with Single Differencing Between Receiver and Satellites

configurations comes in the addition of the two blocks (blocks 1 and 2) which compute the necessary difference between satellites for the double differencing technique. The rest of the implementation is the same as in the previous configuration of Figure 1.3.

1.7 Overview of Thesis

The methodology presented in this chapter is meant to accomplish several goals. The first goal to be accomplished is to speed up the simulation time of the MSOFE runs without sacrificing accuracy. Once this is accomplished, a new measurement technique will be implemented, with the expectation that the accuracy of the system will be increased. Finally, FDIR algorithms will be developed to preserve the system's accuracy in the face of cycle slips brought on by highly dynamic maneuvers.

This thesis consists of five chapters. Chapter I has presented the problem to be solved and the approach to be taken in solving it. Chapter II covers the theory involved in this thesis. Topics covered in Chapter II include an overview of Extended Kalman Filter Theory along with Kalman Filter tuning and filter order reduction techniques. The theory involved with Carrier-Phase GPS includes how the measurement equations are derived, the different differencing techniques, and cycle slips. Finally, the theory of the FDIR techniques and methods implemented will also be covered. Chapter III presents the NRS and PNRS truth, filter, and measurement models implemented in this thesis. The results of the filter simulations are presented in Chapter IV and Chapter V gives conclusions and recommendations for future research.

II. Theory

2.1 Overview

The purpose of this chapter is to provide an overview of the theory involved with the Extended Kalman Filter, Carrier-Phase GPS and proposed FDIR schemes. The Extended Kalman Filter section will provide an overview of the equations used along with a brief discussion of filter order reduction and filter tuning. For the Carrier-Phase GPS section, the theory associated with Carrier-Phase GPS and the associated measurement equations are presented. A detailed explanation of the derivation of the carrier-phase observation equations is also presented. The FDIR section includes theoretical descriptions of the two schemes presented.

For readers unfamiliar with the topics of Extended Kalman Filtering, a review of Maybeck's textbooks (15–17) or other texts on stochastic estimation and control is recommended. Complete derivations and discussions of the noted topics can be found in references (15–17) from which much of the information on Extended Kalman Filters was taken. For more information on Carrier-Phase GPS theory, it is recommended to review (2) and (9), where much of the presented information can be found.

2.2 Extended Kalman Filtering

2.2.1 Extended Kalman Filter Equations. The error state models of the GPS and INS consist of a set of nonlinear state-space differential equations. These nonlinearities eliminate the use of a Linear Kalman Filter. Because of this constraint, an EKF is to be implemented in this thesis. The basic idea of the EKF is to *relinearize* about each state estimate, $\hat{\mathbf{x}}(t_i^+)$, once it has been computed (16). The subsequent derivation and many of the following equations are taken from (16).

Assume the state models are a set of non-linear continuous-time differential equations of the form:

$$\dot{\mathbf{x}}(t) = \mathbf{f}[\mathbf{x}(t), t] + \mathbf{G}(t)\mathbf{w}(t) \tag{2.1}$$

where $\mathbf{f}[\mathbf{x}(t), t]$ is the state dynamics vector which in general is a nonlinear function of the state vector $\mathbf{x}$(t) and of time t. $\mathbf{G}$(t) is a noise distribution matrix which is assumed for this work to be an identity ($\mathbf{I}$) matrix. The vector represented by $\mathbf{w}(t)$ is a white Gaussian noise process with the following statistics:

$$\mathbf{m}_w = E\{\mathbf{w}(t)\} = \mathbf{0} \tag{2.2}$$

and the noise strength, $\mathbf{Q}(t)$:

$$E\{\mathbf{w}(t)\mathbf{w}^T(t+\tau)\} = \mathbf{Q}(t)\delta(\tau) \tag{2.3}$$

It is also assumed that the measurements of the system are discrete-time measurement updates of the form:

$$\mathbf{z}(t_i) = \mathbf{h}[\mathbf{x}(t_i), t_i] + \mathbf{v}(t_i) \tag{2.4}$$

where $\mathbf{z}(t_i)$ is the measurement update at time t_i, $\mathbf{h}$ is a known vector which is a function of the states and time. The vector $\mathbf{h}$ can be either linear or nonlinear. For this thesis, $\mathbf{h}$ is a nonlinear function of the state vector and time due to the nonlinear nature of the GPS measurements. The vector $\mathbf{v}(t_i)$ represents a white Gaussian noise process with the following statistics:

$$\mathbf{m}_v = E\{\mathbf{v}(t_i)\} = \mathbf{0} \tag{2.5}$$

with noise covariance, $\mathbf{R}(t_i)$:

$$E\left\{\mathbf{v}(t_i)\mathbf{v}^T(t_j)\right\} = \begin{cases} \mathbf{R}(t_i) & t_i = t_j \\ \mathbf{0} & t_i \neq t_j \end{cases} \tag{2.6}$$

For the EKF to produce an optimal estimate of the error state vector $\hat{\mathbf{x}}(t)$, the system must first be linearized. To form the linearized perturbation equations, the linearization method described in (15) will be used. The following derivation is the linearization of Equations (2.1) and (2.4) using this method.

First a nominal state trajectory, $\mathbf{x}_n(t)$, is assumed to exist for all time $t \in T$, where T represents the complete time set under consideration, which satisfies the differential equation:

$$\dot{\mathbf{x}}_n(t) = \mathbf{f}[\mathbf{x}_n(t), t] \tag{2.7}$$

which starts from the initial condition $\mathbf{x}_n(t_o) = \mathbf{x}_{no}$ where $\mathbf{f}[\cdot, \cdot]$ is the same as defined in Equation (2.1). The nominal noise-free measurement update equation taken with respect to this nominal trajectory becomes:

$$\mathbf{z}_n(t_i) = \mathbf{h}[\mathbf{x}_n(t_i), t_i] \tag{2.8}$$

where $\mathbf{h}[\cdot, \cdot]$ is as given in (2.4).

To perturb the actual state from this assumed nominal state trajectory, subtract Equation (2.7) from (2.1):

$$[\dot{\mathbf{x}}(t) - \dot{\mathbf{x}}_n(t)] = \mathbf{f}[\mathbf{x}(t), t] - \mathbf{f}[\mathbf{x}_n(t), t] + \mathbf{G}(t)\mathbf{w}(t) \tag{2.9}$$

Now, taking a Taylor series expansion about $\mathbf{x}_n(t)$ on $\mathbf{f}[\mathbf{x}(t), t]$ produces:

$$\mathbf{f}[\mathbf{x}(t), t] = \mathbf{f}[\mathbf{x}_n(t), t] + \left.\frac{\partial \mathbf{f}[\mathbf{x}, t]}{\partial x}\right|_{\mathbf{x}=\mathbf{x}_n(t)} [\mathbf{x}(t) - \mathbf{x}_n(t)] + h.o.t. \tag{2.10}$$

where $h.o.t.$ represents higher order terms which are terms of $\delta\mathbf{x}(t)$ in powers greater than one. Now, by rearranging Equation (2.10) the following relation is produced:

$$\mathbf{f}[\mathbf{x}(t), t] - \mathbf{f}[\mathbf{x}_n(t), t] = \left.\frac{\partial \mathbf{f}[\mathbf{x}, t]}{\partial x}\right|_{\mathbf{x}=\mathbf{x}_n(t)} [\mathbf{x}(t) - \mathbf{x}_n(t)] + h.o.t. \tag{2.11}$$

which now can be substituted into Equation (2.9) to produce:

$$[\dot{\mathbf{x}}(t) - \dot{\mathbf{x}}_n(t)] = \left.\frac{\partial \mathbf{f}[\mathbf{x}, t]}{\partial x}\right|_{\mathbf{x}=\mathbf{x}_n(t)} [\mathbf{x}(t) - \mathbf{x}_n(t)] + h.o.t. + \mathbf{G}(t)\mathbf{w}(t) \tag{2.12}$$

where $\delta\mathbf{x}(t)$ will be used to represent $[\mathbf{x}(t) - \mathbf{x}_n(t)]$. Invoking a first order approximation and substituting Equation (2.12) into Equation (2.9) produces:

$$\delta\dot{\mathbf{x}}(t) = \mathbf{F}[t; \mathbf{x}_n(t)]\delta\mathbf{x}(t) + \mathbf{G}(t)\mathbf{w}(t) \tag{2.13}$$

where $\delta\dot{\mathbf{x}}(t)$ is the perturbation state derivative defined by $[\dot{\mathbf{x}}(t) - \dot{\mathbf{x}}_n(t)]$ and the matrix $\mathbf{F}[t; \mathbf{x}_n(t)]$ is defined by:

$$\mathbf{F}[t; \mathbf{x}_n(t)] = \left.\frac{\partial \mathbf{f}[\mathbf{x}(t), t]}{\partial \mathbf{x}}\right|_{\mathbf{x}=\mathbf{x}_n(t)} \tag{2.14}$$

Using the same procedure on Equation (2.4), the perturbed discrete-time measurement equation is expressed as:

$$\delta\mathbf{z}(t_i) = \mathbf{H}[t_i; \mathbf{x}_n(t_i)]\delta\mathbf{x}(t_i) + \mathbf{v}(t_i) \tag{2.15}$$

where the matrix $\mathbf{H}[t_i; \mathbf{x}_n(t_i)]$ is defined by:

$$\mathbf{H}[t_i; \mathbf{x}_n(t_i)] = \left.\frac{\partial \mathbf{h}[\mathbf{x}(t_i), t_i]}{\partial \mathbf{x}}\right|_{\mathbf{x}=\mathbf{x}_n(t_i)} \tag{2.16}$$

The nonlinear dynamics and measurement update equations have been linearized to form "perturbation" or "error" state equations. This linearization process allows for the application of a linearized Kalman Filter for the system described by Equations (2.13) and (2.15). The filter implemented will output the optimal estimate of the state error vector $\delta\mathbf{x}$ represented by $\widehat{\delta\mathbf{x}}$. The estimate of the total state of the system, $\hat{\mathbf{x}}(t)$, can be computed using:

$$\hat{\mathbf{x}}(t) = \mathbf{x}_n(t) + \widehat{\delta\mathbf{x}} \tag{2.17}$$

The preceding derivation is adequate so long as the "true" and nominal trajectories do not differ significantly, else large unacceptable errors will result, i.e., $\delta\mathbf{x}(t)$ gets large and the higher order terms of the Taylor series can no longer be neglected. This requirement is clearly unreasonable for most navigation scenarios. To avoid the need for a predetermined nominal trajectory, an EKF is to be used in this application. The EKF relinearizes about each new state estimate, $\hat{\mathbf{x}}(t_i^+)$, once it has been computed. This redeclaration of the states about the new nominal trajectory ensures that the deviations from the nominal trajectory will remain small. This validates the assumption made earlier and allows for linear perturbation techniques to be employed with adequate results.

The state estimate and covariance are propagated from time t_i to the next sample time t_{i+1} through the integration of the following equations:

$$\dot{\hat{\mathbf{x}}}(t/t_i) = \mathbf{f}[\hat{\mathbf{x}}(t/t_i), t] \tag{2.18}$$

$$\dot{\mathbf{P}}(t/t_i) = \mathbf{F}[t; \hat{\mathbf{x}}(t/t_i)]\mathbf{P}(t/t_i) + \mathbf{P}(t/t_i)\mathbf{F}^T[t; \hat{\mathbf{x}}(t/t_i)] + \mathbf{G}(t)\mathbf{Q}(t)\mathbf{G}^T(t) \tag{2.19}$$

where:

$$\mathbf{F}[t; \hat{\mathbf{x}}(t/t_i)] = \left.\frac{\partial \mathbf{f}[\mathbf{x}, t]}{\partial \mathbf{x}}\right|_{\mathbf{x}=\hat{\mathbf{x}}(t/t_i)} \tag{2.20}$$

using the results of the previous measurement update cycle as initial conditions:

$$\hat{\mathbf{x}}(t_i/t_i) = \hat{\mathbf{x}}(t_i^+) \tag{2.21}$$

$$\mathbf{P}(t_i/t_i) = \mathbf{P}(t_i^+) \tag{2.22}$$

where the notation (t/t_i) stands for "at time, t, based on measurements up through time t_i.

With the incorporation of discrete-time measurements, $\mathbf{z}_i$, the EKF is accomplished through the following equations:

$$\mathbf{K}(t_i) = \mathbf{P}(t_i^-)\mathbf{H}^T[t_i;\hat{\mathbf{x}}(t_i^-)]\{\mathbf{H}[t_i;\hat{\mathbf{x}}(t_i^-)]\mathbf{P}(t_i^-)\mathbf{H}^T[t_i;\hat{\mathbf{x}}(t_i^-)] + \mathbf{R}(t_i)\}^{-1} \tag{2.23}$$

$$\hat{\mathbf{x}}(t_i^+) = \hat{\mathbf{x}}(t_i^-) + \mathbf{K}(t_i)\{\mathbf{z}_i - \mathbf{h}[\hat{\mathbf{x}}(t_i^-), t_i]\} \tag{2.24}$$

$$\mathbf{P}(t_i^+) = \mathbf{P}(t_i^-) - \mathbf{K}(t_i)\mathbf{H}[t_i;\hat{\mathbf{x}}(t_i^-)]\mathbf{P}(t_i^-) \tag{2.25}$$

The EKF Equations (2.18) through (2.25) are programmed into MSOFE (3) for the simulation.

2.2.2 Kalman Filter Order Reduction. Filter order reduction is an important step in any filter design. Filter order reduction is the design step in which less dominant states of the models are either eliminated, due to lack of contribution to the overall solution, or absorbed into other more dominant states. Often implementation of a full order filter or truth model becomes too computationally burdensome for most computer systems due to the large number of states which must be evaluated. For example, most aircraft's computer systems have several functions which must run simultaneously. To be able to do this on-line and in real time, the different functions are ranked by the importance each function has in keeping the aircraft operating in a stable environment. With this type of system, navigation filters, which are not as crucial as flight control functions, are given lesser priority, computation time, and memory storage allocation. For an on-line navigation filter to be able to complete its job in the time allowed, the number of states in the filter model must be at a minimum. Otherwise, accurate measurement updates can be delayed because the computational time for the filter can be longer than the time allotted to the filter. This will cause the filter to have to wait until the next time computations can be made so as to finish a run and update the states. This justifies the need for filter order reduction. Although

filter order reduction reduces the computational time of the filter, the order reduction forces the filter to be sub-optimal as compared to full order or truth models. To compensate for this sub-optimality problem, a process of filter tuning must be completed. Filter tuning is discussed later in Section 2.2.3.

The models used in this thesis are the results of the previous research of Hansen (9) and Mosle (20). Their work implemented the models of Negast (23) and his predecessors (26,28,29,31). The LN-93 model implemented reduces the 93-state error model (5) to 39 states. This reduction comes from the research of Lewantowicz and Keen and can found in (12). In (12), the authors tested reduced-order models ranging from forty-one to seventeen states. The GPS and RRS models implemented are the results of the masters' theses work of (26,28,29). The CPGPS models used in this research come from (9). For a more detailed description of the INS, RRS, DPGPS, and CPGPS models, see Chapter III.

In Hansen's research (9), a post-processing technique was adopted, as required by CIGTF. CIGTF requires that the filter order be seventy states or less to ensure that a twenty-four hour processing time is kept. This is based on the usage of a Hewlett-Packard 9000 minicomputer running a ten-run Monte Carlo simulation for a two-hour aircraft flight profile (9). For this research a post-processing technique will also be adopted. To reduce the time required to conduct a fifteen-run Monte Carlo simulation from Hansen's research of over two days (9), the reduced order model of Mosle's research (20) will be implemented with the addition of four phase ambiguity states necessary for CPGPS implementation. The use of Mosle's models reduces the number of filter model states from the seventy-one of Hansen's research to nineteen states. A more detailed description of the models implemented in this research is given in Chapter III.

The goal of filter order reduction is to decrease the number of states of the filter model without significant reduction in the accuracy of the state estimates from the full order or truth

model's evaluation. This makes the process of choosing which states to eliminate or combine with other states a critical process in the design and implementation of this type of system.

2.2.3 Kalman Filter Tuning. A Kalman Filter proves to be an optimal estimator of a system implementing dynamics and measurement equations which can be described as linear systems driven by white Gaussian noise and deterministic inputs (15). The construction of a full order filter model requires dynamics and measurement equations along with process and measurement noise strengths between the filter and truth models to be identical. The process of filter order reduction (discussed in Section 2.2.2) causes the filter-assumed process and measurement noise strengths to be adjusted to compensate for the states which were affected in the filter order reduction. For the Extended Kalman Filter implemented in this research, even a full order filter would not be optimal due to the first order perturbation approximations made in deriving the Extended Kalman Filter equations of Section 2.2.1. This process of adjusting noise strengths for model mismatching of states is call Kalman filter "tuning." This section presents an overview of the rationale of the tuning process used in this research.

The tuning process involves the adjustment of the values in this process noise strength matrix $\mathbf{Q}$ and the measurement noise covariance matrix $\mathbf{R}$. The tuning of these values continues until the filter performance tracks the truth models to within acceptable limits. Due to the sub-optimality of the system being implemented, the desired accuracy attained by tuning depends on the type of application and the design engineer's discretion. For the reduction of the filter model from a full order to some desired number of states, the filter-assumed $\mathbf{Q}$ and $\mathbf{R}$ values will in most cases be increased except for special cases where a decrease of the $\mathbf{Q}$ and $\mathbf{R}$ terms will be necessary. An example of a special case would be where the $\mathbf{Q}_d(t_i)$ and $\mathbf{R}(t_i)$ values are representative at one sample period and if the sample time is decreased the amount of uncertainty in the models and measurements could also be decreased because the error propagation time is now shorter.

The tuning of $\mathbf{Q}$ takes place for three reasons. Keeping any value of the Kalman Filter gain, $\mathbf{K}(t_i)$, from going to zero is the first reason behind Kalman Filter tuning. The occurrence of this problem causes the filter to become too confident in its dynamics model and to disregard totally the information of its incoming measurements. This causes the states for which the gain value equals zero to remain constant at the previous value and with no new measurement information being incorporated. This is evident in Equations (2.24) and (2.25). If $\mathbf{K}(t_i) = \mathbf{0}$ then Equations (2.24) and (2.25) become:

$$\widehat{\mathbf{x}}(t_i^+) = \widehat{\mathbf{x}}(t_i^-) \tag{2.26}$$

$$\mathbf{P}(t_i^+) = \mathbf{P}(t_i^-) \tag{2.27}$$

showing that no new information is used in a measurement update. By increasing the $\mathbf{Q}$ matrix values and decreasing the filter's confidence in its dynamics model, the $\mathbf{K}$ matrix can be guaranteed to never go to zero, therefore allowing new measurement information to always be used. Another problem to guard against involves the non-updating of individual states which is caused by individual elements of the of the $\mathbf{K}$ matrix becoming zero as well as the entire $\mathbf{K}$ matrix becoming zero.

The tuning of the $\mathbf{Q}$ values also prevents the filter covariance matrix $\mathbf{P}$ eigenvalues from becoming negative. This problem is rooted in the numerical and computational accuracy of the computer algorithms being used to run the filter simulations. This usually occurs when the range between computed numbers is quite large or the size of the number is beyond the numerical accuracy of the computer (for example having states with values on the order of 10^{+10} and other states having values on the order of 10^{-10}). In these two cases, a computer will often say that one or both of the values associated with significant differences in magnitude are zero. Through increasing the $\mathbf{Q}$ values, the eigenvalues can stay positive without significantly degrading the filter's performance or accuracy.

The third reason for **Q** value tuning is for compensation needed for states eliminated or absorbed in filter order reduction or for the nonlinear effects ignored in the first order approximation methods used. The states remaining after a filter order reduction which are dependent on those states either eliminated or absorbed must be compensated for these "missing" states. The nonlinear effects approximated in the implementation of an Extended Kalman Filter must also receive compensation. This compensation comes in the form of increasing **Q** on those states affected directly by filter order reduction or through relinearization.

The tuning of the measurement noise matrix **R** is necessary because of filter order reduction and nonlinearity compensation. Like with the tuning of **Q** values for filter order reduction, the **R** values associated with the states which are dependent on the states which were eliminated or absorbed must be increased to compensate for these changes to the model. Also where linearization of the measurement equation is needed for implementation into a linear Kalman Filter, **R** tuning is used to compensate for these nonlinear effects.

The Kalman filter tuning process is by far the most time consuming portion of any design. The tuning of **Q** and **R** must be done iteratively and with good engineering insight in order to be successful.

2.3 Carrier-Phase Global Positioning System Measurements

2.3.1 Carrier-Phase GPS Observation Equations. A carrier-phase measurement is the result of subtracting the generated carrier signal of the receiver from the carrier signal transmitted by the GPS satellite being received by the receiver. This subtraction or beating of the two signals leads to finding the phase-range, or the satellite-to-user range based on the carrier-phase. The phase-range term is synonymous with pseudorange which is used in code-phase measurements. The result of this subtraction step is called the *carrier beat phase observable.* This process is

represented by the following equation:

$$\Phi = \Phi^k(T) - \Phi_i(t) \tag{2.28}$$

where Φ represents the carrier beat phase observable at the receiver, $\Phi^k(T)$ represents the phase of the carrier transmitted from the kth satellite at time T and received at time, t, and $\Phi_i(t)$ represents the phase of the carrier at the ith receiver at the reference signal time, t. **Note**: T represents the satellite clock time of transmission while t is the receiver clock time of reception of the signal, and throughout the rest of this thesis the i and k indicators will be dropped and the different Φ terms will be identified by the time variable, T or t for the satellite or receiver carrier phase respectively. The time of travel of the signal δt is:

$$\delta t = t - T \tag{2.29}$$

By rearranging Equation (2.29), we can form:

$$\Phi(t) = \Phi(T + \delta t) \tag{2.30}$$

Next expand Equation (2.30) about T in a Taylor series expansion (see Equation (2.12)) produces:

$$\Phi(T + \delta t) = \Phi(T) + \left.\frac{\partial \Phi(\tau)}{\partial \tau}\right|_{\tau=T} \cdot \delta t + h.o.t. \tag{2.31}$$

where the first derivative of $\Phi(T)$ with respect to time equals the frequency, f. Due to the GPS phase/frequency relationship which is valid for highly stable oscillators over a short time interval (such as δt), the h.o.t. or higher order terms of Equation (2.31) are considered negligible. Equation (2.31) with the frequency taken as a constant becomes:

$$\Phi(T + \delta t) = \Phi(T) + f \cdot \delta t \tag{2.32}$$

Substituting Equation (2.29) into Equation (2.32) and noting that $\Phi(T+\delta t) = \Phi_i(t)$ and $\Phi(T) = \Phi^k(T)$, Equation (2.32) becomes:

$$\Phi_i(t) = \Phi^k(T) + f \cdot (t - T) \tag{2.33}$$

which can be rearranged to form:

$$\Phi = \Phi^k(T) - \Phi_i(t) = -f \cdot (t - T) \tag{2.34}$$

Now to obtain a relation of the transmission and reception times, T and t respectively, we note the clocks of the satellite and receiver are independent of each other. Not only are these clocks independent of each other, but each one is offset from true GPS time by some small error. If we are to represent true GPS time as t_{GPS}, then the reception time in relation to true GPS time is:

$$t_{GPS} = t + dt \tag{2.35}$$

where dt represents the user clock offset from true GPS time. Like with the reception time, the transmission time, T, can be related to true GPS time by its own offset term, dT, plus the time it takes for the GPS signal to propagate between the satellite and receiver. The propagation time is the distance traveled plus errors (true range to the satellite plus ionospheric and tropospheric errors) divided by the speed of the signal (speed of light). This relation is represented by the following expression:

$$T_{propagation} = \frac{(\rho - d_{ion} + d_{trop})}{c} \tag{2.36}$$

where ρ is the true range between the satellite and receiver, d_{ion} is the range equivalent of the ionospheric delay, and d_{trop} is the range equivalent of the tropospheric delay. The minus sign associated with the ionospheric delay term is due to the fact that the ionosphere actually advances

the phase of the carrier signal, making it *appear* as if the signal travels faster than the speed of light (9). The relation between the transmission time of Equation (2.36) and true GPS time is presented in the following equation:

$$t_{GPS} = T + dT + \frac{(\rho - d_{ion} + d_{trop})}{c} \tag{2.37}$$

By setting Equations (2.35) and (2.37) equal to each other, the relation between the transmission time and reception time is:

$$T + dT + \frac{(\rho - d_{ion} + d_{trop})}{c} = t + dt \tag{2.38}$$

Rearranging Equation (2.38), the following is obtained:

$$t - T = dT - dt + \frac{(\rho - d_{ion} + d_{trop})}{c} \tag{2.39}$$

The carrier phase observation equation is now obtained through substituting Equation (2.39) into Equation (2.34) giving:

$$\Phi = -f \cdot (dT - dt) - \frac{f}{c} \cdot (\rho - d_{ion} + d_{trop}) \tag{2.40}$$

As can be seen in Equation (2.40), the carrier phase observable is a function of the frequency of transmission, satellite and user clock biases, the true range, and the atmospheric delay terms.

2.3.2 Carrier-Phase GPS Phase Range Measurement Equations. A carrier phase measurement is a measure of the phase shift between the satellite-generated signal and receiver-generated signal. Because it is a phase shift, it represents only a fraction of a total wavelength. The total phase-range measurement at some time epoch, t, is represented by the following equation:

$$\Phi_{total}(t) = \Phi_{frac}(t) + \Phi_{int}(t_o, t) + N(t_o) \tag{2.41}$$

where $\Phi_{frac}(t)$ is the fractional part of the total wavelength, $\Phi_{int}(t_o, t)$ is an integer number of phase cycles from an initial epoch, t_o, to the current epoch, t, and $N(t_o)$ is an integer phase ambiguity term. The phase ambiguity term is also know as the *cycle ambiguity* and it represents the difference between the true integer count at time t_o, and the current integer count at t_o measured or calculated by the receiver (9). Figure 2.1 gives a pictorial representation of Equation (2.41). The

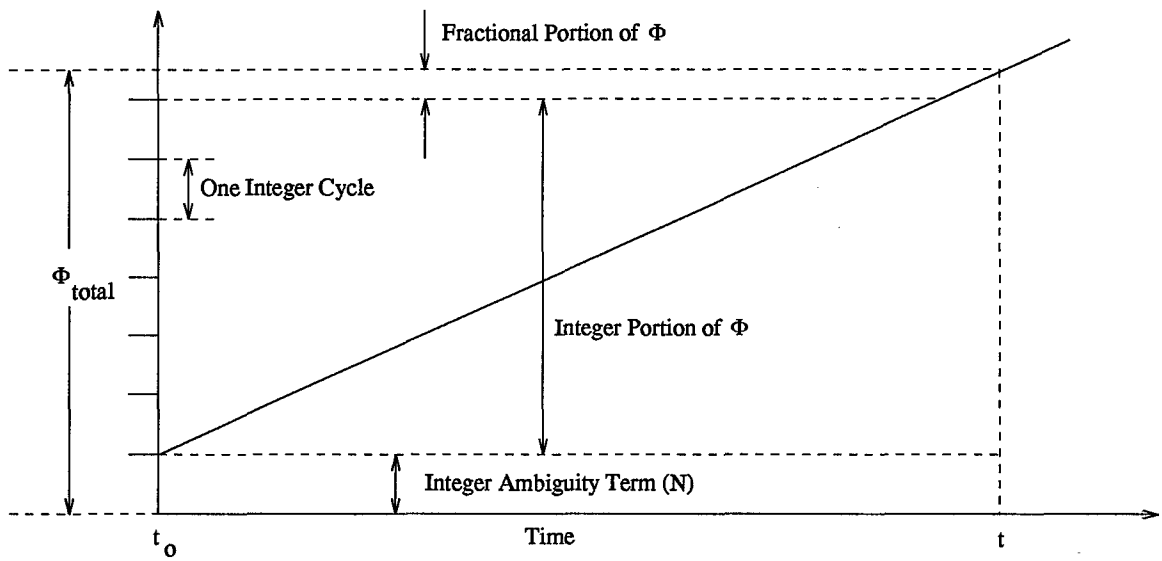

Figure 2.1 Pictorial Representation of the Total Phase-Range Measurement

phase ambiguity term, N, remains constant as long as no cycle slips occur (See Chapter I, Section 1.3 or Section 2.3.4 of this chapter for a more detailed explanation of cycle slips). Because of the unpredictability of the occurrence of cycle slips, the phase ambiguity term is a time-varying integer.

The carrier phase observation represented by Equation (2.40) is equal to the sum of the fraction observation at time epoch, t, and the integer count at the same time epoch, t, and can be represented by:

$$\Phi_{measured}(t) = \Phi_{frac}(t) + \Phi_{int}(t_o, t) \tag{2.42}$$

The total phase range at time epoch, t, from Equation (2.41) can now be written as:

$$\Phi_{total}(t) = \Phi_{measured}(t) + N(t) \tag{2.43}$$

Substituting Equation (2.40) into Equation (2.43) produces the measured phase-range for the GPS carrier-phase observable:

$$\Phi_{measured}(t) = -f \cdot (dT - dt) - \frac{f}{c} \cdot (\rho - d_{ion} + d_{trop}) - N(t) \tag{2.44}$$

Equation (2.44) represents the measured phase range in carrier cycles. For this type of application, we desire the measured phase-range in length units (feet). To convert from cycle units to length units, we multiply Equation (2.44) by the negative value of the carrier wavelength, λ, to produce:

$$\Phi(t) = \rho + c \cdot (dT - dt) - d_{ion} + d_{trop} + \lambda \cdot N(t) \tag{2.45}$$

where: $\Phi(t)$ = $-\Phi_{measured}(t) \cdot \lambda$ = the phase-range measurement at time epoch, t, or

ρ = true (but unknown) range from the satellite to the user

c = speed of light

dt = user clock offset

dT = satellite clock offset

λ = carrier wavelength

$N(t)$ = the integer phase ambiguity term at time epoch, t

d_{ion} = the range equivalent ionospheric delay term

d_{trop} = the range equivalent tropospheric delay term

2.3.3 Differencing Techniques. This section covers the various differencing techniques which can be used to improve the accuracies of CPGPS measurments. The three methods to be discussed are distinguished by the number of differences taken for each measurement. A description of how each difference is taken is given, along with its specific effect on CPGPS errors such as user clock bias, atmospheric errors, and phase ambiguity errors. Table 2.1 defines the symbols used to describe the different differencing methods.

Table 2.1 CPGPS Measurement Difference Symbols

Symbol	Definition
Δ	Difference Taken Between Two Receivers
∇	Difference Taken Between Two Satellites
δ_t	Difference Taken Between Two Time Epochs

2.3.3.1 Single Differencing. Single Differencing of CPGPS measurements has three different forms: the between-receivers single difference, between-satellites single difference, and the between-epoch (Doppler) single difference. The between-receivers single difference is the difference in the phase-range measurements between two receivers which are simultaneously tracking the *same* satellite. Figure 2.2 provides an illustration of this differencing method. The ith receiver's

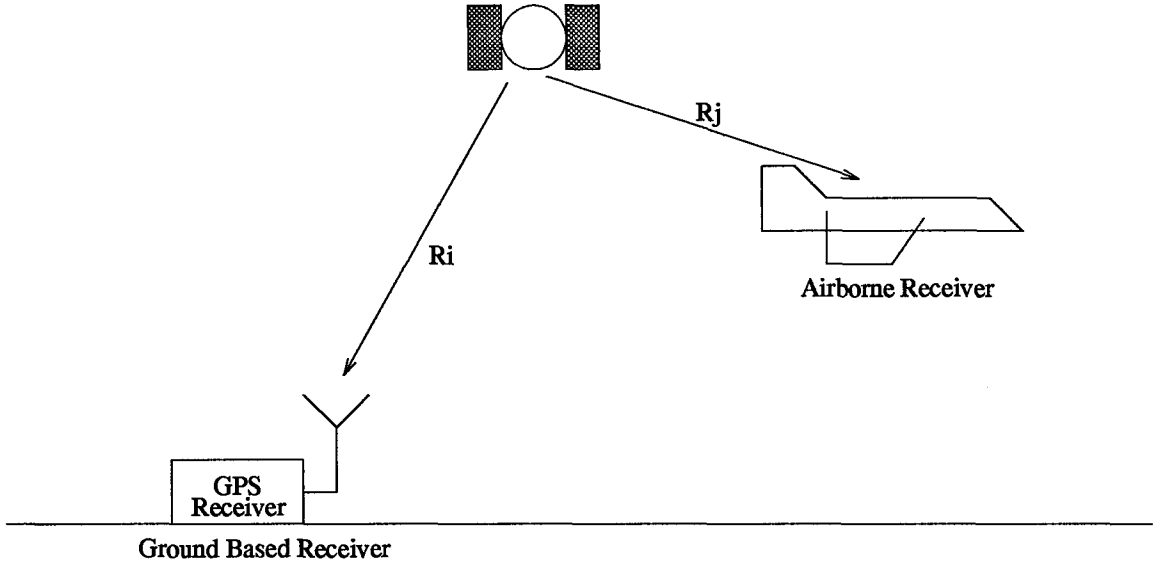

Figure 2.2 Illustration of CPGPS Between-Receivers Single Difference: $\Delta R_{ij} = R_i - R_j$

phase-range measurement is represent by the following equation:

$$R_i = R_{t_i} + \delta R_{Uclk_i} + \delta R_{Sclk} - \delta R_{ion_i} + \delta R_{trop_i} + \delta R_{N_i} + v_i \tag{2.46}$$

where: R_i = the phase-range measurement to the satellite from the ith receiver

R_{t_i} = the true (but unknown) range from the satellite to the ith receiver

δR_{Uclk_i} = range error due to user clock error of the ith receiver

δR_{Sclk} = range error due to the satellite clock error

δR_{ion_i} = range error due to ionospheric delay term of the ith receiver

δR_{trop_i} = range error due to tropospheric delay term of the ith receiver

δR_{N_i} = range error due to phase ambiguity error of the ith receiver

v_i = measurement noise term

Subtracting R_j from R_i, the phase-ranges from two different receivers, produces the between-receivers single difference which eliminates the satellite clock range error term, R_{Sclk}. A mathematical representation of the between-receivers single difference is presented in the following equation:

$$\Delta R_{ij} = \Delta R_{t_{ij}} + \Delta\delta R_{Uclk_{ij}} - \Delta\delta R_{ion_{ij}} + \Delta\delta R_{trop_{ij}} + \Delta\delta R_{N_{ij}} + \Delta v_{ij} \tag{2.47}$$

The measurement noise term, v, will still be a zero-mean, white Gaussian process but the second order statistics of v will change because of the differencing. This process creates an expression for the relative distance between the two receivers and reduces the effects of the atmospheric delay terms (if the receivers are relatively close to each other, within 200 km). The described technique is also very similar to Differential GPS because it uses two receivers tracking the same satellites. To have this differencing method be identical to DGPS, one of the receivers must be placed at a fixed survey point as in DGPS. The two receivers used in this difference method must be tracking the same four satellites in order to produce a reduced error navigation solution. This is necessary so the errors which are satellite dependent will be consistent in the differencing conducted.

The between-satellites single difference is similar to the between-receivers single difference except that the difference is taken between two satellite phase-range measurements to the same

receiver. Using the notation of Equation (2.46), the representation of the phase-range measurement from the ith satellite to the receiver can be represented by:

$$R^i = R^i_t + \delta R_{Uclk} + \delta R^i_{Sclk} - \delta R^i_{ion} + \delta R^i_{trop} + \delta R^i_N + v^i \tag{2.48}$$

Figure 2.3 depicts the between-satellites single difference. Taking the difference of the phase ranges

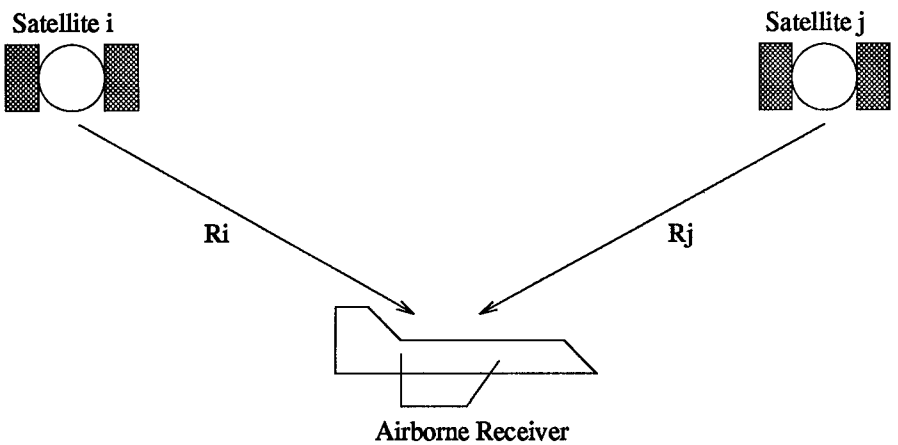

Figure 2.3 Illustration of CPGPS Between-Satellites Single Difference: $\nabla R^{ij} = R^i - R^j$

between the ith and jth satellites produces the following relation:

$$\nabla R^{ij} = \nabla R^{ij}_t + \nabla \delta R^{ij}_{Sclk} - \nabla \delta R^{ij}_{ion} + \nabla \delta R^{ij}_{trop} + \nabla \delta R^{ij}_N + \nabla v^{ij} \tag{2.49}$$

where this equation represent the relative distance between the two satellites. Note, the user clock error, δR_{Uclk}, is eliminated in the differencing.

The between-time-epochs (Doppler) single difference is the difference of the phase-range measurements between time epochs t_1 and t_2. This method requires that the difference be made between the same receiver/satellite pair. Figure 2.4 gives a pictorial representation of this differencing technique. Taking the notation used previously, the phase-range at the ith time epoch can

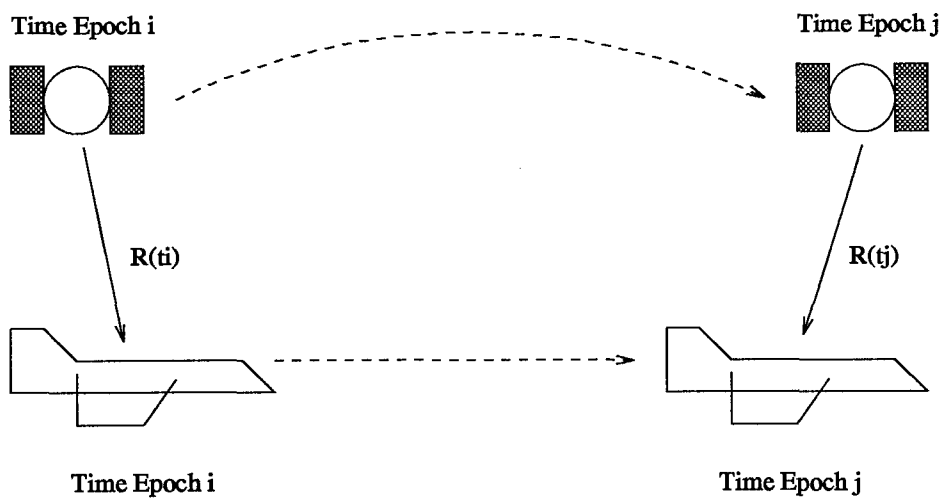

Figure 2.4 Illustration of CPGPS Between-Time Epochs Single Difference: $\delta_t R(t_i - t_j) = R(t_i) - R(t_j)$

be represented by:

$$R(t_i) = R_t(t_i) + \delta R_{Uclk}(t_i) + \delta R_{Sclk}(t_i) - \delta R_{ion}(t_i) + \delta R_{trop}(t_i) + \delta R_N(t_i) + v(t_i) \qquad (2.50)$$

To form the single difference, the phase-range measurement between the ith and jth epochs are subtracted to form:

$$\begin{aligned}\delta_t R(t_i - t_j) = \delta_t R_t(t_i - t_j) + \delta_t \delta R_{Uclk}(t_i - t_j) + \delta_t \delta R_{Sclk}(t_i - t_j) \\ -\delta_t \delta R_{ion}(t_i - t_j) + \delta_t \delta R_{trop}(t_i - t_j) + \delta_t v \qquad (2.51)\end{aligned}$$

The time-invariant phase ambiguity term is eliminated and the satellite clock and user clock errors would be eliminated if they were time-invariant. **Note**: The phase ambiguity term is only time-invariant as long as no cycle slips occur between epochs t_i and t_j. If a cycle slip does occur between epochs t_i and t_j, then a bias equal to the number of cycles slipped would be present in Equation (2.51) (9).

2.3.3.2 Double Differencing. The subtraction of two different single differencing measurements described in Section 2.3.3.1 forms the double difference measurement. Three double differencing methods exist: between receivers/time-epochs, between receivers/satellites, and between satellites/time-epochs. The between receivers/time-epochs double difference takes the difference of a between receivers-single difference measurement at one time-epoch of one receiver pair from another measurement at a later time-epoch using the same receiver pair which is tracking the same satellite. This method produces the following equation for a difference between the ith and jth receiver:

$$\delta_t \Delta R(t_i - t_j) = \delta_t \Delta \delta R_{t_i}(t_i - t_j) + \delta_t \Delta \delta R_{Uclk_i}(t_i - t_j) - \delta_t \Delta \delta R_{ion_i}(t_i - t_j) + \delta_t \Delta \delta R_{trop_i}(t_i - t_j) + \delta_t \Delta v_i \quad (2.52)$$

This differencing technique eliminates the time-invariant phase ambiguity term along with the satellite clock error. It also further reduces the atmospheric delay errors from the single differencing reduction.

The between-receiver/satellites double differencing method is the method to be implemented in this research and is depicted in Figure 2.5. This method subtracts a between-receiver single difference with another between-receiver single difference using the same receivers and a different satellite to produce the following equation:

$$\nabla \Delta R^{ij} = \nabla \Delta R_t^{ij} - \nabla \Delta \delta R_{ion}^{ij} + \nabla \Delta \delta R_{trop}^{ij} + \nabla \Delta \delta R_N^{ij} + \nabla \Delta v^{ij} \quad (2.53)$$

where i and j represent the two different satellites from which measurement are taken. This double difference method can be formed by using two different receivers and the same pair of satellites as is done in Equation (2.53). The satellite clock and user clock error bias term are eliminated in

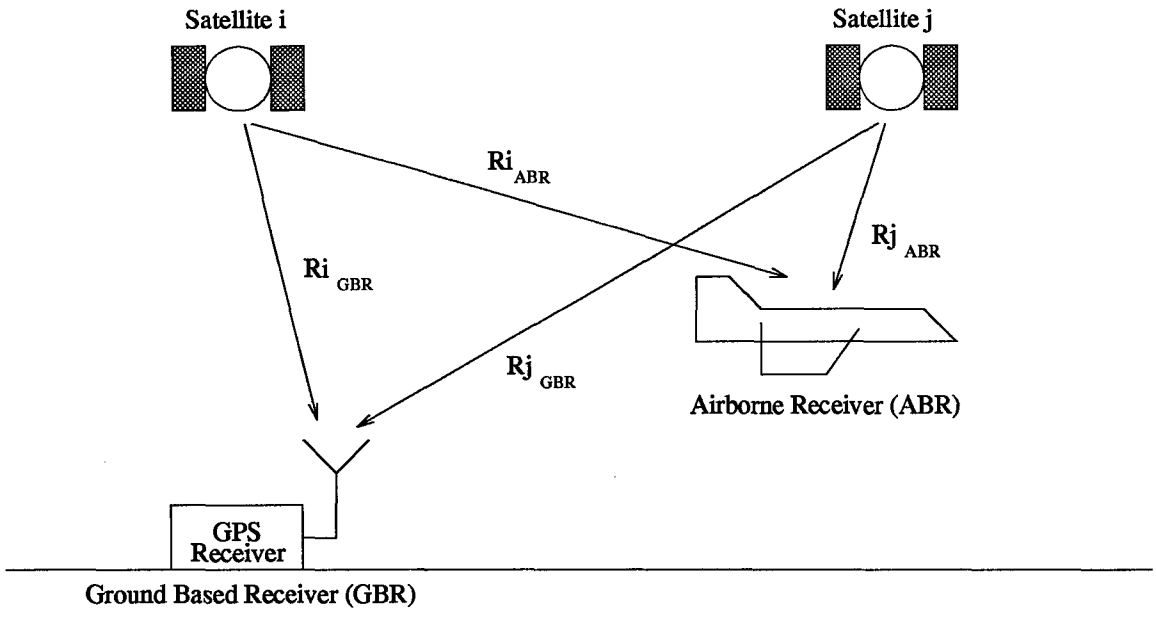

Figure 2.5 Illustration of CPGPS Between Receivers/Satellites Double Difference: $\nabla\Delta R^{ij} = \Delta R^{i}_{GBR,ABR} - \Delta R^{j}_{GBR,ABR}$

using this method along with a further reduction of the atmospheric errors from just using a single differencing method.

The between satellites/time-epochs double difference is the difference between a between-satellites single difference at one time epoch and a between-satellites single difference at a later time epoch using the same receiver. This differencing method can be written mathematically as:

$$\delta_t \nabla R(t_i - t_j) = \delta_t \nabla \delta R^i_t(t_i - t_j) + \delta_t \nabla \delta R^i_{Sclk}(t_i - t_j) - \delta_t \nabla \delta R^i_{ion}(t_i - t_j) + \delta_t \nabla \delta R^i_{trop}(t_i - t_j) + \delta_t \nabla \delta v^i \quad (2.54)$$

This method results in the elimination of the user clock bias (if constant) and time-invariant phase ambiguity (if no cycle slips occur). The satellite clock bias term would also be eliminated if it is a time-invariant quantity.

2.3.3.3 Triple Differencing. This differencing method is the result of subtracting a between receiver/satellites double difference at one time epoch from another double difference at a

later time epoch. The triple difference is expressed in the following equation:

$$\delta_t \nabla \Delta R^{ij}(t_i - t_j) = \delta_t \nabla \Delta R_t^{ij}(t_i - t_j) - \delta_t \nabla \Delta \delta R_{ion}^{ij}(t_i - t_j)$$
$$+\delta_t \nabla \Delta \delta R_{trop}^{ij}(t_i - t_j) + \delta_t \nabla \Delta v^{ij} \quad (2.55)$$

This differencing method results in the elimination of the satellite and user clock biases along with the phase ambiguity error provided no cycle slips occur. The effects of the atmospheric delay terms are also greatly reduced by the use of a Triple Differencing method. Table 2.2 presents each differencing method and each error either eliminated or reduced through the implementation of each differencing method.

Table 2.2 Effects of CPGPS Difference Measurement Methods

Difference Method	Terms Eliminated	Terms Reduced
Between Receiver Single Difference	Satellite Clock Bias	Ionospheric Delay Tropospheric Delay
Between Satellite Single Difference	User Clock Bias	
Between Time-Epochs Single Difference	Phase Ambiguity Term	Ionospheric Delay Tropospheric Delay
Between Receiver/Satellite Double Difference	Satellite Clock Bias User Clock Bias	Ionospheric Delay Tropospheric Delay
Between Receiver/Time-Epochs Double Difference	Satellite Clock Bias Phase Ambiguity Term	Ionospheric Delay Tropospheric Delay
Between Satellite/Time-Epochs Double Difference	User Clock Bias Phase Ambiguity Term	Ionospheric Delay Tropospheric Delay
Triple Difference	Satellite Clock Bias User Clock Bias Phase Ambiguity Term	Ionospheric Delay Tropospheric Delay

2.3.4 Cycle Slips. A cycle slip is the loss of carrier signal lock between the receiver and the satellite. When this occurs the receiver will attempt to reacquire the signal from the lost satellite. While attempting to reacquire the satellite, the receiver will not be counting phase

cycles and these cycles which go uncounted are called "slipped" cycles. Once lock onto the satellite has been reestablished, the receiver will continue to count phase cycles again as if the cycle slip never happened. The receiver will be able to determine the fractional portion of the measurement correctly because this remains unchanged. As for the integer portion of the measurement, a different integer phase cycle may be locked onto without the receiver knowing this has happened. The difference in the number of phase integer cycles from before and after the cycle slips produces a "jump" in the phase-range measurement. This jump is equal to the number of phase cycles which were "slipped" or which went uncounted.

The frequency and duration of cycle slips is an unpredictable phenomenon due to the many different things which can cause cycle slips. Terrain, high dynamic maneuvers such as rolls and banked turns, weather, multipath reflections, spoofing or jamming, and noise bursts are some common causes of cycle slips.

2.3.4.1 Simulation of Cycle Slips. The purpose of simulating cycle slips has two main objectives: to test the robustness of the filter, and to test the robustness of Failure Detection, Isolation, and Recovery (FDIR) algorithms for accuracy, speed, and reliability. The simulations of cycle slips used by Hansen (the large slip, the small slip, and the loss of satellite lock) (9) will be used to test the robustness of the reduced-order filter and FDIR algorithms.

The cycle slip is simulated as a step bias in the phase ambiguity term of the satellite in which the cycle slip is occurring. This is done as a step bias because, as mentioned earlier, as long as a cycle slip does not occur, the phase ambiguity term remains constant. Due to the phase ambiguity term, R_N, being in range units (feet) in MSOFE, the bias which represents a cycle slip must also be in range units. To ensure that proper units are used to provide a realistic simulation, the following relation from (9) will be used:

$$\delta R_N(t^+) = \delta R_N(t^-) + K \cdot \lambda \tag{2.56}$$

where: t^+ = the time just after the cycle slip occurs

t^- = the time just before the cycle slip occurs

K = the number of cycles slipped (+ or -)

λ = the carrier signal's wavelength

2.4 Failure Detection, Isolation, and Recovery (FDIR) Scheme

The theory involved with two different FDIR schemes are presented in this section. The first method, the Chi-Square test, can only be used as a failure detection scheme and, if set up properly, it can be used for isolation by looking for patterns in the Chi-Square random variable. The second method is proposed as a FDIR scheme which can be used to successfully detect, isolate, and recover successfully from cycle slips. The second scheme is the Multiple Model Adaptive Estimator (MMAE). In MMAE, the Chi-Square test is used in the implementation of the MMAE and this along with a proposed MMAE structure is developed.

2.4.1 The Chi-Square Test. The Chi-Square test uses the residuals of the Kalman filter to detect problems which can be failures in the system. The Chi-Square test operates on a window in time to monitor the magnitudes of the residuals, and it will declare a failure if the magnitude of the residuals remains larger than anticipated through the filter-computed residual covariance matrix (20).

The extended Kalman filter residuals determine if the Chi-Square test will declare a failure. The residual, $\gamma(t_i)$, is given by the following realtion:

$$\gamma(t_i) = z_i - h[\hat{x}(t_i), t_i] \tag{2.57}$$

These residuals are assumed to be a zero-mean white processes, to first order, with a known covariance, $\mathbf{\Lambda}(t_i)$, which is given in Equation (2.58):

$$\mathbf{\Lambda}(t_i) = \mathbf{H}(t_i)\mathbf{P}(t_i^-)\mathbf{H}^T(t_i) + \mathbf{R}(t_i) \tag{2.58}$$

The Chi-Square test is a function of the Chi-Square random variable, $\chi(t_k)$, and is given by:

$$\chi(t_k) = \sum_{i=k-N+1}^{k} \gamma^T(t_i)\Lambda^{-1}(t_i)\gamma(t_i) \tag{2.59}$$

where N is the size of the sliding window in time and k is the sample period the test is taken (20). To remove any possibility of sign cancellation in the summation of Equation (2.59), the residual values are squared. The use of the inversion of the residual covariance is to scale the square of the residuals by the filter's confidence in the residuals. The implementation of the time window, N, is to reduce the computational load and increase the accuracy of the algorithm. Of course, by setting a time window, there will be a time lag between the failure onset and detection which is dependent on the size of the time window. This dependence on N leaves a tradeoff to be made between the speed of failure detection and the accuracy of the detection algorithm. By making N smaller, the time necessary to detect a failure will be reduced but it will increase the likelihood of false alarms. The Chi-Square test declares failures through a simple threshold test. If the Chi-Square random variable exceeds the set threshold, then a failure will be declared.

2.4.2 The Multiple Model Adaptive Estimator (MMAE). The MMAE is a bank of n Kalman filters in which each filter is modelled to represent a specific satellite undergoing a cycle slip and in which one represents a fully functional system. Each filter receives the same measurements, $z(t_i)$, and calculates its best estimates of the state vector, $\hat{x}(t_i)$, and residuals, $r(t_i)$. The residuals

of each filter are then passed on to a conditional probability tester which is defined by the following:

$$p_k(t_i) = Prob\{\mathbf{a} = \mathbf{a}_k | \mathbf{Z}(t_i) = \mathbf{Z}_i\} \tag{2.60}$$

where $\mathbf{a}$ represents the vector of uncertain parameters (which is the satellite undergoing a cycle slip) and $\mathbf{Z}(t_i)$ represents the measurement time history to time t_i. To obtain a recursive relation of $p_k(t_i)$ (for $k = 1, 2, \ldots, K$) complete the following iteration:

$$p_k(t_i) = \frac{f_{\mathbf{z}(t_i)|\mathbf{a},\mathbf{Z}(t_{i-1})}(\mathbf{z}_i|\mathbf{a}_k, \mathbf{Z}_{i-1}) p_k(t_{i-1})}{\sum_{j=1}^{K} f_{\mathbf{z}(t_i)|\mathbf{a},\mathbf{Z}(t_{i-1})}(\mathbf{z}_i|\mathbf{a}_j, \mathbf{Z}_{i-1}) p_j(t_{i-1})} \tag{2.61}$$

where each $f_{\mathbf{z}(t_i)|\mathbf{a},\mathbf{Z}(t_{i-1})}(\mathbf{z}_i|\mathbf{a}_k, \mathbf{Z}_{i-1})$ can be evaluated as:

$$\begin{aligned} f_{\mathbf{z}(t_i)|\mathbf{a},\mathbf{Z}(t_{i-1})}(\mathbf{z}_i|\mathbf{a}_k, \mathbf{Z}_{i-1}) &= \frac{1}{(2\pi)^{m/2}|\mathbf{\Lambda}_k(t_i)|^{1/2}} exp\{\cdot\} \\ \{\cdot\} &= -\frac{1}{2}\gamma^T(t_i)\mathbf{\Lambda}_k^{-1}(t_i)\gamma(t_i) \end{aligned} \tag{2.62}$$

where $\gamma(t_i)$ and $\Lambda_k(t_i)$ are given in Equations (2.57) and (2.58). To rewrite the exponent of Equation (2.62) in terms of the Chi-Square random variable at one particular time, the following is produced:

$$\{\cdot\} = -\frac{1}{2}\chi(t_i) \tag{2.63}$$

These calculated probability values, $p_k(t_i)$, are used as weighting factors on each Kalman filter state estimate. Next the MMAE adds up all of the "weighted" state estimates to produce the optimal state estimate:

$$\hat{\mathbf{x}}(t_i) = \sum_{j=1}^{K} \hat{\mathbf{x}}_j(t_i) p_j(t_i) \tag{2.64}$$

Figure 2.6 pictorially illustrates the MMAE algorithm.

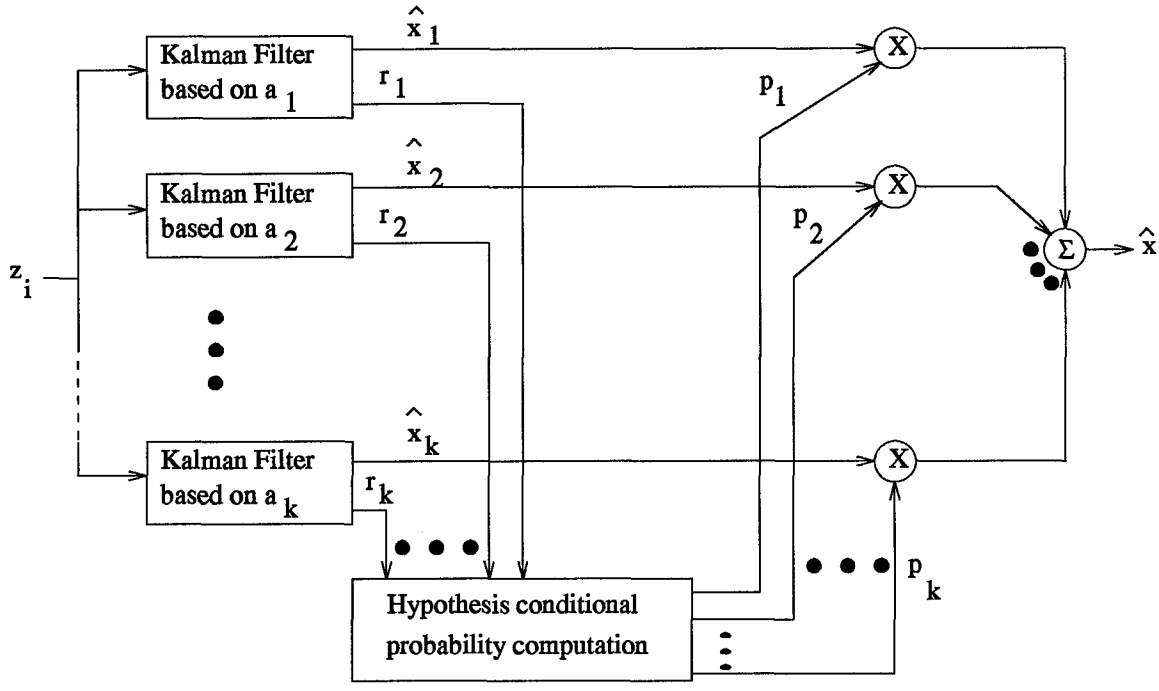

Figure 2.6 Block Diagram of MMAE Algorithm (16)

To implement this algorithm into the PNRS filter structure for the detection, isolation, and recovery from cycle slips, each extended Kalman filter modeled must be structured for an assumed cycle slip on a particular satellite. With this in mind, Figure 2.6 is modified to produce the structure shown in Figure 2.7. The setup depicted in Figure 2.7 will work well for a single cycle slip, but to compensate for multiple cycle slips which occur during a cycle slip a "Hierarchical Structure for Multiple Failures" as used by Menke (19) could be implemented to cope with this problem. In the "Hierarchical Structure" once a cycle slip or failure is declared a new set of filters would be established. The new filters would still run with the first cycle slip occurring and model any other possible single cycle slip combinations with the first cycle slip. Also included in these newly generated filters would be a filter modelling the system as if no cycle slip occurred (like a "back door" filter) in case the cycle slip ended before another slip occurred. Figure 2.8 illustrates this concept. This proposed structure is similar to the MMAE structure of Mosle (20). Mosle implemented a system where the different filters were run and each filter use different sets of measurements.

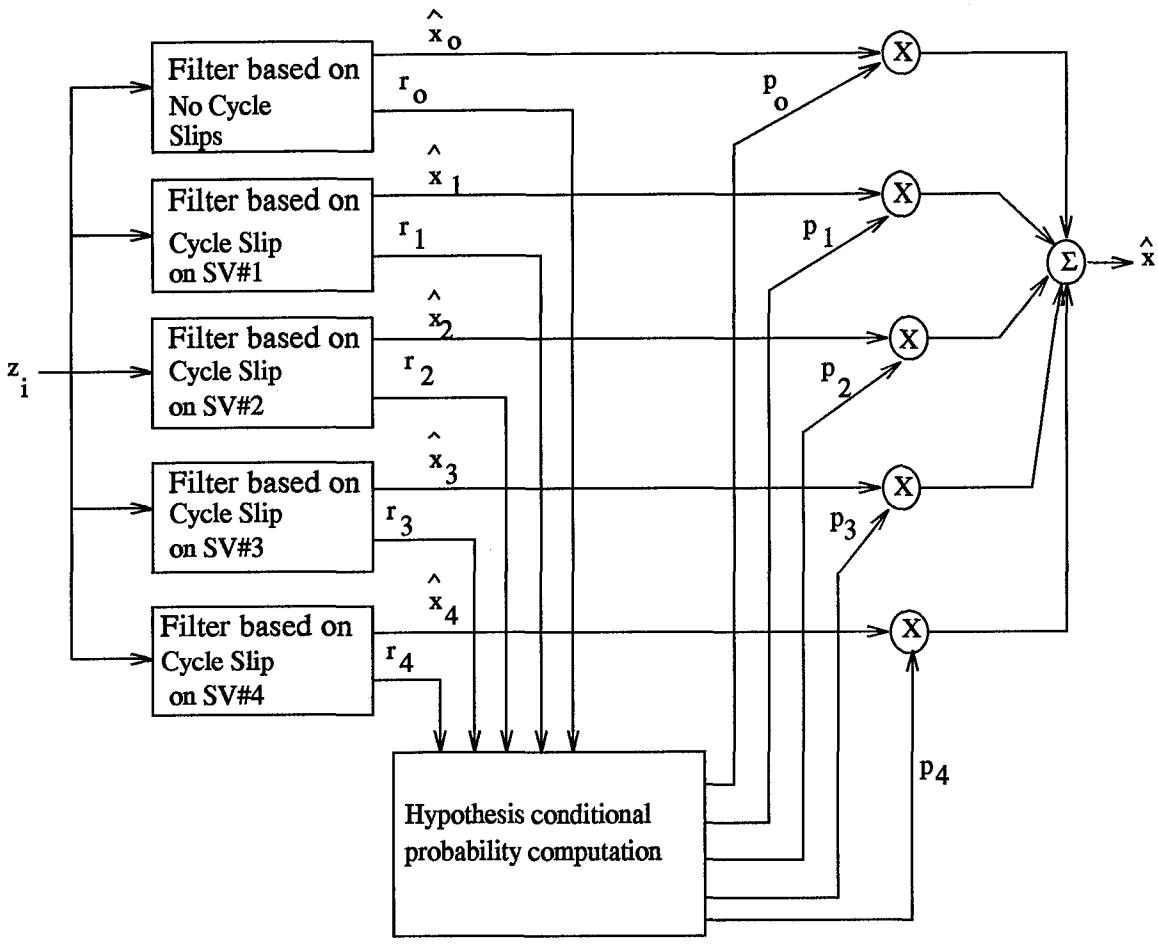

Figure 2.7 Block Diagram of Proposed PNRS MMAE Algorithm

Due to time limitations, this type of FDIR scheme could not be implemented. This presentation is made to show what seems to be the most robust FDIR scheme for accurate implementation.

2.5 Summary

This chapter has given a brief introduction into extended Kalman filter theory to include filter order reduction and filter tuning discussions. Also given is a detailed description of the theory involved with CPGPS measurements. The CPGPS discussion includes descriptions of the different measurement differencing techniques and a discussion of cycle slips and how they are put into simulation. Finally, a description of two FDIR schemes proposed for this research is given.

The material presented in this chapter is essential to form a solid base of information for the understanding of how the simulation packages implemented in this thesis produce the results to be presented later.

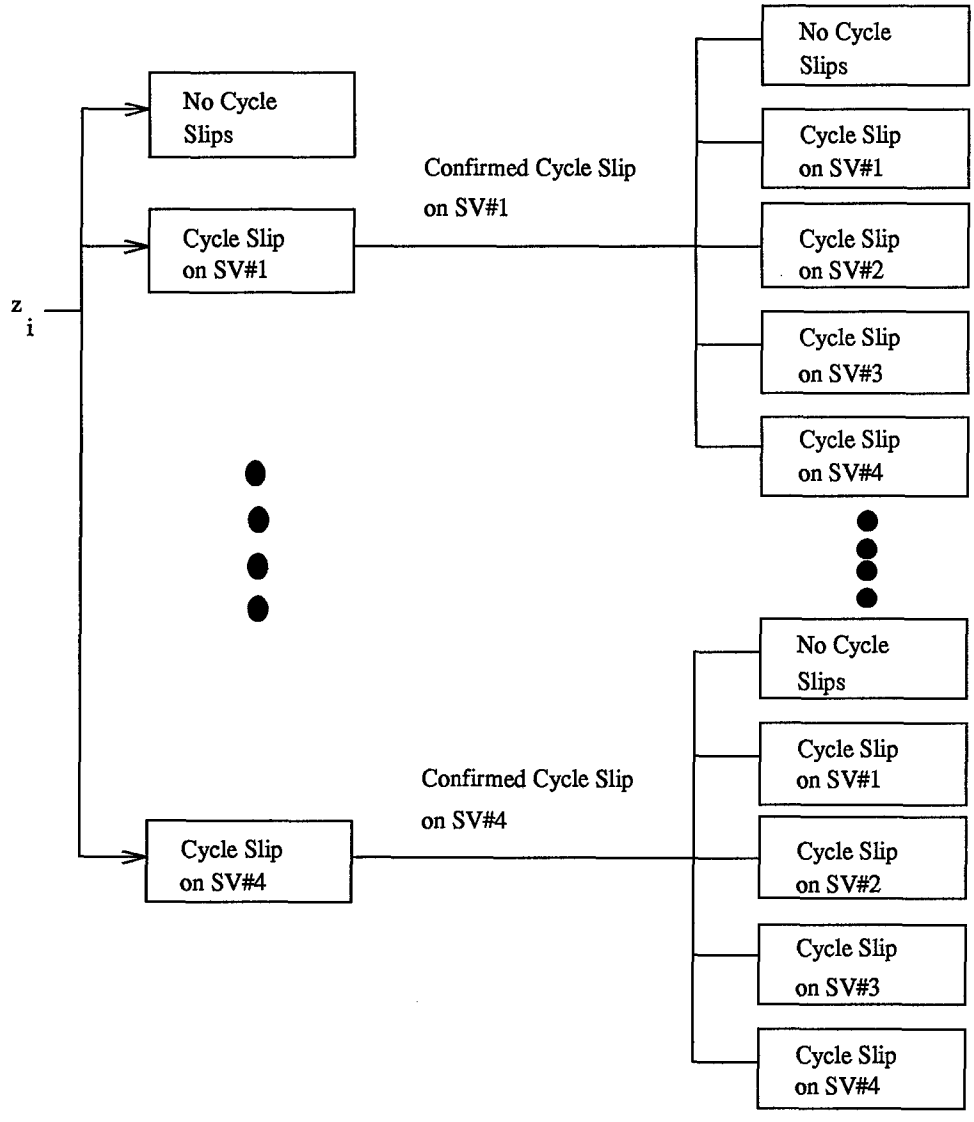

Figure 2.8 Block Diagram of MMAE Algorithm with Hierarchical Structure

III. The ENRS and PNRS Models

3.1 Overview

The dynamics and measurement models and equations of the Enhanced Navigation Reference System (ENRS) (23), the Precision Navigation Reference System (PNRS) (9), and the additional INS measurement models of the barometric altimeter and Doppler velocity aiding are developed in this chapter. The development of the ENRS is being conducted rather than the NRS because the PNRS is based upon the use of Differential GPS as used in the ENRS. For a detailed description of the NRS model development and for a source of where the values of noise strengths and initial conditions used in this thesis can be found, see (9,23,26,28,29).

The truth and filter models presented are those of the PNRS and the Double-Differenced PNRS (DDPNRS). The PNRS models presented include the truth model from (9) and the reduced order filter implemented by this author. The DDPNRS models are those implemented with the double differencing method to be discussed in Section 3.4.2.

The ENRS and PNRS are divided into three components: the LN-93 Inertial Navigation System Error State Model, the Range/Range-Rate System Error State Model, and the GPS Error State Model, which covers DGPS and CPGPS of the ENRS and PNRS, respectively.

3.2 The ENRS Model

The ENRS model is composed of a truth and a filter model. The truth model is used as the representation of the "real world" in the computer simulation. The truth model is taken as our best representation of the real world for simulation runs to be completed. The filter model is to represent the real world but is of reduced order so that it can be embedded into a filter which can be run in real time in a computer system on an aircraft. The reduction of order of the truth model allows for a simulation to be run faster with adequate results, and increases the number of simulation scenarios which can be evaluated in a given time span.

As stated in the overview, the ENRS and PNRS are made up of three separate navigational systems or components. Figure 1.1 depicts the setup of the ENRS and PNRS. Each component represents a different facet of Equations (3.1) and (3.2) (the ENRS and PNRS Propagation and Measurement Equations):

$$\dot{\delta \mathbf{x}}_{NRS} = \begin{bmatrix} \mathbf{F}_{INS} & \mathbf{0} & \mathbf{0} \\ \mathbf{0} & \mathbf{F}_{RRS} & \mathbf{0} \\ \mathbf{0} & \mathbf{0} & \mathbf{F}_{GPS} \end{bmatrix} \cdot \delta \mathbf{x}_{NRS} + \begin{bmatrix} \mathbf{w}_{INS} \\ \mathbf{w}_{RRS} \\ \mathbf{w}_{GPS} \end{bmatrix} \tag{3.1}$$

$$\delta z_{NRS} = \begin{bmatrix} \mathbf{H}_{INS} \\ \mathbf{H}_{RRS} \\ \mathbf{H}_{GPS} \end{bmatrix} \cdot \delta \mathbf{x}_{NRS} + \begin{bmatrix} \mathbf{v}_{INS} \\ \mathbf{v}_{RRS} \\ \mathbf{v}_{GPS} \end{bmatrix} \tag{3.2}$$

where: NRS = the ENRS or PNRS (to be discussed in Section 3.3), whichever is being used

INS = the Litton LN-93 Inertial Navigation System

GPS = DGPS or CPGPS, whichever is being used

RRS = the CIGTF Range/Range-Rate System

The models associated with each component of Equations (3.1) and (3.2) will now be discussed in greater detail.

3.2.1 Litton LN-93 Error State Models. This section covers the 93-state Litton truth model, the reduced 39-state truth model, and the 11-state filter model used in this research. The 93-state error state model is taken from (5) and the 39-state error model is taken from (12).

3.2.1.1 The 93-State Error Model. The Litton LN-93 INS 93-State Error Model has been developed by Litton and documented in (5). The 93 states of the error model are broken into

six categories:

$$\delta\mathbf{x} = \begin{bmatrix} \delta\mathbf{x}_1^T & \delta\mathbf{x}_1^T & \delta\mathbf{x}_3^T & \delta\mathbf{x}_4^T & \delta\mathbf{x}_5^T & \delta\mathbf{x}_6^T \end{bmatrix}^T \tag{3.3}$$

where: $\delta\mathbf{x}$ = a 93 × 1 column vector of error states

$\delta\mathbf{x}_1$ = Category 1: 13 position, velocity, altitude, and vertical channel states (representative of the basic Pinson error model for a baro-INS

$\delta\mathbf{x}_2$ = Category 2: 16 gyro, accelerometer, baro-altimeter, and "trend" states which are modelled as first-order Markov processes

$\delta\mathbf{x}_3$ = Category 3: 18 gyro bias states which are modelled as random constants

$\delta\mathbf{x}_4$ = Category 4: 22 accelerometer bias errors which are modelled as random constants

$\delta\mathbf{x}_5$ = Category 5: 6 thermal transient errors which are modelled as first order Markov processes

$\delta\mathbf{x}_6$ = Category 6: 18 gyro compliance errors which are modelled as biases

A state space representation of the LN-93 error state model is as follows:

$$\begin{bmatrix} \dot{\delta\mathbf{x}}_1 \\ \dot{\delta\mathbf{x}}_2 \\ \dot{\delta\mathbf{x}}_3 \\ \dot{\delta\mathbf{x}}_4 \\ \dot{\delta\mathbf{x}}_5 \\ \dot{\delta\mathbf{x}}_6 \end{bmatrix} = \begin{bmatrix} \mathbf{F}_{11} & \mathbf{F}_{12} & \mathbf{F}_{13} & \mathbf{F}_{14} & \mathbf{F}_{15} & \mathbf{F}_{16} \\ \mathbf{0} & \mathbf{F}_{22} & \mathbf{0} & \mathbf{0} & \mathbf{0} & \mathbf{0} \\ \mathbf{0} & \mathbf{0} & \mathbf{0} & \mathbf{0} & \mathbf{0} & \mathbf{0} \\ \mathbf{0} & \mathbf{0} & \mathbf{0} & \mathbf{0} & \mathbf{0} & \mathbf{0} \\ \mathbf{0} & \mathbf{0} & \mathbf{0} & \mathbf{0} & \mathbf{F}_{55} & \mathbf{0} \\ \mathbf{0} & \mathbf{0} & \mathbf{0} & \mathbf{0} & \mathbf{0} & \mathbf{0} \end{bmatrix} \cdot \begin{bmatrix} \delta\mathbf{x}_1 \\ \delta\mathbf{x}_2 \\ \delta\mathbf{x}_3 \\ \delta\mathbf{x}_4 \\ \delta\mathbf{x}_5 \\ \delta\mathbf{x}_6 \end{bmatrix} + \begin{bmatrix} \mathbf{w}_1 \\ \mathbf{w}_2 \\ \mathbf{0} \\ \mathbf{0} \\ \mathbf{0} \\ \mathbf{0} \end{bmatrix} \tag{3.4}$$

A listing of the submatrices of the $\mathbf{F}$ and $\mathbf{w}$ matrices in Equation (3.4) can be found in Appendix B, Tables B.1 through B.10. For a more detailed description of each component of Equation (3.4), see (5).

3.2.1.2 The 39-State Error Model. Through the work of Lewantowicz and Keen in (12), the very accurate 93-state model was reduced to a 39-state model without a significant loss of accuracy from the 93-state model. The most essential and important states of Equation (3.4) are retained in the 39-state model which produces:

$$\begin{bmatrix} \dot{\delta \mathbf{x}_1} \\ \dot{\delta \mathbf{x}_2} \\ \dot{\delta \mathbf{x}_3} \\ \dot{\delta \mathbf{x}_4} \end{bmatrix} = \begin{bmatrix} \mathbf{F}_{11} & \mathbf{F}_{12} & \mathbf{F}_{13} & \mathbf{F}_{14} \\ \mathbf{0} & \mathbf{F}_{22} & \mathbf{0} & \mathbf{0} \\ \mathbf{0} & \mathbf{0} & \mathbf{0} & \mathbf{0} \\ \mathbf{0} & \mathbf{0} & \mathbf{0} & \mathbf{0} \end{bmatrix} \cdot \begin{bmatrix} \delta \mathbf{x}_1 \\ \delta \mathbf{x}_2 \\ \delta \mathbf{x}_3 \\ \delta \mathbf{x}_4 \end{bmatrix} + \begin{bmatrix} \mathbf{w}_1 \\ \mathbf{w}_2 \\ \mathbf{0} \\ \mathbf{0} \end{bmatrix} \tag{3.5}$$

The noise values of each filter implementation added to each state of the truth model can be found in Appendix C, Tables C.1 through C.3.

3.2.1.3 The 11-State Error Model. The eleven most essential states of the 39-state truth model are retained in the filter model. Theses states cover the INS position, velocity, tilt, and vertical channel errors. These eleven states have proven to yield a Kalman filter which can track the truth states adequately with sufficient GPS and RRS updates (20). Table A.15 of Appendix A gives these eleven states and their correlation to the states of the 93-state error model. To compensate for the order reduction from the truth to the filter model, dynamics driving noise has been added to each state, as described in Chapter II, Section 2.2.2. The noise values added to each state can be found in Appendix C, Tables C.1 through C.3.

3.2.2 Range/Range-Rate System Error State Model. The RRS system is comprised of a network of ground based transponders and an airborne receiver. The transponders are located at surveyed sites to improve the accuracy of the measurements made by the RRS. The receiver interrogates the ground transponder's signal to determine the range between the transponder and receiver. This produces a three-dimensional position and velocity navigation solution which is used

as a measurement update in the extended Kalman filter. Figure 3.1 gives a pictorial representation of the RRS system.

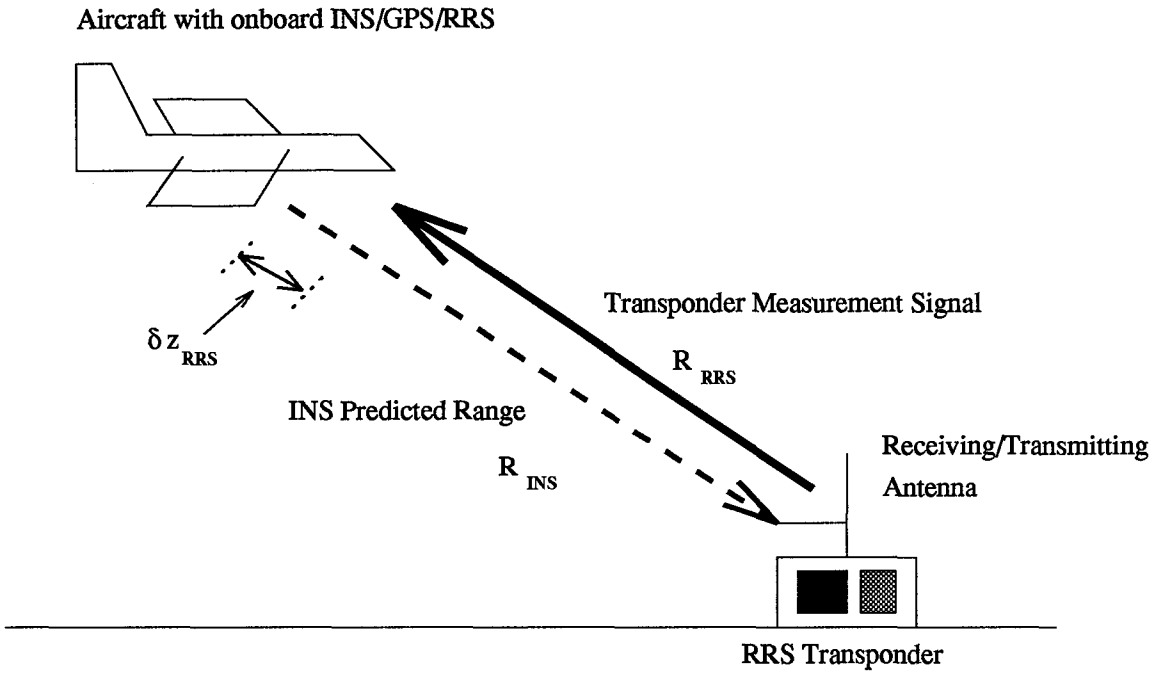

Figure 3.1 Pictorial Representation of RRS Measurements

This section gives the RRS MSOFE error state models and the measurement equations used in this thesis. The development of these models can be found in (23, 26, 29). The organization of this section will follow the pattern of the INS section. First the truth model is given, which is followed by the filter model. Finally, the measurement equations of the truth and filter models are given.

3.2.2.1 The 26-State RRS Truth Model. The truth model of the RRS can be broken into seven categories. The first category consists of the states which are considered to be the "common" errors of the RRS. These two common states are representative of the errors in the user hardware. These states are modelled as random constants as depicted in the following state space

equations:

$$\begin{bmatrix} \dot{\delta x}_{br} \\ \dot{\delta x}_{vr} \end{bmatrix} = \begin{bmatrix} 0 & 0 \\ 0 & 0 \end{bmatrix} \cdot \begin{bmatrix} \delta x_{br} \\ \delta x_{vr} \end{bmatrix} \tag{3.6}$$

where: δx_{br} = Range error due to equipment bias

δx_{vr} = Velocity or "range rate" error due to equipment bias

The initial condition of these states are:

$$E\left\{\begin{bmatrix} \delta x_{br}(t_o) \\ \delta x_{vr}(t_o) \end{bmatrix}\right\} = \begin{bmatrix} 0 \\ 0 \end{bmatrix} \tag{3.7}$$

and

$$\mathbf{P}_{\delta x_{br}, \delta x_{vr}}(t_o) = \begin{bmatrix} 1 \text{ ft}^2 & 0 \\ 0 & 10^{-4} \frac{\text{ft}^2}{\text{sec}^2} \end{bmatrix} \tag{3.8}$$

The remaining twenty-four states are divided up into six transponder-dependent categories of four states each. These four states represent the x, y, and z position errors of the transponder and the atmospheric propagation delay of the transponder signal. The transponder position errors are modeled as random constants and the atmospheric delay error is modelled as a first order Markov process with a 300-second time constant. The following equations depict the state space formulations of these error states:

$$\begin{bmatrix} \dot{\delta x}_i \\ \dot{\delta y}_i \\ \dot{\delta z}_i \\ \dot{\delta R}_{atm_i} \end{bmatrix} = \begin{bmatrix} 0 & 0 & 0 & 0 \\ 0 & 0 & 0 & 0 \\ 0 & 0 & 0 & 0 \\ 0 & 0 & 0 & -\frac{1}{300} \end{bmatrix} \cdot \begin{bmatrix} \delta x_i \\ \delta y_i \\ \delta z_i \\ \delta R_{atm_i} \end{bmatrix} + \begin{bmatrix} 0 \\ 0 \\ 0 \\ w_{atm_i} \end{bmatrix} \tag{3.9}$$

where: i = $1, \ldots, 6$ Number of specific transponder.

The initial conditions of these states are:

$$E\{\delta \mathbf{x}_{x,y,z,atm}(t_o)\} = \mathbf{0} \tag{3.10}$$

and

$$\mathbf{P}_{x,y,z,atm}(t_o) = \begin{bmatrix} 25 \text{ ft}^2 & 0 & 0 & 0 \\ 0 & 25 \text{ ft}^2 & 0 & 0 \\ 0 & 0 & 25 \text{ ft}^2 & 0 \\ 0 & 0 & 0 & 100 \text{ ft}^2 \end{bmatrix} \tag{3.11}$$

The dynamics driving noise is modelled with the following statistics:

$$E[\mathbf{w}_{x,y,z,atm}(t)] = \mathbf{0} \tag{3.12}$$

and

$$E[\mathbf{w}_{x,y,z,atm}(t)\mathbf{w}^T_{x,y,z,atm}(t+\tau)] = \begin{bmatrix} 0 & 0 & 0 & 0 \\ 0 & 0 & 0 & 0 \\ 0 & 0 & 0 & 0 \\ 0 & 0 & 0 & \frac{2\sigma^2_{atm}}{300} \end{bmatrix} \frac{\text{ft}^2}{\text{sec}} \cdot \delta(\tau) \tag{3.13}$$

where $\sigma^2_{atm} = 10 \text{ ft}^2$. The preceding equations (3.6) through (3.13) were developed by Cubic Corporation, the RRS designers for CIGTF, and are consistent with the previous thesis research of (9,20,23,26,28,29,31). Table A.7 in Appendix A gives a tabular listing of the 26-state RRS truth model.

3.2.2.2 The 2-State RRS Filter Model. The filter model of the RRS consists of only the two common states of the 26-state truth model. These states are the range and velocity biases due to the equipment used. The reduction of order from the truth to the filter requires the addition of dynamics driving noise to the model for order reduction compensation. Due to this addition of

the dynamics driving noise, the state space formulation of Equation (3.6) is changed to become:

$$\begin{bmatrix} \dot{\delta x}_{br_f} \\ \dot{\delta x}_{vr_f} \end{bmatrix} = \begin{bmatrix} 0 & 0 \\ 0 & 0 \end{bmatrix} \cdot \begin{bmatrix} \delta x_{br_f} \\ \delta x_{vr_f} \end{bmatrix} + \begin{bmatrix} w_{br_f} \\ w_{vr_f} \end{bmatrix} \tag{3.14}$$

The initial mean and covariances of these filter states are assumed to be zero (20). The strengths of the noise states, w_{br_f} and w_{vr_f}, are determined through filter tuning and can be found in Appendix C, Table C.1.

3.2.2.3 RRS Measurement Equations. The transponder measurement to be input into the extended Kalman filter is the result of a difference measurement between two independent range measurements between the transponder and the aircraft. The two independent measurements which make up this difference measurement are the INS-computed range, R_{INS}, and the RRS-computed range, R_{RRS}. The filter difference measurement input, δz_{RRS}, is as follows:

$$\delta z_{RRS} = R_{INS} - R_{RRS} \tag{3.15}$$

The INS range measurement is the difference between the INS computed user position, $\mathbf{X}_U$, and the known transponder position, $\mathbf{X}_T$, and is given in the following equation:

$$R_{INS} = |\mathbf{X}_U - \mathbf{X}_T| \tag{3.16}$$

Writing Equation (3.16) in terms of the error states of the filter (i.e. the user and transponder position errors), we have:

$$R_{INS} = \sqrt{(X_U - X_T)^2 + (Y_U - Y_T)^2 + (Z_U - Z_T)^2} \tag{3.17}$$

To represent this equation in term of the filter error states, a Taylor series approximation of Equation (3.17) must be taken with respect to $\delta\mathbf{X}_U$ and $\delta\mathbf{X}_T$ (as explained in Chapter II) to produce:

$$R_{INS} = R_t + \left.\frac{\partial R_{INS}(\mathbf{X}_U, \mathbf{X}_T)}{\partial \mathbf{X}_U}\right|_{(\mathbf{X}_U, \mathbf{X}_T)nom} \cdot \delta\mathbf{X}_U + \left.\frac{\partial R_{INS}(\mathbf{X}_U, \mathbf{X}_T)}{\partial \mathbf{X}_T}\right|_{(\mathbf{X}_U, \mathbf{X}_T)nom} \cdot \delta\mathbf{X}_T \quad (3.18)$$

where: $\delta\mathbf{X}_U = [\delta X_U \ \delta Y_U \ \delta Z_U]^T$ = errors in the user position

$\delta\mathbf{X}_T = [\delta X_T \ \delta Y_T \ \delta Z_T]^T$ = errors in the transponder position

Substituting Equation (3.17) into Equation (3.18) and solving for the partial derivatives about their respective nominals yields the following result:

$$\begin{aligned} R_{INS} = R_t &- \frac{X_T - X_U}{|R_{INS}|} \cdot \delta X_U - \frac{Y_T - Y_U}{|R_{INS}|} \cdot \delta Y_U - \frac{Z_T - Z_U}{|R_{INS}|} \cdot \delta Z_U \\ &+ \frac{X_T - X_U}{|R_{INS}|} \cdot \delta X_T + \frac{Y_T - Y_U}{|R_{INS}|} \cdot \delta Y_T + \frac{Z_T - Z_U}{|R_{INS}|} \cdot \delta Z_T \end{aligned} \quad (3.19)$$

The RRS range measurement is a combination of the true range from the aircraft to the transponder plus the inherent errors of the RRS system:

$$R_{RRS} = R_t + \delta R_{atm} + \delta R_{br} - v \quad (3.20)$$

where: R_{RRS} = RRS range measurement between user and transponder

R_t = true (but unknown) range between user and transponder

δR_{atm} = range error due to atmospheric delay

δR_{br} = range error due to equipment bias

v = zero-mean white Gaussian measurement noise

The measurement noise term, v, in Equation (3.20) looks as if the noise is being subtracted from the measurement. This is done so that when the difference measurement is taken as described in Equation (3.15), the measurement noise will be added to the measurement which is implemented

into the extended Kalman filter and follows the form of Equation 2.4. The addition of the negative produces the same results statistically but is implemented to produce difference measurement equations where the noise will be added in the final results, not subtracted. This convention is used in all similar developments in this chapter. Substituting Equations (3.19) and (3.20) into Equation (3.15) and taking the necessary differences produces:

$$\begin{aligned}\delta z_{RRS} = &-\frac{X_T - X_U}{|R_{INS}|}\cdot\delta X_U - \frac{Y_T - Y_U}{|R_{INS}|}\cdot\delta Y_U - \frac{Z_T - Z_U}{|R_{INS}|}\cdot\delta Z_U \\ &+\frac{X_T - X_U}{|R_{INS}|}\cdot\delta X_T + \frac{Y_T - Y_U}{|R_{INS}|}\cdot\delta Y_T + \frac{Z_T - Z_U}{|R_{INS}|}\cdot\delta Z_T \\ &-\delta R_{atm} - \delta R_{br} + v \end{aligned} \tag{3.21}$$

where the coefficients of Equation (3.21) are the components of the **H** matrix of the extended Kalman filter equations described in Chapter II Section 2.2.1. As can be seen in Equation (3.21), the true range, R_t, is cancelled out in the differencing of the two measurements as required to have δz_{RRS} represent an error state measurement update to the extended Kalman filter. Equation (3.21) represents the RRS truth model linearized measurement equation.

In the formation of the RRS filter measurement equation, the transponder position error states are dropped because they are not included as states in the filter model (for a detailed description of the filter model, see Sections 3.5.2 and 3.6.2 or Appendix A, Tables A.15 and A.20). With this in mind, Equation (3.21), excluding the transponder position error states becomes:

$$\delta z_{RRS} = -\frac{X_T - X_U}{|R_{INS}|}\cdot\delta X_U - \frac{Y_T - Y_U}{|R_{INS}|}\cdot\delta Y_U - \frac{Z_T - Z_U}{|R_{INS}|}\cdot\delta Z_U - \delta R_{br} + v \tag{3.22}$$

Due to the filter order reduction conducted, the measurement noise covariance, $\mathbf{R}(t_i)$, is increased to compensate for the missing states like the process noise covariance, $\mathbf{Q}(t)$, was increased in the filter model implementation.

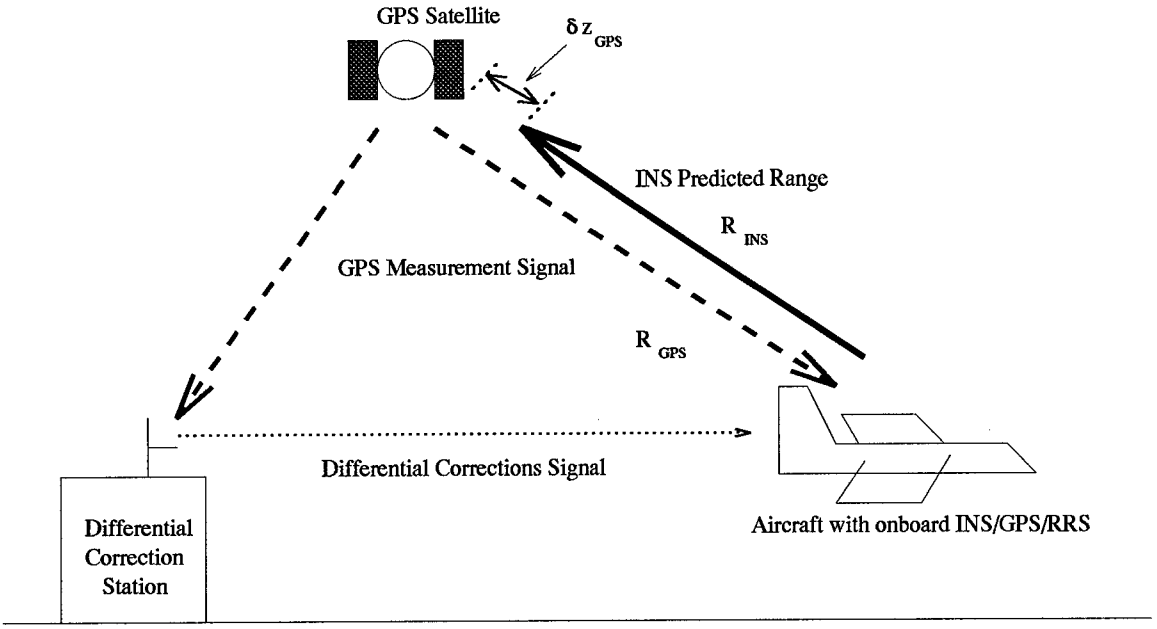

Figure 3.2 Pictorial Representation of DGPS Measurements

3.2.3 Differential GPS Error State Model. The concept of differentially correcting GPS measurements is used to improve the accuracy of the airborne receiver's navigation solution. DGPS uses a fixed known reference station to determine inherent GPS errors such as atmospheric delays, satellite clock bias, and satellite line-of-sight position errors. By knowing the accuracy of the reference station with respect to its exact position, these GPS errors can be determined very accurately for implementation with another nonstationary receiver. With these errors determined, they are used to correct the GPS signals of an airborne receiver. Figure 3.2 gives a pictorial representation of how DGPS is implemented with an airborne receiver. For a detailed description of where the DGPS models are derived and the differences in the code-phase GPS models of the research conducted by (20, 26, 28, 29, 31), the reader is suggested to review (23) and (9).

3.2.3.1 The 22-State Differential GPS Truth Model. The DGPS truth model is broken into five categories: the airborne or users' receiver common states and the four sets of satellite dependent states. The two common airborne Receiver (ABR) states are the ABR's clock

errors: the clock bias and clock drift. These common states are modelled as:

$$\begin{bmatrix} \dot{\delta x}_{Uclk-b} \\ \dot{\delta x}_{Uclk-dr} \end{bmatrix} = \begin{bmatrix} 0 & 1 \\ 0 & 0 \end{bmatrix} \cdot \begin{bmatrix} \delta x_{Uclk-b} \\ \delta x_{Uclk-dr} \end{bmatrix} \tag{3.23}$$

where: δx_{Uclk-b} = range equivalent of the ABR clock bias

$\delta x_{Uclk-dr}$ = range equivalent of the ABR clock drift

Where the initial conditions of these states are taken to be:

$$E\left\{\begin{bmatrix} \delta x_{Uclk-b} \\ \delta x_{Uclk-dr} \end{bmatrix}\right\} = \begin{bmatrix} 0 \\ 0 \end{bmatrix} \tag{3.24}$$

and

$$\mathbf{P}_{\delta x_{Uclk-b}, \delta x_{Uclk-dr}}(t_o) = \begin{bmatrix} 9 \times 10^{14}\text{ft}^2 & 0 \\ 0 & 9 \times 10^{10}\frac{\text{ft}^2}{\text{sec}^2} \end{bmatrix} \tag{3.25}$$

These errors are the most dominant and largest sources of error in GPS measurements, hence the large uncertainties associated with these states initially. This large uncertainty remains until an estimate of the errors is established, which in turn reduces the dominance of these errors in the system.

The remaining four categories of DGPS error states are the satellite-dependent errors. Each satellite has five inherent errors associated with it. Two of these errors are the atmospheric propagational delay errors caused by the troposphere and ionosphere. The tropospheric and ionospheric delay terms are modelled as first order Markov processes with time constants of 500 and 1500 seconds, respectively. The remaining three satellite dependent errors are the line-of-sight errors between the satellite and the receiver in the x, y, and z directions. These three errors are modelled as random constants. The state space representation of these five satellite dependent errors is

presented in the following equation:

$$\begin{bmatrix} \dot{\delta R}_{trop_i} \\ \dot{\delta R}_{ion_i} \\ \dot{\delta x}_{S_i} \\ \dot{\delta y}_{S_i} \\ \dot{\delta z}_{S_i} \end{bmatrix} = \begin{bmatrix} -\frac{1}{500} & 0 & 0 & 0 & 0 \\ 0 & -\frac{1}{1500} & 0 & 0 & 0 \\ 0 & 0 & 0 & 0 & 0 \\ 0 & 0 & 0 & 0 & 0 \\ 0 & 0 & 0 & 0 & 0 \end{bmatrix} \cdot \begin{bmatrix} \delta R_{trop_i} \\ \delta R_{ion_i} \\ \delta x_{S_i} \\ \delta y_{S_i} \\ \delta z_{S_i} \end{bmatrix} + \begin{bmatrix} w_{trop_i} \\ w_{ion_i} \\ 0 \\ 0 \\ 0 \end{bmatrix} \tag{3.26}$$

where: δR_{trop_i} = range equivalent of the tropospheric delay

δR_{ion_i} = range equivalent of the ionospheric delay

δx_{S_i} = satellite x position error

δy_{S_i} = satellite y position error

δz_{S_i} = satellite z position error

The initial conditions associated with these states are:

$$E\{\delta \mathbf{x}_{DGPS}\} = \mathbf{0} \tag{3.27}$$

and

$$\mathbf{P}_{DGPS} = \begin{bmatrix} 1 \text{ ft}^2 & 0 & 0 & 0 & 0 \\ 0 & 1 \text{ ft}^2 & 0 & 0 & 0 \\ 0 & 0 & 0.35 \text{ ft}^2 & 0 & 0 \\ 0 & 0 & 0 & 0.35 \text{ ft}^2 & 0 \\ 0 & 0 & 0 & 0 & 0.35 \text{ ft}^2 \end{bmatrix} \tag{3.28}$$

with dynamic driving noise, $\mathbf{w}(t)$, statistics:

$$E[\mathbf{w}_{DGPS}(t)] = \mathbf{0} \tag{3.29}$$

and

$$E[\mathbf{w}_{DGPS}(t)\mathbf{w}_{DGPS}^{T}(t+\tau)] = \begin{bmatrix} 0.001 & 0 & 0 & 0 & 0 \\ 0 & 0.0004 & 0 & 0 & 0 \\ 0 & 0 & 0 & 0 & 0 \\ 0 & 0 & 0 & 0 & 0 \\ 0 & 0 & 0 & 0 & 0 \end{bmatrix} \frac{\text{ft}^2}{\text{sec}} \cdot \delta(\tau) \tag{3.30}$$

The values for the initial variance and atmospheric error dynamic driving noise strengths were obtained from (9). These models are conservative as compared to those recommended to Negast by CIGTF (9). A tabular listing of the 22-state DGPS error state vector can be found in Appendix A, Table A.9. Note, the values presented in Equations (3.27) through (3.47) are for each of the four satellites used in the system.

3.2.3.2 The 2-State DGPS Filter Model. The filter model of the DGPS error states consists of the two common clock states plus some additive dynamics driving noise to compensate for the filter order reduction. The state space representation of the DGPS filter model is:

$$\begin{bmatrix} \dot{\delta x}_{Uclk-b_f} \\ \dot{\delta x}_{Uclk-dr_f} \end{bmatrix} = \begin{bmatrix} 0 & 1 \\ 0 & 0 \end{bmatrix} \cdot \begin{bmatrix} \delta x_{Uclk-b_f} \\ \delta x_{Uclk-dr_f} \end{bmatrix} + \begin{bmatrix} w_{x_{Uclk-b_f}} \\ w_{x_{Uclk-dr_f}} \end{bmatrix} \tag{3.31}$$

The added dynamics driving noise strengths are determined through filter tuning and these values can be found in Appendix C, Tables C.1 through C.2.

3.2.3.3 Differential GPS Pseudorange Measurement Equations. The DGPS pseudorange measurement equation is derived from the code-phase pseudorange measurement equation. Taking into account that the differential corrections are applied to the signal before being sent to the extended Kalman filter, as stated in Chapter I, Section 1.4, Assumption 6, the pseudorange

measurement equation is:

$$R_{DGPS} = R_t + \delta R_{Uclk} + \delta R_{ion} + \delta R_{trop} - v \tag{3.32}$$

where: R_{DGPS} = DGPS Pseudorange Measurement

R_t = true (but unknown) range from user to satellite

δR_{Uclk} = range error due to ABR clock error

δR_{ion} = range error due to ionospheric delay

δR_{trop} = range error due to tropospheric delay

v = zero-mean white Gaussian noise

Similar to the case with the RRS Measurement Equation (see Section 3.2.2.3), the extended Kalman filter measurement update requires two measurement sources to formulate the following difference measurement:

$$\delta z_{DGPS} = R_{INS} - R_{DGPS} \tag{3.33}$$

The INS computed range, R_{INS}, is computed in the same way as for the range to the transponders (See Equations (3.16) through (3.19)). The difference in this range calculation is that the position of the transponders, $\mathbf{X}_T$, is replaced by the position of the GPS satellites, $\mathbf{X}_S$. Following the same methodology and invoking the first order Taylor series approximation of Equation (3.18) gives:

$$\begin{aligned} R_{INS} = R_t &- \frac{X_S - X_U}{|R_{INS}|} \cdot \delta X_U - \frac{Y_S - Y_U}{|R_{INS}|} \cdot \delta Y_U - \frac{Z_S - Z_U}{|R_{INS}|} \cdot \delta Z_U \\ &+ \frac{X_S - X_U}{|R_{INS}|} \cdot \delta X_S + \frac{Y_T - Y_U}{|R_{INS}|} \cdot \delta Y_S + \frac{Z_S - Z_U}{|R_{INS}|} \cdot \delta Z_S \end{aligned} \tag{3.34}$$

Substituting Equations (3.32) and (3.34) into Equation (3.33) produces the measurement update equation for the truth model of the extended Kalman filter:

$$\delta z_{DGPS} = -\frac{X_S - X_U}{|R_{INS}|} \cdot \delta X_U - \frac{Y_S - Y_U}{|R_{INS}|} \cdot \delta Y_U - \frac{Z_S - Z_U}{|R_{INS}|} \cdot \delta Z_U$$
$$+\frac{X_S - X_U}{|R_{INS}|} \cdot \delta X_S + \frac{Y_T - Y_U}{|R_{INS}|} \cdot \delta Y_S + \frac{Z_S - Z_U}{|R_{INS}|} \cdot \delta Z_S$$
$$-\delta R_{U\,clk} - \delta R_{ion} - \delta R_{trop} + v \tag{3.35}$$

Again the true range, R_t, is eliminated from the measurement equation as with the RRS measurement update equation.

To form the DGPS filter measurement update equation, the satellite position error states and atmospheric error states are removed from the equation because these states are not modelled in the filter. The removing of these states transforms Equation (3.35) into the following filter measurement update equation:

$$\delta z_{DGPS} = -\frac{X_S - X_U}{|R_{INS}|} \cdot \delta X_U - \frac{Y_S - Y_U}{|R_{INS}|} \cdot \delta Y_U - \frac{Z_S - Z_U}{|R_{INS}|} \cdot \delta Z_U - \delta R_{U\,clk} + v \tag{3.36}$$

where the measurement noise covariance is increased to account for those states eliminated in the filter order reduction.

3.3 The PNRS Model

The PNRS model developed by Hansen (9) incorporates Carrier-Phase GPS measurements into the ENRS system developed by Negast (23). The models, measurement equations, and system quantity values presented in this section are taken from (9). The double differencing section is developed by this author from (8) for implementation into MSOFE.

3.3.1 The PNRS Truth Model Equations. The implementation of the PNRS model into the already existing ENRS model requires only the addition of the phase ambiguity states to the

truth model, one for each satellite. These states are modelled as time-invariant random constants as long as no cycle slips occur (9):

$$\begin{bmatrix} \dot{\delta R}_{N1} \\ \dot{\delta R}_{N2} \\ \dot{\delta R}_{N3} \\ \dot{\delta R}_{N4} \end{bmatrix} = \begin{bmatrix} 0 & 0 & 0 & 0 \\ 0 & 0 & 0 & 0 \\ 0 & 0 & 0 & 0 \\ 0 & 0 & 0 & 0 \end{bmatrix} \cdot \begin{bmatrix} \delta R_{N1} \\ \delta R_{N2} \\ \delta R_{N3} \\ \delta R_{N4} \end{bmatrix} \tag{3.37}$$

with initial conditions:

$$E\{\delta \mathbf{R}_N\} = \mathbf{0} \tag{3.38}$$

and

$$\mathbf{P}_{\delta \mathbf{R}_N} = \begin{bmatrix} 13 \text{ ft}^2 & 0 & 0 & 0 \\ 0 & 13 \text{ ft}^2 & 0 & 0 \\ 0 & 0 & 13 \text{ ft}^2 & 0 \\ 0 & 0 & 0 & 13 \text{ ft}^2 \end{bmatrix} \tag{3.39}$$

The value of $13ft^2$ for the initial state covariance was taken from (9) using the idea that the "initially" differentially corrected carrier-phase measurement cannot be more accurate than the differentially corrected code-phase measurement.

3.3.1.1 The PNRS Filter Model Equations. For implementation into the filter model only the common states of Section 3.2.3.2 and the phase ambiguity states of the previous section are used. To compensate for the filter order reduction, dynamics driving noise in the form of zero-mean

white Gaussian noise processes are added to Equation (3.37) to produce:

$$\begin{bmatrix} \dot{\delta R}_{N1_f} \\ \dot{\delta R}_{N2_f} \\ \dot{\delta R}_{N3_f} \\ \dot{\delta R}_{N4_f} \end{bmatrix} = \begin{bmatrix} 0 & 0 & 0 & 0 \\ 0 & 0 & 0 & 0 \\ 0 & 0 & 0 & 0 \\ 0 & 0 & 0 & 0 \end{bmatrix} \cdot \begin{bmatrix} \delta R_{N1_f} \\ \delta R_{N2_f} \\ \delta R_{N3_f} \\ \delta R_{N4_f} \end{bmatrix} + \begin{bmatrix} w_{R_{N1_f}} \\ w_{R_{N2_f}} \\ w_{R_{N3_f}} \\ w_{R_{N4_f}} \end{bmatrix} \tag{3.40}$$

where the added dynamics driving noise possess the following statistics:

$$E[\mathbf{w}_{R_{N_f}}(t)] = \mathbf{0} \tag{3.41}$$

and

$$E[\mathbf{w}_{R_{N_f}}(t)\mathbf{w}^T_{R_{N_f}}(t+\tau)] = \begin{bmatrix} a & 0 & 0 & 0 \\ 0 & b & 0 & 0 \\ 0 & 0 & c & 0 \\ 0 & 0 & 0 & d \end{bmatrix} \frac{\text{ft}^2}{\text{sec}} \cdot \delta(\tau) \tag{3.42}$$

where the values of Equation (3.42) are determined through filter tuning and are listed in Appendix C, Tables C.1 through C.3.

3.3.2 The PNRS Measurement Equations. To form the carrier-phase range measurement equation, R_{CPGPS}, Equation (2.45) is changed using the nomenclature of Section 3.2.3.3 to become:

$$R_{CPGPS} = R_t + \delta R_{Uclk} + \delta R_{Sclk} - \delta R_{ion} + \delta R_{trop} + \delta R_N - v \tag{3.43}$$

where every term in Equation (3.43) is the same as the DGPS measurement equation, except for R_{CPGPS} which represents the phase-range measurement and δR_N which represents the range equivalent of the cycle ambiguity term N(t). Taking into account the assumption that differential corrections are applied to the signal prior to entrance as a measurement update to the extended

Kalman filter, Equation (3.43) becomes:

$$R_{CPGPS} = R_t + \delta R_{Uclk} - \delta R_{ion} + \delta R_{trop} + \delta R_N - v \tag{3.44}$$

Note the satellite clock bias term is eliminated due to the differential corrections being applied. This equation is a between-receivers single difference as described in Chapter II, Section 2.3.3.1.

Like with the RRS and DGPS measurement equations, the INS computed range is used as the second measurement source for the difference measurement. Once the Taylor series expansion of Equation (3.18) is invoked, and the difference between the INS and CPGPS ranges is taken, the measurement update equation of the extended Kalman filter truth model is formed:

$$\begin{aligned}\delta z_{CPGPS} = R_{INS} - R_{CPGPS} = &-\frac{X_S - X_U}{|R_{INS}|}\cdot\delta X_U - \frac{Y_S - Y_U}{|R_{INS}|}\cdot\delta Y_U - \frac{Z_S - Z_U}{|R_{INS}|}\cdot\delta Z_U \\ &+\frac{X_S - X_U}{|R_{INS}|}\cdot\delta X_S + \frac{Y_T - Y_U}{|R_{INS}|}\cdot\delta Y_S + \frac{Z_S - Z_U}{|R_{INS}|}\cdot\delta Z_S \\ &-\delta R_{Uclk} + \delta R_{ion} - \delta R_{trop} - \delta R_N + v\end{aligned} \tag{3.45}$$

To form the filter model measurement equation, the satellite position and atmospheric delay terms are eliminated (because these errors are not modelled in the filter) to produce:

$$\begin{aligned}\delta z_{CPGPS} = R_{INS} - R_{CPGPS} = &-\frac{X_S - X_U}{|R_{INS}|}\cdot\delta X_U - \frac{Y_S - Y_U}{|R_{INS}|}\cdot\delta Y_U - \frac{Z_S - Z_U}{|R_{INS}|}\cdot\delta Z_U \\ &-\delta R_{Uclk} - \delta R_N + v\end{aligned} \tag{3.46}$$

where the measurement noise covariance terms are increased to account for the filter order reduction conducted.

3.4 The PNRS Double Difference Model

3.4.1 The PNRS Double Difference Error State Model. As stated in Section 2.3.3.2 of Chapter II, the implementation of the Double Differencing between receivers/satellites significantly reduces the ionospheric and tropospheric errors and eliminates the user clock errors. To simulate this reduction in MSOFE, the dynamics driving noise strengths of Equation (3.47) are reduced to produce the following relation:

$$E[\mathbf{w}_{DDPNRS}(t)\mathbf{w}^T_{DDPNRS}(t+\tau)] = \begin{bmatrix} 0.0005 & 0 & 0 & 0 & 0 \\ 0 & 0.0002 & 0 & 0 & 0 \\ 0 & 0 & 0 & 0 & 0 \\ 0 & 0 & 0 & 0 & 0 \\ 0 & 0 & 0 & 0 & 0 \end{bmatrix} \frac{\text{ft}^2}{\text{sec}} \cdot \delta(\tau) \tag{3.47}$$

The decision to reduce the noise strengths by half was done because a reduction of this magnitude is consistent with (18, 25). The reduction of the noise strengths is also consistent with the research of Negast (23) who reduced the noise strengths when he implemented DGPS into MSOFE, thereby reducing the effects of the ionospheric and tropospheric errors.

3.4.2 The PNRS Double Difference Measurement Equations. To incorporate a between-satellites single difference to the already differentially corrected CPGPS phase-range measurement to form a between-receiver/satellites double difference, some changes to Equation (3.45) must be made. To begin to form the double difference measurement equation, we start with the differentially corrected CPGPS phase-range measurement Equation (3.44):

$$R_{CPGPS} = R_t + \delta R_{Uclk} - \delta R_{ion} + \delta R_{trop} + \delta R_N + v \tag{3.48}$$

Taking the between-satellites single difference between satellites i and j transforms Equation (3.44) into:

$$\nabla R^{ij}_{CPGPS} = \nabla R^{ij}_{t} - \nabla \delta R^{ij}_{ion} + \nabla \delta R^{ij}_{trop} + \nabla \delta R^{ij}_{N} + \nabla v^{ij} \tag{3.49}$$

This differencing eliminates the user clock bias term, and the variance of the differenced measurement noise term is now $2 \times E[v^2]$. This value is determined through the assumption that the noises in the satellite measurements are independent of each other. For implementation into MSOFE, four satellite measurements are to be used to construct the three satellite pairs necessary for this differencing method. The satellite combinations to be used are $\nabla R^{14}_{CPGPS}, \nabla R^{24}_{CPGPS}, \nabla R^{34}_{CPGPS}$ where satellite four, SV4, is taken to be the base satellite for reasons stated in Chapter I, Section 1.4, Assumption 12. With this convention of satellite combinations, the noises in the satellite measurements are assumed independent of each other.

Completing the between-satellites single difference on the INS computed range, R_{INS}, as taken from (8) produces:

$$\begin{aligned} \nabla R^{ij}_{INS} = \nabla R^{ij}_{t} &- A\delta X_U - B\delta Y_U - C\delta Z_U \\ &+ A\nabla\delta X^{ij}_{S} + B\nabla\delta Y^{ij}_{S} + C\nabla\delta Z^{ij}_{S} \end{aligned} \tag{3.50}$$

where: $A = \frac{X^i_S - X_U}{|R^i_{INS}|} - \frac{X^j_S - X_U}{|R^j_{INS}|}$

$B = \frac{Y^i_S - Y_U}{|R^i_{INS}|} - \frac{Y^j_S - Y_U}{|R^j_{INS}|}$

$C = \frac{Z^i_S - Z_U}{|R^i_{INS}|} - \frac{Z^j_S - Z_U}{|R^j_{INS}|}$

The extended Kalman filter measurement update equation which implements this double differencing step is:

$$\delta z_{CPGPS_{DD}} = \nabla R^{ij}_{INS} - \nabla R^{ij}_{CPGPS} \tag{3.51}$$

By substituting Equations (3.49) and (3.50) into Equation (3.51) produces:

$$\begin{aligned}\delta z_{CPGPS_{DD}} = &-A\delta X_U - B\delta Y_U - C\delta Z_U \\ &+A\nabla\delta X_S^{ij} + B\nabla\delta Y_S^{ij} + C\nabla\delta Z_S^{ij} \\ &+\nabla\delta R_{ion}^{ij} - \nabla\delta R_{trop}^{ij} - \nabla\delta R_N^{ij} + \nabla v^{ij}\end{aligned} \tag{3.52}$$

where Equation (3.52) can be implemented into MSOFE. This differencing method eliminates the user clock bias and greatly reduces the effect of the atmospheric delays, δR_{ion} and δR_{trop}, and reduces the phase ambiguity error term, δR_N.

3.5 The PNRS Truth and Filter Models

This section presents the truth and filter models to be implemented in this research. The changes to the truth and filter models which are caused by the implementation of the double differencing measurement technique are also presented and described.

3.5.1 The 91-State Truth Model. The truth model implemented in this research is the same truth model used in Hansen's research (9). The 91-state truth model consists of the 39-state LN-93 INS error state model, the 26-state RRS error state model, the 22-state DGPS error state model, and the 4-state CPGPS error state model. The truth model order of states does not exactly follow the order described. For a complete listing of the 91-state truth model see Appendix A, Tables A.11 through A.14.

3.5.2 The 19-State Filter Model. The filter model used consists of the first 15 states of the truth model plus the 4-state CPGPS model. This filter model is a combination of the reduced order filter from Mosle's research (20) and the four phase ambiguity states from Hansen's research (9). The filter model is made up of the 11-state INS filter model described in Section 3.2.1.3, the 2-state RRS filter model described in Section 3.2.2.2, the 2-state DGPS filter model from Section

3.2.3.2, and the 4-state CPGPS filter model described in Section 3.3.1.1. A complete listing of the 19-state filter model can be found in Appendix A, Table A.15.

3.6 The Double Difference Truth and Filter Models

This section describes the changes made to implement the double differencing method in the truth and filter models from Section 3.5. For more detailed descriptions of the different differencing techniques, see Chapter II, Section 2.3.3.

3.6.1 The 89-State Double Difference Truth Model. The implementation of the double differencing method described in Section 3.4.2 reduces the order of the truth model from 91 states to 89 states. This reduction is due to the removal of the user clock bias and drift states which results from the differencing. The satellite-dependent states are changed slightly because of the differencing implemented. The satellite states of the first three satellites no longer just represent the atmospheric and line-of-sight errors of the individual satellite. These modified states (states 70 through 82) are changed to represent the difference between the satellite corresponding to the incoming measurement and the fourth satellite which is taken to be the base satellite. The remaining states (States 83 through 89) are modelled to continue the propagation and measurement updates of the fourth satellite. This allows for the accurate CPGPS measurements to continually update these states which are used in the double differencing. Tables A.16 through A.19 in Appendix A list and describe the states of the 89-state truth model.

3.6.2 The 17-State Double Difference Filter Model. The filter model associated with the double differencing method reduces the order of the original filter from 19 states to 17 states. The user clock bias and drift terms along with the fourth satellite's phase ambiguity terms are eliminated for the same reasons described in Section 3.6.1. Table A.20 of Appendix A gives a listing of the 17-state double differenced filter model.

3.6.3 The 69-State Double Difference Filter Model. Due to the reduced accuracy of the reduced order model, the 71-state filter model of Hansen's research (9) is used to investigate the effects of the double differencing on his filter model. This filter model consists of the first 69 states of of the 89-state truth model discussed in Section 3.6.1. Descriptions of these filter states are the first 69 states of the truth model found in Tables A.16 through A.19 of Appendix A.

3.7 Other Measurements

This section discusses the two additional measurements necessary for stable implementation of this filter scheme in MSOFE. The measurements to be discussed are the barometric altimeter and the velocity aiding measurement. Much of the information presented in these two sections comes from (20).

3.7.1 Barometric Altimeter Measurement. The purpose of this additional measurement in the filter and truth models is to compensate for the inherent instability of the INS in the vertical channel. The difference measurement necessary for the error state system being developed comes from the difference between the INS predicted altitude, H_{INS}, and the baro-altimeter's predicted altitude, H_{baro}, which is presented in the following relation:

$$\delta z_{Altitude} = H_{INS} - H_{baro} \tag{3.53}$$

We must now develop the individual measurements of Equation (3.53). The INS-predicted altitude consists of the aircraft's true altitude above the earth, h_{true}, plus the INS error in the aircraft's altitude above the reference ellipsoid, δh, which is depicted in the following relation:

$$H_{INS} = h_{true} + \delta h \tag{3.54}$$

The barometric altimeter measurement also consists of the true altitude of the aircraft above the earth, h_{true}, but differs from H_{INS} in that it includes the total time-correlated error in the barometric altimeter, δh_B, plus a random measurement noise, v. The addition of the random measurement noise is to take into account the fact that this is the "white part" of the measurement errors. This measurement is represented by the following:

$$H_{baro} = h_{true} + \delta h_B - v \tag{3.55}$$

Taking Equations (3.54) and (3.55) and substituting them into Equation (3.53) produces the altitude difference measurement:

$$\delta z_{Altitude} = \delta h - \delta h_B + v \tag{3.56}$$

where Equation (3.56) is encoded into MSOFE.

3.7.2 Velocity Aided Measurement. The velocity aiding of the INS through perfect Doppler measurements is used to ensure the stability of the filter in MSOFE. This has been a very poor assumption used in previous AFIT research. The velocity difference measurement used takes the difference between the truth state velocity, δV_{t_i}, and the filter state velocity, δV_{f_i}, to produce:

$$\delta z_i = \delta V_{t_i} - \delta V_{f_i} \tag{3.57}$$

where $i = x, y, z$ (east, north, and vertical directions). This relation provides the filter with the exact difference measurement of the vehicle's velocity. The velocity model equations are the same for both the filter and truth models with differences in the noise levels of the two models.

The measurements described in this section were necessary for the filters in the research of (9, 20, 23, 31) to remain stable. As was found in this research, these measurements are no longer

necessary to maintain stability. The results presented in Chapter IV make comparisons between the filters of this research which were run with and without these measurements.

3.8 Summary

This chapter presented the modelling equations associated with each component of the NRS. Also presented and developed are the measurement equations of the RRS, GPS, and Barometric Altimeter. The truth and filter models of the PNRS and the Double Differenced PNRS are presented. The models described are those which have been encoded into MSOFE and are used for simulation purposes to produce the results to be presented in Chapter IV.

IV. Filter Implementation Results

4.1 Overview

This chapter analyzes the results of the simulation runs of all versions of the PNRS filters, both with and without the perfect Doppler velocity aiding measurements, along with an analysis of the potential for using FDIR algorithms against large cycle slips. The chapter begins with a description of the simulation specifications to provide background information into the meaning of the presented results. The performance of Hansen's 71-state PNRS filter is evaluated without the perfect velocity aiding measurements. Next, the performance of the Reduced Order PNRS (ROPNRS) filter, both with and without the velocity aiding, and the filter's performance against the cycle slips of (9) is discussed. The performance of the Double Difference PNRS (DDPNRS) filter without the velocity aiding, and against the cycle slips of (9), is evaluated. Finally, a feasibility study for the development of FDIR algorithms is presented.

The filters evaluated in this chapter are tuned conservatively for state performance. Tuning for state performance was favored over tuning for residual performance because enhancement of the PNRS's accuracy was the main objective of this research. For a true FDIR research effort, tuning for residual accuracy is recommended.

4.2 Simulation Specifications

The purpose of this section is to provide the reader with specific information concerning the conditions under which the simulations used in this thesis were conducted. The flight profile used is discussed, along with information concerning the RRS transponders and GPS satellites.

The flight profile used is the same profile employed by previous AFIT students (9, 20). It is used in this thesis so direct comparison to previous research can be conducted. The flight profile consists of a two-hour fighter profile which was generated by PROFGEN (22). For baseline and tuning runs, the full two hours of the profile are used for analysis. For cycle slip analysis, only

the first one thousand seconds of the two hours are used. This use of only the first one thousand seconds is to reduce the time necessary to complete a simulation run without any substantive loss of analysis. Figure 4.1 gives a three-dimensional representation of the flight profile and Figure 4.2 gives the latitude, longitude, and the altitude of the flight profile in two-dimensions versus time.

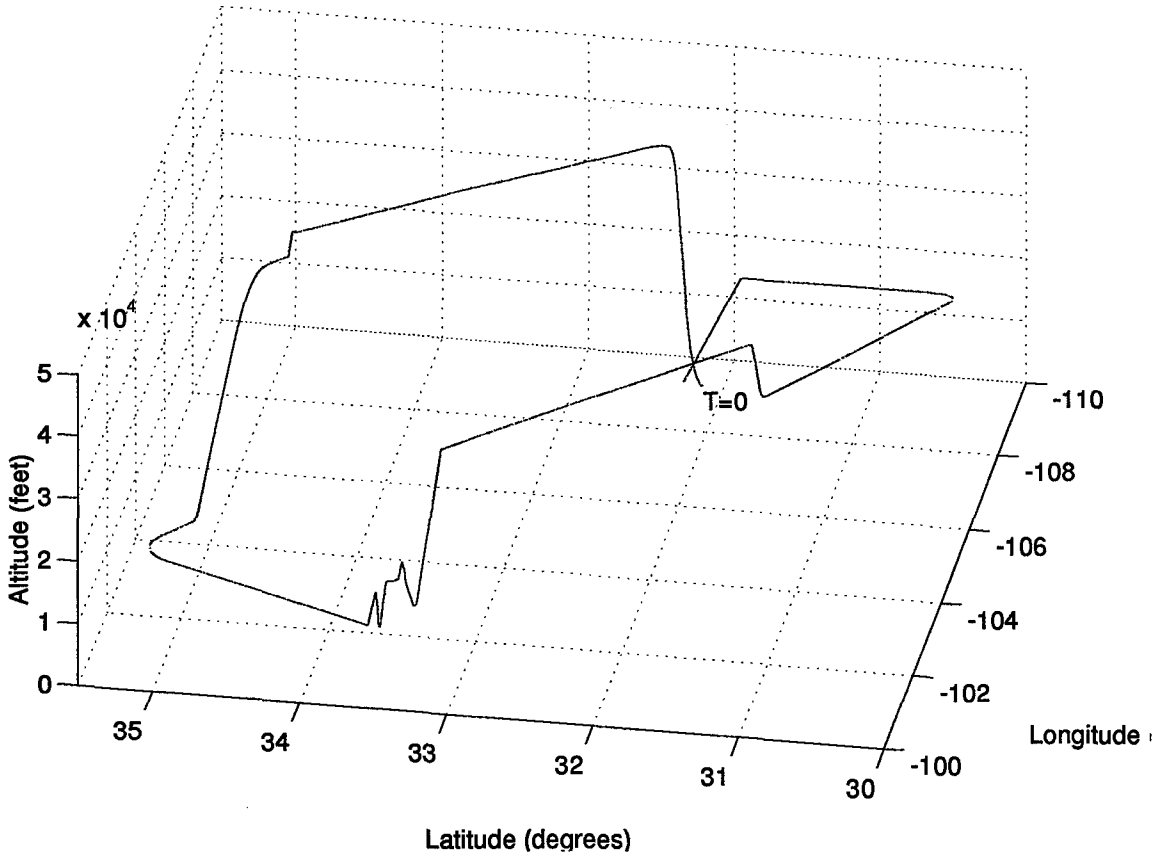

Figure 4.1 Three-Dimensional Representation of Fighter Flight Profile

Note that, in Figure 4.2, the time scale label for the multiple plots is placed on the bottom of the figure. This convention is constant throughout this thesis. The flight profile's latitude and longitude coordinates are oriented over the CIGTF RRS Test Range for the implementation of RRS measurement updates into the extended Kalman filter. Although CIGTF operates numerous transponders, the number used in this thesis is limited to six. Six has been chosen to remain consistent with previous research, and to keep the number of RRS states necessary low so as not to

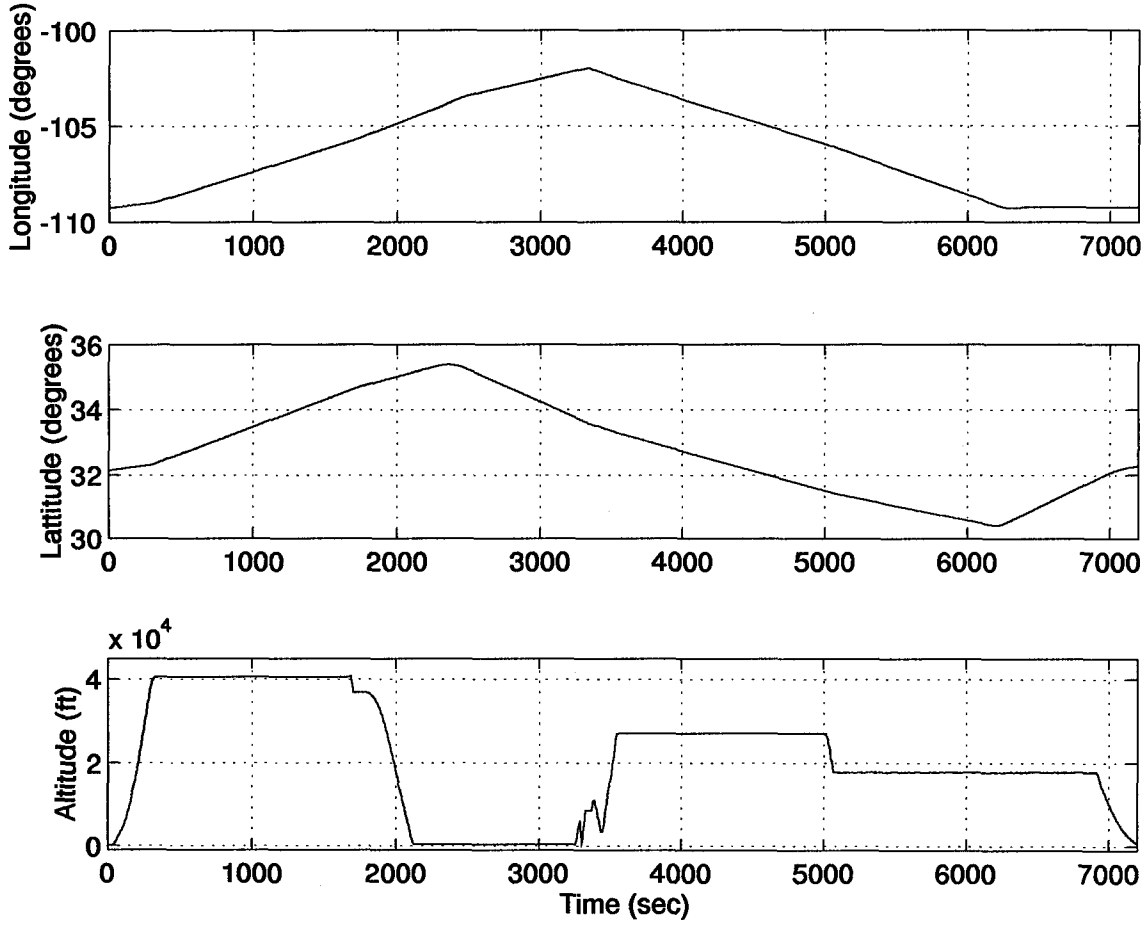

Figure 4.2 Two-Dimensional Representation of Fighter Flight Profile

overburden the system computationally. For each transponder, four states must be implemented, as discussed in Chapter III, Section 3.2.2.1. To add any transponders to the simulation would require the addition of four states per transponder, a burden that was deemed to be unwarranted. Table 4.1 gives the geographic locations of the transponders used in this simulation (20). Figure 4.3 gives a three-dimensional representation of the transponder locations with respect to the aircraft flight profile.

The measurement updates to the filter also come from the Global Positioning System Satellites. The satellite positions are calculated in MSOFE (3) as described in Chapter I, Section 1.4, Assumption 8. The four satellites chosen by the MSOFE user subroutine CALDOP consist of the

Table 4.1 RRS Transponder Transmitter Locations in the PNRS Simulations

#	Location	Longitude	Latitude	Altitude
T1	Tula PK, NM	$33.01°36'$	$-106.08°20'$	$1322.5272ft$
T2	TDC, NM	$32.55°58'$	$-106.08°50'$	$1241.7552ft$
T3	Oscura Park, NM	$33.44°58'$	$-106.22°14'$	$2417.5144ft$
T4	Salinas, NM	$33.17°55'$	$-106.31°44'$	$2695.11ft$
T5	Sac Peak, NM	$32.47°16'$	$-105.49°15'$	$2804.81ft$
T6	Twin Buttes, NM	$32.42°12'$	$-106.07°38'$	$1365.71ft$

four satellites which have the lowest PDOP and are in view of the receiver of the 10626 different combinations of four satellites available from the twenty-four satellite constellation used in MSOFE. Over the two-hour profile, the four satellites initially chosen do not change for two reasons. The first reason is that the calculated PDOP does not exceed the maximum PDOP (MAXDOP) set by the user. For this simulation, MAXDOP is equal to 5. The PDOP initially starts out at a value of 1.539 and increases to a value of 2.466 at the end of the two hours. The increase in PDOP is due to the changing geometry of the satellites due to the constant motion of the satellites and receiver. The second factor which allows for the original four satellites to be used throughout the two-hour profile is that all four satellites "remain in view" or can be seen by the GPS receiver. This is because none of the satellites drop below the necessary elevation angle for the receiver to be able to lock onto the satellite signal.

4.3 The Removal of the Perfect Doppler Velocity Aiding

The research of (9, 20, 23, 31) implemented a perfect Doppler velocity measurement scheme into the EKF of MSOFE in order to ensure filter stability (a discussion of how this measurement is modelled can be found in Chapter III, Section 3.7.2). The use of this perfect velocity aiding has left doubt in the validity of the results of this previous research and has been a frequent suggestion into the improvement of the validity of the results of current research. Through discussion with Dr. Peter S. Maybeck (18), this author discovered that Mr. Robert Gray, GE-94D, was running his GPS/INS integration EKF in MSOFE without the perfect velocity aiding and maintaining stability.

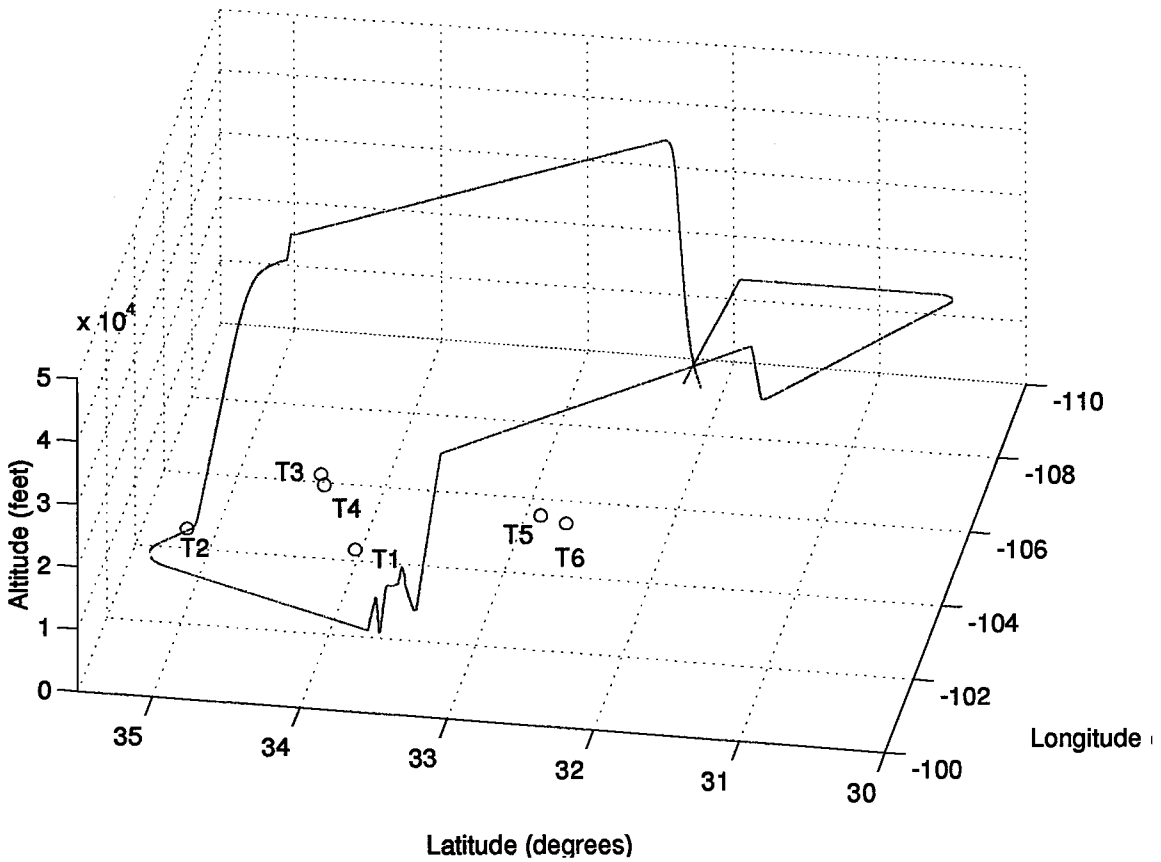

Figure 4.3 Three-Dimensional Representation of Fighter Flight Profile with Transponder Locations

This prompted the removal of the velocity measurement updates from this simulation to test if the PNRS EKF would remain stable without the perfect Doppler velocity aiding.

The following sections present the results of MSOFE simulations without the perfect Doppler velocity aiding measurements included in the MSOFE simulations. Later sections compare the filter results both with and without velocity aiding to show how the removal of these measurements affect the filter's performance.

4.4 The 71-State PNRS Filter without Velocity Aiding

The 71-state PNRS filter of Hansen's research (9) was run without the perfect velocity measurements and some interesting results were found. Using the same setup and tuning parameters

from Hansen without the perfect velocity aiding produced a stable filter design, as can be seen in Figures D.1 through D.9 in Appendix D. In fact, not only did the filter remain stable, some of the parameters of interest actually became more accurate. The only parameter which showed a significant decrease in accuracy was the vertical velocity error state, as expected due to the inherent instability of the INS in the vertical channel. Even though the vertical velocity error state degraded in accuracy, it seems this degradation could be improved through tuning to compensate for the missing measurements, but retuning of this filter was not completed. Figure 4.4 depicts the vertical velocity error state of the PNRS both with and without the perfect Doppler velocity aiding. Table 4.2 tabulates the true one-sigma errors' temporal average of the PNRS with and

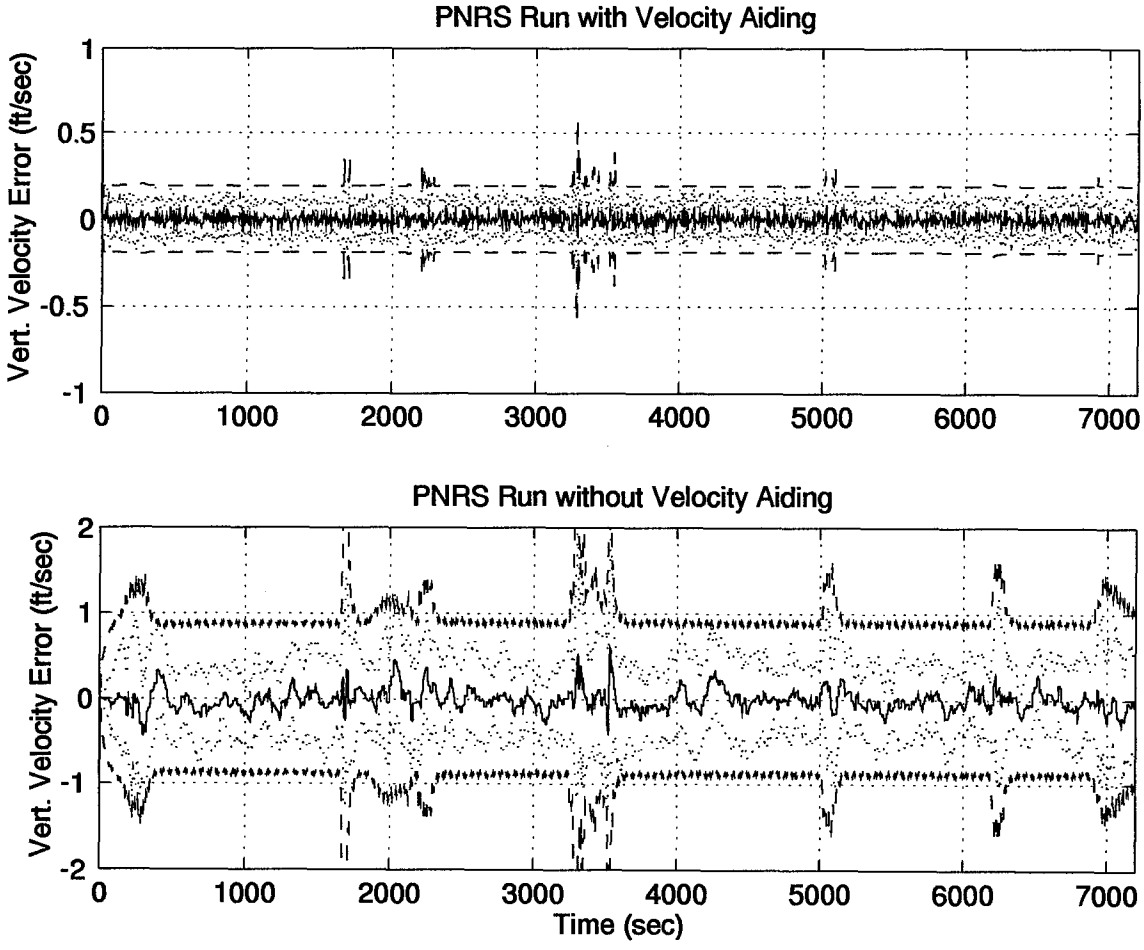

Figure 4.4 Comparison of Vertical Velocity Error States

without velocity aiding for the parameters of interest.

Table 4.2 Comparison of PNRS True Filter Errors with and without Velocity Aiding

Velocity Aiding (Y/N)	Longitude (feet)	Latitude (feet)	Altitude (feet)	Baro-Alt (feet)
Yes	1.42	1.47	6.00	36.31
No	1.99	1.82	5.85	36.07

Velocity Aiding (Y/N)	North Tilt (degrees)	West Tilt (degrees)	Azimuth Tilt (degrees)	North Velocity (fps)	West Velocity (fps)	Vertical Velocity (fps)
Yes	3.00×10^{-4}	3.00×10^{-4}	2.20×10^{-4}	0.10	0.10	0.10
No	1.97×10^{-4}	1.80×10^{-4}	1.97×10^{-4}	0.10	0.11	0.50

Velocity Aiding (Y/N)	Xpr Range (feet)	Xpr Velocity (fps)	Xpr Atm. (feet)	RRSX Position (feet)	RRSY Position (feet)	RRSZ Position (feet)
Yes	1.76	0.0072	0.106	3.88	2.96	1.42
No	1.74	0.0072	0.117	3.81	3.13	1.48

Comparison of Figures D.1 through D.9 with those of Hansen's research, which can be found in (9), show definite filter stability, with some differences which can be attributed to the lack of the velocity aiding. Figures D.1 through D.4 show the INS errors of the system in position, tilt, and velocity errors. The changes exhibited in these plots due to the lack of velocity aiding are consistent. The first notable difference occurs in all of the error states except for the barometric altimeter error state. That is, all of the filter-predicted standard deviations (1σ's) on the plots (the dashed line) have greater values than their counterparts in (9). The plots of the Longitude errors from both filters are given in Figure 4.5 as an example. The overall steady state values of the filter-predicted standard deviation is slightly greater and the span of error propagation between measurement updates is also greater. This phenomenon is consistent in the other INS error states. The barometric altimeter error state is unaffected by the lack of velocity measurement because the barometric altimeter has its own separate measurement update. This increase in the filter-predicted standard deviation can be attributed to the filter realizing that the velocity measurements are not being taken and

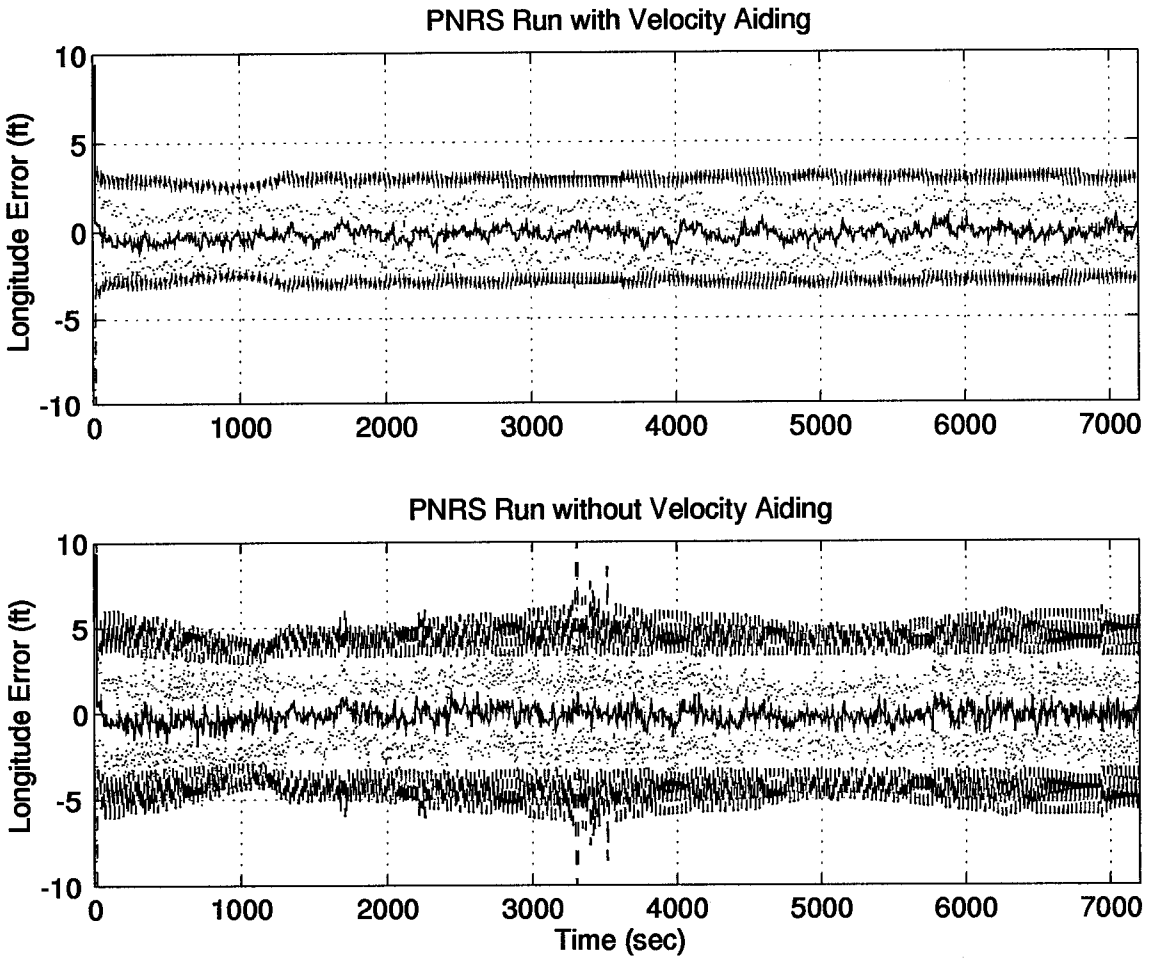

Figure 4.5 Comparison of Longitude Error States

compensating for those missing measurements through a decrease in confidence in its results. The mean error and mean error plus-and-minus the true standard deviation of the filter plots remain for the most part unchanged except for an increase in the vertical velocity, as discussed earlier. In Figures D.1 and D.2 another interesting phenomenon is observed. These states, the longitude, latitude, and altitude errors, show even greater increases in the filter-predicted standard deviations during major changes in the aircraft's direction and/or altitude when the aircraft's velocity is most likely undergoing significant changes. By comparing the timing of these increases with the timing of changes in the aircraft's trajectory in Figure 4.2, one can easily see this phenomenon. For example, the Longitude error state exhibits one of these increases in its predicted standard deviation at

approximately 3500 seconds. This "spike" or increase can be linked to the change in longitude and altitude at the same time, as shown in Figure 4.2. This phenomenon shows an increase in the sensitivity of the filter to changes in the aircraft's velocity during dynamic maneuvers. The increase in sensitivity observed can be attributed to the lack of velocity measurements causing the filter to lose confidence in itself during velocity changes which cause these errors.

This section discussed the effect that removing the perfect Doppler velocity aiding had on the 71-state PNRS filter of Hansen's research. The following sections will cover the results from the filter order reduction of the filter from 71 states to 19 states, and the implementation of the Double Differencing scheme discussed in Chapter III, Sections 3.4.2 and 3.6.2, and how these filter models handled the removal of the perfect Doppler velocity aiding.

4.5 The Reduced Order PNRS Filter Results

The following section presents the results obtained from the 19-state Reduced Order PNRS (ROPNRS) filter. The results presented involve simulation runs of the filter both with and without the perfect Doppler velocity aiding measurements taken. The performance of the filter in the presence of cycle slips is also discussed.

4.5.1 Normal-Running Filter with Velocity Aiding. The reduction of the filter order decreased the overall accuracy of the filter from Hansen's research, as expected, but surprisingly some of the parameters of interest actually became more accurate. Table 4.3 gives the temporal averages of the filter's true 1σ errors for Hansen's filter (PNRS) (9), the ROPNRS filter, and of Mosle's reduced-order filter (ROF) (20) for the full two-hour fighter flight profile for direct comparison. In Table 4.3, XprRng stands for the Transponder range error and XprVel stands for the Transponder velocity error. The blanks left in the results from Mosle's research are due to the fact that these values were not listed in his results. The inclusion of the results from Mosle's research is done for a more realistic comparison of filter performance because Mosle used the same

Table 4.3 Temporal Averages of True Filter Errors (1σ)

Filter Analyzed	Long. (feet)	Lat. (feet)	Alt. (feet)	Baro. (feet)	NTilt (degrees)	WTilt (degrees)	AziTilt (degrees)
PNRS	1.42	1.47	6.00	36.31	3.00×10^{-4}	3.00×10^{-4}	3.00×10^{-4}
ROPNRS	4.66	4.00	4.67	35.20	1.60×10^{-5}	1.50×10^{-5}	1.16×10^{-5}
ROF	6.04	3.45	15.76		1.18×10^{-5}	1.50×10^{-5}	1.36×10^{-4}

Filter Analyzed	NVel (fps)	WVel (fps)	VertVel (fps)	XprRng (feet)	XprVel (fps)
PNRS	0.10	0.10	0.10	1.76	0.0072
ROPNRS	0.062	0.062	0.11	2.59	0.0072
ROF	0.062	0.062	0.14		

reduced order filter model, but without carrier-phase measurements. The most significant factor which can be attributed to the increase in the accuracy of some parameters is the reduction of the RRS transponders and GPS satellite sample rates from six and ten seconds respectively, to two seconds for both sets of measurements. Past research of (9, 23, 26, 29) most likely used such low measurement update rates to keep the simulation times of such high order models down as low as possible. With the reduction of order and the availability of faster computer systems (now SPARC 20's at AFIT), the reduction of the measurement update time does not greatly increase the simulation run time. The benefit of the decrease in the measurement update rate is shorter error propagation times and an increase in the number of measurements taken to aid the filter in accurately predicting the errors of it models.

Figures E.1 through E.8 of Appendix E depict the filter's performance during the two-hour flight simulation as described in Section 4.2. The results presented show that the filter remains stable throughout the simulation with only minor times when the error mean plus/minus the true filter standard deviation plots (the dotted line) exceed the filter-predicted standard deviation (the dashed line) as in Figures E.1, E.7, and E.8. These results show the filter has less confidence in its models due to the order reduction. The results presented are also of a conservatively tuned

filter. Fine tuning was not attempted in the essence of time available for research and because conservative tuning was decided to be acceptable for simulation purposes.

This section described the results of the PNRS filters order reduction and compared them to the results of $(9, 20)$. The next section discusses the results of the ROPNRS filter without the perfect Doppler velocity aiding.

4.5.1.1 Normal-Running Filter without Velocity Aiding. As described in Section 4.4, the perfect Doppler velocity aiding measurements have been a point of skepticism for results obtained in the past. The ROPNRS filter was also run without the perfect velocity aiding to check for filter stability. The ROPNRS filter, like Hansen's 71-state filter (9), also remained stable over the two-hour flight profile. The ROPNRS's vertical velocity, as in Hansen's filter, suffered the greatest accuracy degradation but remained stable. Figure 4.6 depicts the vertical velocity error without the velocity aiding prior to filter retuning. To account for these missing measurements, the filter was retuned and these tuning values can be found in Appendix C, Table C.2. The results of the tuned ROPNRS filter are depicted in Appendix F, Figures F.1 through F.8. As was the case with Hansen's filter, where some of the parameters of interest increased in accuracy, the same held true for the ROPNRS filter. Table 4.4 gives the temporal averages of the true 1σ errors for the ROPNRS both with and without the velocity aiding measurements. As shown in the running of Hansen's filter

Table 4.4 Temporal Averages of True Filter Errors (1σ) of ROPNRS Filter

Velocity Aiding (Y/N)	Long. (feet)	Lat. (feet)	Alt. (feet)	Baro. (feet)	NTilt (degrees)	WTilt (degrees)	AziTilt (degrees)
Y	4.66	4.00	4.67	35.20	1.60×10^{-5}	1.50×10^{-5}	1.16×10^{-5}
N	4.70	4.20	3.65	31.13	1.60×10^{-5}	1.70×10^{-5}	1.45×10^{-4}

Velocity Aiding (Y/N)	NVel (fps)	WVel (fps)	VertVel (fps)	XprRng (feet)	XprVel (fps)
Y	0.062	0.062	0.11	2.59	0.0072
N	0.060	0.052	2.23	2.70	0.0072

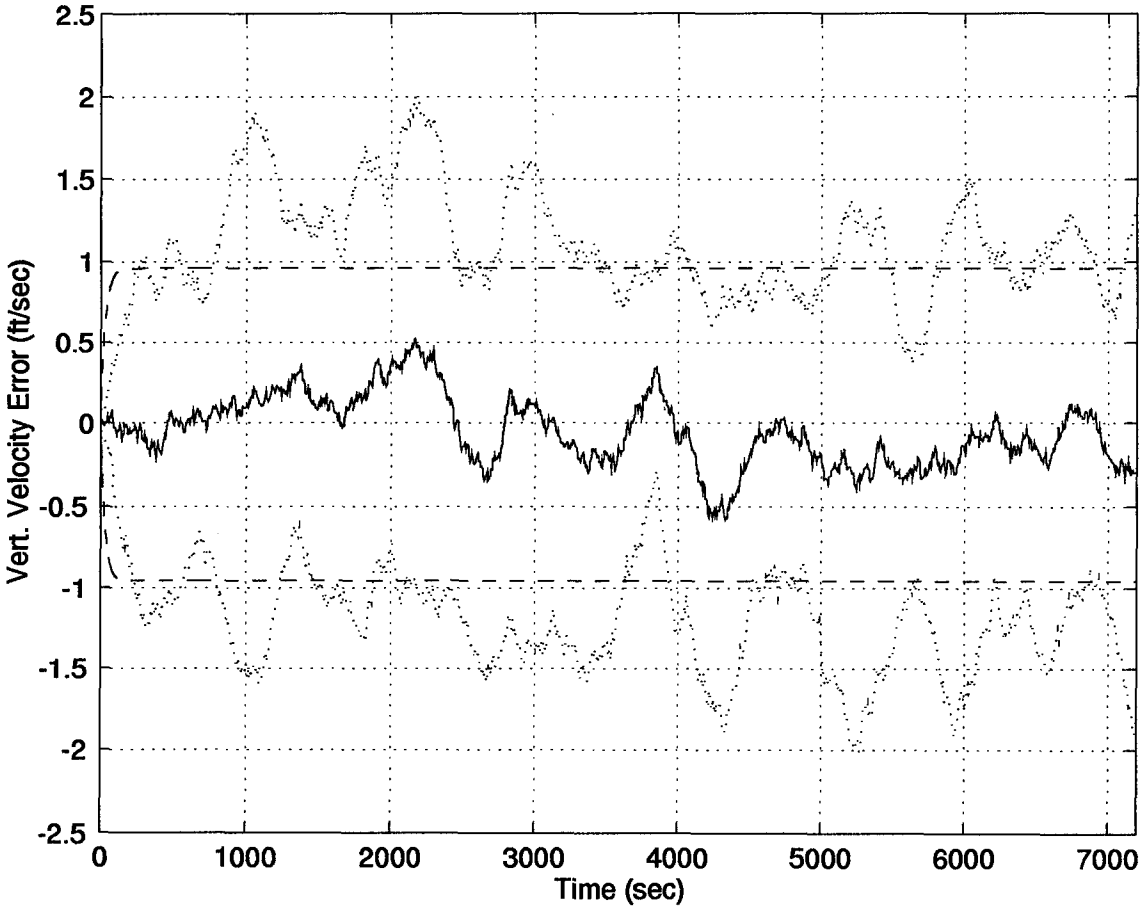

Figure 4.6 Untuned Vertical Velocity Error without Velocity Aiding

without velocity aiding, the filter-predicted standard deviations of the INS parameters (latitude, longitude, altitude, tilts, and velocities) were all increased, showing that the filter realizes that the velocity aiding measurements are no longer being taken. The sensitivity of the filter to changes in the vehicle's velocity, as exhibited in Hansen's filter and shown in Figure 4.5, does not show up in the latitude, longitude, and altitude error plots of Figures F.1 and F.2. Another major difference in the two filters is the accuracy of the vertical velocity . Hansen's filter-predicted vertical velocity 1σ error only slightly increased, as compared to the order of magnitude increase in error of the same parameter in the ROPNRS filter. This lack of filter sensitivity and significant decrease in the vertical velocity accuracy can be attributed to the filter order reduction. The ROPNRS filter only models 11 INS states compared to the 39 INS states of Hansen's filter. The states which were

removed in the filter order reduction represent factors which affect the INS's velocity computations, thereby eliminating the sensitivity and accuracy maintainability observed in Hansen's filter without the velocity aiding measurements.

The filter stability observed without the perfect Doppler velocity measurements can possibly be attributed to the technology improvement in the computer system or the FORTRAN compiler under which MSOFE is run. The research of Negast (23), where the perfect Doppler system assumption originated, was run on the old VAX system of AFIT. The research of Hansen and Mosle (9,20) converted MSOFE from the VAX system to SUN SPARC stations. In their conversion, they also made improvements to the core code of MSOFE, csofe, to implement fully the double precision capabilities of the machine and the different FORTRAN compiler. This increase in numerical accuracy may explain why we do not need the perfect velocity aiding measurements to maintain filter stability, whereas Negast did need them. Now that it is proven that the filter can maintain stability without the perfect velocity aiding, implementation of a realistic Doppler model should be conducted to improve the degraded accuracy of the vertical velocity of the filter back to the results obtained with the perfect velocity aiding, if so desired.

4.5.2 Cycle Slip Simulation Results. The simulated cycle slips of Hansen's research (9) were used to see how the ROPNRS filter would respond to these induced errors. The same method of cycle slip injection was used as in (9), except for the large cycle slip setup, due to an error found in the MSOFE code. In (9), Hansen described a large cycle slip as a twenty-second loss of lock with Satellite 1 followed by a 30,000 foot change in the range between the receiver and the satellite. How this was implemented by Hansen is illustrated in Figure 4.7. The cycle slip is to start at t=400 seconds and follow the previously stated description, but as can be seen in Figure 4.7, the 30,000 foot change in the phase range comes at t=400 seconds and lasts until t=420 seconds. During the period of a cycle slip, a receiver is no longer counting cycles and therefore cannot know how much the cycle count is changing due to aircraft dynamics. To simulate this large cycle slip

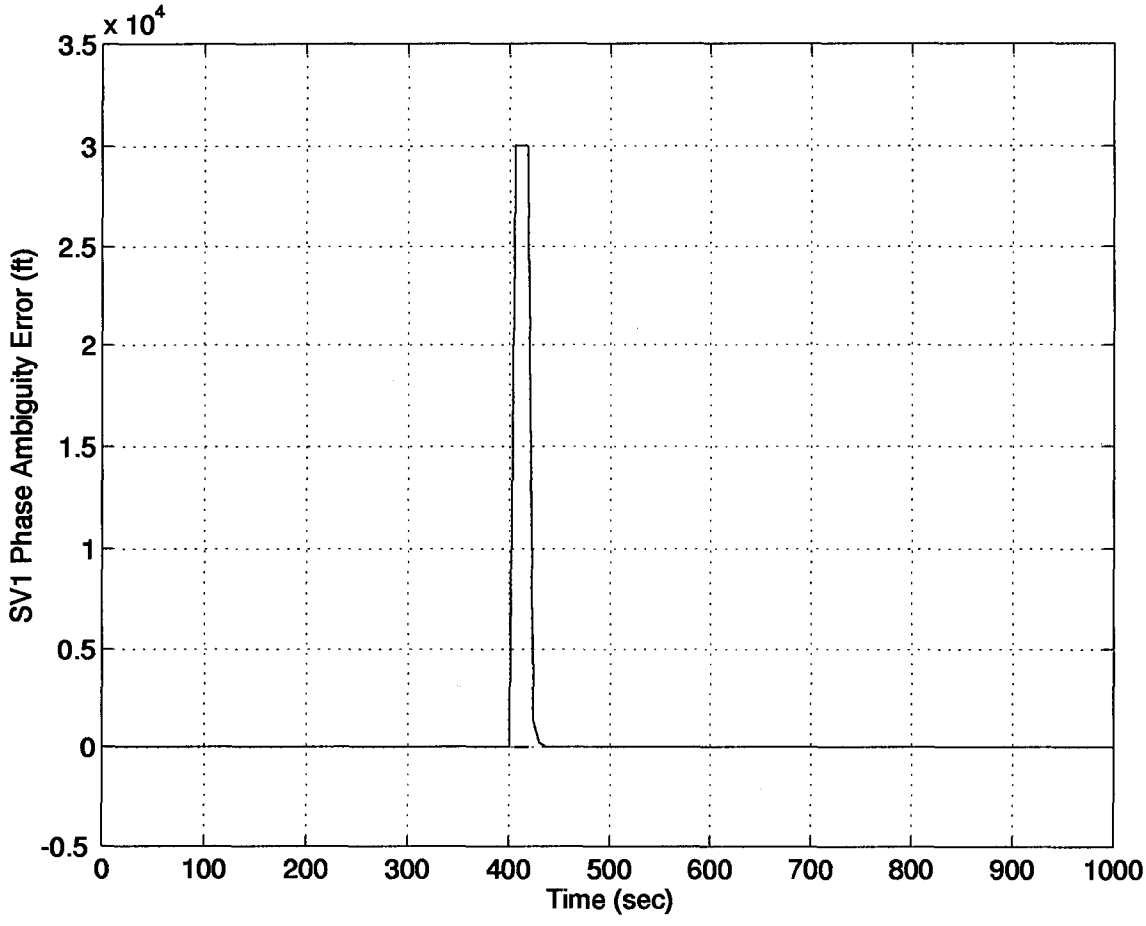

Figure 4.7 Incorrect Implementation of a Large Cycle Slip

properly, the satellite loss takes place at t=400 seconds and lasts for twenty seconds, at which time the receiver relocks onto the slipped satellite, and now can interpret a change in the cycle count and determine that the range to Satellite 1 has changed by 30,000 feet. Figure 4.8 depicts the proper implementation of a large cycle slip.

The ROPNRS filter responded practically the same way as Hansen's filter to all of the cycle slips simulated in (9). The recovery times associated with each of the filters are relatively the same, with justifiable differences due to the order reduction in the ROPNRS filter. The major difference in filter responses comes from the fact that the measurement update periods of the GPS were reduced from ten seconds to two seconds. In (9), the large cycle slip would end, and after one

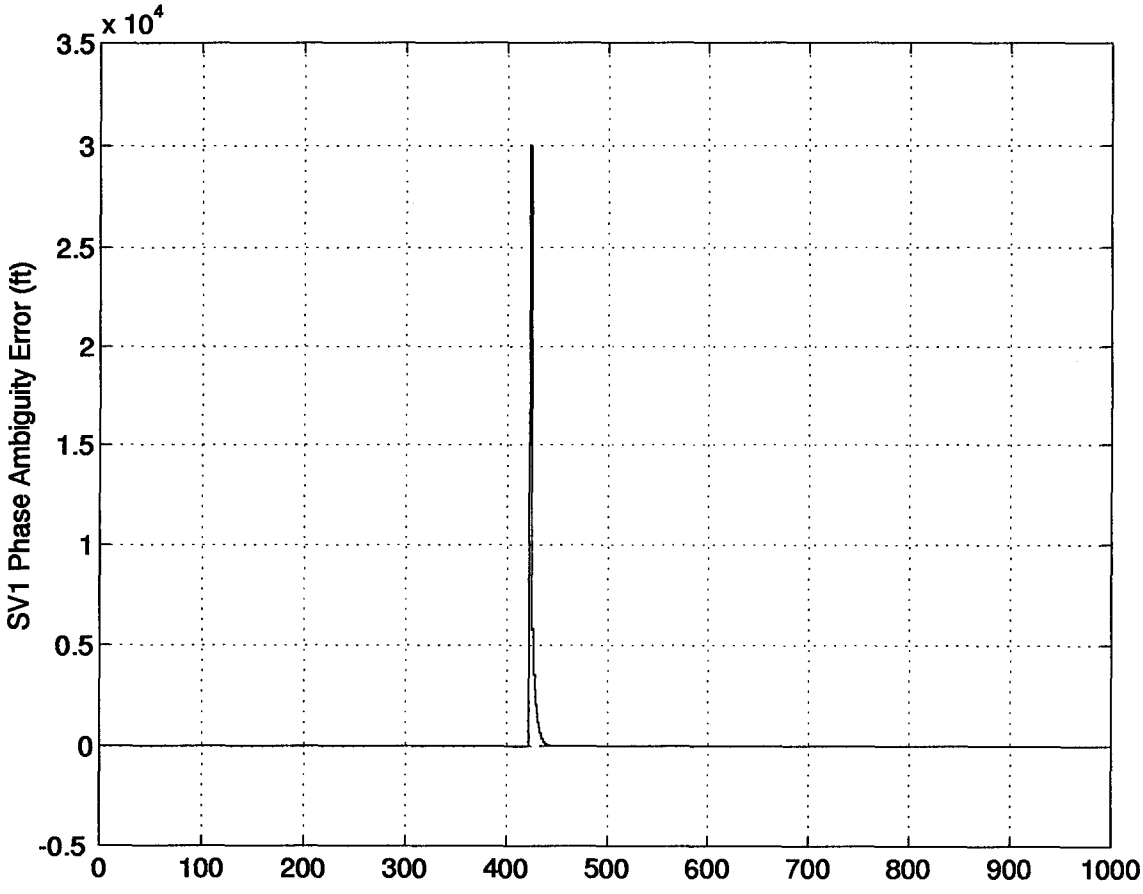

Figure 4.8 Correct Implementation of a Large Cycle Slip

measurement update, or ten seconds later, the effects of the cycle slip would become observable in all other states except for the transponder velocity. By reducing the update period to two seconds, the effect of the cycle slip becomes observable in all other states only two seconds later.

4.6 The Reduced Order PNRS Filter with Double Differencing

The following sections present the results of the implementation of the Double Differencing scheme described in Chapter III, Section 3.4. The results discussed are for the Double Differenced filter without the velocity measurements taken. Also discussed is how the Double Difference PNRS (DDPNRS) filter is affected by cycle slips.

4.6.1 Normal-Running Double Difference Filter. The implementation of the double differencing between receivers/satellites produced a stable filter without the perfect velocity aiding, as expected. The expected improvement in the overall accuracy of the filter over that seen in Section 4.5.1.1 however, was not observed. Table 4.5 compares the temporal averages of the true filter errors between the ROPNRS filter and the DDPNRS filter. As is shown, the filter exhibited improvements in the temporal averages of the true 1σ errors in some of the parameters of interest but also showed some degradation in other parameters from the ROPNRS filter. The DDPNRS filter, like the ROPNRS filter, is conservatively tuned and the tuning values of the DDPNRS filter can be found in Appendix C, Table C.3.

The DDPNRS filter's performance is depicted in Appendix G, Figures G.1 through G.7. The implementation of the double differencing is evident in the figures of the INS parameters and the CPGPS phase ambiguity errors. The evidence is in the decrease in the filter-predicted standard deviations, which reflects the filter recognition of the more accurate CPGPS measurements available through the differencing conducted. The transponder velocity mean error is practically eliminated, but the true 1σ values are increased to exceed the filter-predicted standard deviations. This is depicted in Figure G.5. This increase in the true standard deviation (1σ value) shows a possible

Table 4.5 Temporal Averages of True Filter Errors (1σ) of ROPNRS and DDPNRS Filter

Double Differencing (Y/N)	Long. (feet)	Lat. (feet)	Alt. (feet)	Baro. (feet)	NTilt (degrees)	WTilt (degrees)	AziTilt (degrees)
N	4.70	4.20	3.65	31.13	1.60×10^{-5}	1.70×10^{-5}	1.45×10^{-4}
Y	4.13	3.29	3.23	28.29	1.90×10^{-5}	1.80×10^{-5}	1.90×10^{-5}

Double Differencing (Y/N)	NVel (fps)	WVel (fps)	VertVel (fps)	XprRng (feet)	XprVel (fps)
N	0.060	0.052	2.23	2.70	0.0072
Y	0.034	0.059	2.27	2.46	0.0119

correlation between the RRS and GPS measurements which is made observable in the double differencing.

The increase in the filter's overall accuracy is encouraging but the lack of significant increase leaves a question of how accurate are the current models being implemented in the system. Another explanation of this lack of significance could be that a fine tuning effort has to be made to reap the benefits of CPGPS and a CPGPS double differencing scheme.

4.6.2 Cycle Slip Simulation with a Double Difference Filter. The double differencing combinations used in this research have a profound affect on how the filter responds to the induced cycle slips. The use of Satellite 4 as the base satellite for the three difference measurements causes changes in the condition of the fourth satellite to be reflected instantaneously in the other three satellite measurements. In contrast, changes in the states of the other three satellites do not immediately affect the other satellites but wait until the next GPS measurement update time, as is the case with the ROPNRS filter. This is because the measurements of these three satellites only differ from the ROPNRS by the fact that the fourth satellite measurement is subtracted from them, which leaves an error state that behaves the same in all cases.

The injection of a small cycle slip into the simulation at t=400 seconds for a 10 foot error on Satellites 1, 2, or 3 exhibits the same response as found in Hansen's research and the ROPNRS filter. The slip becomes "lost in the noise" and is only observable in the "slipped" satellite's phase ambiguity error term and residual, as shown in Figures H.6 and H.8 of Appendix H for a small cycle slip on Satellite 1. When the same cycle slip is induced on Satellite 4, the results show how the double differencing method affects the filter's response. The cycle slip clearly shows up in all of the filter's GPS satellite residuals but only in the phase ambiguity error of Satellite 4. Figure 4.9 depicts the residual plots of the individual residuals for a small cycle slip on Satellite 4. What can be clearly seen is that the satellite affected by the cycle slip produces a negative spike, as opposed to an equal positive spike which is produced in the other three residuals. This is because of the way

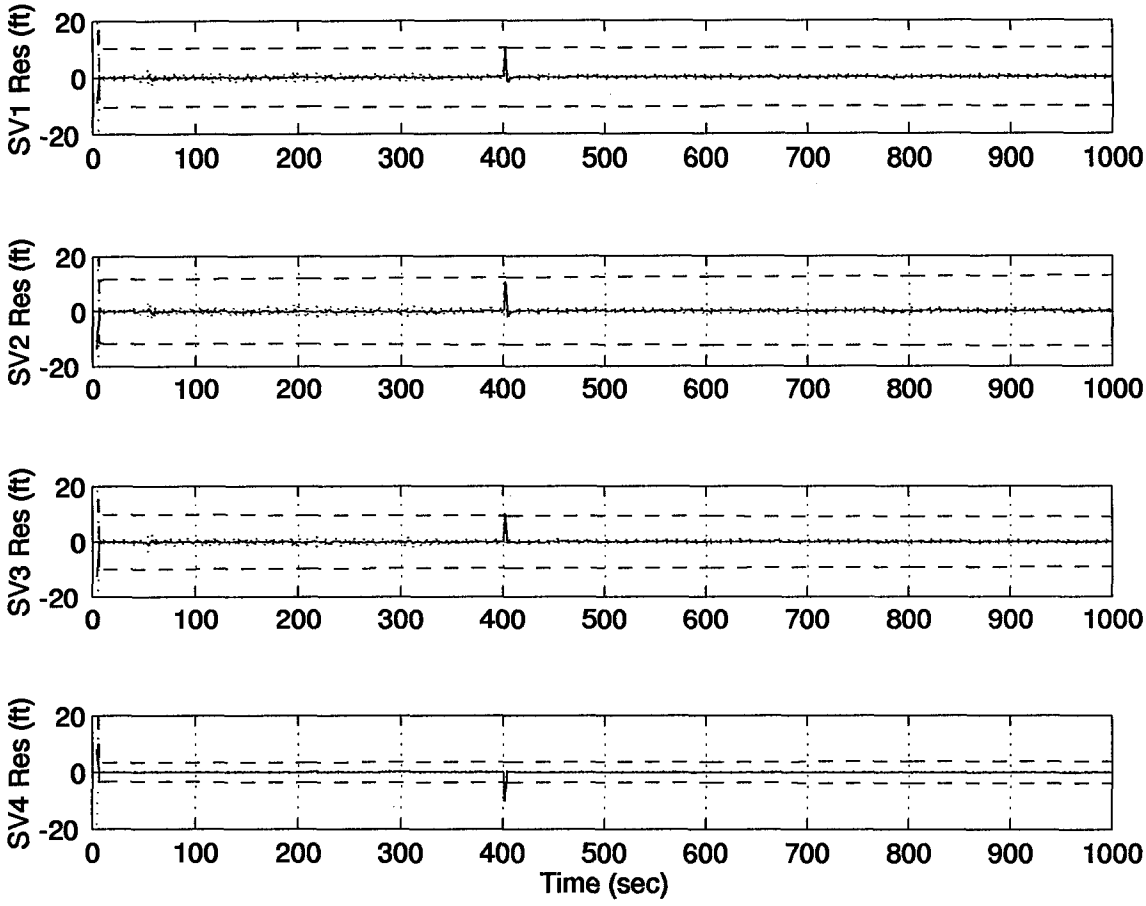

Figure 4.9 DDPNRS Filter Residuals for a Small Cycle Slip on Satellite 4

cycle slips are encoded in MSOFE. The range error of a cycle slip is added to the phase ambiguity error state value of the specific satellite and then this value is subtracted from the measurement to form the residual, which causes the negative "spike" in the residual of the affected satellite. When differencing the fourth satellite from the other three, this error is now positive in the unaffected satellites due to the differencing conducted. The induction of the small slip onto Satellite 4 also causes a noticeable spike in the latitude error, which indicates correlation.

The simulation of a 200-second satellite loss, as used in Hansen (9), produced some interesting results. All states except for the phase ambiguity error states and the residuals remained relatively unaffected by the satellite loss. The only evidence of the satellite loss outside of the GPS error states and residuals show up as increases in the true 1σ errors and the filter-predicted standard deviations

for the duration of the satellite loss, which indicate that the filter realizes that something is wrong with the GPS satellite measurements. An example of the phenomenon is depicted in Figures I.1 through I.9 of Appendix I. These figures show how a loss of Satellite 1 for 200 seconds affects the filter's performance. The latitude, longitude, and altitude errors of Figures I.1 and I.2 clearly shows the increases in the standard deviations as previously discussed. The effect that this 200-second satellite loss has on the GPS satellite states is very interesting. In the phase ambiguity errors states, and in the residuals, this type of cycle slip presents itself as an increase in the filter-predicted standard deviation. In the phase ambiguity error states a satellite loss on Satellites 1, 2, or 3 shows up only on the satellite upon which the cycle slip occurred, whereas if the loss occurs on Satellite 4, it becomes observable in all of the satellite phase ambiguity errors simultaneously. In the residuals, the observability of the loss of a satellite is limited to the specific satellite upon which the loss occurs. This is because the loss of a satellite is simulated as an increase in the measurement noise variance of the lost satellite and this increase in the variance does not affect all of the residuals due to the differencing scheme implemented as is the case in the phase ambiguity terms. Another interesting phenomenon observed with a satellite loss is that, as the error was induced in each satellite individually, the maximum magnitude of the filter-predicted standard deviation increase decreased as the loss was induced on each satellite. Figure 4.10 depicts this phenomenon in the phase ambiguity error states. This phenomenon can be attributed to the scalar measurement updating inherent in MSOFE. The updates are computed as scalars rather than as vectors. The use of vector updating should eliminate this phenomenon because of the individual updating of the states which occurs in the scalar updating would be eliminated.

The implementation of the large cycle slip exhibits the greatest effects of this double differencing method. The large cycle slip is induced as a 30,000 foot range difference at 422 seconds after a 20-second loss of the slipped satellite. When implemented on Satellites 1, 2, or 3, the results resemble those of the ROPNRS filter. The recovery times associated with each of the parameters of interest are comparable with those of the ROPNRS filter. Figures J.1 through J.9 of Appendix

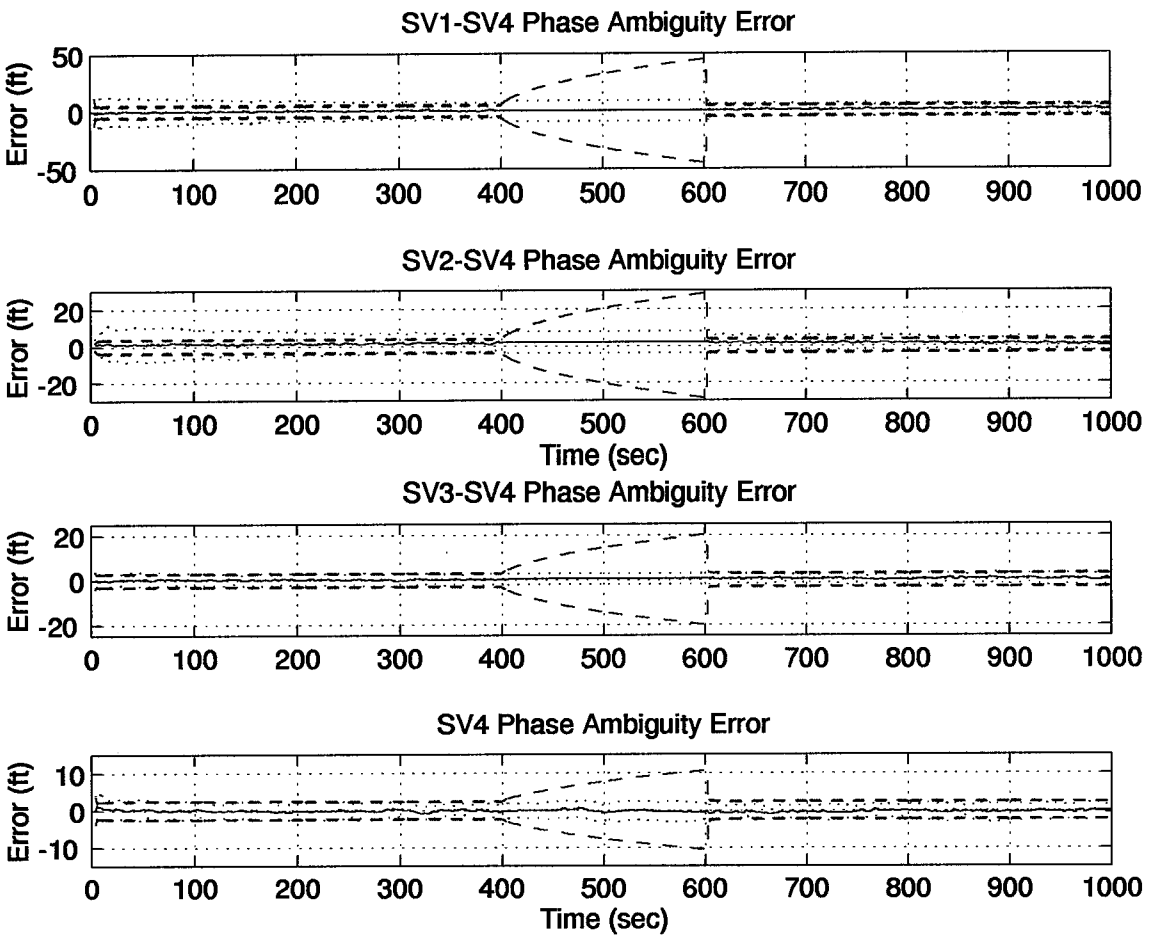

Figure 4.10 DDPNRS Phase Ambiguity Error States for a Satellite Loss Cycle Slip

J depict a large cycle slip injected on Satellite 1. The results of Satellite 1 are presented to represent what happens when a large cycle slip is induced on any of the first three satellites satellites. Although a large cycle slip on each satellite causes different residual and state behavior, the trends exhibited are similar enough to justify the need for only one set of plots.

The disparity in results comes when the cycle slip occurs on the fourth satellite. The cycle slip becomes observable on all of the satellite states instantaneously and becomes observable on all of the remaining parameters except the transponder velocity after the next GPS measurement update. The major problem involved with a large cycle slip on Satellite 4 lies in the recovery times. All of the observed parameters take more time to recover (than they do in the ROPNRS filter) and

in the case of the Azimuth Tilt error, it does not recover by t=1000 seconds when the simulation ends, as can be seen in Figure K.3. Table 4.6 gives approximate recovery times of the DDPNRS filter for a large slip on Satellite 1 and 4, where DNR stands for Did Not Recover. Figures K.1 through K.9 of Appendix K depict the the DDPNRS filter's performance with a large cycle slip on Satellite 4. The cause of this increase in recovery times can be attributed to the correlation of the CPGPS measurements caused by the differencing scheme implemented. To avoid this problem, one can use six satellites in the creation of the three differences needed, without the correlation in the measurements exhibited in this filter implementation that treats one satellite (#4) as prime.

4.7 FDIR Simulation Results

The following sections will discuss the results of the analysis completed on how large cycle slips affect the ROPNRS and DDPNRS filters. Only large cycle slips are analyzed because it was determined that large cycle slips are the most detrimental to the system's accuracy. The analysis provided is for a Chi-Square Test performed on each of the filter's CPGPS residuals. A discussion of how the MMAE algorithm proposed in Chapter II, Section 2.4.2 would perform against each cycle slip simulation is also presented. Each filter had a 30,000 foot range cycle slip induced on it at t=422 seconds, after a 20-second loss of lock to each satellite. The last simulation of each filter discussed involves a multiple cycle slip scenario. In this simulation, all four satellites are

Table 4.6 Large Cycle Slip Recovery Times of Satellites 1 and 4 of the DDPNRS Filter

Satellite Number	Long. (sec)	Lat. (sec)	Alt. (sec)	Baro. (sec)	NTilt (sec)	WTilt (sec)	AziTilt (sec)
1	20	40	20	20	30	20	20
4	60	160	30	30	60	230	DNR

Satellite Number	NVel (sec)	WVel (sec)	VertVel (sec)	XprRng (sec)
1	40	20	30	30
4	280	170	30	190

slipped within a ten second period. Table 4.7 provides the specifics of each induced cycle slip. The

Table 4.7 Multiple Cycle Slip Induction Parameters

Satellite Number	Cycle Slip Range (feet)	Induction Time (seconds)
1	30,000	400
2	20,000	402
3	10,000	402
4	15,000	404

parameters used in this scenario were arbitrarily chosen assuming the aircraft could complete a 180 degree roll in 4 seconds, which for a F-16 is a realistic assumption.

The window size, N, of the Chi-Square test for this analysis is N=1. For the simulations conducted, the choice of N=1 is acceptable because of the well-behaved residuals and lack of large noise spikes in the residuals. For a real data analysis, a larger N would be necessary to reduce false alarms caused by noisy residuals. This size N was chosen so results obtained could be used to predict the performance of the proposed MMAE algorithm. The size of the time window represents one GPS measurement update period which would be used by the MMAE algorithm to update its measurement time history.

4.7.1 FDIR Results from the ROPNRS Filter. The Chi-Square test does a good job in the detection of the original cycle slip. This can be seen in Appendix L, Section L.1, Figures L.1 through L.5. For the single cycle slip induced on each individual satellite, it clearly begins to show up at t=422 seconds and peaks at the next measurement update, t=424 seconds. For this scenario, the Chi-Square test can be used to detect and isolate the error except for the observability of the cycle slip in the other GPS states at t=424 seconds. This problem can be seen starting at t=424 seconds in the Chi-Square tests of the unslipped satellites in Figures L.1 through L.4. This phenomenon would cause failures to be declared in the other three satellites at t=424 seconds unless the FDIR algorithm could compensate for the cycle slip by t=424 seconds which would eliminate the observability problem. If the recovery portion of the FDIR algorithm could not compensate

for the cycle slip by t=424 seconds, then missed alarms would be the biggest problem associated with this form of FDIR. Using the proposed MMAE algorithm of Chapter II, Section 2.4.2, the failure detection, isolation, and recovery would be completed when the Kalman filter bank switched once a cycle slip was detected. For example, consider the large cycle slip on Satellite 1. As the Chi-Square random variable would begin to grow because of the cycle slip, the probability of the fully functional filter and any other filter modelling Satellite 1 would be driven towards zero. On the other hand, the filter designated for a cycle slip on Satellite 1 would only be modeling Satellites 2, 3, and 4 and the probability associated with this filter would be close to one. The extended Kalman filter bank would switch to this filter, which is not corrupted by the bad measurement, and the observability of the cycle slip on the other residuals at t=424 seconds would be avoided.

As can be seen in Figure L.5, each cycle slip of the multiple cycle slip scenario shows up clearly for the Chi-Square test. Looking back on the previous discussion, the Chi-Square test cannot be sure the increase in the values associated with Satellites 2 and 3 is not the observability of Satellite 1's cycle slip occurring unless a recovery algorithm compensates for this cycle slip by t=424 seconds. In the MMAE algorithm, the hierarchical structure proposed would be able to handle this situation. The first cycle slip would be picked up and the filter bank would be switched to the filter which models a cycle slip on Satellite 1. When the simultaneous cycle slips on Satellites 2 and 3 occur, either one of the two cycle slips will be picked up first and the second cycle slips will also be picked up before the cycle slip on Satellite 4 if the MMAE algorithm is programmed to do so. Once the detection and recovery from the first three cycle slips is complete, the cycle slip on Satellite 4 will be picked up and the recovery of Satellite 1 from the induced cycle slip in the filter will give the minimum one satellite needed to run this tightly coupled system. As the other satellites return to fully functional states, the MMAE algorithm will also return to running with the fully functional filter. Due to the lack of simulation of this MMAE structure, this conclusion should be considered a conjecture. Section 5.3.6 recommends what steps should be taken in order to test fully this proposed FDIR algorithm.

4.7.2 FDIR Results from the DDPNRS Filter. The differencing scheme used in the DDPNRS filter again has a profound affect on the detectability and isolation of cycle slips. Like in the discussion concerning the DDPNRS filter's response to cycle slips, a cycle slip on Satellite 4 causes the greatest troubles in the detection and isolation of a cycle slip. When the single cycle slip is induced on Satellites 1, 2, or 3, which are depicted in Appendix L, Section L.2, Figures L.6 through L.8, one can easily see that the results follow the same pattern exhibited by the ROPNRS filter for the same scenarios. The induction of the same cycle slip on Satellite 4, which can be found in Figure L.9, shows that a stand alone Chi-Square test could not detect the failure of just the fourth satellite unless programmed with the knowledge that a cycle slip on satellite 4, the base satellite, causes this type of response. A Chi-Square tester would need to complete further testing in order to determine if this pattern was a cycle slip only on satellite 4 or a loss of all four satellites. The MMAE algorithm proposed would be able to discern between the cycle slip on Satellite 4 and the observable correlations on Satellites 1, 2, and 3. This is because the filter which models a cycle slip on Satellite 4 would be modelling Satellites 1, 2, and 3 only, and the observable correlations would not be present in this filter, and the probability evaluation algorithm would give this filter the highest probability.

Analyzing the multiple cycle slip case for the same parameters listed in Table 4.7 provided some interesting results. The plots of the Chi-Square test for this case can be found in Figure L.10. Again, with just a stand-alone Chi-Square test detecting the cycle slips and differentiating them from the observability of the cycle slips of the other satellites would require a recovery algorithm to properly compensate for the cycle slip to eliminate this observability. The MMAE algorithm would perform the same way as described in Section 4.7.1, where the only difficulty in accurate detection and recovery would come when the simultaneous cycle slips on Satellites 2 and 3 occur. Another possible problem with the Chi-Square test could occur when the cycle slip on Satellite 4 causes the Chi-Square random variables of the other three satellites either to increase again, as exhibited with Satellite 1, or to increase in value, as exhibited with Satellites 2 and 3, which could

possibly cause false or missed alarms in the Chi-Square test unless properly compensated for in the FDIR algorithm. As for the MMAE algorithm, this problem would not exist because the cycle slip on Satellite 4 would cause the filter bank to switch to the filter which does not model Satellite 4, and the observability of the cycle slip in the other residuals due to the correlation in the satellite measurements would not exist.

4.8 Summary

The necessity for the perfect and thus highly unrealistic Doppler velocity aiding measurements claimed in earlier research is no longer required to maintain filter stability. Improvements to the MSOFE code itself and to the computer systems which run MSOFE allow the filter to be run without any velocity aiding. The removal of the velocity aiding removes the doubts plaguing past research which implemented the velocity aiding. Removal of the velocity does not come without its drawbacks though. The magnitude of the vertical velocity error is increased by an order of magnitude. The surprising point in the removal of the velocity aiding measurements is that some of the parameters of interest actually became more accurate, which suggests possible over-modelling involved with these measurements. This possible over-modeling can be described as an over-compensation for the errors which are modelled in the filter. This would cause greater than normal values of the errors to be added to the measurements which the filter cannot accurately estimate.

The implementation of a double differencing method proved to be more accurate than the single difference method employed by Hansen and this author, but not significantly. This lack of significant improvement can be attributed to additional uncertainty in the phase ambiguity states or incorrect simulation of CPGPS measurements in the MSOFE code.

The use of Satellite 4 as the base satellite for the double differencing causes significant problems when large cycle slips occur on Satellite 4. The correlation between the satellite measurements

is clearly evident and extends the recovery times of the filter by an order of magnitude in some parameters. Another problem with this phenomenon is that a simple FDIR algorithm, such as a Chi-Square test, could not isolate cycle slips unless programmed to do so properly. The use of a MMAE algorithm is proposed and described as a way to combat this problem.

V. *Conclusions and Recommendations*

5.1 Overview

This chapter presents the conclusions arrived during this thesis research on the different Precision Navigation Reference System (PNRS) filters analyzed and the proposed Failure Detection, Isolation, and Recovery (FDIR) schemes. Also presented are recommendations of future research topics which stem from this research in the area of the enhancement of the PNRS filters and FDIR applications for cycle slips.

5.2 Conclusions

5.2.1 The Removal of the Perfect Doppler Velocity Aiding Measurements. The past skepticism over previous results (9,20,23,31) due to the perfect Doppler velocity aiding measurements has been eliminated. While no longer taking the velocity measurements, the PNRS filter remained stable. This was shown for Hansen's 71-state PNRS filter (9), the Reduced Order PNRS (ROPNRS) filter, and the Double Difference PNRS (DDPNRS) filter. The vertical velocity was the parameter most severely affected by the removal of the velocity measurements, as expected. Although the accuracy decreased, the filter still maintained stability over the entire simulation run of two hours. In Hansen's filter, the decrease in the accuracy of the vertical velocity error was not too severe, resulting only in an increase in the temporal average of the true 1σ error of 0.4 feet/second. The minor decrease in accuracy of this filter can be attributed to the high order of the filter model which incorporates more states of the INS error model. The ROPNRS filter exhibited an order of magnitude increase in the temporal average of the true 1σ error from 0.10 feet/second to 2.23 feet/second. This significant increase can be attributed to the filter order reduction. A surprising result comes from the increase in the accuracy of some of the parameters, which suggests possible over-modelling in the system where an over-compensation for the modeled errors is conducted. The

removal of the perfect velocity aiding measurements provided usefulness to the results presented in this thesis.

5.2.2 The PNRS Filter Order Reduction. The reduction of the PNRS filter order from 71 states to 19 states reduced the simulation time from over 60 hours for 15 Monte Carlo runs to approximately 8 hours, as expected. The retuning of the filter required by the order reduction produced a more accurate filter than the reduced order filter of Mosle's research (20), also as expected. When the velocity aiding measurements were removed, the filter remained stable with only the vertical velocity error showing a great decrease in accuracy. Once retuned, the filter's performance still showed improvement over Mosle's results except for the vertical velocity error which is most affected by the removal of the perfect velocity aiding. The behavior of the filter against the cycle slip simulations from (9) in all four satellites basically mimicked Hansen's results which justified the use of the ROPNRS filter throughout the rest of this research.

5.2.3 The Implementation of Double Differencing. The double differencing implementation did reduce the temporal averages of the filter's true one sigma errors in the system, but not as significantly as was expected. The lack of significant improvement motivates the need to investigate why a significant improvement was not observed. This lack of improvement suggests two things: either there is something wrong with the models, such as not modeling correlations in the measurements, or a fundamental lower bound on the simulation as it is currently set up has been reached.

The correlation in the satellite measurements cannot be neglected as is shown when cycle slips are induced into the system. The injection of a cycle slip onto the base satellite reeks havoc throughout the system because no compensation for the obvious correlation with this type of double differencing scheme has been completed. The filter's robustness to recover from a large cycle slip is severely degraded. Also, the use of a simple FDIR algorithm would run into some difficulty detecting a cycle slip on satellite 4 because of this correlation unless programmed to compensate

for this correlation. As for cycle slips on the other three satellites, the results exhibited are very similar to the ROPNRS filter's response.

5.2.4 The FDIR Algorithm Against Large Cycle Slips. The use of a Chi-Square test for cycle slip detection and isolation could work with the ROPNRS filter against large cycle slips. False and missed alarms would plague this setup if used as a stand-alone system without proper compensation for the observability of cycle slips in the other satellite states and residuals. This could be accomplished through a recovery algorithm which would eliminate the observability of the cycle slip in the other satellite components. In the DDPNRS filter, the same setup for the ROPNRS filter would have to be setup with an additional component to deal with a large cycle slips on satellite 4. This additional component would be another test to check for a cycle slip on satellite 4 only, or cycle slips on all of the satellites.

The use of a MMAE algorithm with a hierarchical structure to detect multiple cycle slips is the most practical and robust scheme available to detect, isolate, and recover accurately from cycle slips and also to recover back to a fully operational GPS setup of four satellites. This method provides the greatest promise in accurate FDIR performance and should be investigated further. A shortcoming of MMAE is in the number of extended Kalman filters which need to be modelled, which could cause a problem if limited computer time and storage space are available.

5.3 Recommendations

The following recommendations are just a few of the many possible avenues this research can continue down. The recommendations presented represent the most important ones to improve the results of this thesis work.

5.3.1 Incorporation of a Realistic Doppler Velocity Model. As was exhibited in this research, the perfect Doppler velocity aiding measurements are no longer needed to maintain filter

stability. This goal was not reached without a price. The accuracy of the vertical velocity error suffered the greatest degradation in accuracy. The incorporation of actual Doppler measurements and of a realistic Doppler velocity model should bring the 1σ vertical velocity errors back to 0.10 foot/second and could possibly improve the other parameters in the system.

5.3.2 Implementation of the True Double Differencing of (8). The current double differencing model consists of the single difference between-receivers, the Differential Global Positioning System corrections being assumed completed before entering the simulation. The encoding of this single difference in MSOFE, like the current double difference between receivers/satellites, could possibly enhance the accuracy of the PNRS filters and make it easier to track all values involved in the calculations. The current setup only allows for tracking of the values in the double difference portion of the code because of the assumption that the differential corrections are applied prior to entering the simulation.

5.3.3 Investigation or Elimination of the Correlation Involved with Double Differencing. To investigate the severity of this problem, recoding of MSOFE to accept off diagonal terms in the measurement noise covariance matrix, $\mathbf{R}(t_i)$, is needed. To eliminate this problem, implementing a GPS solution of six satellites to create the three difference pairs needed, would eliminate the correlation in the satellite measurement noises. If the elimination of this problem is chosen, a scheme to determine which satellite in a differenced pair is experiencing a cycle slip may be needed to isolate the slipped satellite once a cycle slip is detected. The problems experienced in this research motivate the need for this recommendation to be implemented.

5.3.4 Test PNRS Filters Against Real Data. Incorporation of real data from the NRS of CIGTF to further test and verify the models of the PNRS filters currently being implemented. Also, the usage of real data may bring out problems in the current models which cannot be determined in a simulation environment, such as over-modeling or incorrect modelling of certain errors.

5.3.5 Investigation of CPGPS Measurements in MSOFE. An investigation into how the CPGPS measurements are simulated in MSOFE may reveal inadequacies which are the cause of the lack of any observed significant improvement in the PNRS filters. Use or analysis of real CPGPS data may also aid in this investigation.

5.3.6 Continued Development of Proposed MMAE Algorithm. The proposed MMAE algorithm seems to be the most promising and robust FDIR scheme for cycle slips. Full implementation of this algorithm should be completed to verify all conjectures made in Section 5.2.4 and Chapter IV, Sections 4.7.1 and 4.7.2. Implementation of Captain Robert Nielsen's Multiple Model Simulation for Optimal Filter Evaluation (MMSOFE) (24) for the PNRS filter may be a useful tool in this development.

Appendix A. Error State Models Definitions

This appendix contains tabular listings of the 93-state LN-93 INS, 26-state RRS, 30-state GPS, and the four-state CPGPS error models. These listings are followed by listings of the 91-state PNRS truth and 19-state PNRS filter models. Also presented are the 89-state DDPNRS truth model along with the 17-state and 69-state filter models.

Tables A.1 through A.6 presents the 93-states of the LN-93 Errors State Model from (5). The listing of the 26-state RRS Error State Model is presented in Table A.7. Listings of the DGPS and CPGPS error states can be found in Tables A.9 and A.10.

The listings of the different truth and filter models are found in Tables A.11 through A.20. The 91-state PNRS truth model is listed in Tables A.11 through A.14 and the 19-state filter model is in Table A.15. The Double Difference PNRS truth model and 69-state filter model is listed in Tables A.16 through A.19. The 17-state Double Difference PNRS filter models is listed in Table A.20.

Table A.1 93-state LN-93 INS Model, Category I: General Errors

State Number	State Symbol	Definition
1	$\delta\Theta_X$	X component of vector angle from true to computer frame
2	$\delta\Theta_Y$	Y component of vector angle from true to computer frame
3	$\delta\Theta_Z$	Z component of vector angle from true to computer frame
4	ϕ_X	X component of vector angle from true to platform frame
5	ϕ_Y	Y component of vector angle from true to platform frame
6	ϕ_Z	Z component of vector angle from true to platform frame
7	δV_X	X component of error in computer velocity
8	δV_Y	Y component of error in computer velocity
9	δV_Z	Z component of error in computer velocity
10	δh	Error in vehicle altitude above reference ellipsoid
11	δh_L	Error in lagged inertial altitude
12	δS_3	Error in vertical channel aiding state
13	δS_4	Error in vertical channel aiding state

Table A.2 93-state LN-93 INS Model, Category II: First Order Markov Process Error States

State Number	State Symbol	Definition
14	b_{Xc}	X component of gyro correlated drift rate
15	b_{Yc}	Y component of gyro correlated drift rate
16	b_{Zc}	Z component of gyro correlated drift rate
17	∇_{Xc}	X component of accelerometer & velocity quantizer correlated noise
18	∇_{Yc}	Y component of accelerometer & velocity quantizer correlated noise
19	∇_{Zc}	Z component of accelerometer & velocity quantizer correlated noise
20	δg_X	X component of gravity vector errors
21	δg_Y	Y component of gravity vector errors
22	δg_Z	Z component of gravity vector errors
23	δh_B	Total baro-altimeter correlated error
24	b_{Xt}	X component of gyro trend
25	b_{Yt}	Y component of gyro trend
26	b_{Zt}	Z component of gyro trend
27	∇_{Xc}	X component of accelerometer trend
28	∇_{Yc}	Y component of accelerometer trend
29	∇_{Zc}	Z component of accelerometer trend
30	b_X	X component of gyro drift rate repeatability
31	b_Y	Y component of gyro drift rate repeatability
32	b_Z	Z component of gyro drift rate repeatability
33	S_{gx}	X component of gyro scale factor error
34	S_{gy}	Y component of gyro scale factor error
35	S_{gz}	Z component of gyro scale factor error
36	χ_1	X gyro misalignment about Y axis
37	χ_2	Y gyro misalignment about X axis
38	χ_3	Z gyro misalignment about X axis
39	ν_1	X gyro misalignment about Z axis
40	ν_2	Y gyro misalignment about Z axis
41	ν_3	Z gyro misalignment about Y axis

Table A.3 93-state LN-93 INS Model, Category III: Gyro Bias Error States

State Number	State Symbol	Definition
42	D_{XXX}	X gyro scale factor non-linearity
43	D_{YYY}	Y gyro scale factor non-linearity
44	D_{ZZZ}	Z gyro scale factor non-linearity
45	S_{Qbx}	X gyro scale factor asymmetry error
46	S_{Qby}	Y gyro scale factor asymmetry error
47	S_{Qbz}	Z gyro scale factor asymmetry error

Table A.4 93-state LN-93 INS Model, Category IV: Accelerometer Bias Error States

State Number	State Symbol	Definition
48	∇_{bx}	X component of accelerometer bias repeatability
49	∇_{by}	Y component of accelerometer bias repeatability
50	∇_{bz}	Z component of accelerometer bias repeatability
51	S_{Ax}	X component of accelerometer & velocity quantizer scale factor error
52	S_{Ay}	Y component of accelerometer & velocity quantizer scale factor error
53	S_{Az}	Z component of accelerometer & velocity quantizer scale factor error
54	S_{QAx}	X component of accelerometer & velocity quantizer scale factor asymmetry
55	S_{QAy}	Y component of accelerometer & velocity quantizer scale factor asymmetry
56	S_{QAz}	Z component of accelerometer & velocity quantizer scale factor asymmetry
57	f_{XX}	Coefficient of error proportional to square of measured acceleration
58	f_{YY}	Coefficient of error proportional to square of measured acceleration
59	f_{ZZ}	Coefficient of error proportional to square of measured acceleration
60	f_{XY}	Coefficient of error proportional to products of acceleration along & orthogonal to accelerometer sensitive axis
61	f_{XZ}	Coefficient of error proportional to products of acceleration along & orthogonal to accelerometer sensitive axis
62	f_{YX}	Coefficient of error proportional to products of acceleration along & orthogonal to accelerometer sensitive axis
63	f_{YZ}	Coefficient of error proportional to products of acceleration along & orthogonal to accelerometer sensitive axis
64	f_{ZX}	Coefficient of error proportional to products of acceleration along & orthogonal to accelerometer sensitive axis
65	f_{ZY}	Coefficient of error proportional to products of acceleration along & orthogonal to accelerometer sensitive axis
66	μ_1	X accelerometer misalignment about Z axis
67	μ_2	Y accelerometer misalignment about Z axis
68	μ_3	Z accelerometer misalignment about Y axis
69	σ_3	Z accelerometer misalignment about X axis

Table A.5 93-state LN-93 INS Model, Category V: Thermal Transient Error States

State Number	State Symbol	Definition
70	∇_{Xq}	X component of accelerometer bias thermal transient
71	∇_{Yq}	Y component of accelerometer bias thermal transient
72	∇_{Zq}	Z component fo accelerometer bias thermal transient
73	b_{Xq}	X component of initial gyro drift rate bias thermal transient
74	b_{Yq}	Y component of initial gyro drift rate bias thermal transient
75	b_{Zq}	Z component of initial gyro drift rate bias thermal transient

Table A.6 93-state LN-93 INS Model, Category VI: Gyro Compliance Error States

State Number	State Symbol	Definition
76	F_{XYZ}	X gyro compliance term
77	F_{XYY}	X gyro compliance term
78	F_{XYX}	X gyro compliance term
79	F_{XZY}	X gyro compliance term
80	F_{XZZ}	X gyro compliance term
81	F_{XZX}	X gyro compliance term
82	F_{YZX}	Y gyro compliance term
83	F_{YZZ}	Y gyro compliance term
84	F_{YZY}	Y gyro compliance term
85	F_{YXZ}	Y gyro compliance term
86	F_{YXX}	Y gyro compliance term
87	F_{YXY}	Y gyro compliance term
88	F_{ZXY}	Z gyro compliance term
89	F_{ZXX}	Z gyro compliance term
90	F_{ZXZ}	Z gyro compliance term
92	F_{ZYX}	Z gyro compliance term
93	F_{ZYY}	Z gyro compliance term
93	F_{ZYZ}	Z gyro compliance term

Table A.7 26-state RRS Error Model

State Number	State Symbol	Definition
1	δR_b	Range Error due to equipment bias
2	δv_b	Velocity Error due to equipment bias
3	δP_{T1x}	Transponder 1 X component of position error
4	δP_{T1y}	Transponder 1 Y component of position error
5	δP_{T1z}	Transponder 1 Z component of position error
6	δR_{T1a}	Transponder 1 range error due to atmospheric propagation
7	δP_{T2x}	Transponder 2 X component of position error
8	δP_{T2y}	Transponder 2 Y component of position error
9	δP_{T2z}	Transponder 2 Z component of position error
10	δR_{T2a}	Transponder 2 range error due to atmospheric propagation
11	δP_{T3x}	Transponder 3 X component of position error
12	δP_{T3y}	Transponder 3 Y component of position error
13	δP_{T3z}	Transponder 3 Z component of position error
14	δR_{T3a}	Transponder 3 range error due to atmospheric propagation
15	δP_{T4x}	Transponder 4 X component of position error
16	δP_{T4y}	Transponder 4 Y component of position error
17	δP_{T4z}	Transponder 4 Z component of position error
18	δR_{T4a}	Transponder 4 range error due to atmospheric propagation
19	δP_{T5x}	Transponder 5 X component of position error
20	δP_{T5y}	Transponder 5 Y component of position error
21	δP_{T5z}	Transponder 5 Z component of position error
22	δR_{T5a}	Transponder 5 range error due to atmospheric propagation
23	δP_{T6x}	Transponder 6 X component of position error
24	δP_{T6y}	Transponder 6 Y component of position error
25	δP_{T6z}	Transponder 6 Z component of position error
26	δR_{T6a}	Transponder 6 range error due to atmospheric propagation

Table A.8 30-state GPS Error Model

State Number	State Symbol	Definition
1	δR_{uclk}	User clock bias
2	δD_{uclk}	User clock drift
3	δR_{cloop1}	SV 2 code loop error
4	δR_{trop1}	SV 1 tropospheric error
5	δR_{ion1}	SV 1 ionospheric
6	δR_{clk1}	SV clock error
7	δX_1	SV X 1 component of position error
8	δY_1	SV Y 1 component of position error
9	δZ_1	SV Z 1 component of position error
10	δR_{cloop2}	SV 2 code loop error
11	δR_{trop2}	SV 2 tropospheric error
12	δR_{ion2}	SV 2 ionospheric
13	δR_{clk2}	SV 2 clock error
14	δX_2	SV X 2 component of position error
15	δY_2	SV Y 2 component of position error
16	δZ_2	SV Z 2 component of position error
17	δR_{cloop3}	SV 3 code loop error
18	δR_{trop3}	SV 3 tropospheric error
19	δR_{ion3}	SV 3 ionospheric
20	δR_{clk3}	SV 3 clock error
21	δX_3	SV X 3 component of position error
22	δY_3	SV Y 3 component of position error
23	δZ_3	SV Z 3 component of position error
24	δR_{cloop4}	SV 4 code loop error
25	δR_{trop4}	SV 4 tropospheric error
26	δR_{ion4}	SV 4 ionospheric
27	δR_{clk4}	SV 4 clock error
28	δX_4	SV X 4 component of position error
29	δY_4	SV Y 4 component of position error
30	δZ_4	SV Z 4 component of position error

Table A.9 22-state DGPS Error Model

State Number	State Symbol	Definition
1	δR_{uclk}	User clock bias
2	δD_{uclk}	User clock drift
3	δR_{trop1}	SV 1 tropospheric error
4	δR_{ion1}	SV 1 ionospheric
5	δX_1	SV X 1 component of position error
6	δY_1	SV Y 1 component of position error
7	δZ_1	SV Z 1 component of position error
8	δR_{trop2}	SV 2 tropospheric error
9	δR_{ion2}	SV 2 ionospheric
10	δX_2	SV X 2 component of position error
11	δY_2	SV Y 2 component of position error
12	δZ_2	SV Z 2 component of position error
13	δR_{trop3}	SV 3 tropospheric error
14	δR_{ion3}	SV 3 ionospheric
15	δX_3	SV X 3 component of position error
16	δY_3	SV Y 3 component of position error
17	δZ_3	SV Z 3 component of position error
18	δR_{trop4}	SV 4 tropospheric error
19	δR_{ion4}	SV 4 ionospheric
20	δX_4	SV X 4 component of position error
21	δY_4	SV Y 4 component of position error
22	δZ_4	SV Z 4 component of position error

Table A.10 4-state CPGPS Error Model

State Number	State Symbol	Definition
1	δR_{N1}	SV 1 range equivalent cycle ambiguity term
2	δR_{N2}	SV 2 range equivalent cycle ambiguity term
3	δR_{N3}	SV 3 range equivalent cycle ambiguity term
4	δR_{N4}	SV 4 range equivalent cycle ambiguity term

Table A.11 91-state PNRS Truth Model: States 1-24

State Number	State Symbol	Definition	Related State
1	$\delta\Theta_X$	X component of vector angle from true to computer frame	INS 1
2	$\delta\Theta_Y$	Y component of vector angle from true to computer frame	INS 2
3	$\delta\Theta_Z$	Z component of vector angle from true to computer frame	INS 3
4	ϕ_X	X component of vector angle from true to platform frame	INS 4
5	ϕ_Y	Y component of vector angle from true to platform frame	INS 5
6	ϕ_Z	Z component of vector angle from true to platform frame	INS 6
7	δV_X	X component of error in computer velocity	INS 7
8	δV_Y	Y component of error in computer velocity	INS 8
9	δV_Z	Z component of error in computer velocity	INS 9
10	δh	Error in vehicle altitude above reference ellipsoid	INS 10
11	δh_B	Total baro-altimeter correlated error	INS 23
12	δR_b	Range Error due to equipment bias	RRS 1
13	δv_b	Velocity Error due to equipment bias	RRS 2
14	δR_{uclk}	User clock bias	GPS 1
15	δD_{uclk}	User clock drift	GPS 2
16	δh_L	Error in lagged inertial altitude	INS 11
17	δS_3	Error in vertical channel aiding state	INS 12
18	δS_4	Error in vertical channel aiding state	INS 13
19	∇_{Xc}	X component of accelerometer & velocity quantizer correlated noise	INS 17
20	∇_{Yc}	Y component of accelerometer & velocity quantizer correlated noise	INS 18
21	∇_{Zc}	Z component of accelerometer & velocity quantizer correlated noise	INS 19
22	δg_X	X component of gravity vector errors	INS 20
23	δg_Y	Y component of gravity vector errors	INS 21
24	δg_Z	Z component of gravity vector errors	INS 22

Table A.12 91-state PNRS Truth Model: States 25-43

State Number	State Symbol	Definition	Related State
25	b_X	X component of gyro drift rate repeatability	INS 30
26	b_Y	Y component of gyro drift rate repeatability	INS 31
27	b_Z	Z component of gyro drift rate repeatability	INS 32
28	S_{gx}	X component of gyro scale factor error	INS 33
29	S_{gy}	Y component of gyro scale factor error	INS 34
30	S_{gz}	Z component of gyro scale factor error	INS 35
31	∇_{bx}	X component of accelerometer bias repeatability	INS 48
32	∇_{by}	Y component of accelerometer bias repeatability	INS 49
33	∇_{bz}	Z component of accelerometer bias repeatability	INS 50
34	S_{Ax}	X component of accelerometer & velocity quantizer scale factor error	INS 51
35	S_{Ay}	Y component of accelerometer & velocity quantizer scale factor error	INS 52
36	S_{Az}	Z component of accelerometer & velocity quantizer scale factor error	INS 53
37	S_{QAx}	X component of accelerometer & velocity quantizer scale factor asymmetry	INS 54
38	S_{QAy}	Y component of accelerometer & velocity quantizer scale factor asymmetry	INS 55
39	S_{QAz}	Z component of accelerometer & velocity quantizer scale factor asymmetry	INS 56
40	μ_1	X accelerometer misalignment about Z axis	INS 66
41	μ_2	Y accelerometer misalignment about Z axis	INS 67
42	μ_3	Z accelerometer misalignment about Y axis	INS 68
43	σ_3	Z accelerometer misalignment about X axis	INS 69

Table A.13 91-state PNRS Truth Model: States 44-67

State Number	State Symbol	Definition	Related State
44	δP_{T1x}	Transponder 1 X component of position error	RRS 3
45	δP_{T1y}	Transponder 1 Y component of position error	RRS 4
46	δP_{T1z}	Transponder 1 Z component of position error	RRS 5
47	δR_{T1a}	Transponder 1 range error due to atmospheric propagation	RRS 6
48	δP_{T2x}	Transponder 2 X component of position error	RRS 7
49	δP_{T2y}	Transponder 2 Y component of position error	RRS 8
50	δP_{T2z}	Transponder 2 Z component of position error	RRS 9
51	δR_{T2a}	Transponder 2 range error due to atmospheric propagation	RRS 10
52	δP_{T3x}	Transponder 3 X component of position error	RRS 11
53	δP_{T3y}	Transponder 3 Y component of position error	RRS 12
54	δP_{T3z}	Transponder 3 Z component of position error	RRS 13
55	δR_{T3a}	Transponder 3 range error due to atmospheric propagation	RRS 14
56	δP_{T4x}	Transponder 4 X component of position error	RRS 15
57	δP_{T4y}	Transponder 4 Y component of position error	RRS 16
58	δP_{T4z}	Transponder 4 Z component of position error	RRS 17
59	δR_{T4a}	Transponder 4 range error due to atmospheric propagation	RRS 18
60	δP_{T5x}	Transponder 5 X component of position error	RRS 19
61	δP_{T5y}	Transponder 5 Y component of position error	RRS 20
62	δP_{T5z}	Transponder 5 Z component of position error	RRS 21
63	δR_{T5a}	Transponder 5 range error due to atmospheric propagation	RRS 22
64	δP_{T6x}	Transponder 6 X component of position error	RRS 23
65	δP_{T6y}	Transponder 6 Y component of position error	RRS 24
66	δP_{T6z}	Transponder 6 Z component of position error	RRS 25
67	δR_{T6a}	Transponder 6 range error due to atmospheric propagation	RRS 26

Table A.14 91-state PNRS Truth Model: States 68-91

State Number	State Symbol	Definition	Related State
68	δR_{N1}	SV 1 range equivalent cycle ambiguity term	CPGPS 1
69	δR_{N2}	SV 2 range equivalent cycle ambiguity term	CPGPS 2
70	δR_{N3}	SV 3 range equivalent cycle ambiguity term	CPGPS 3
71	δR_{N4}	SV 4 range equivalent cycle ambiguity term	CPGPS 4
72	δR_{trop1}	SV 1 tropospheric error	DGPS 3
73	δR_{ion1}	SV 1 ionospheric	DGPS 4
74	δX_1	SV X 1 component of position error	DGPS 5
75	δY_1	SV Y 1 component of position error	DGPS 6
76	δZ_1	SV Z 1 component of position error	DGPS 7
77	δR_{trop2}	SV 2 tropospheric error	DGPS 8
78	δR_{ion2}	SV 2 ionospheric	DGPS 9
79	δX_2	SV X 2 component of position error	DGPS 10
80	δY_2	SV Y 2 component of position error	DGPS 11
81	δZ_2	SV Z 2 component of position error	DGPS 12
82	δR_{trop3}	SV 3 tropospheric error	DGPS 13
83	δR_{ion3}	SV 3 ionospheric	DGPS 14
84	δX_3	SV X 3 component of position error	DGPS 15
85	δY_3	SV Y 3 component of position error	DGPS 16
86	δZ_3	SV Z 3 component of position error	DGPS 17
87	δR_{trop4}	SV 4 tropospheric error	DGPS 18
88	δR_{ion4}	SV 4 ionospheric	DGPS 19
89	δX_4	SV X 4 component of position error	DGPS 20
90	δY_4	SV Y 4 component of position error	DGPS 21
91	δZ_4	SV Z 4 component of position error	DGPS 22

Table A.15 19-state PNRS Filter Model

State Number	State Symbol	Definition	Related State
1	$\delta\Theta_X$	X component of vector angle from true to computer frame	INS 1
2	$\delta\Theta_Y$	Y component of vector angle from true to computer frame	INS 2
3	$\delta\Theta_Z$	Z component of vector angle from true to computer frame	INS 3
4	ϕ_X	X component of vector angle from true to platform frame	INS 4
5	ϕ_Y	Y component of vector angle from true to platform frame	INS 5
6	ϕ_Z	Z component of vector angle from true to platform frame	INS 6
7	δV_X	X component of error in computer velocity	INS 7
8	δV_Y	Y component of error in computer velocity	INS 8
9	δV_Z	Z component of error in computer velocity	INS 9
10	δh	Error in vehicle altitude above reference ellipsoid	INS 10
11	δh_B	Total baro-altimeter correlated error	INS 23
12	δR_b	Range Error due to equipment bias	RRS 1
13	δv_b	Velocity Error due to equipment bias	RRS 2
14	δR_{uclk}	User clock bias	GPS 1
15	δD_{uclk}	User clock drift	GPS 2
16	δR_{N1}	SV 1 range equivalent cycle ambiguity term	CPGPS 1
17	δR_{N2}	SV 2 range equivalent cycle ambiguity term	CPGPS 2
18	δR_{N3}	SV 3 range equivalent cycle ambiguity term	CPGPS 3
19	δR_{N4}	SV 4 range equivalent cycle ambiguity term	CPGPS 4

Table A.16 89-State DDPNRS Double Difference Truth Model States 1-22 and Filter Model States 1-22

State Number	State Symbol	Definition	Related State
1	$\delta\Theta_X$	X component of vector angle from true to computer frame	INS 1
2	$\delta\Theta_Y$	Y component of vector angle from true to computer frame	INS 2
3	$\delta\Theta_Z$	Z component of vector angle from true to computer frame	INS 3
4	ϕ_X	X component of vector angle from true to platform frame	INS 4
5	ϕ_Y	Y component of vector angle from true to platform frame	INS 5
6	ϕ_Z	Z component of vector angle from true to platform frame	INS 6
7	δV_X	X component of error in computer velocity	INS 7
8	δV_Y	Y component of error in computer velocity	INS 8
9	δV_Z	Z component of error in computer velocity	INS 9
10	δh	Error in vehicle altitude above reference ellipsoid	INS 10
11	δh_B	Total baro-altimeter correlated error	INS 23
12	δR_b	Range Error due to equipment bias	RRS 1
13	δv_b	Velocity Error due to equipment bias	RRS 2
14	δh_L	Error in lagged inertial altitude	INS 11
15	δS_3	Error in vertical channel aiding state	INS 12
16	δS_4	Error in vertical channel aiding state	INS 13
17	∇_{Xc}	X component of accelerometer & velocity quantizer correlated noise	INS 17
18	∇_{Yc}	Y component of accelerometer & velocity quantizer correlated noise	INS 18
19	∇_{Zc}	Z component of accelerometer & velocity quantizer correlated noise	INS 19
20	δg_X	X component of gravity vector errors	INS 20
21	δg_Y	Y component of gravity vector errors	INS 21
22	δg_Z	Z component of gravity vector errors	INS 22

Table A.17 89-State DDPNRS Double Difference Truth Model States 23-41 and Filter Model States 23-41

State Number	State Symbol	Definition	Related State
23	b_X	X component of gyro drift rate repeatability	INS 30
24	b_Y	Y component of gyro drift rate repeatability	INS 31
25	b_Z	Z component of gyro drift rate repeatability	INS 32
26	S_{gx}	X component of gyro scale factor error	INS 33
27	S_{gy}	Y component of gyro scale factor error	INS 34
28	S_{gz}	Z component of gyro scale factor error	INS 35
29	∇_{bx}	X component of accelerometer bias repeatability	INS 48
30	∇_{by}	Y component of accelerometer bias repeatability	INS 49
31	∇_{bz}	Z component of accelerometer bias repeatability	INS 50
32	S_{Ax}	X component of accelerometer & velocity quantizer scale factor error	INS 51
33	S_{Ay}	Y component of accelerometer & velocity quantizer scale factor error	INS 52
34	S_{Az}	Z component of accelerometer & velocity quantizer scale factor error	INS 53
35	S_{QAx}	X component of accelerometer & velocity quantizer scale factor asymmetry	INS 54
36	S_{QAy}	Y component of accelerometer & velocity quantizer scale factor asymmetry	INS 55
37	S_{QAz}	Z component of accelerometer & velocity quantizer scale factor asymmetry	INS 56
38	μ_1	X accelerometer misalignment about Z axis	INS 66
39	μ_2	Y accelerometer misalignment about Z axis	INS 67
40	μ_3	Z accelerometer misalignment about Y axis	INS 68
41	σ_3	Z accelerometer misalignment about X axis	INS 69

Table A.18 89-State DDPNRS Double Difference Truth Model States 42-65 and Filter Model States 42-65

State Number	State Symbol	Definition	Related State
42	δP_{T1x}	Transponder 1 X component of position error	RRS 3
43	δP_{T1y}	Transponder 1 Y component of position error	RRS 4
44	δP_{T1z}	Transponder 1 Z component of position error	RRS 5
45	δR_{T1a}	Transponder 1 range error due to atmospheric propagation	RRS 6
46	δP_{T2x}	Transponder 2 X component of position error	RRS 7
47	δP_{T2y}	Transponder 2 Y component of position error	RRS 8
48	δP_{T2z}	Transponder 2 Z component of position error	RRS 9
49	δR_{T2a}	Transponder 2 range error due to atmospheric propagation	RRS 10
50	δP_{T3x}	Transponder 3 X component of position error	RRS 11
51	δP_{T3y}	Transponder 3 Y component of position error	RRS 12
52	δP_{T3z}	Transponder 3 Z component of position error	RRS 13
53	δR_{T3a}	Transponder 3 range error due to atmospheric propagation	RRS 14
54	δP_{T4x}	Transponder 4 X component of position error	RRS 15
55	δP_{T4y}	Transponder 4 Y component of position error	RRS 16
56	δP_{T4z}	Transponder 4 Z component of position error	RRS 17
57	δR_{T4a}	Transponder 4 range error due to atmospheric propagation	RRS 18
58	δP_{T5x}	Transponder 5 X component of position error	RRS 19
59	δP_{T5y}	Transponder 5 Y component of position error	RRS 20
60	δP_{T5z}	Transponder 5 Z component of position error	RRS 21
61	δR_{T5a}	Transponder 5 range error due to atmospheric propagation	RRS 22
62	δP_{T6x}	Transponder 6 X component of position error	RRS 23
63	δP_{T6y}	Transponder 6 Y component of position error	RRS 24
64	δP_{T6z}	Transponder 6 Z component of position error	RRS 25
65	δR_{T6a}	Transponder 6 range error due to atmospheric propagation	RRS 26

Table A.19 89-State DDPNRS Double Difference Truth Model States 66-89 and Filter Model States 66-69

State Number	State Symbol	Definition	Related State
66	$\nabla\delta R_{N1-4}$	SV 1-SV 4 range equivalent cycle ambiguity term	CPGPS 1-4
67	$\nabla\delta R_{N2-4}$	SV 2-SV 4 range equivalent cycle ambiguity term	CPGPS 2-4
68	$\nabla\delta R_{N3-4}$	SV 3-SV 4 range equivalent cycle ambiguity term	CPGPS 3-4
69	$\nabla\delta R_{N4}$	SV 4 range equivalent cycle ambiguity term	CPGPS 4
70	$\nabla\delta R_{trop1-4}$	SV 1-SV 4 tropospheric error	DGPS 3-18
71	$\nabla\delta R_{ion1-4}$	SV 1-SV 4 ionospheric	DGPS 4-19
72	$\nabla\delta X_{1-4}$	SV X 1-SV 4 X component of position error	DGPS 5-20
73	$\nabla\delta Y_{1-4}$	SV Y 1-SV 4 Y component of position error	DGPS 6-21
74	$\nabla\delta Z_{1-4}$	SV Z 1-SV 4 Z component of position error	DGPS 7-22
75	$\nabla\delta R_{trop2-4}$	SV 2-SV 4 tropospheric error	DGPS 8-18
76	$\nabla\delta R_{ion2-4}$	SV 2-SV 4 ionospheric	DGPS 9-19
77	$\nabla\delta X_{2-4}$	SV X 2-SV 4 X component of position error	DGPS 10-20
78	$\nabla\delta Y_{2-4}$	SV Y 2-SV 4 Y component of position error	DGPS 11-21
79	$\nabla\delta Z_{2-4}$	SV Z 2-SV 4 Z component of position error	DGPS 12-22
80	$\nabla\delta R_{trop3-4}$	SV 3-SV 4 tropospheric error	DGPS 13-18
81	$\nabla\delta R_{ion3-4}$	SV 3-SV 4 ionospheric	DGPS 14-19
82	$\nabla\delta X_{3-4}$	SV X 3-SV 4 X component of position error	DGPS 15-20
83	$\nabla\delta Y_{3-4}$	SV Y 3-SV 4 Y component of position error	DGPS 16-21
84	$\nabla\delta Z_{3-4}$	SV Z 3-SV 4 Z component of position error	DGPS 17-22
85	$\nabla\delta R_{trop4}$	SV 4 tropospheric error	DGPS 18
86	$\nabla\delta R_{ion4}$	SV 4 ionospheric	DGPS 19
87	$\nabla\delta X_4$	SV X 4 component of position error	DGPS 20
88	$\nabla\delta Y_4$	SV Y 4 component of position error	DGPS 21
89	$\nabla\delta Z_4$	SV Z 4 component of position error	DGPS 22

Table A.20 17-State DDPNRS Filter Model

State Number	State Symbol	Definition	Related State
1	$\delta\Theta_X$	X component of vector angle from true to computer frame	INS 1
2	$\delta\Theta_Y$	Y component of vector angle from true to computer frame	INS 2
3	$\delta\Theta_Z$	Z component of vector angle from true to computer frame	INS 3
4	ϕ_X	X component of vector angle from true to platform frame	INS 4
5	ϕ_Y	Y component of vector angle from true to platform frame	INS 5
6	ϕ_Z	Z component of vector angle from true to platform frame	INS 6
7	δV_X	X component of error in computer velocity	INS 7
8	δV_Y	Y component of error in computer velocity	INS 8
9	δV_Z	Z component of error in computer velocity	INS 9
10	δh	Error in vehicle altitude above reference ellipsoid	INS 10
11	δh_B	Total baro-altimeter correlated error	INS 23
12	δR_b	Range Error due to equipment bias	RRS 1
13	δv_b	Velocity Error due to equipment bias	RRS 2
14	$\nabla\delta R_{N1-4}$	SV 1-SV 4 range equivalent cycle ambiguity term	CPGPS 1-4
15	$\nabla\delta R_{N2-4}$	SV 2-SV 4 range equivalent cycle ambiguity term	CPGPS 2-4
16	$\nabla\delta R_{N3-4}$	SV 3-SV 4 range equivalent cycle ambiguity term	CPGPS 3-4
17	$\nabla\delta R_{N4}$	SV 4 range equivalent cycle ambiguity term	CPGPS 4

Appendix B. Litton LN-93 INS Error State Model Dynamics and Noise Matrices

This appendix contains tabular listings of the elements of the LN-93 INS Error State Dynamics matrix (**F** matrix) and the Process Noise matrix (**Q** matrix) developed by Litton. Both matrices (**F** and **Q**) are 93 × 93 arrays which contain many zero elements, only the non-zero elements are presented in this appendix. The elements presented in Tables B.1 through B.10 are taken directly from (5).

Tables B.1 through B.8 list the sub-matrices of the **F** matrix. These sub-matrices are the separate components of the **F** matrix presented in Equation (3.4) in Chapter III.

Tables B.9 and B.10 list the sub-matrices of the **Q** matrix. These sub-matrices are the separate components of the **Q** matrix presented in Equation (3.4) in Chapter III.

Table B.1 Elements of Dynamics Submatrix $\mathbf{F}_{11}$

Element	Term	Element	Term
(1,3)	$-\rho_Y$	(1,8)	$-C_{RY}$
(2,3)	ρ_X	(2,7)	C_{RX}
(3,1)	ρ_Y	(3,2)	$-\rho_X$
(4,2)	$-\Omega_Z$	(4,3)	Ω_Y
(4,5)	ω_Z	(4,6)	$-\omega_Y$
(4,8)	$-C_{RY}$		
(5,1)	Ω_Z	(5,3)	$-\Omega_X$
(5,4)	$-\omega_Z$	(5,6)	ω_X
(5,7)	C_{RX}		
(6,1)	$-\Omega Y$	(6,2)	Ω_X
(6,4)	ωY	(6,5)	$-\omega_X$
(7,1)	$-2V_Y\Omega_Y - 2V_Z\Omega_Z$	(7,2)	$2V_Y\Omega_X$
(7,3)	$-2V_Z\Omega_X$	(7,5)	$-A_Z$
(7,6)	A_Y	(7,7)	$-V_Z C_{RX}$
(7,8)	$2\Omega_Z$	(7,9)	$-\rho_Y - 2\Omega_Y$
(8,1)	$2V_X\Omega_Y$	(8,2)	$-2V_Y\Omega_X - 2V_X\Omega_Z$
(8,3)	$2V_Z\Omega_Y$	(8,4)	A_Z
(8,6)	$-A_X$	(8,7)	$-2\Omega_Z$
(8,8)	$-V_Z C_{RY}$	(8,9)	$\rho_X + 2\Omega_X$
(9,1)	$2V_X\Omega_Z$	(9,2)	$2V_Y\Omega_Z$
(9,3)	$-2V_Y\Omega_Y - 2V_X\Omega_X$	(9,4)	$-A_Y$
(9,5)	A_X	(9,7)	$\rho_Y + 2\Omega_Y + V_X C_{RX}$
(9,8)	$-\rho_X - 2\Omega_X + V_Y C_{RY}$	(9,10)	$\frac{2g_o}{a}$
(9,11)	$-k_2$	(9,12)	-1.0
(9,13)	k_2		
(10,9)	1.0	(10,11)	k_1
(10,13)	$k_1 - 1.0$		
(11,10)	1.0	(11,11)	-1.0
(12,11)	k_3	(12,13)	$-k_3$
(13,10)	k_4	(13,11)	$-k_4$
(13,13)	$k_4 - 1$		

Table B.2 Elements of Dynamics Submatrix $\mathbf{F}_{12}$

Element	Term	Element	Term
(4,14)	$C_{11}t$	(4,15)	$C_{12}t$
(4,16)	$C_{13}t$	(4,24)	$C_{11}t$
(4,25)	$C_{12}t$	(4,26)	$C_{13}t$
(5,14)	$C_{21}t$	(5,15)	$C_{22}t$
(5,16)	$C_{23}t$	(5,24)	$C_{21}t$
(5,25)	$C_{22}t$	(5,26)	$C_{23}t$
(6,14)	$C_{31}t$	(6,15)	$C_{32}t$
(6,16)	$C_{33}t$	(6,24)	$C_{31}t$
(6,25)	$C_{32}t$	(6,26)	$C_{33}t$
(7,17)	$C_{11}t$	(7,18)	$C_{12}t$
(7,19)	$C_{13}t$	(7,20)	1.0
(7,27)	$C_{11}t$	(7,28)	$C_{12}t$
(7,29)	$C_{13}t$		
(8,17)	$C_{21}t$	(8,18)	$C_{22}t$
(8,19)	$C_{23}t$	(8,21)	1.0
(8,27)	$C_{21}t$	(8,28)	$C_{22}t$
(8,29)	$C_{23}t$		
(9,17)	$C_{31}t$	(9,18)	$C_{32}t$
(9,19)	$C_{33}t$	(9,22)	1.0
(9,23)	k_2	(9,27)	$C_{31}t$
(9,28)	$C_{32}t$	(9,29)	$C_{33}t$
(10,23)	k_1		
(12,23)	$-k_3$		

Table B.3 Elements of Dynamics Submatrix $\mathbf{F}_{13}$

Element	Term	Element	Term
(4,30)	C_{11}	(4,31)	C_{12}
(4,32)	C_{13}	(4,33)	$C_{11}\omega_X$
(4,34)	$C_{12}\omega_Y$	(4,35)	$C_{13}\omega_Z$
(4,36)	$C_{11}\omega_Z$	(4,37)	$C_{12}\omega_Z$
(4,38)	$C_{13}\omega_Y$	(4,39)	$C_{11}\omega_Y$
(4,40)	$C_{12}\omega_X$	(4,41)	$C_{13}\omega_X$
(4,42)	$C_{11}\omega_X^2$	(4,43)	$C_{12}\omega_Y^2$
(4,44)	$C_{13}\omega_Z^2$	(4,45)	$.5C_{11}\lvert\omega_X\rvert$
(4,46)	$.5C_{12}\lvert\omega_Y\rvert$	(4,47)	$.5C_{13}\lvert\omega_Z\rvert$
(5,30)	C_{21}	(5,31)	C_{22}
(5,32)	C_{23}	(5,33)	$C_{21}\omega_X$
(5,34)	$C_{22}\omega_Y$	(5,35)	$C_{23}\omega_Z$
(5,36)	$C_{21}\omega_Z$	(5,37)	$C_{22}\omega_Z$
(5,38)	$C_{23}\omega_Y$	(5,39)	$C_{21}\omega_Y$
(5,40)	$C_{22}\omega_X$	(5,41)	$C_{23}\omega_X$
(5,42)	$C_{21}\omega_X^2$	(5,43)	$C_{22}\omega_Y^2$
(5,44)	$C_{23}\omega_Z^2$	(5,45)	$.5C_{21}\lvert\omega_X\rvert$
(5,46)	$.5C_{22}\lvert\omega_Y\rvert$	(5,47)	$.5C_{23}\lvert\omega_Z\rvert$
(6,30)	C_{31}	(6,31)	C_{32}
(6,32)	C_{33}	(6,33)	$C_{31}\omega_X$
(6,34)	$C_{32}\omega_Y$	(6,35)	$C_{33}\omega_Z$
(6,36)	$C_{31}\omega_Z$	(6,37)	$C_{32}\omega_Z$
(6,38)	$C_{33}\omega_Y$	(6,39)	$C_{31}\omega_Y$
(6,40)	$C_{32}\omega_X$	(6,41)	$C_{33}\omega_X$
(6,42)	$C_{31}\omega_X^2$	(6,43)	$C_{32}\omega_Y^2$
(6,44)	$C_{33}\omega_Z^2$	(6,45)	$.5C_{31}\lvert\omega_X\rvert$
(6,46)	$.5C_{32}\lvert\omega_Y\rvert$	(6,47)	$.5C_{33}\lvert\omega_Z\rvert$

Table B.4 Elements of Dynamics Submatrix $\mathbf{F}_{14}$

Element	Term	Element	Term
(7,48)	C_{11}	(7,49)	C_{12}
(7,50)	C_{13}	(7,51)	$C_{11}A_X^B$
(7,52)	$C_{12}A_Y^B$	(7,53)	$C_{13}A_Z^{B'}$
(7,54)	$C_{11}\lvert A_X^B\rvert$	(7,55)	$C_{12}\lvert A_Y^B\rvert$
(7,56)	$C_{13}\lvert A_Z^{B'}\rvert$	(7,57)	$C_{11}A_X^{B^2}$
(7,58)	$C_{12}A_Y^{B^2}$	(7,59)	$C_{13}A_Z^{B^2}$
(7,60)	$C_{11}A_X^BA_Y^B$	(7,61)	$C_{11}A_X^BA_Z^B$
(7,62)	$C_{12}A_Y^BA_X^B$	(7,63)	$C_{12}A_Y^BA_Z^B$
(7,64)	$C_{13}A_X^BA_Z^B$	(7,65)	$C_{13}A_Y^BA_Z^B$
(7,66)	$C_{11}A_Y^B$	(7,67)	$C_{12}A_X^B$
(7,68)	$C_{13}A_Y^B$	(7,69)	$C_{13}A_X^B$
(8,48)	C_{21}	(8,49)	C_{22}
(8,50)	C_{23}	(8,51)	$C_{21}A_X^B$
(8,52)	$C_{22}A_Y^B$	(8,53)	$C_{23}A_Z^{B'}$
(8,54)	$C_{21}\lvert A_X^B\rvert$	(8,55)	$C_{22}\lvert A_Y^B\rvert$
(8,56)	$C_{23}\lvert A_Z^{B'}\rvert$	(8,57)	$C_{21}A_X^{B^2}$
(8,58)	$C_{22}A_Y^{B^2}$	(8,59)	$C_{23}A_Z^{B^2}$
(8,60)	$C_{21}A_X^BA_Y^B$	(8,61)	$C_{21}A_X^BA_Z^B$
(8,62)	$C_{22}A_Y^BA_X^B$	(8,63)	$C_{22}A_Y^BA_Z^B$
(8,64)	$C_{23}A_X^BA_Z^B$	(8,65)	$C_{23}A_Y^BA_Z^B$
(8,66)	$C_{21}A_Y^B$	(8,67)	$C_{22}A_X^B$
(8,68)	$C_{23}A_Y^B$	(8,69)	$C_{23}A_X^B$
(9,48)	C_{31}	(9,49)	C_{32}
(9,50)	C_{33}	(9,51)	$C_{31}A_X^B$
(9,52)	$C_{32}A_Y^B$	(9,53)	$C_{33}A_Z^{B'}$
(9,54)	$C_{31}\lvert A_X^B\rvert$	(9,55)	$C_{32}\lvert A_Y^B\rvert$
(9,56)	$C_{33}\lvert A_Z^{B'}\rvert$	(9,57)	$C_{31}A_X^{B^2}$
(9,58)	$C_{32}A_Y^{B^2}$	(9,59)	$C_{33}A_Z^{B^2}$
(9,60)	$C_{31}A_X^BA_Y^B$	(9,61)	$C_{31}A_X^BA_Z^B$
(9,62)	$C_{32}A_Y^BA_X^B$	(9,63)	$C_{32}A_Y^BA_Z^B$
(9,64)	$C_{33}A_X^BA_Z^B$	(9,65)	$C_{33}A_Y^BA_Z^B$
(9,66)	$C_{31}A_Y^B$	(9,67)	$C_{32}A_X^B$
(9,68)	$C_{33}A_Y^B$	(9,69)	$C_{33}A_X^B$

Table B.5 Elements of Dynamics Submatrix $\mathbf{F}_{15}$

Element	Term	Element	Term
(4,73)	C_{11}	(4,74)	C_{12}
(4,75)	C_{13}		
(5,73)	C_{21}	(5,74)	C_{22}
(5,75)	C_{23}		
(6,73)	C_{31}	(6,74)	C_{32}
(6,75)	C_{33}		
(7,70)	C_{11}	(7,71)	C_{12}
(7,72)	C_{13}		
(8,70)	C_{21}	(8,71)	C_{22}
(8,72)	C_{23}		
(9,70)	C_{31}	(9,71)	C_{32}
(9,72)	C_{33}		

Table B.6 Elements of Dynamics Submatrix $\mathbf{F}_{16}$

Element	Term	Element	Term
(4,76)	$C_{11}A_Y^B\omega_{ibZ}$	(4,77)	$C_{11}A_Y^B\omega_{ibY}$
(4,78)	$C_{11}A_Y^B\omega_{ibX}$	(4,79)	$C_{11}A_Z^B\omega_{ibY}$
(4,80)	$C_{11}A_Z^B\omega_{ibZ}$	(4,81)	$C_{11}A_Z^B\omega_{ibX}$
(4,82)	$C_{12}A_Z^B\omega_{ibX}$	(4,83)	$C_{12}A_Z^B\omega_{ibZ}$
(4,84)	$C_{12}A_Z^B\omega_{ibY}$	(4,85)	$C_{12}A_X^B\omega_{ibZ}$
(4,86)	$C_{12}A_Y^B\omega_{ibX}$	(4,87)	$C_{12}A_X^B\omega_{ibY}$
(4,88)	$C_{13}A_X^B\omega_{ibY}$	(4,89)	$C_{13}A_X^B\omega_{ibX}$
(4,90)	$C_{13}A_X^B\omega_{ibZ}$	(4,91)	$C_{13}A_Y^B\omega_{ibX}$
(4,92)	$C_{13}A_Y^B\omega_{ibY}$	(4,93)	$C_{13}A_Y^B\omega_{ibZ}$
(5,76)	$C_{21}A_Y^B\omega_{ibZ}$	(5,77)	$C_{21}A_Y^B\omega_{ibY}$
(5,78)	$C_{21}A_Y^B\omega_{ibX}$	(5,79)	$C_{21}A_Z^B\omega_{ibY}$
(5,80)	$C_{21}A_Z^B\omega_{ibZ}$	(5,81)	$C_{21}A_Z^B\omega_{ibX}$
(5,82)	$C_{22}A_Z^B\omega_{ibX}$	(5,83)	$C_{22}A_Z^B\omega_{ibZ}$
(5,84)	$C_{22}A_Z^B\omega_{ibY}$	(5,85)	$C_{22}A_X^B\omega_{ibZ}$
(5,86)	$C_{22}A_Y^B\omega_{ibX}$	(5,87)	$C_{22}A_X^B\omega_{ibY}$
(5,88)	$C_{23}A_X^B\omega_{ibY}$	(5,89)	$C_{23}A_X^B\omega_{ibX}$
(5,90)	$C_{23}A_X^B\omega_{ibZ}$	(5,91)	$C_{23}A_Y^B\omega_{ibX}$
(5,92)	$C_{23}A_Y^B\omega_{ibY}$	(5,93)	$C_{23}A_Y^B\omega_{ibZ}$
(6,76)	$C_{31}A_Y^B\omega_{ibZ}$	(6,77)	$C_{31}A_Y^B\omega_{ibY}$
(6,78)	$C_{31}A_Y^B\omega_{ibX}$	(6,79)	$C_{31}A_Z^B\omega_{ibY}$
(6,80)	$C_{31}A_Z^B\omega_{ibZ}$	(6,81)	$C_{31}A_Z^B\omega_{ibX}$
(6,82)	$C_{32}A_Z^B\omega_{ibX}$	(6,83)	$C_{32}A_Z^B\omega_{ibZ}$
(6,84)	$C_{32}A_Z^B\omega_{ibY}$	(6,85)	$C_{32}A_X^B\omega_{ibZ}$
(6,86)	$C_{32}A_Y^B\omega_{ibX}$	(6,87)	$C_{32}A_X^B\omega_{ibY}$
(6,88)	$C_{33}A_X^B\omega_{ibY}$	(6,89)	$C_{33}A_X^B\omega_{ibX}$
(6,90)	$C_{33}A_X^B\omega_{ibZ}$	(6,91)	$C_{33}A_Y^B\omega_{ibX}$
(6,92)	$C_{33}A_Y^B\omega_{ibY}$	(6,93)	$C_{33}A_Y^B\omega_{ibZ}$

Table B.7 Elements of Dynamics Submatrix $\mathbf{F}_{22}$

Element	Term	Element	Term
(14,14)	$-\beta_{b_{x_c}}$	(15,15)	$-\beta_{b_{y_c}}$
(16,16)	$-\beta_{b_{z_c}}$	(17,17)	$-\beta_{\nabla_{x_c}}$
(18,18)	$-\beta_{\nabla_{y_c}}$	(19,19)	$-\beta_{\nabla_{z_c}}$
(20,20)	$-\beta_{\delta_{g_x}}$	(21,21)	$-\beta_{\delta_{g_y}}$
(22,22)	$-\beta_{\delta_{g_z}}$	(23,23)	$-\beta_{\delta_{h_c}}$

Table B.8 Elements of Dynamics Submatrix $\mathbf{F}_{55}$

Element	Term	Element	Term
(70,70)	$-\beta_{\nabla_{x_q}}$	(71,71)	$-\beta_{\nabla_{y_q}}$
(72,72)	$-\beta_{\nabla_{z_q}}$	(73,73)	$-\beta_{b_{x_{q1}}}$
(74,74)	$-\beta_{b_{y_{q1}}}$	(75,75)	$-\beta_{b_{z_{q1}}}$

Table B.9 Elements of Process Noise Submatrix $\mathbf{Q}_{11}$

Element	Term	Element	Term
(4,4)	$\omega^2_{\eta_{b_X}}$	(5,5)	$\omega^2_{\eta_{b_Y}}$
(6,6)	$\omega^2_{\eta_{b_Z}}$	(7,7)	$\omega^2_{\eta_{A_X}}$
(8,8)	$\omega^2_{\eta_{A_Y}}$	(9,9)	$\omega^2_{\eta_{A_Z}}$

Table B.10 Elements of Process Noise Submatrix $\mathbf{Q}_{22}$

Element	Term	Element	Term
(14,14)	$2\beta_{b_{x_c}}\omega^2_{b_{x_c}}$	(15,15)	$2\beta_{b_{y_c}}\omega^2_{b_{y_c}}$
(16,16)	$2\beta_{b_{z_c}}\omega^2_{b_{z_c}}$	(17,17)	$2\beta_{\nabla_{x_c}}\omega^2_{\nabla_{x_c}}$
(18,18)	$2\beta_{\nabla_{y_c}}\omega^2_{\nabla_{y_c}}$	(19,19)	$2\beta_{\nabla_{z_c}}\omega^2_{\nabla_{z_c}}$
(20,20)	$2\beta_{\delta g_x}\omega^2_{\delta g_x}$	(21,21)	$2\beta_{\delta g_y}\omega^2_{\delta g_y}$
(22,22)	$2\beta_{\delta g_z}\omega^2_{\delta g_z}$	(23,23)	$2\beta_{\delta_{h_c}}\omega^2_{\delta h_c}$

Appendix C. PNRS and DDPNRS Noise Matrcies ($\mathbf{Q}(t)$ and $\mathbf{R}(t)$) Values

This appendix contains tabular listings of the truth and filter models dynamics driving and measurement noise values. The tables with the dynamic driving noise values contain only the states in which dynamics driving noise was added to other than the random processes from the models themselves. Theses values are the scaling factors which come from $(5, 9, 20, 23, 26, 28, 29)$ and from the tuning conducted by this author.

Table C.1 PNRS Truth and Reduced Order Filter Model Tuning Values of $\mathbf{Q}(t)$ Matrix with Velocity Aiding

Truth State Number	Truth Model Noise Value	Filter State Number	Filter Model Noise Value	Units
1	0.0	1	0.5×10^{-13}	$(arc\text{-}sec)^2/sec$
2	0.0	2	0.5×10^{-13}	$(arc\text{-}sec)^2/sec$
3	0.0	3	5×10^{-14}	$(arc\text{-}sec)^2/sec$
4	190.4×10^{-15}	4	9.52×10^{-12}	$(arc\text{-}sec)^2/sec$
5	190.4×10^{-15}	5	9.52×10^{-12}	$(arc\text{-}sec)^2/sec$
6	190.4×10^{-15}	6	95.2×10^{-12}	$(arc\text{-}sec)^2/sec$
7	102.9×10^{-9}	7	1.5435×10^{-3}	ft^2/sec^3
8	102.9×10^{-9}	8	1.5435×10^{-3}	ft^2/sec^3
9	102.9×10^{-9}	9	15.435×10^{-3}	ft^2/sec^3
10	0.0	10	50.0	ft^2/sec
11	33.34	11	1667.0	ft^2/sec
12	0.0	12	5.0	ft^2/sec
13	0.0	13	1.0×10^{-10}	ft^2/sec^3
14	0.0	14	1.0	ft^2/sec
15	0.0	15	1.0×10^{-9}	ft^2/sec^3
16	0.0		*not modeled*	ft^2/sec
17	0.0		*not modeled*	ft^2/sec
18	$(time\text{-}varying)^{note1}$		*not modeled*	ft^2/sec^5
19	2.7451×10^{-11}		*not modeled*	$\mu g^2/sec$
20	2.7451×10^{-11}		*not modeled*	$\mu g^2/sec$
21	2.7451×10^{-11}		*not modeled*	$\mu g^2/sec$
22	1.9548		*not modeled*	$\mu g^2/sec$
23	1.9548		*not modeled*	$\mu g^2/sec$
24	1.9548		*not modeled*	$\mu g^2/sec$
47	6.667×10^{-13}		*not modeled*	ft^2/sec
51	6.667×10^{-13}		*not modeled*	ft^2/sec
55	6.667×10^{-13}		*not modeled*	ft^2/sec
59	6.667×10^{-13}		*not modeled*	ft^2/sec
63	6.667×10^{-13}		*not modeled*	ft^2/sec
67	6.667×10^{-13}		*not modeled*	ft^2/sec
68	0.0	16	2.0	ft^2/sec
69	0.0	17	2.0	ft^2/sec
70	0.0	18	2.0	ft^2/sec
71	0.0	19	2.0	ft^2/sec

Table C.2 PNRS Truth and Reduced Order Filter Model Tuning Values of $\mathbf{Q}(t)$ Matrix without Velocity Aiding

Truth State Number	Truth Model Noise Value	Filter State Number	Filter Model Noise Value	Units
1	0.0	1	0.5×10^{-13}	$(arc\text{-}sec)^2/sec$
2	0.0	2	0.5×10^{-13}	$(arc\text{-}sec)^2/sec$
3	0.0	3	1×10^{-13}	$(arc\text{-}sec)^2/sec$
4	190.4×10^{-15}	4	9.52×10^{-12}	$(arc\text{-}sec)^2/sec$
5	190.4×10^{-15}	5	9.52×10^{-12}	$(arc\text{-}sec)^2/sec$
6	190.4×10^{-15}	6	285.6×10^{-12}	$(arc\text{-}sec)^2/sec$
7	102.9×10^{-9}	7	1.029×10^{-3}	ft^2/sec^3
8	102.9×10^{-9}	8	1.029×10^{-3}	ft^2/sec^3
9	102.9×10^{-9}	9	10.29	ft^2/sec^3
10	0.0	10	30.0	ft^2/sec
11	33.34	11	833.5	ft^2/sec
12	0.0	12	5.0	ft^2/sec
13	0.0	13	1.0×10^{-10}	ft^2/sec^3
14	0.0	14	1.0	ft^2/sec
15	0.0	15	1.0×10^{-9}	ft^2/sec^3
16	0.0		*not modeled*	ft^2/sec
17	0.0		*not modeled*	ft^2/sec
18	$(time\text{-}varying)^{note1}$		*not modeled*	ft^2/sec^5
19	2.7451×10^{-11}		*not modeled*	$\mu g^2/sec$
20	2.7451×10^{-11}		*not modeled*	$\mu g^2/sec$
21	2.7451×10^{-11}		*not modeled*	$\mu g^2/sec$
22	1.9548		*not modeled*	$\mu g^2/sec$
23	1.9548		*not modeled*	$\mu g^2/sec$
24	1.9548		*not modeled*	$\mu g^2/sec$
47	6.667×10^{-13}		*not modeled*	ft^2/sec
51	6.667×10^{-13}		*not modeled*	ft^2/sec
55	6.667×10^{-13}		*not modeled*	ft^2/sec
59	6.667×10^{-13}		*not modeled*	ft^2/sec
63	6.667×10^{-13}		*not modeled*	ft^2/sec
67	6.667×10^{-13}		*not modeled*	ft^2/sec
68	0.0	16	10.0	ft^2/sec
69	0.0	17	8.0	ft^2/sec
70	0.0	18	2.0	ft^2/sec
71	0.0	19	2.0	ft^2/sec

Table C.3 DDPNRS Truth and Filter Model Tuning Values of $\mathbf{Q}(t)$ Matrix

Truth State Number	Truth Model Noise Value	Filter State Number	Filter Model Noise Value	Units
1	0.0	1	0.5×10^{-13}	$(arc\text{-}sec)^2/sec$
2	0.0	2	0.75×10^{-14}	$(arc\text{-}sec)^2/sec$
3	0.0	3	5×10^{-14}	$(arc\text{-}sec)^2/sec$
4	190.4×10^{-15}	4	9.52×10^{-12}	$(arc\text{-}sec)^2/sec$
5	190.4×10^{-15}	5	9.52×10^{-12}	$(arc\text{-}sec)^2/sec$
6	190.4×10^{-15}	6	142.8×10^{-12}	$(arc\text{-}sec)^2/sec$
7	102.9×10^{-9}	7	514.5×10^{-6}	ft^2/sec^3
8	102.9×10^{-9}	8	514.5×10^{-6}	ft^2/sec^3
9	102.9×10^{-9}	9	6.174	ft^2/sec^3
10	0.0	10	30.0	ft^2/sec
11	33.34	11	500.1	ft^2/sec
12	0.0	12	5.0	ft^2/sec
13	0.0	13	1.0×10^{-10}	ft^2/sec^3
14	0.0		*not modeled*	ft^2/sec
15	0.0		*not modeled*	ft^2/sec
16	$(time\text{-}varying)^{note1}$		*not modeled*	ft^2/sec^5
17	2.7451×10^{-11}		*not modeled*	$\mu g^2/sec$
18	2.7451×10^{-11}		*not modeled*	$\mu g^2/sec$
19	2.7451×10^{-11}		*not modeled*	$\mu g^2/sec$
20	1.9548		*not modeled*	$\mu g^2/sec$
21	1.9548		*not modeled*	$\mu g^2/sec$
22	1.9548		*not modeled*	$\mu g^2/sec$
45	6.667×10^{-13}		*not modeled*	ft^2/sec
49	6.667×10^{-13}		*not modeled*	ft^2/sec
53	6.667×10^{-13}		*not modeled*	ft^2/sec
57	6.667×10^{-13}		*not modeled*	ft^2/sec
61	6.667×10^{-13}		*not modeled*	ft^2/sec
65	6.667×10^{-13}		*not modeled*	ft^2/sec
66	0.0	16	10.0	ft^2/sec
67	0.0	17	4.0	ft^2/sec
68	0.0	18	2.0	ft^2/sec
69	0.0	19	1.0	ft^2/sec

Table C.4 Measurement Noise Covariance Values of $\mathbf{R}(t_i)$ Matrix for PNRS Filter

Measurment	Truth Model Value	Filter Model Value	Units
RRS Range	4.0	6.0	ft^2
RRS Velocity	0.09	0.12	ft^2/sec^2
DGPS	9.0	30.0	ft^2
CPGPS	2.641×10^{-4}	3.0×10^{-4}	ft^2
Baro-altimeter	2500	2500	ft^2

Table C.5 Measurement Noise Covariance Values of $\mathbf{R}(t_i)$ Matrix for DDPNRS Filter

Measurment	Truth Model Value	Filter Model Value	Units
RRS Range	4.0	6.0	ft^2
RRS Velocity	0.09	0.12	ft^2/sec^2
DGPS	9.0	30.0	ft^2
CPGPS	$2.641 \times 10^{-4^{note2}}$	$3.0 \times 10^{-4^{note2}}$	ft^2
Baro-altimeter	2500	2500	ft^2

Notes:

1. Time varying from 0.0 to 26.9667

2. Values presented are for Satellite #4 only. The values used in the differenced pairs is twice that of the presented value in Table C.5.

Appendix D. 71-States PNRS Filter without Velocity Aiding Results

This appendix contains the plots using Hansen's 71-State PNRS Filter without the Perfect Doppler Velocity Aiding measurements. The plots are ordered as in (9) for direct comparison between these plots and those of (9).

A legend for the presented figures is given below.

Table D.1 Legend for Filter Tuning Plots

Symbol	Definition
— Solid Line	Mean Error
··· Dotted Line	Mean Error ± True Sigma
– – Dashed Line	± Filter Predicted Sigma

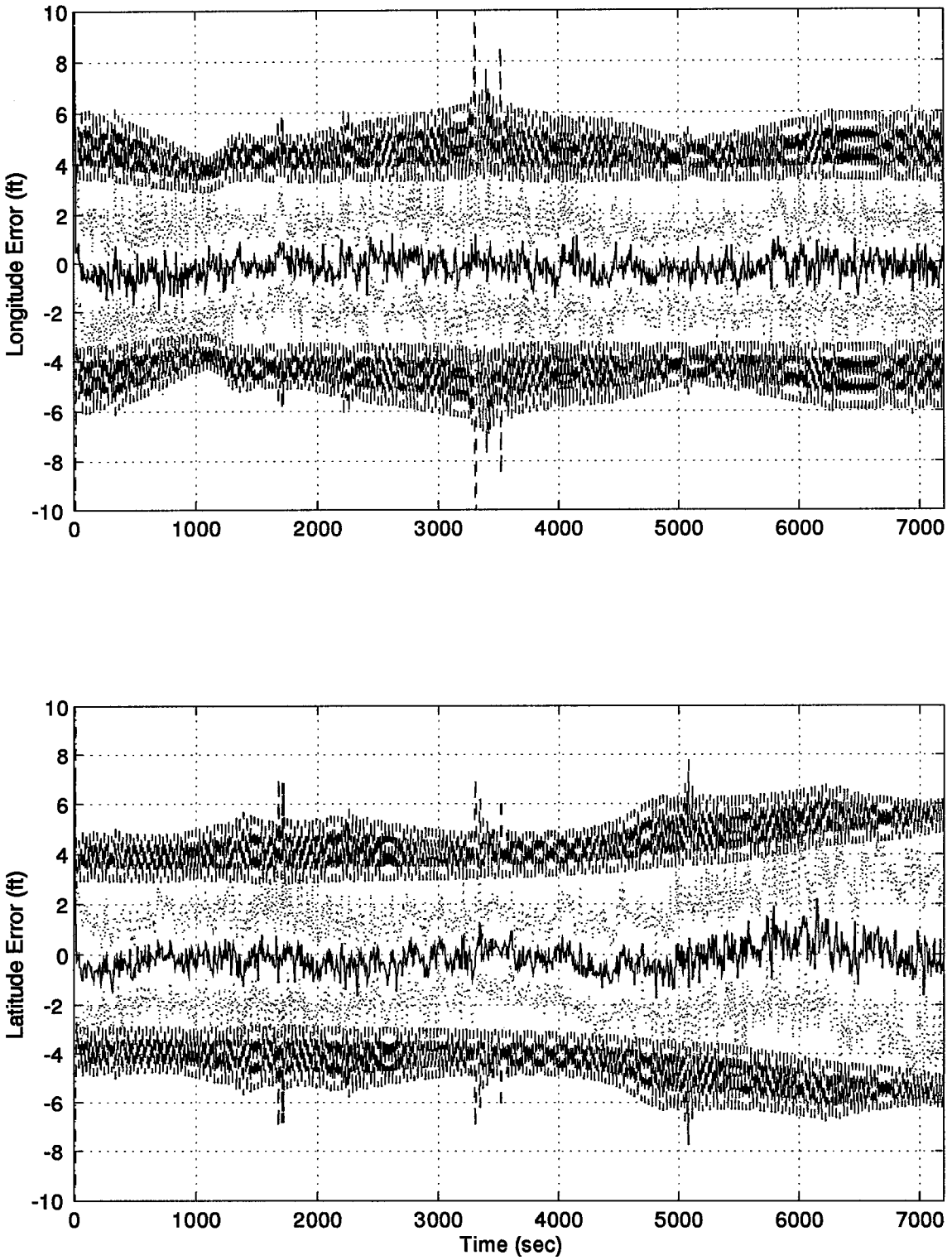

Figure D.1 Longitude and Latitude Error Plots

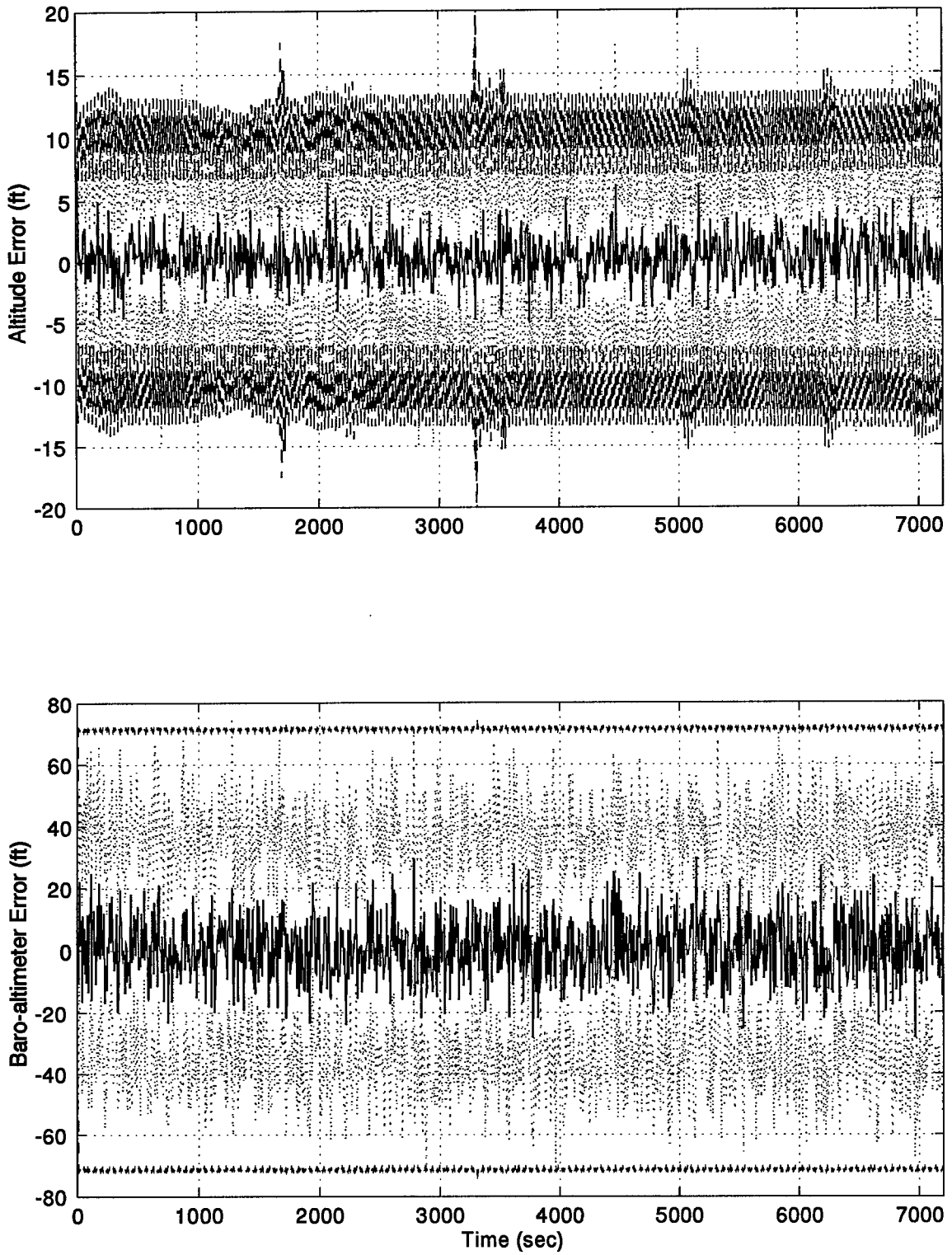

Figure D.2 Altitude and Barometric Altimeter Error Plots

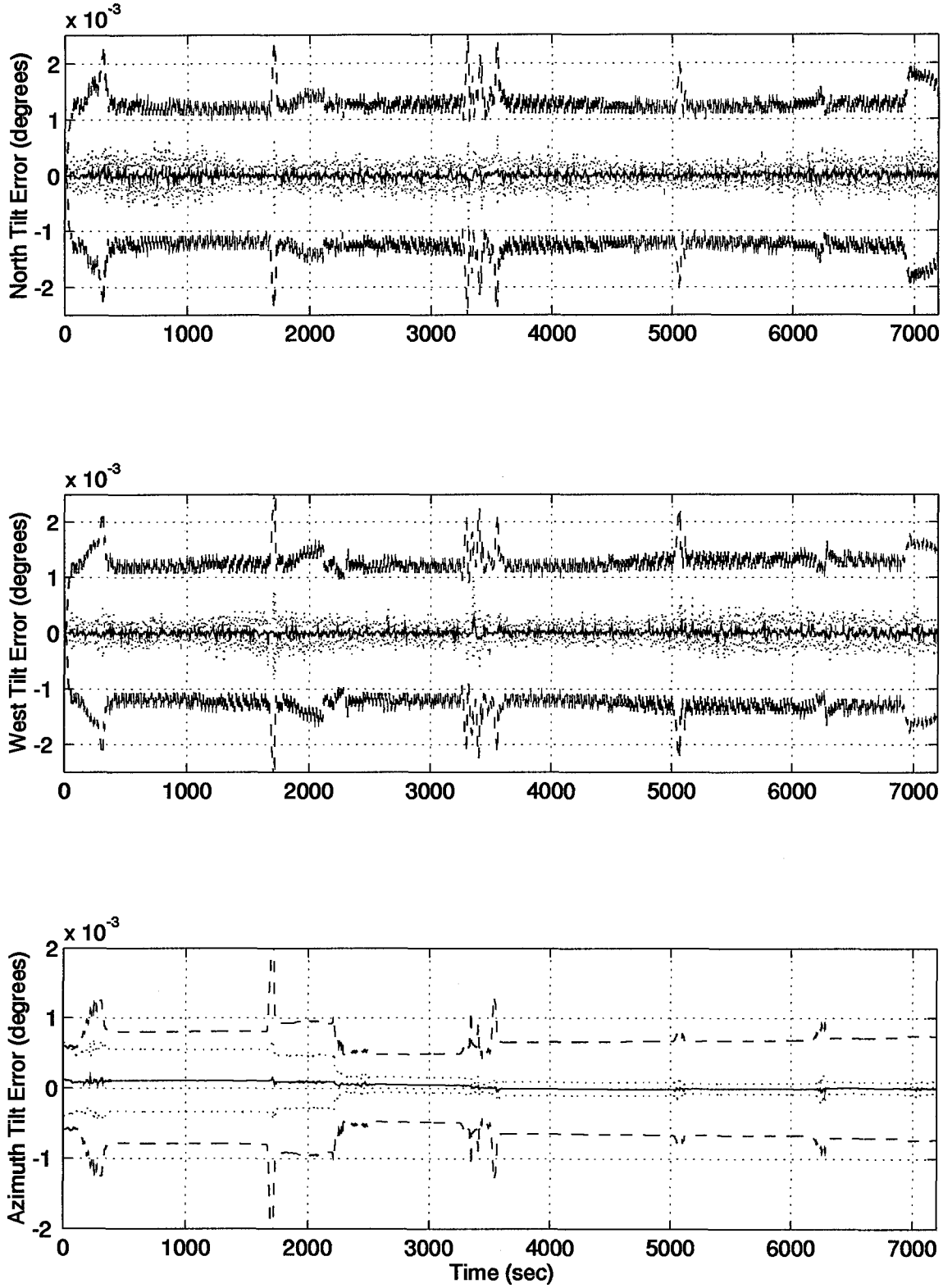

Figure D.3 North, West, and Azimuth Tilt Error Plots

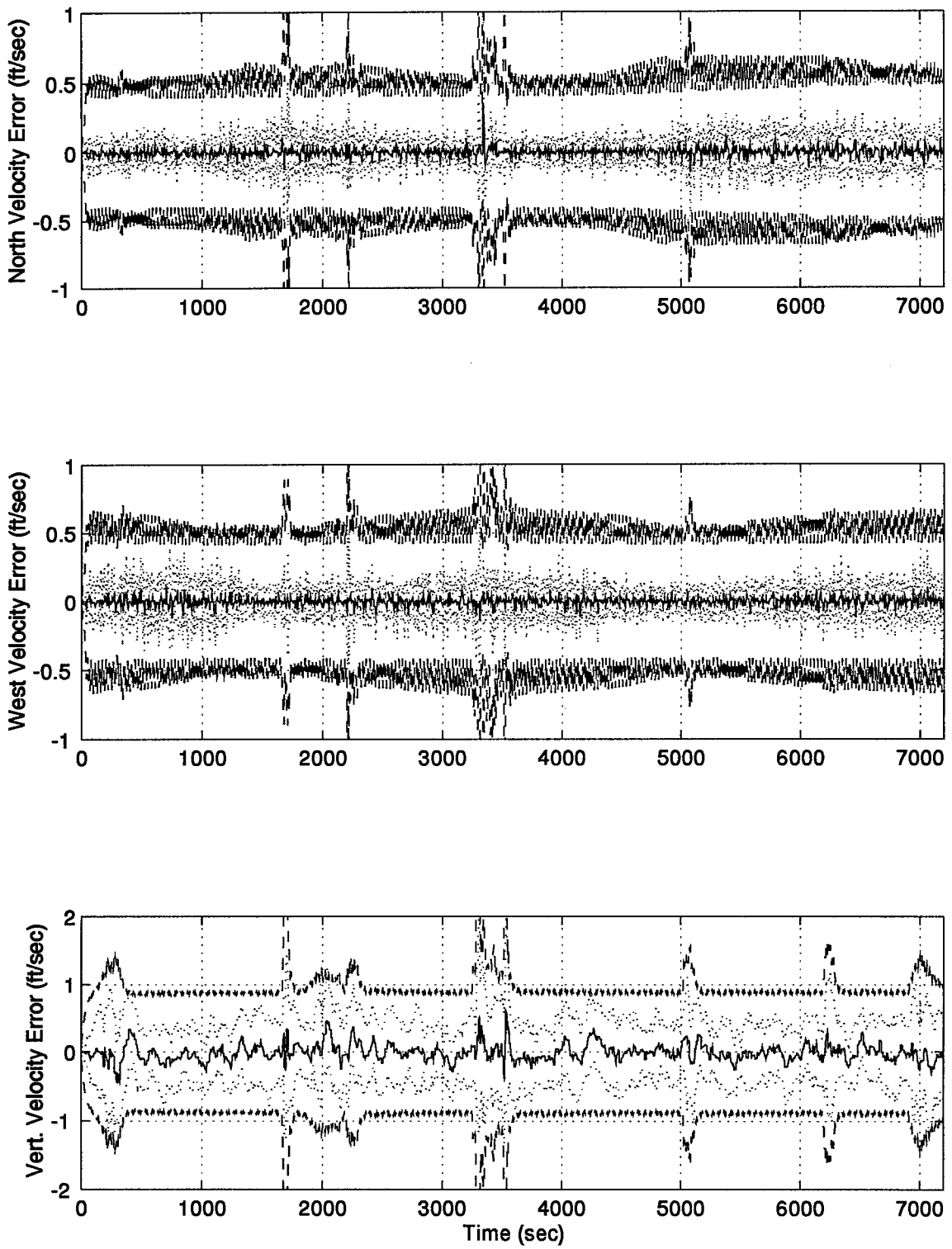

Figure D.4 North, West, and Vertical Velocity Error Plots

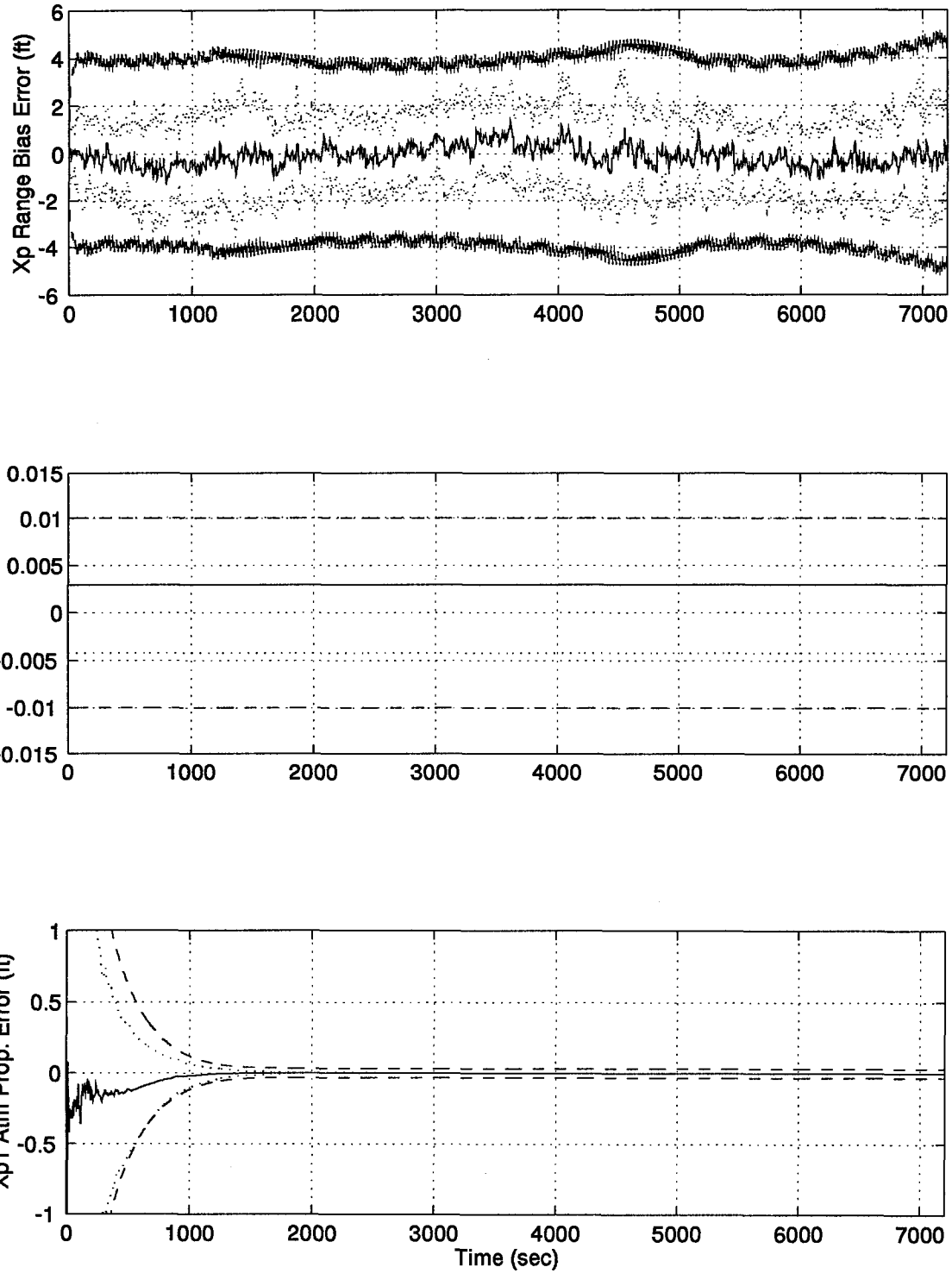

Figure D.5 RRS Range Bias, Range Velocity, and Atmospheric Propagation Delay Error Plots

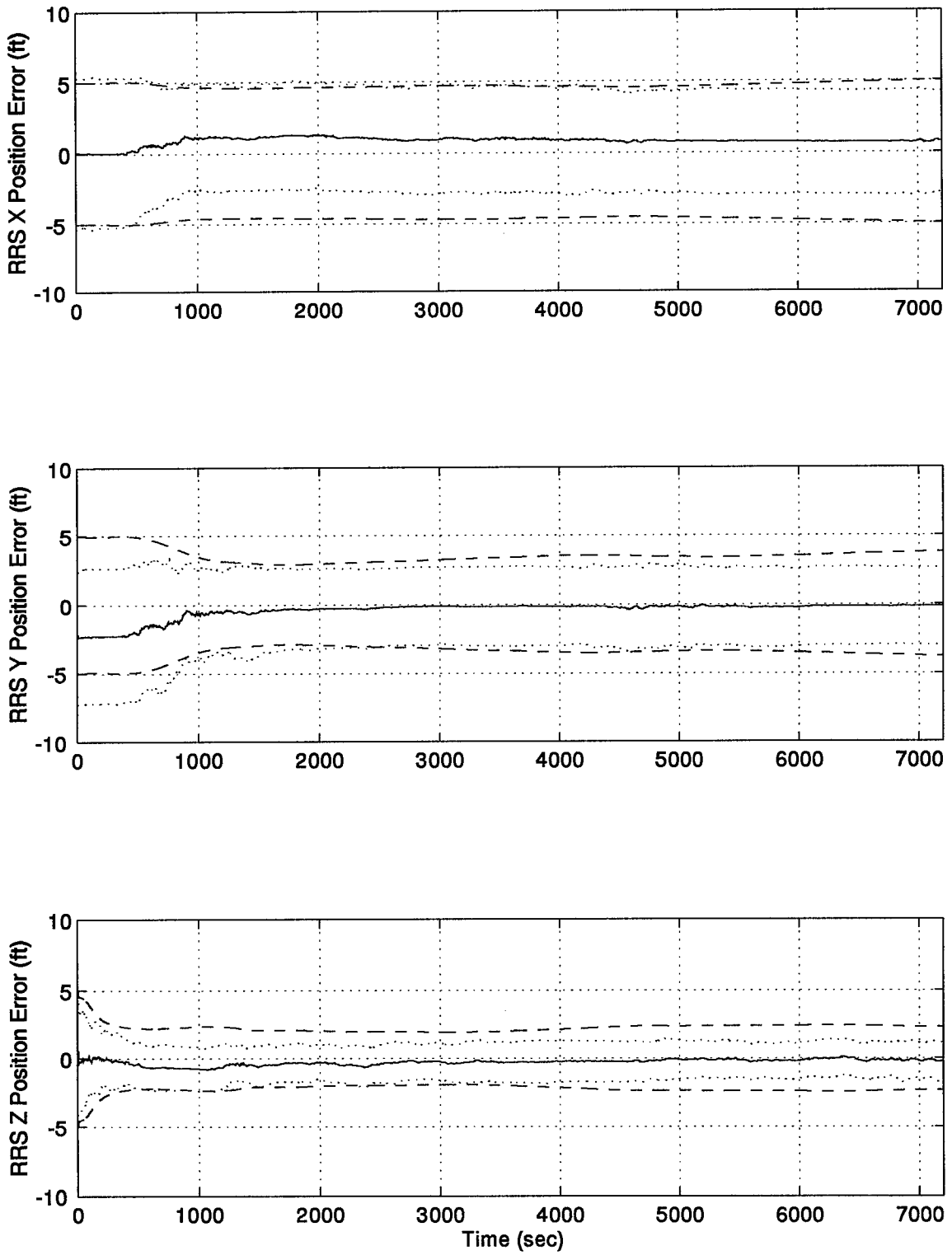

Figure D.6 RRS X, Y, and Z Position Error Plots

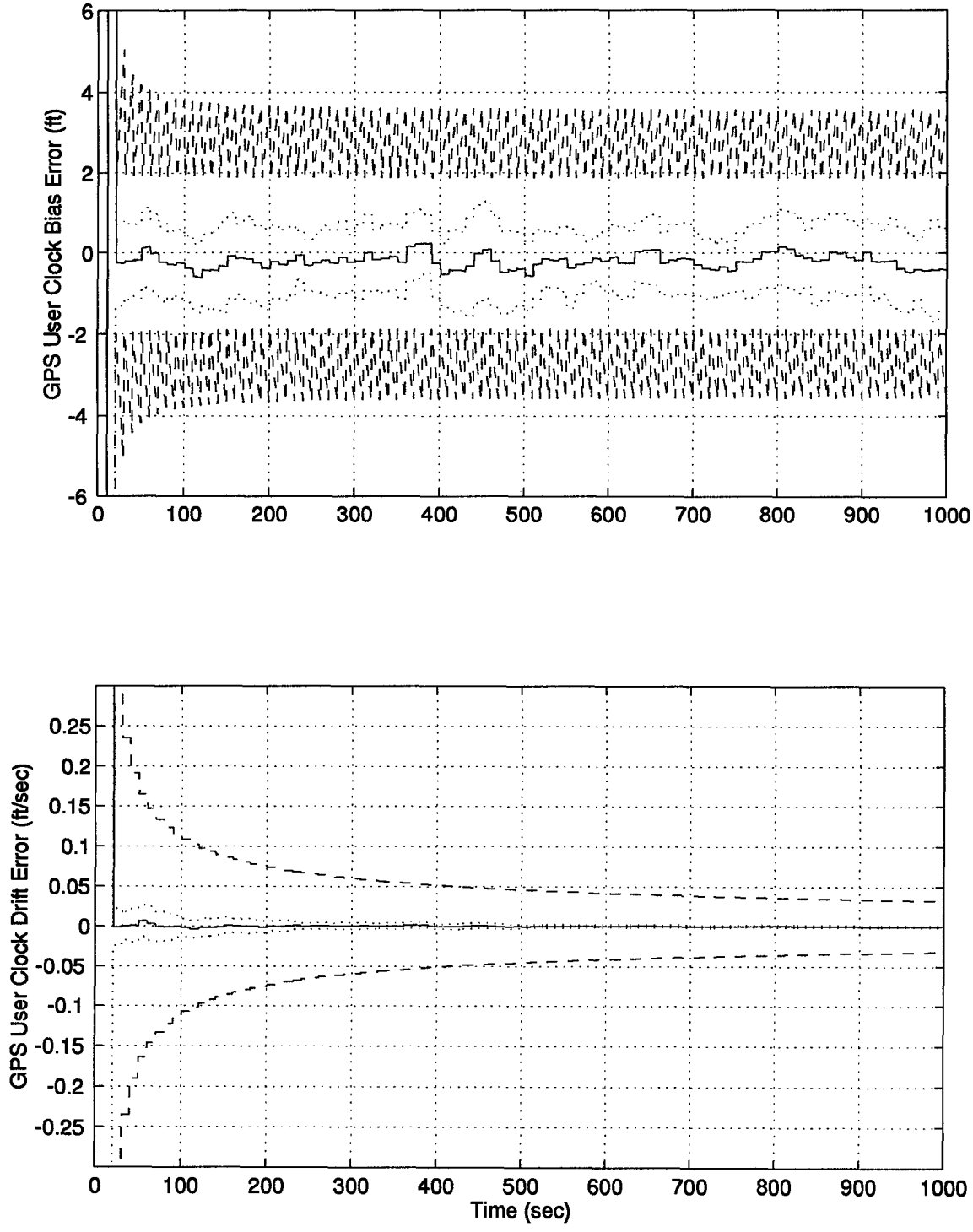

Figure D.7 GPS User Clock Bias and User Clock Drift Error Plots

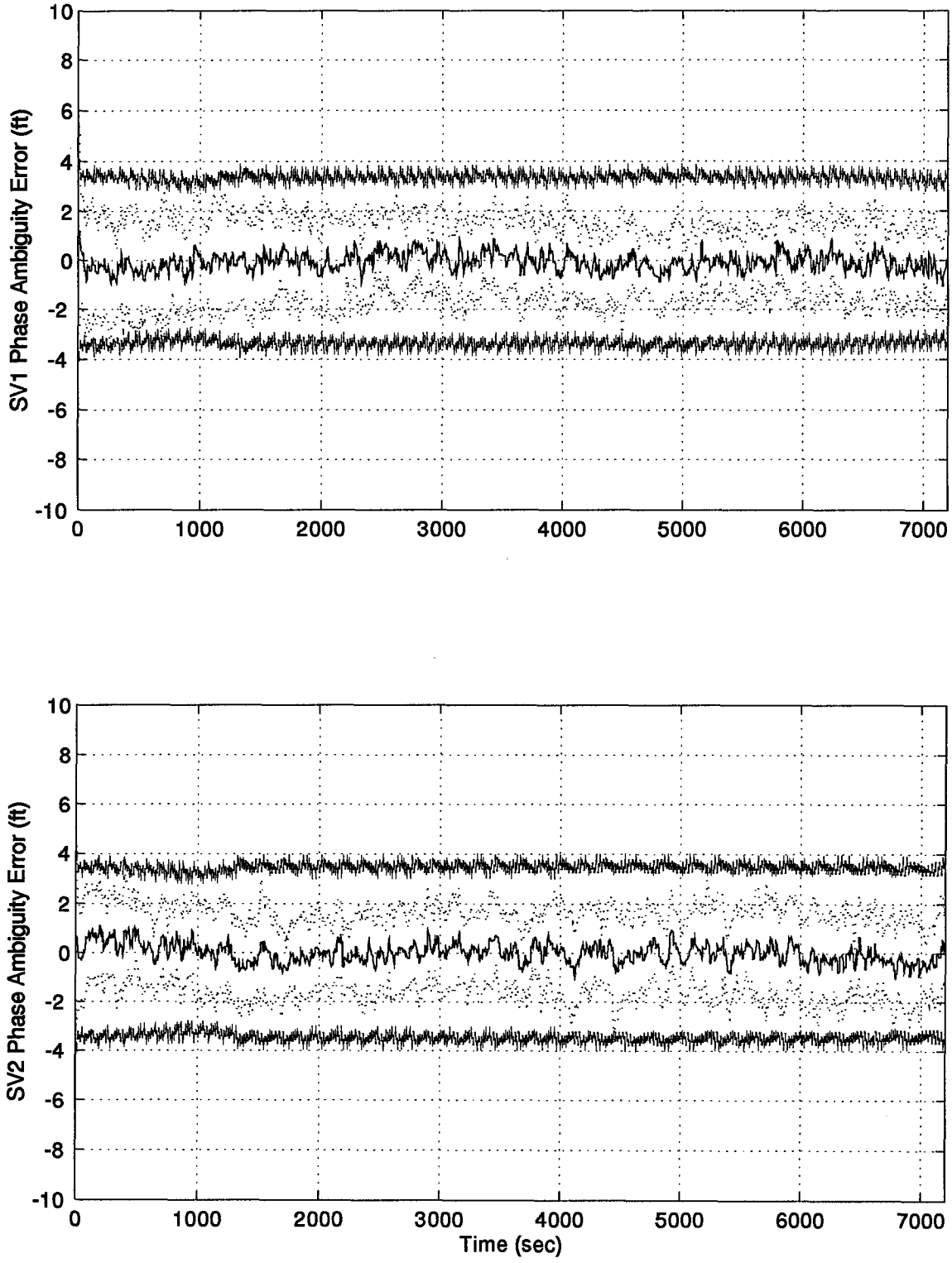

Figure D.8 GPS Satellites 1 and 2 Phase Ambiguity Error Plots

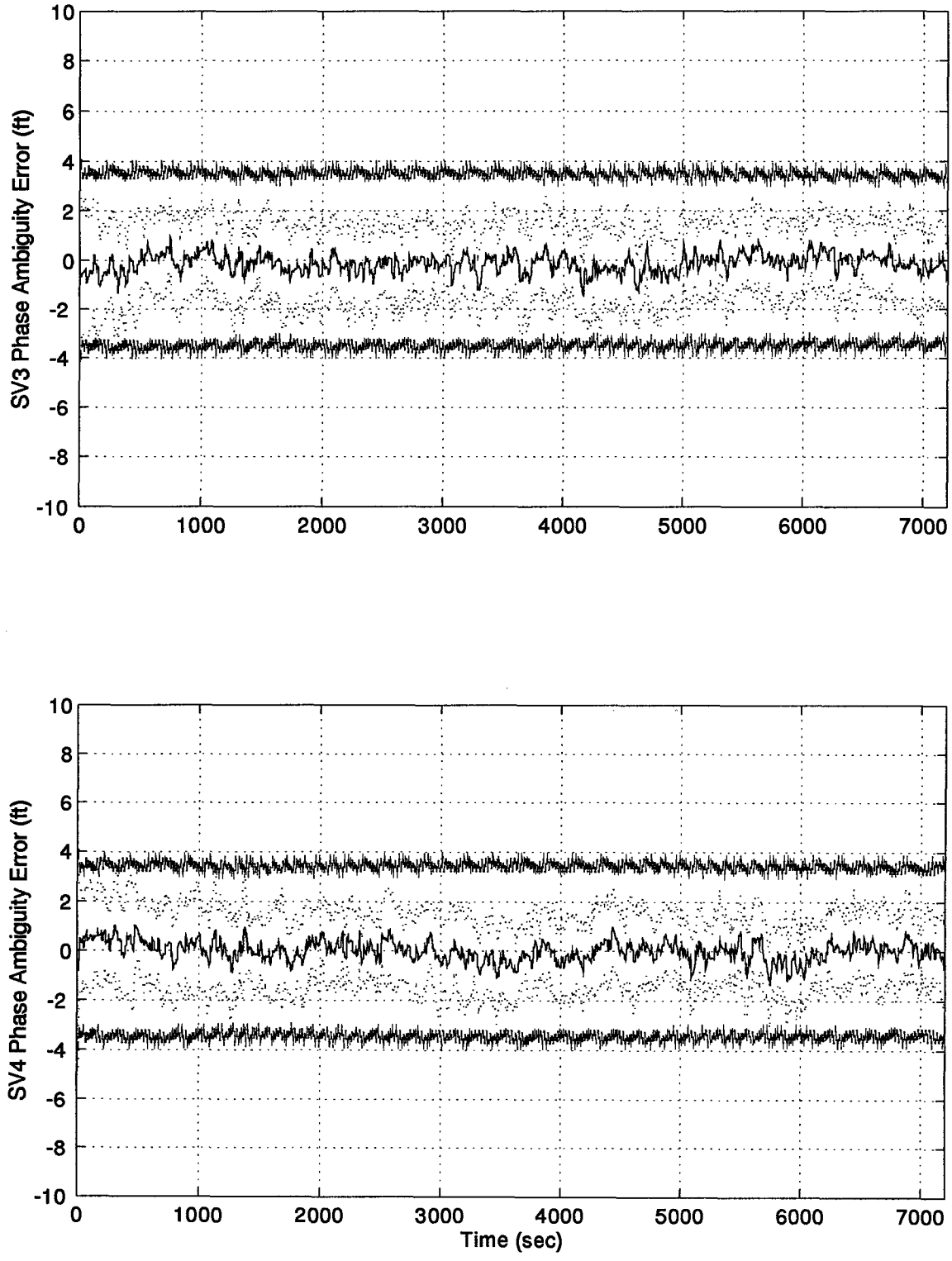

Figure D.9 GPS Satellites 3 and 4 Phase Ambiguity Error Plots

Appendix E. Reduced Order PNRS Filter Results with Velocity Aiding

This appendix contains the results from the two-hour simulation run of the Reduced Order PNRS filter. The results presented still contain the perfect Doppler velocity aiding measurements. These results are used for direct comparison with the same filter run without the perfect Doppler velocity aiding measurements of Appendix F. The plots are in the same order as Appendix D, also for direct comparison.

A legend for the presented figures is given below.

Table E.1 Legend for Filter Tuning Plots

Symbol	Definition
— Solid Line	Mean Error
··· Dotted Line	Mean Error ± True Sigma
– – Dashed Line	± Filter Predicted Sigma

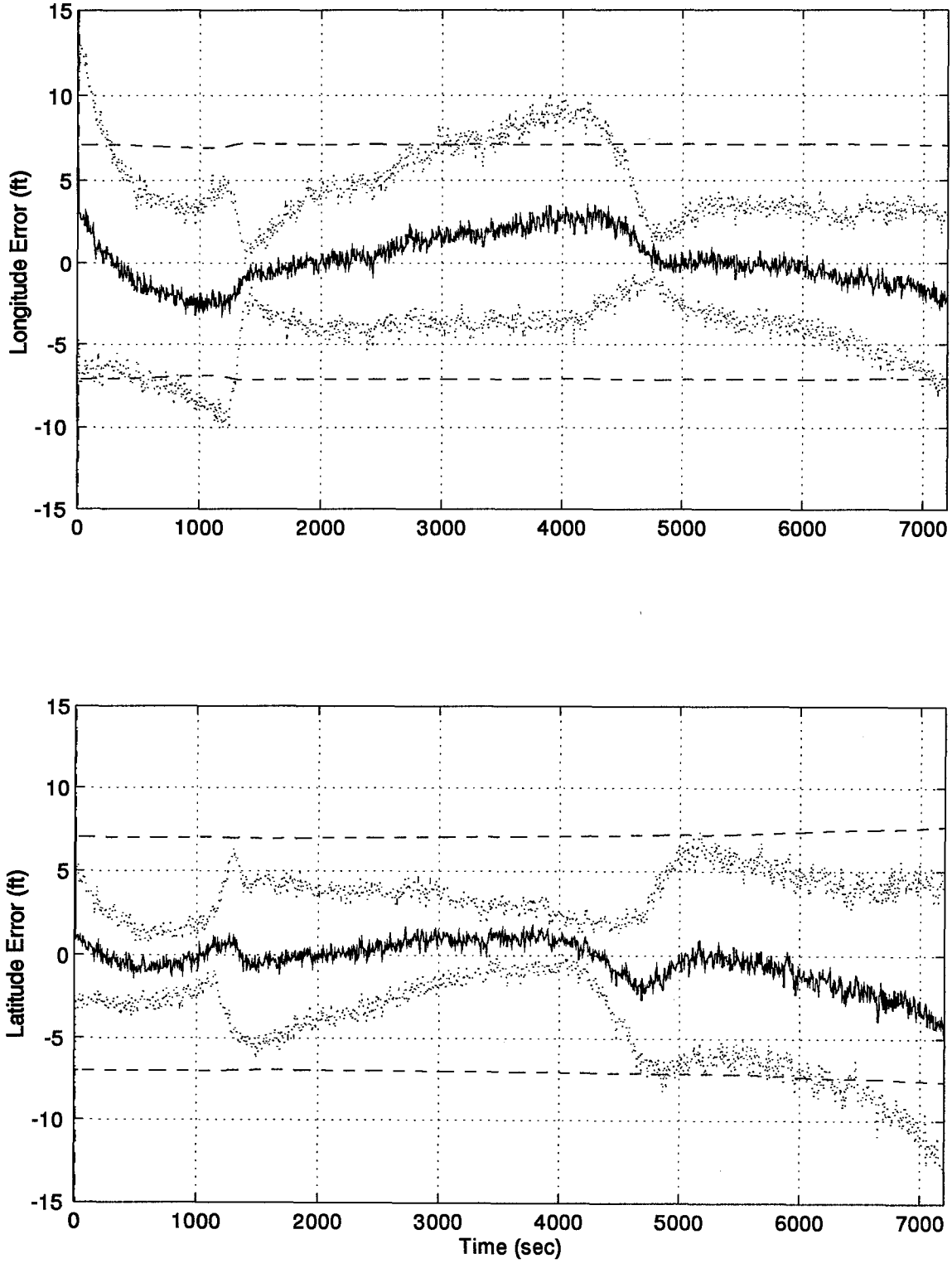

Figure E.1 Longitude and Latitude Error Plots

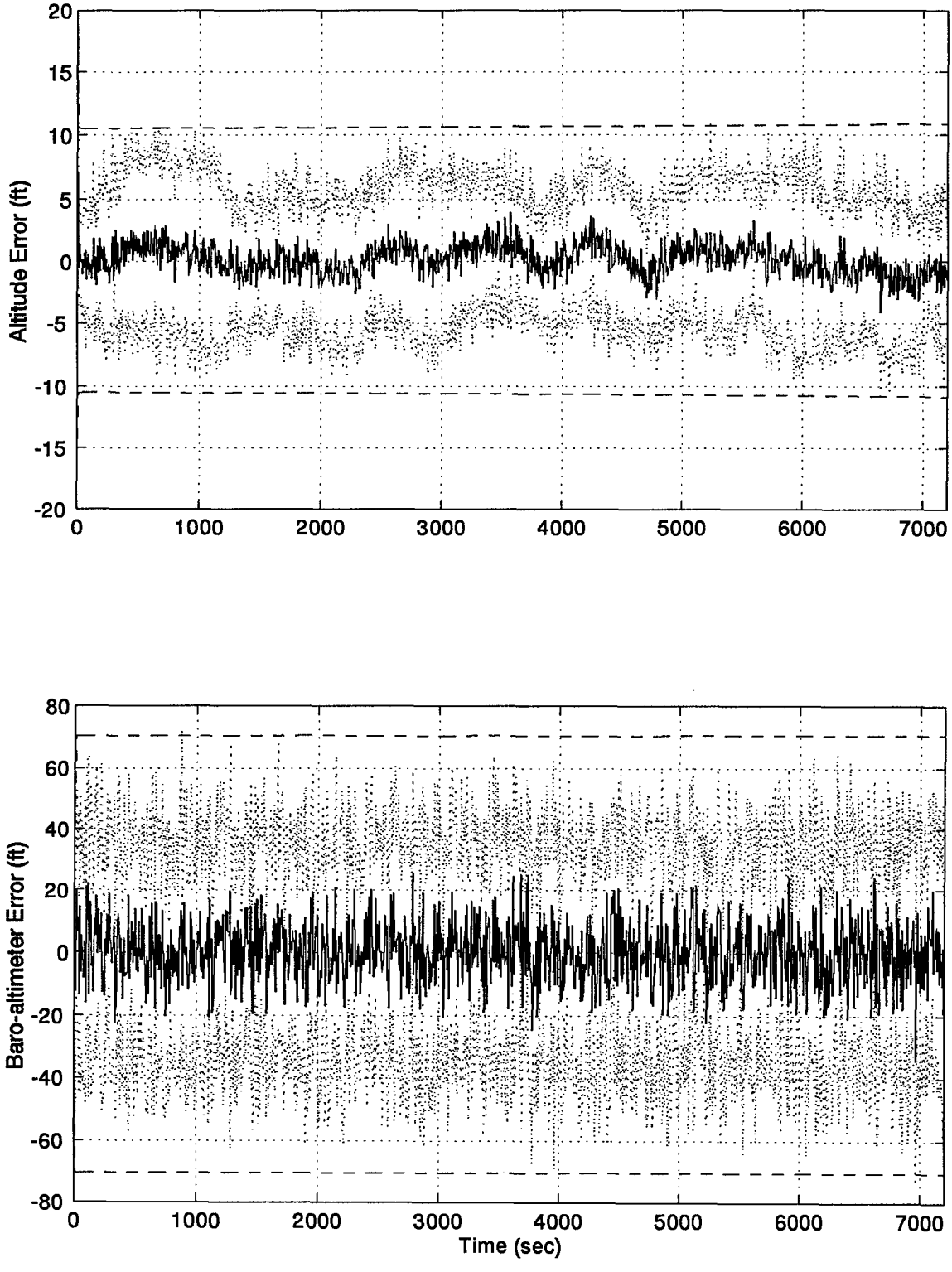

Figure E.2 Altitude and Barometric Altimeter Error Plots

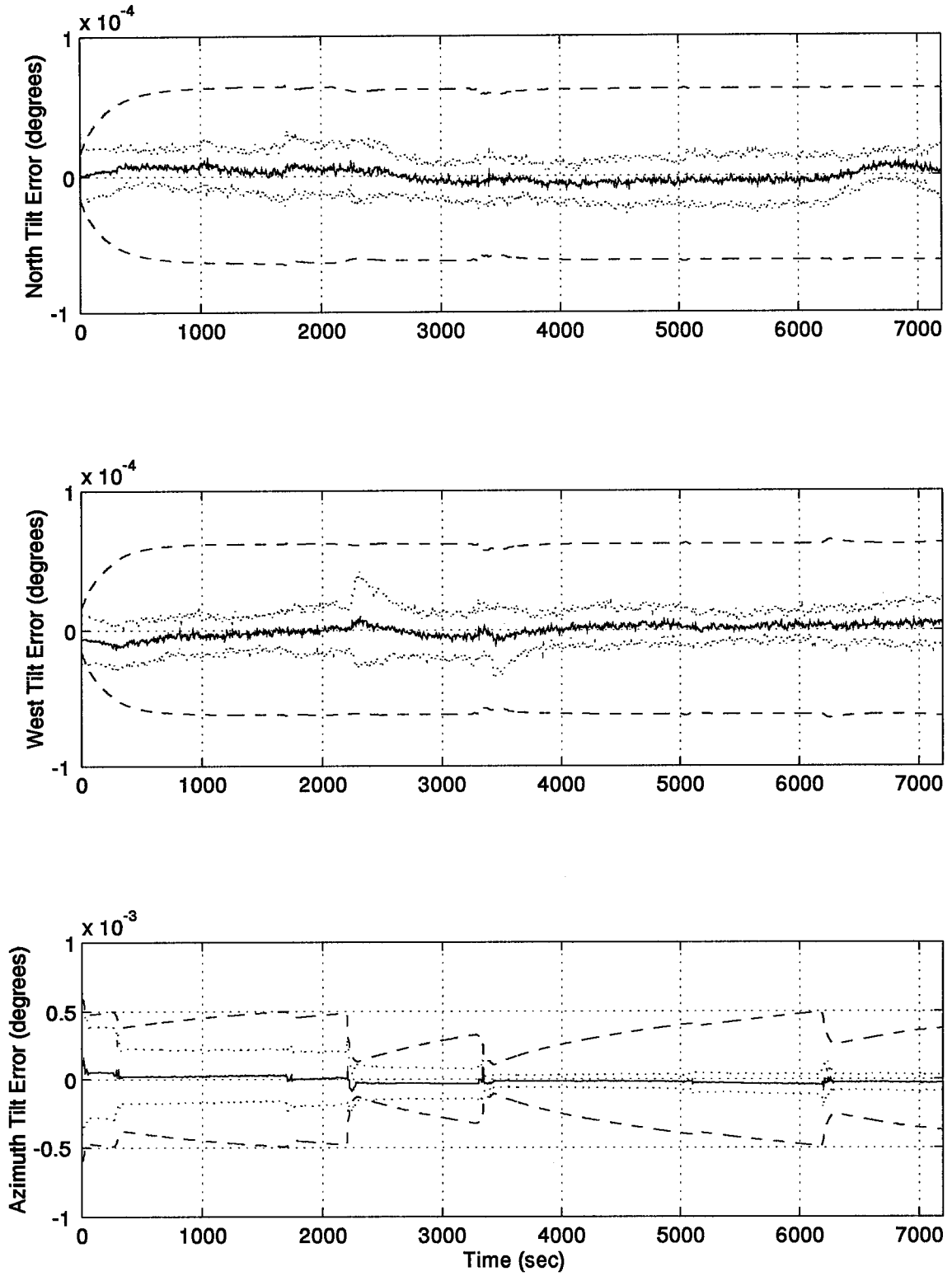

Figure E.3 North, West, and Azimuth Tilt Error Plots

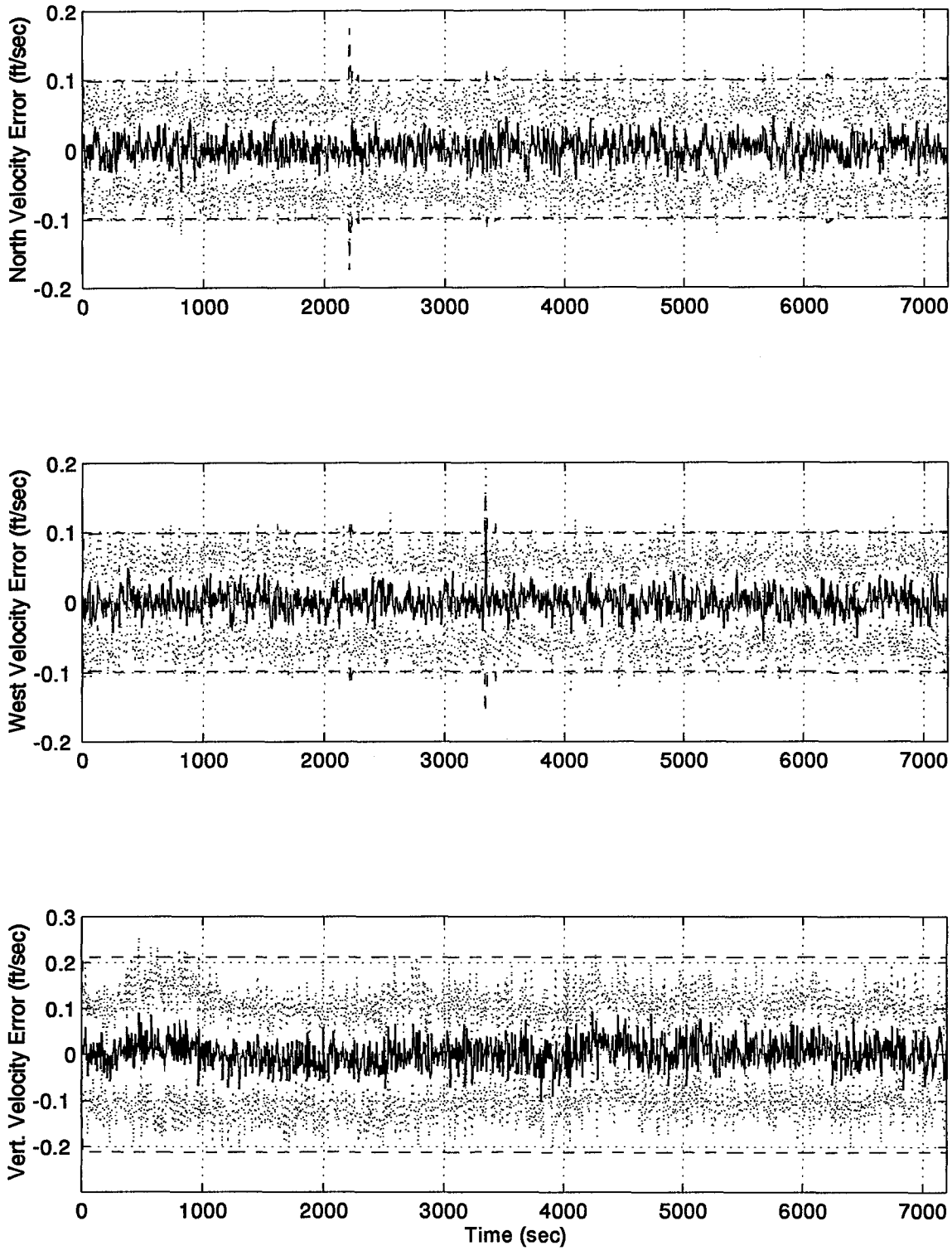

Figure E.4 North, West, and Vertical Velocity Error Plots

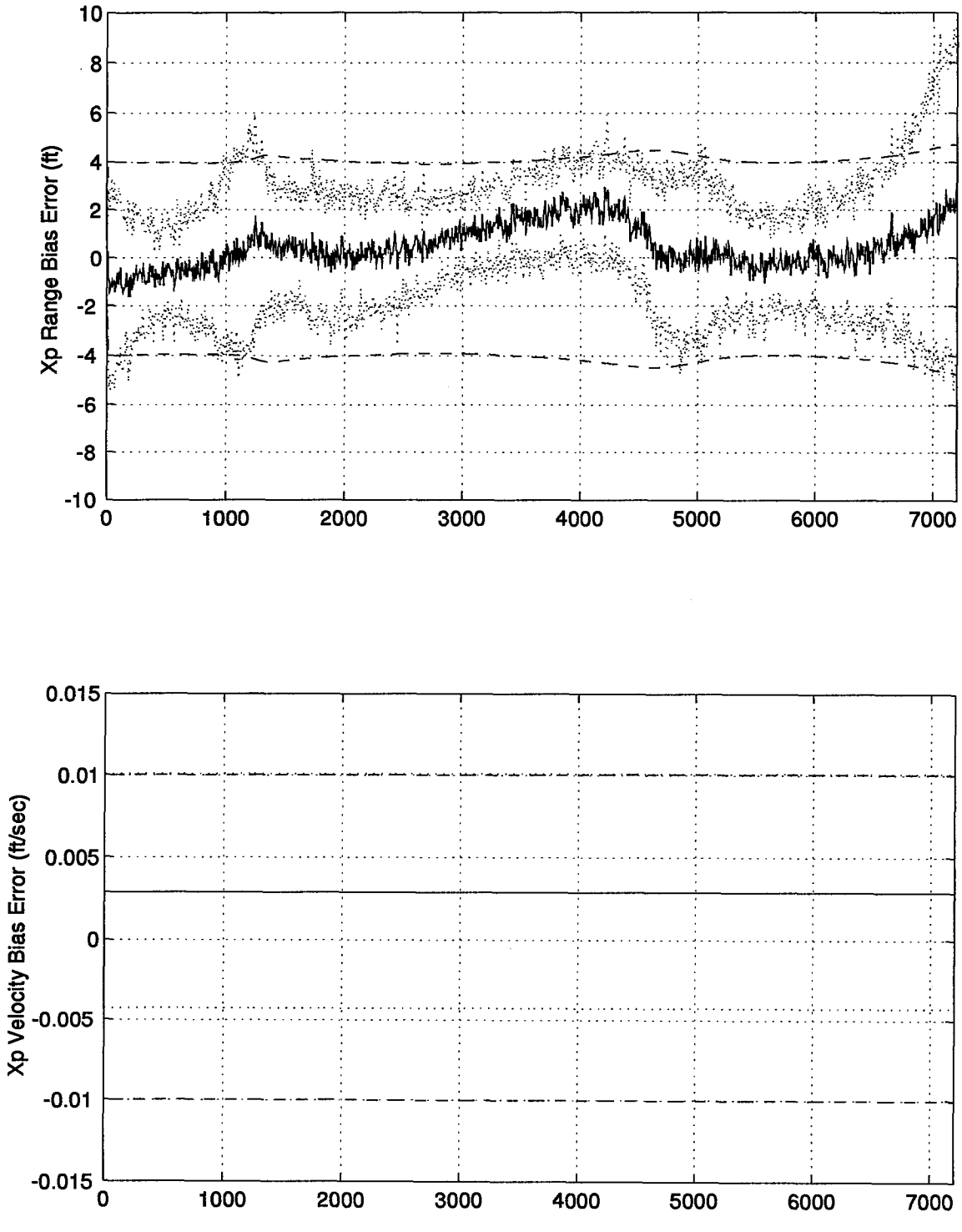

Figure E.5 RRS Range Bias and Range Velocity Error Plots

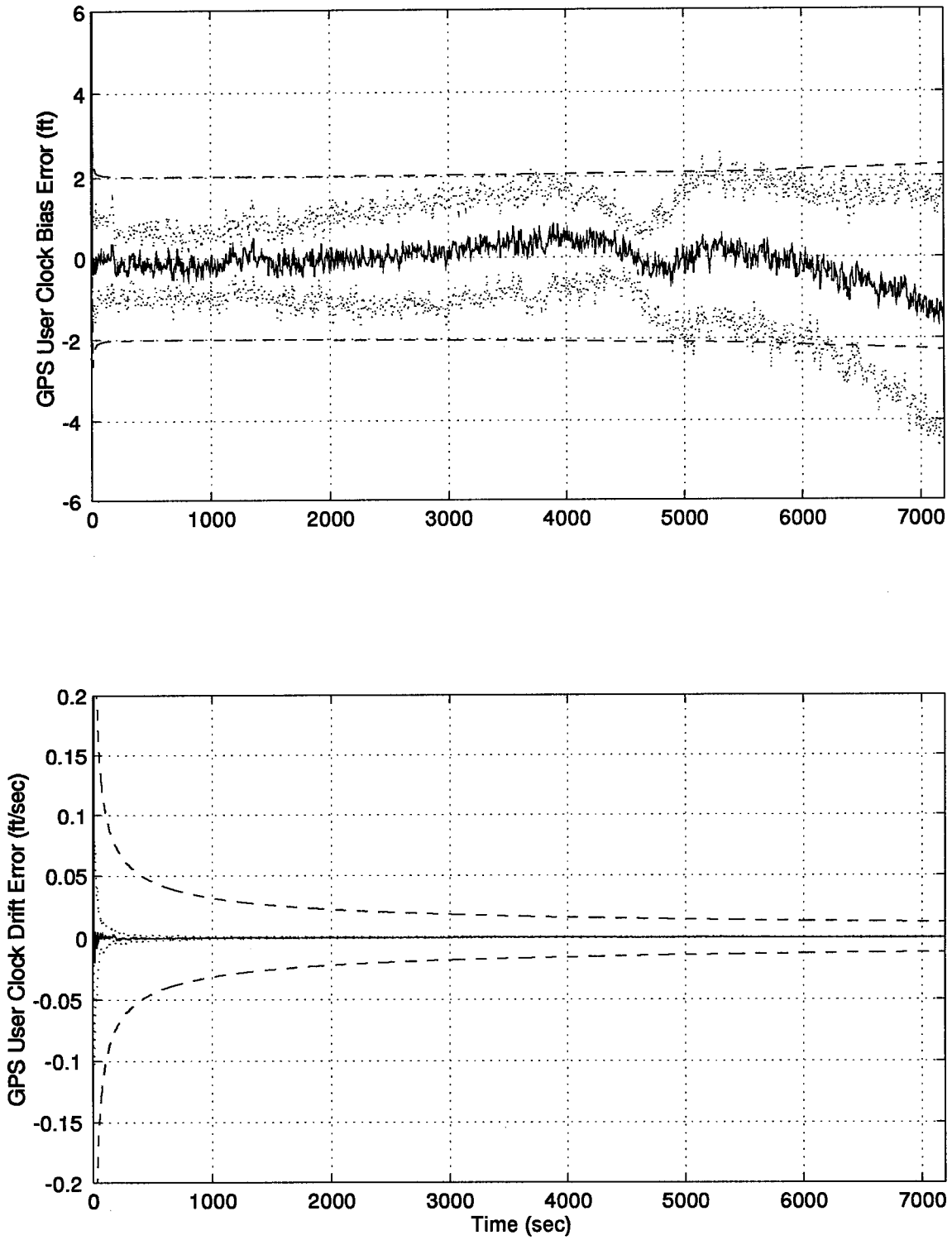

Figure E.6 GPS Clock Bias and Drift Error Plots

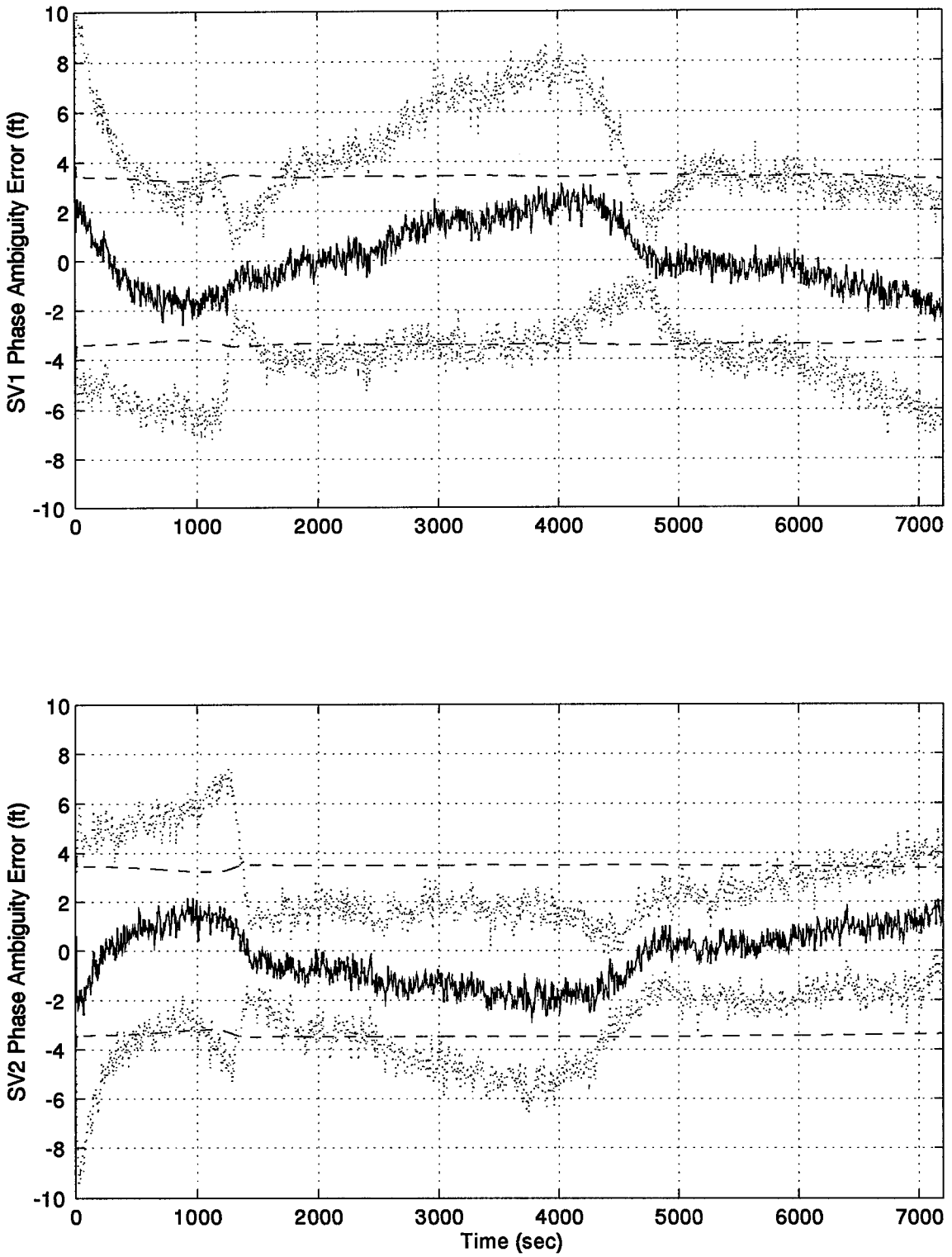

Figure E.7 GPS Satellites 1 and 2 Phase Ambiguity Error Plots

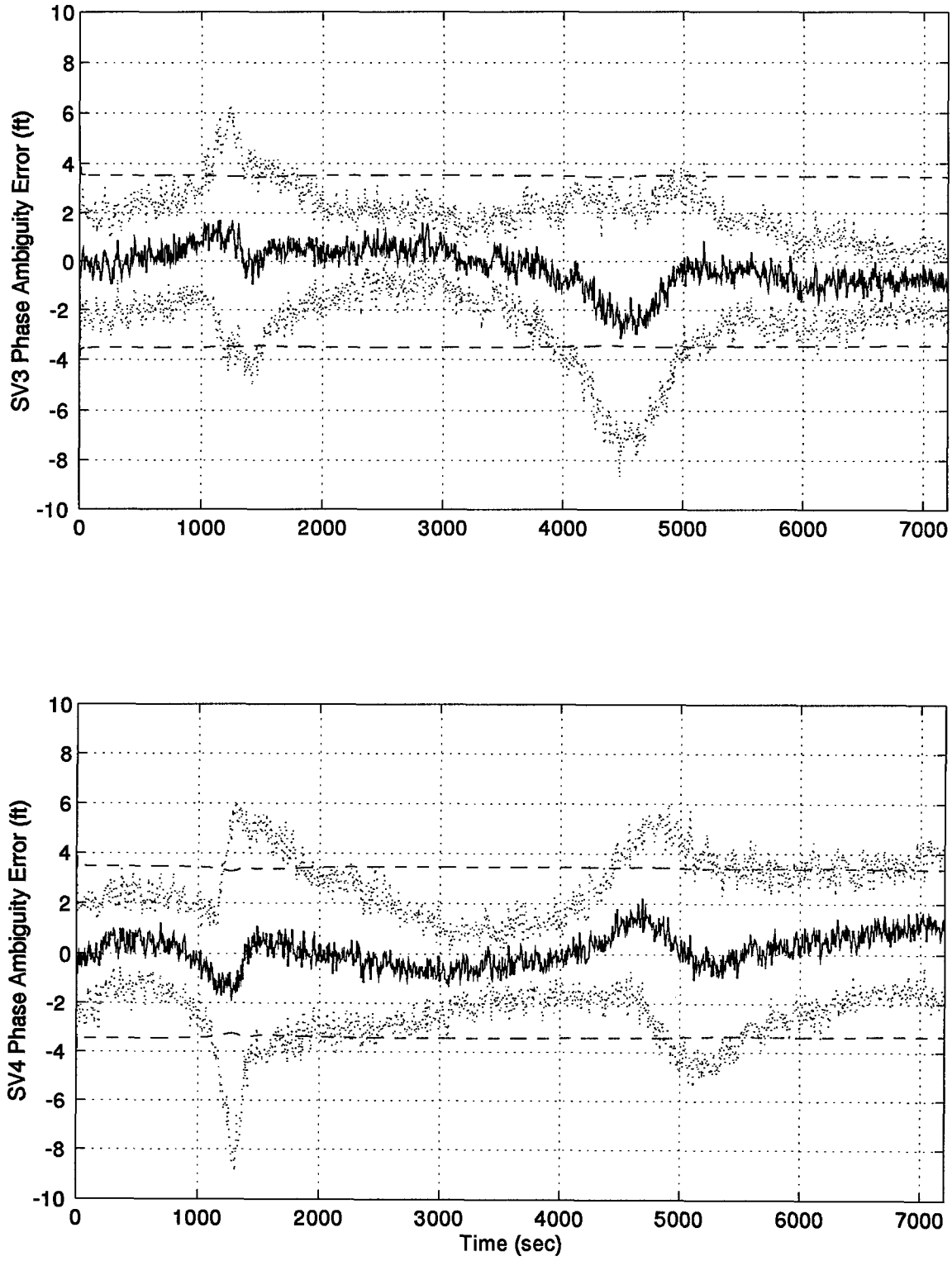

Figure E.8 GPS Satellites 3 and 4 Phase Ambiguity Error Plots

Appendix F. Reduced Order PNRS Filter Results without Velocity Aiding

This appendix contains the results from the two-hour simulation run of the Reduced Order PNRS filter. The results presented do not contain the perfect Doppler velocity aiding measurements. These results are used for direct comparison with the same filter with the perfect Doppler velocity aiding measurements of Appendix E. The plots are in the same order as Appendix D for direct comparison.

A legend for the presented figures is given below.

Table F.1 Legend for Filter Tuning Plots

Symbol	Definition
— Solid Line	Mean Error
··· Dotted Line	Mean Error ± True Sigma
– – Dashed Line	± Filter Predicted Sigma

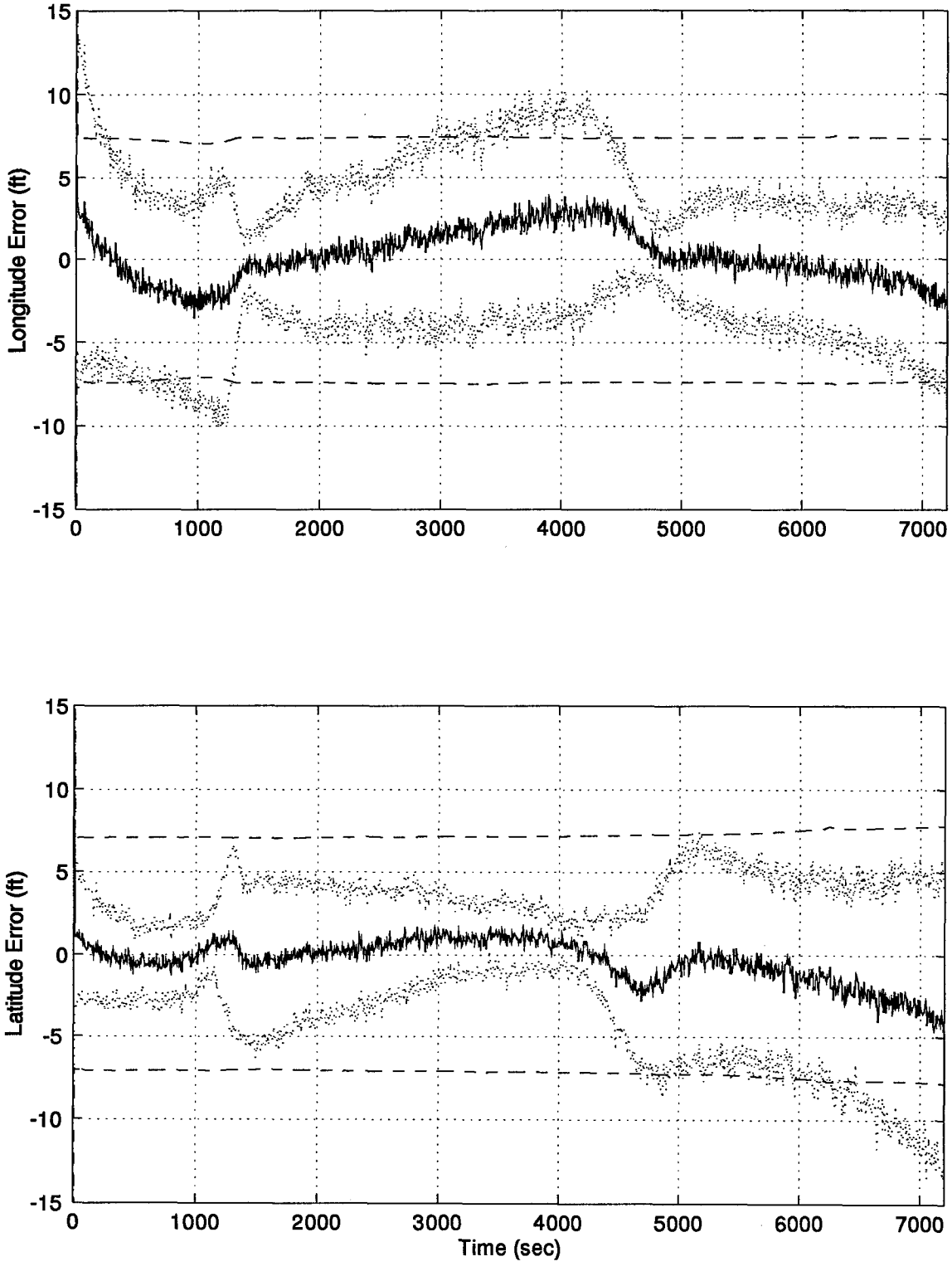

Figure F.1 Longitude and Latitude Error Plots

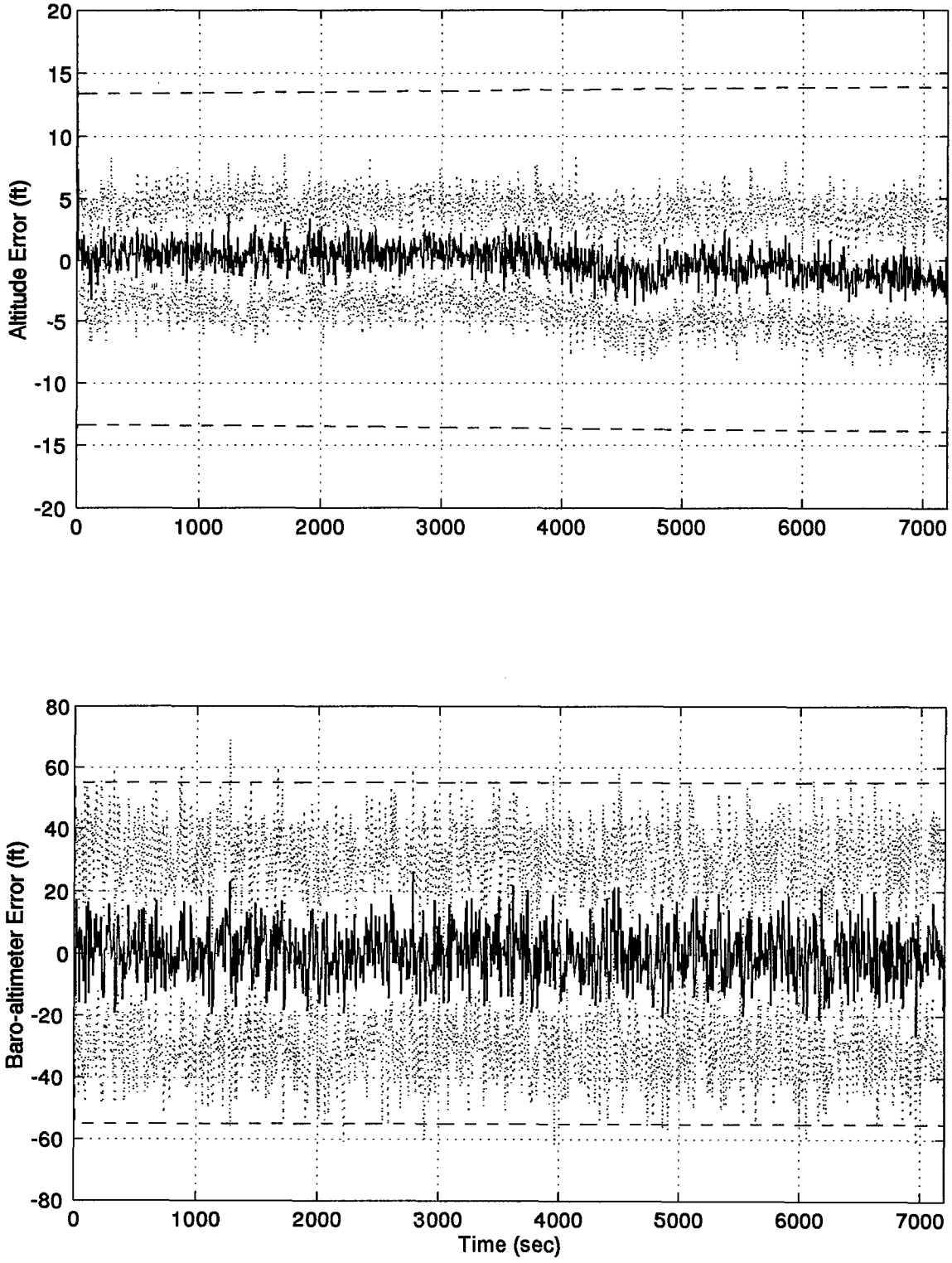

Figure F.2 Altitude and Barometric Altimeter Error Plots

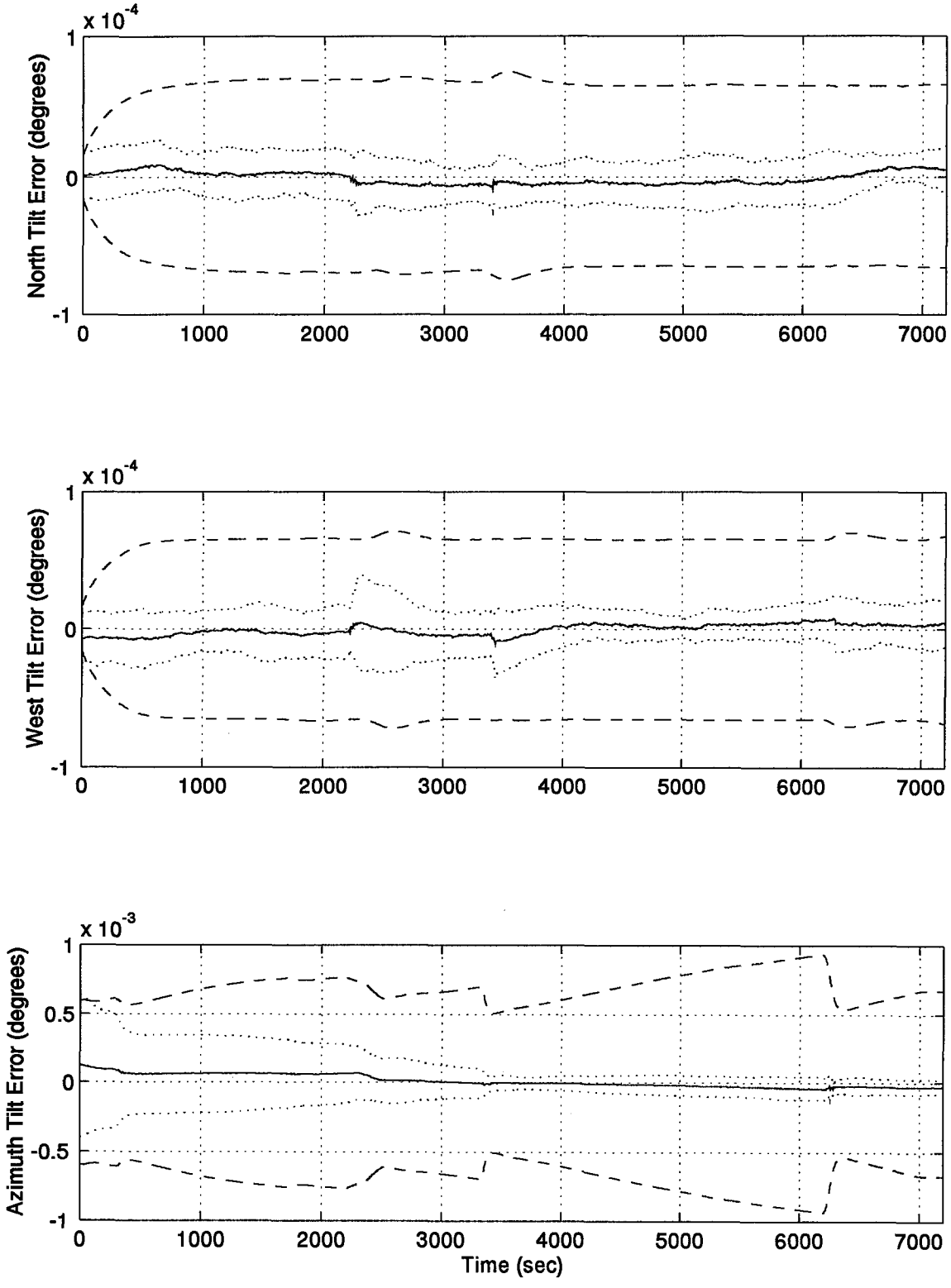

Figure F.3 North, West, and Azimuth Tilt Error Plots

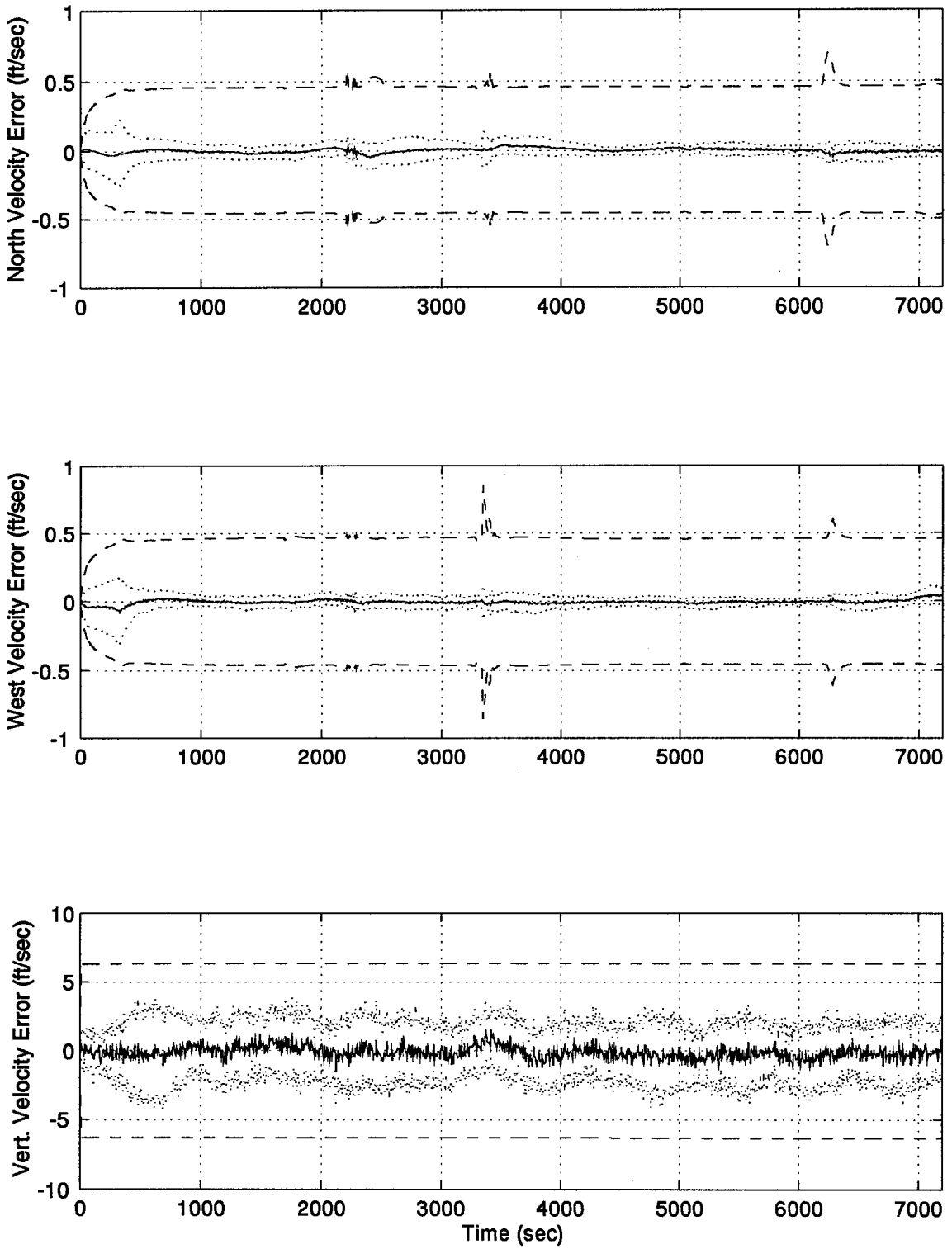

Figure F.4 North, West, and Vertical Velocity Error Plots

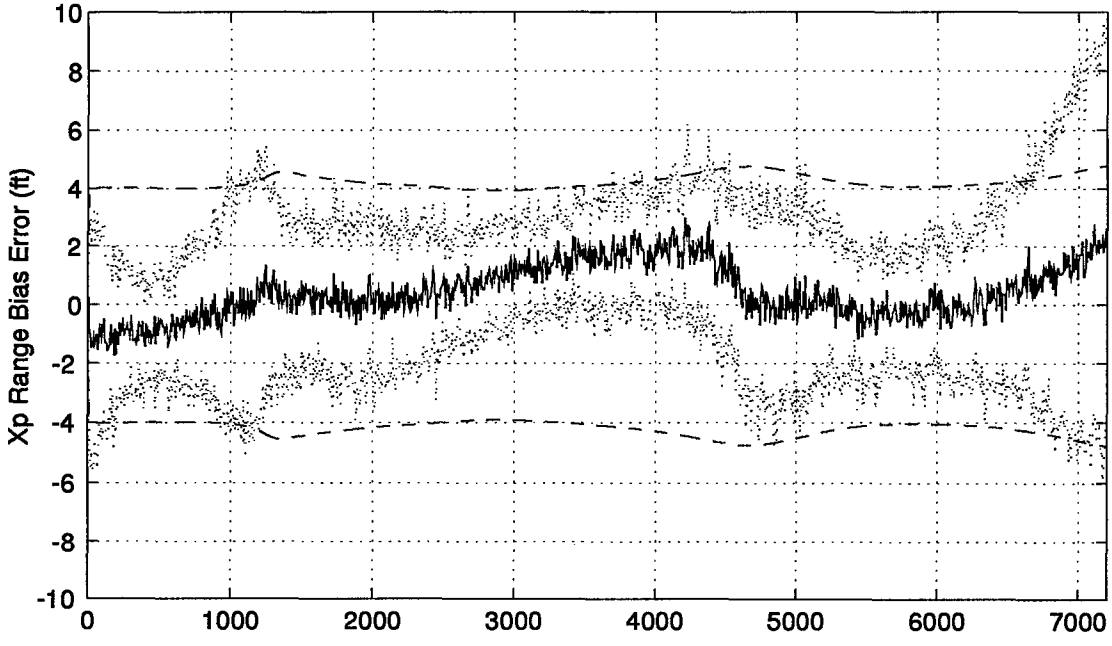

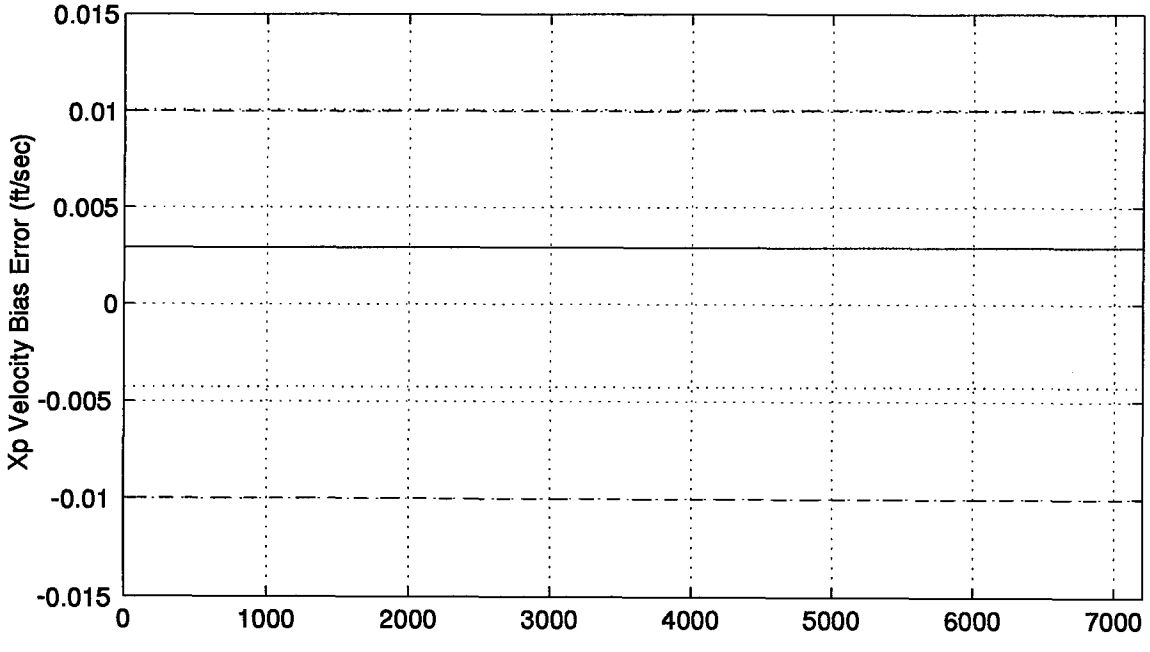

Figure F.5 RRS Range Bias and Range Velocity Error Plots

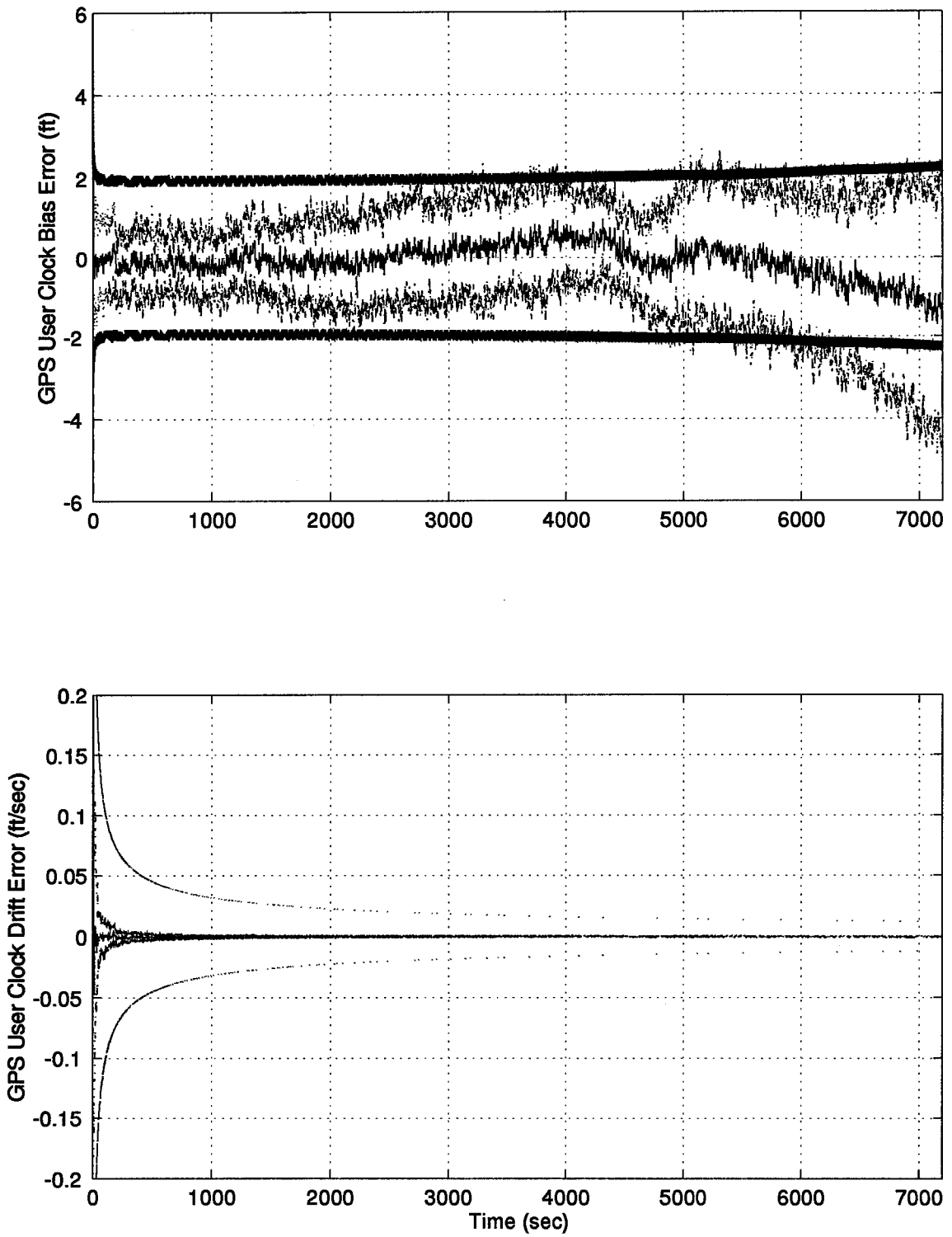

Figure F.6 GPS Clock Bias and Drift Error Plots

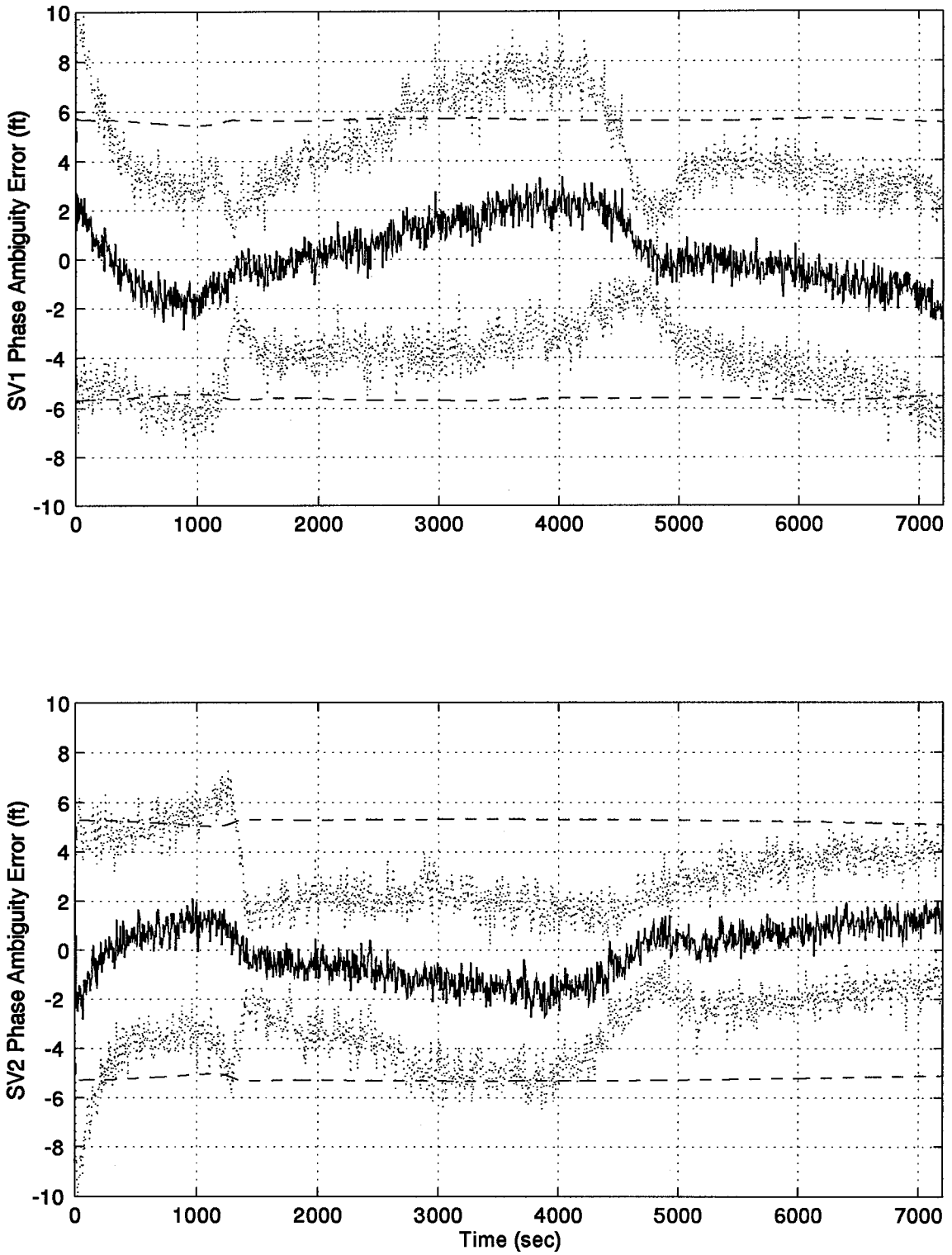

Figure F.7 GPS Satellites 1 and 2 Phase Ambiguity Error Plots

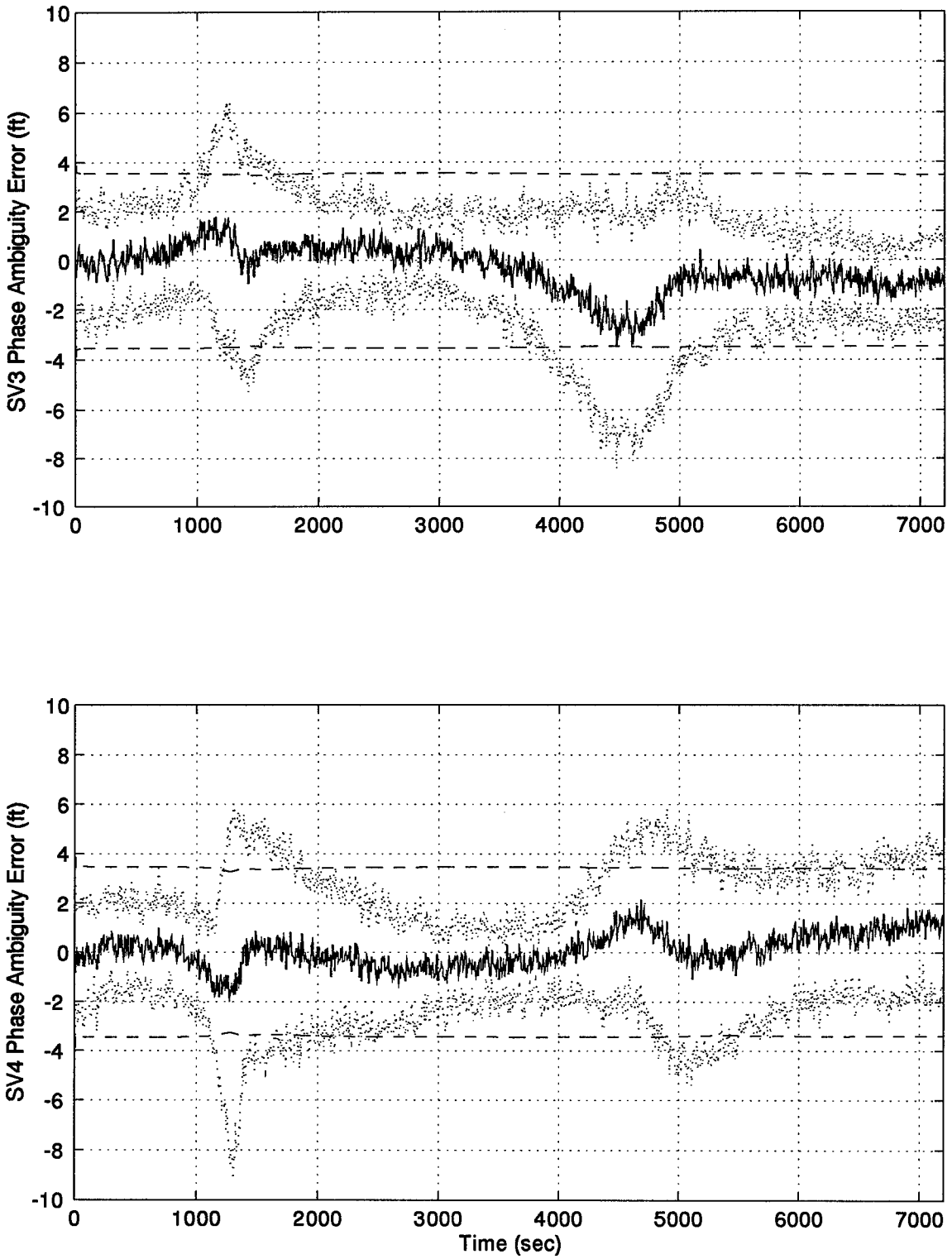

Figure F.8 GPS Satellites 3 and 4 Phase Ambiguity Error Plots

Appendix G. The Double Difference PNRS Filter Results

This appendix contains the results from the two-hour simulation run of the Double Difference PNRS filter. The plots are in the same order as Appendix D minus the GPS clock error plots which are not modeled in this filter. The ordering of this appendix is for direct comparison to previous results.

A legend for the presented figures is given below.

Table G.1 Legend for Filter Tuning Plots

Symbol	Definition
— Solid Line	Mean Error
··· Dotted Line	Mean Error ± True Sigma
– – Dashed Line	± Filter Predicted Sigma

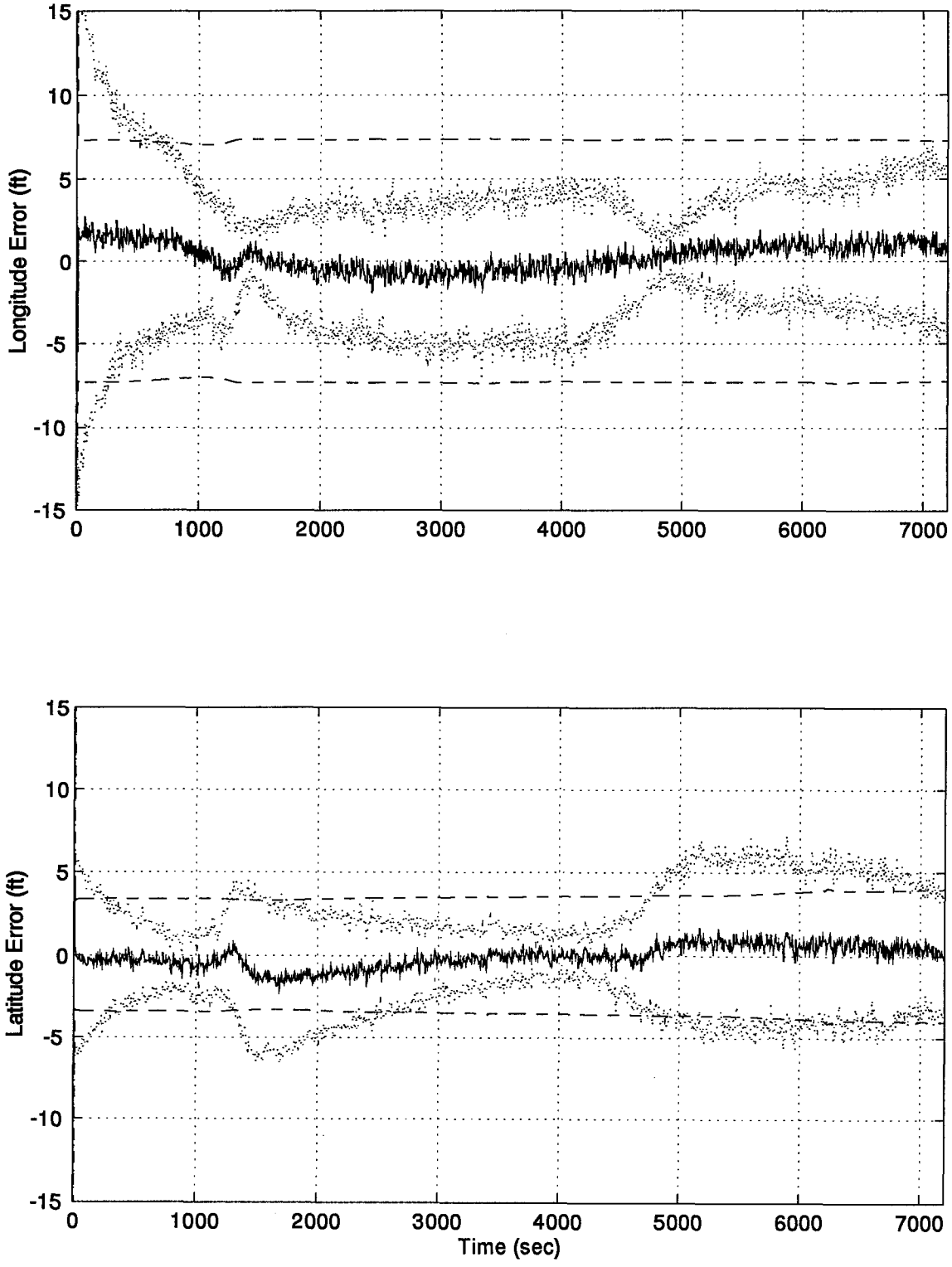

Figure G.1 Longitude and Latitude Error Plots

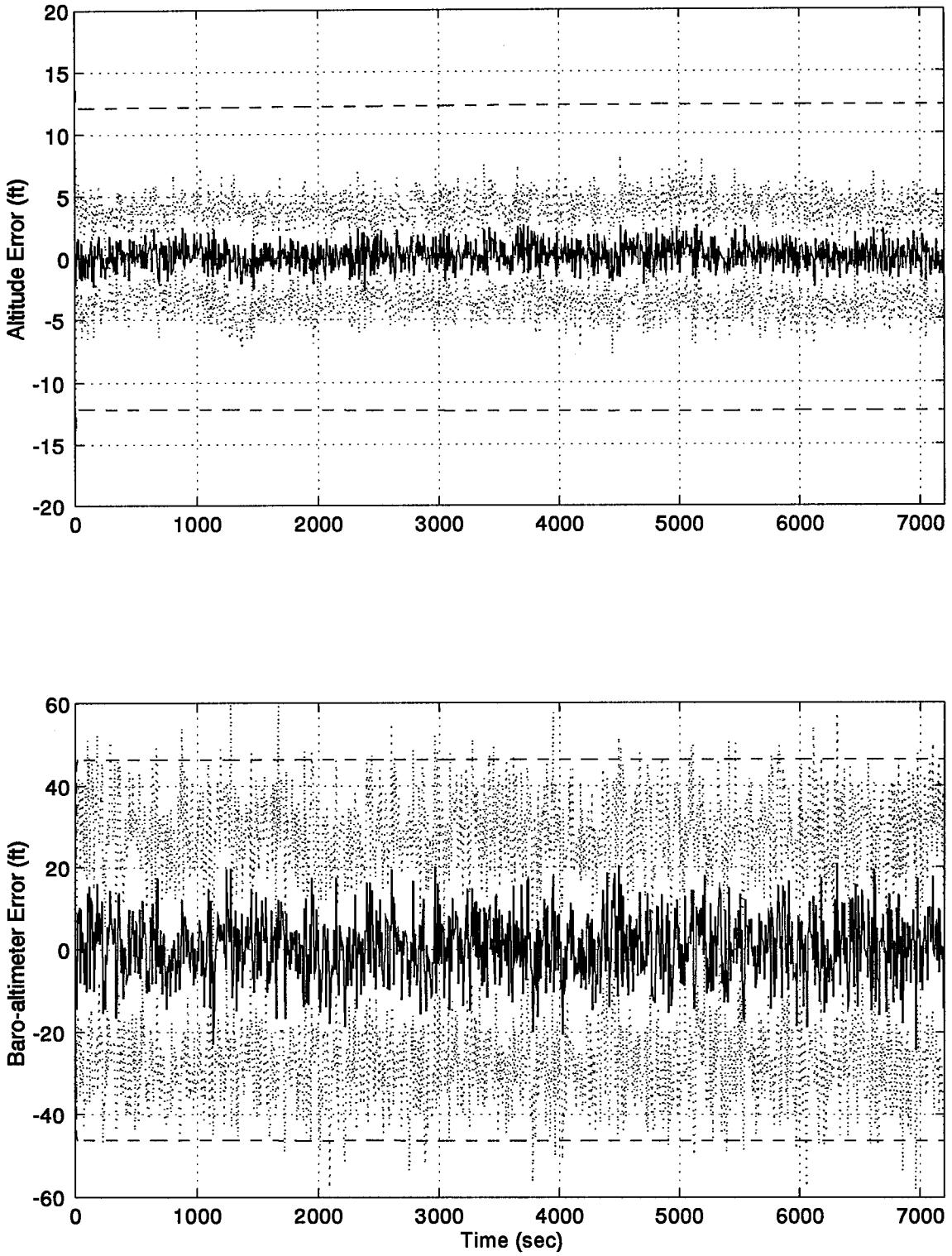

Figure G.2 Altitude and Barometric Altimeter Error Plots

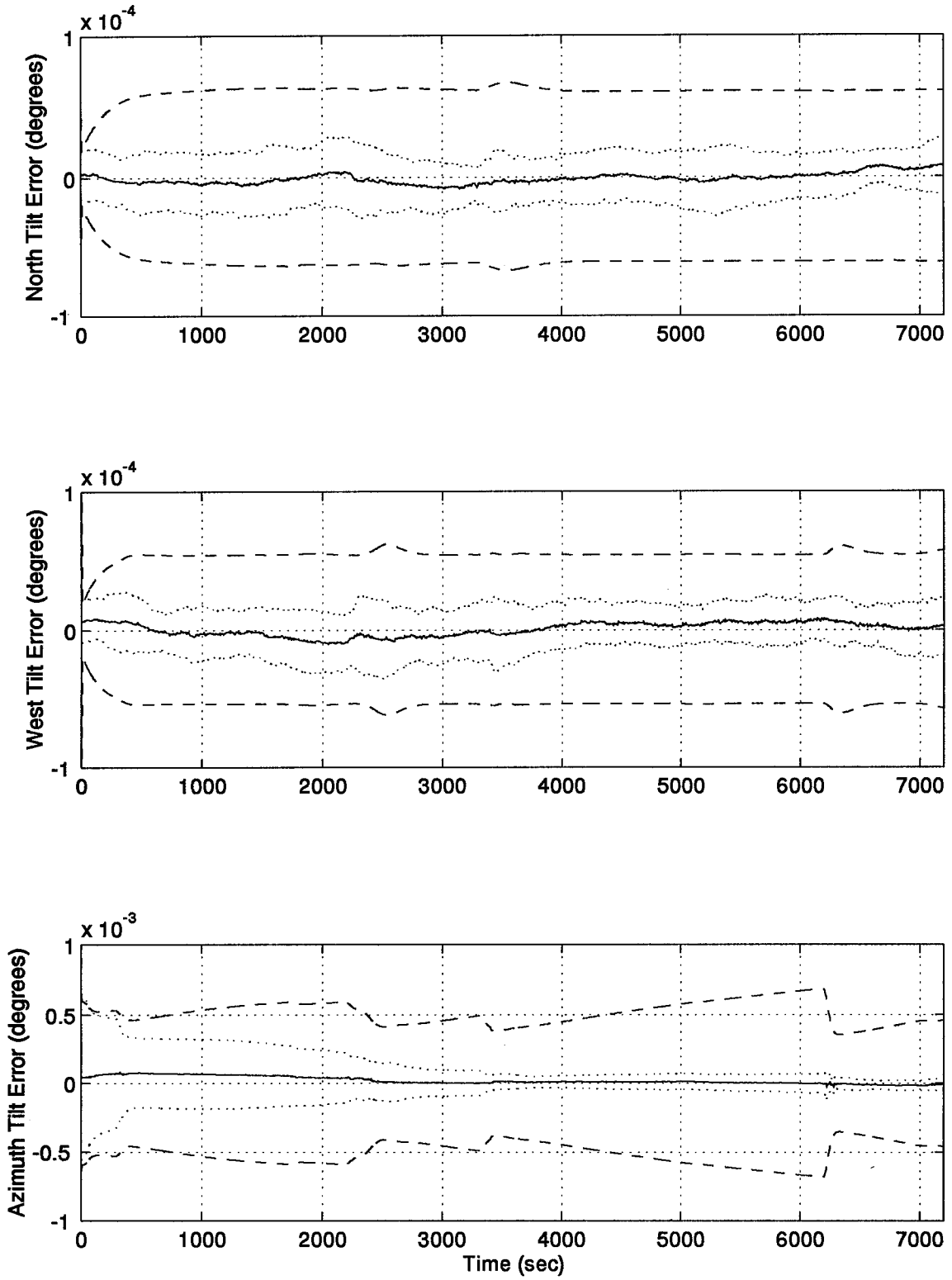

Figure G.3 North, West, and Azimuth Tilt Error Plots

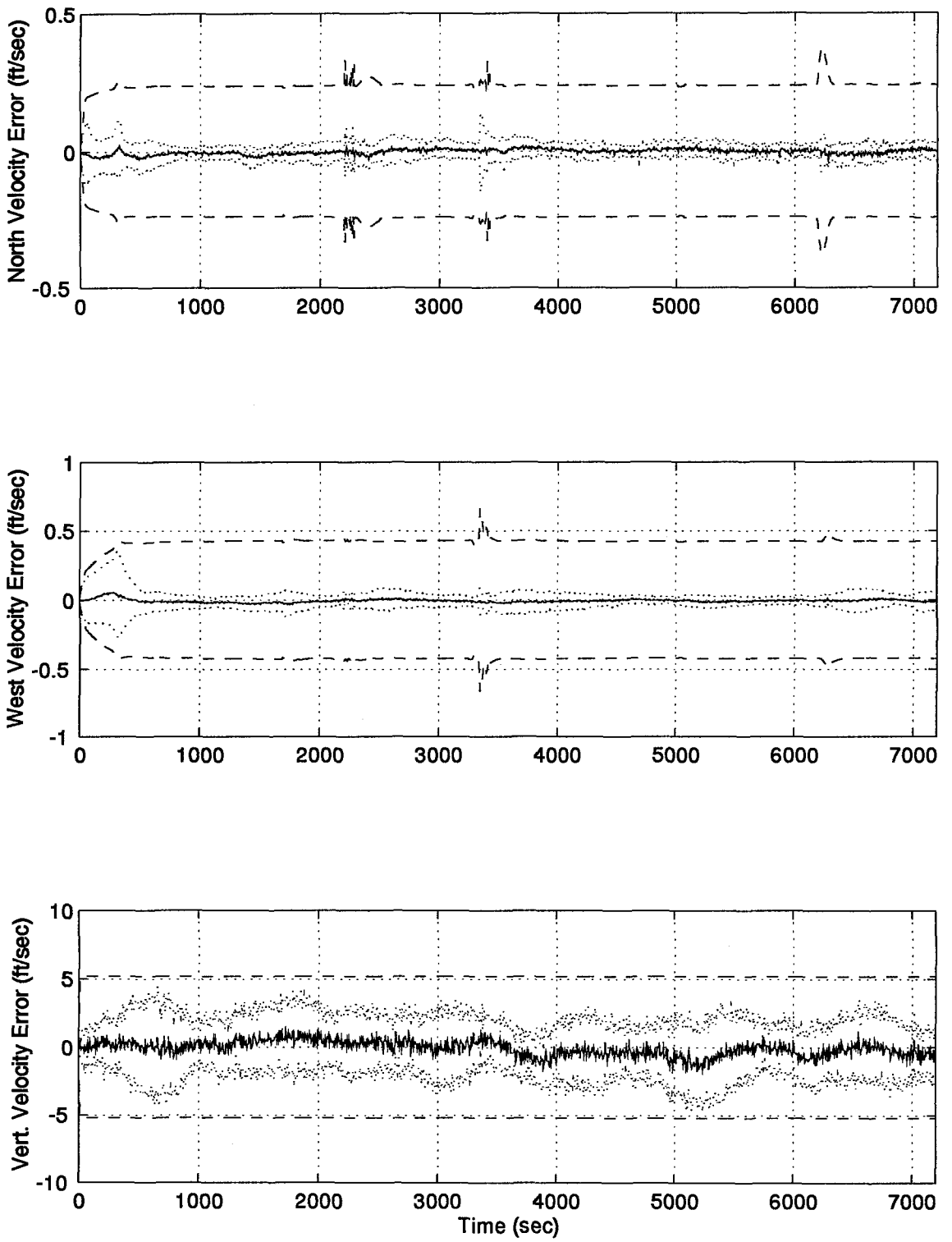

Figure G.4 North, West, and Vertical Velocity Error Plots

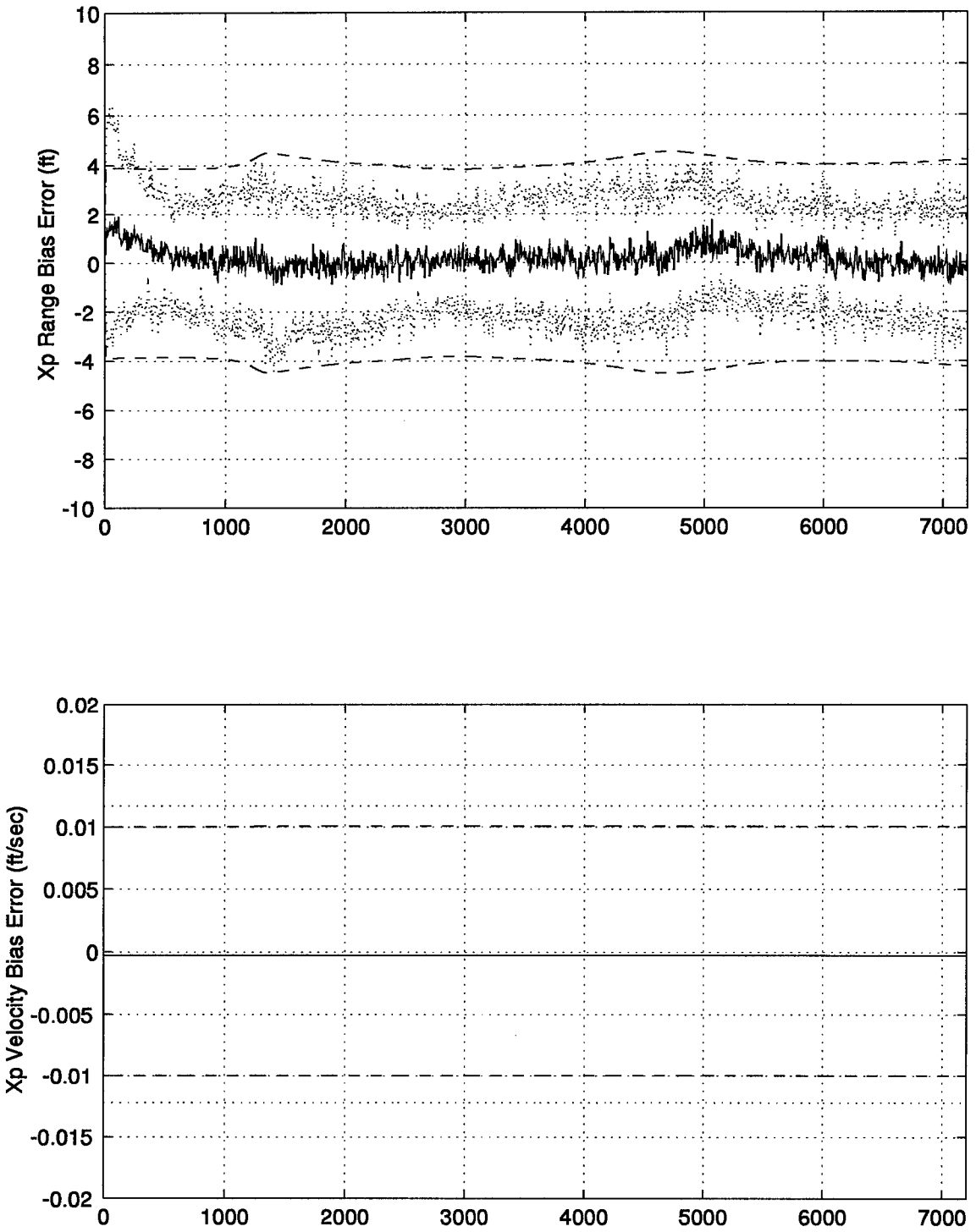

Figure G.5 RRS Range Bias and Range Velocity Error Plots

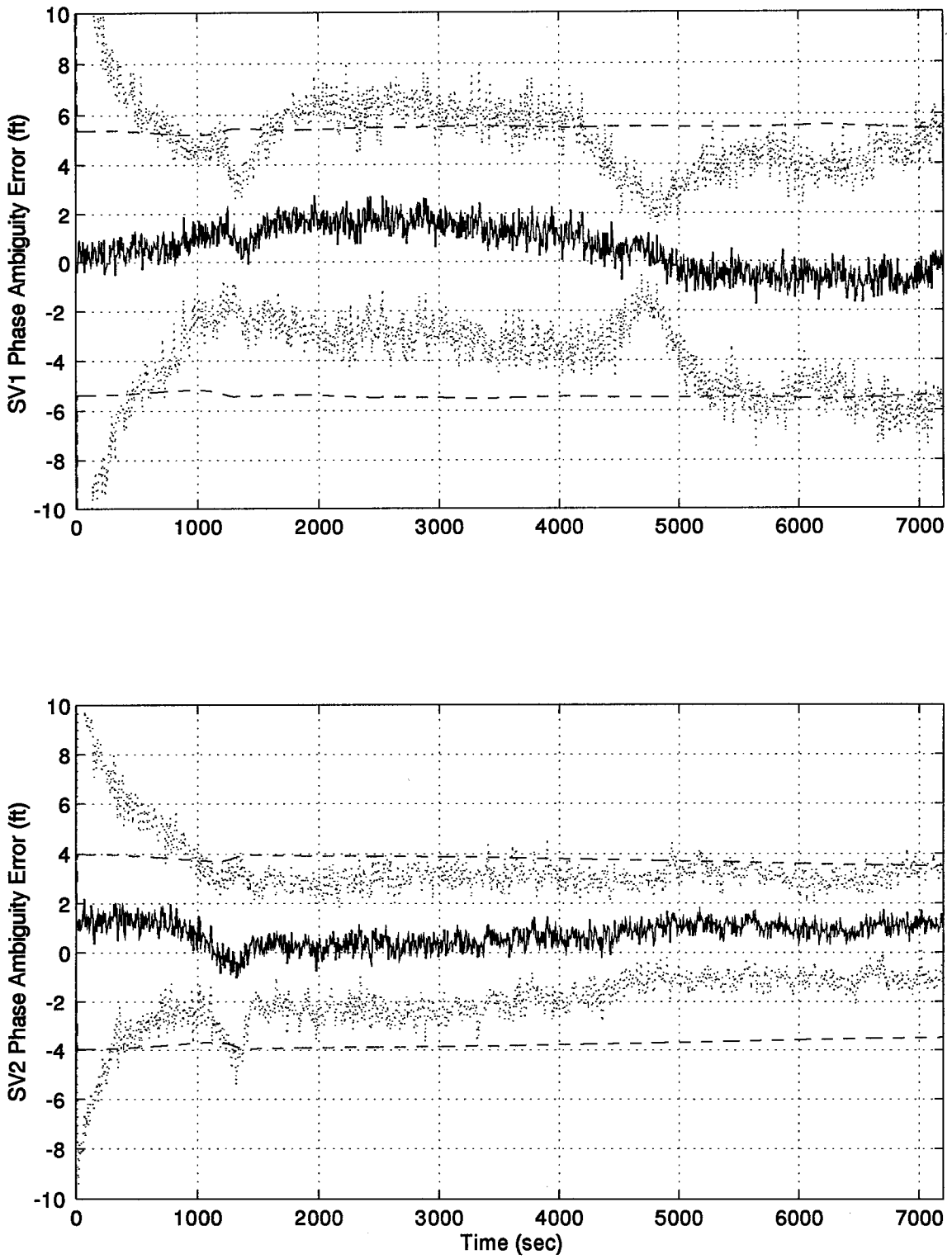

Figure G.6 GPS Satellites 1 and 2 Phase Ambiguity Error Plots

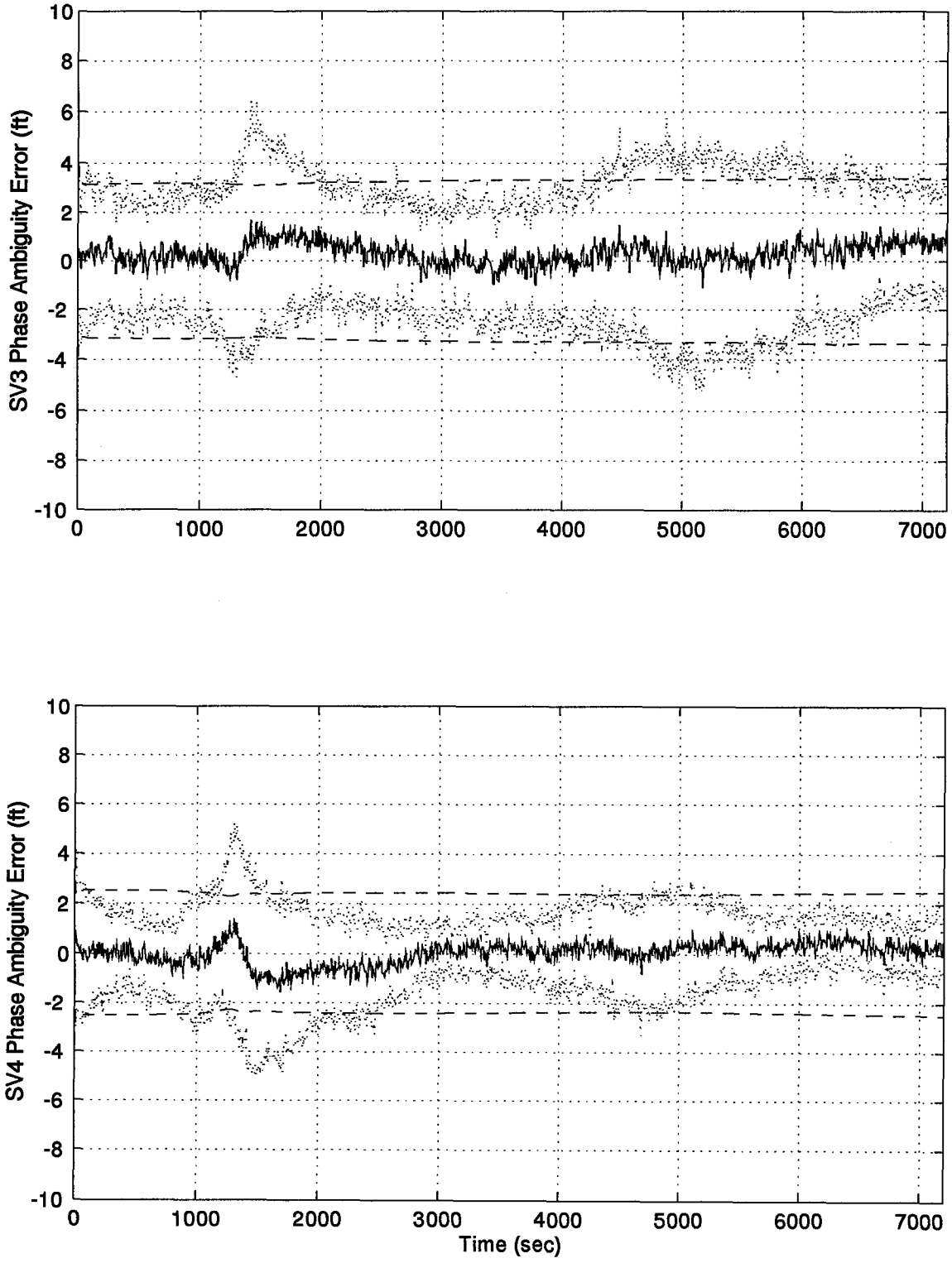

Figure G.7 GPS Satellites 3 and 4 Phase Ambiguity Error Plots

Appendix H. Double Difference PNRS Small Cycle Slip on Satellite #1 Results

This appendix contains the results of the 1000 second simulation run of the Double Difference PNRS filter with a small cycle slip on satellite #1. The plots are in the same order of Appendix G for direct comparison.

A legend for the presented figures is given below.

Table H.1 Legend for Filter Tuning Plots

Symbol	Definition
—- Solid Line	Mean Error
$\cdots$ Dotted Line	Mean Error $\pm$ True Sigma
$- -$ Dashed Line	$\pm$ Filter Predicted Sigma

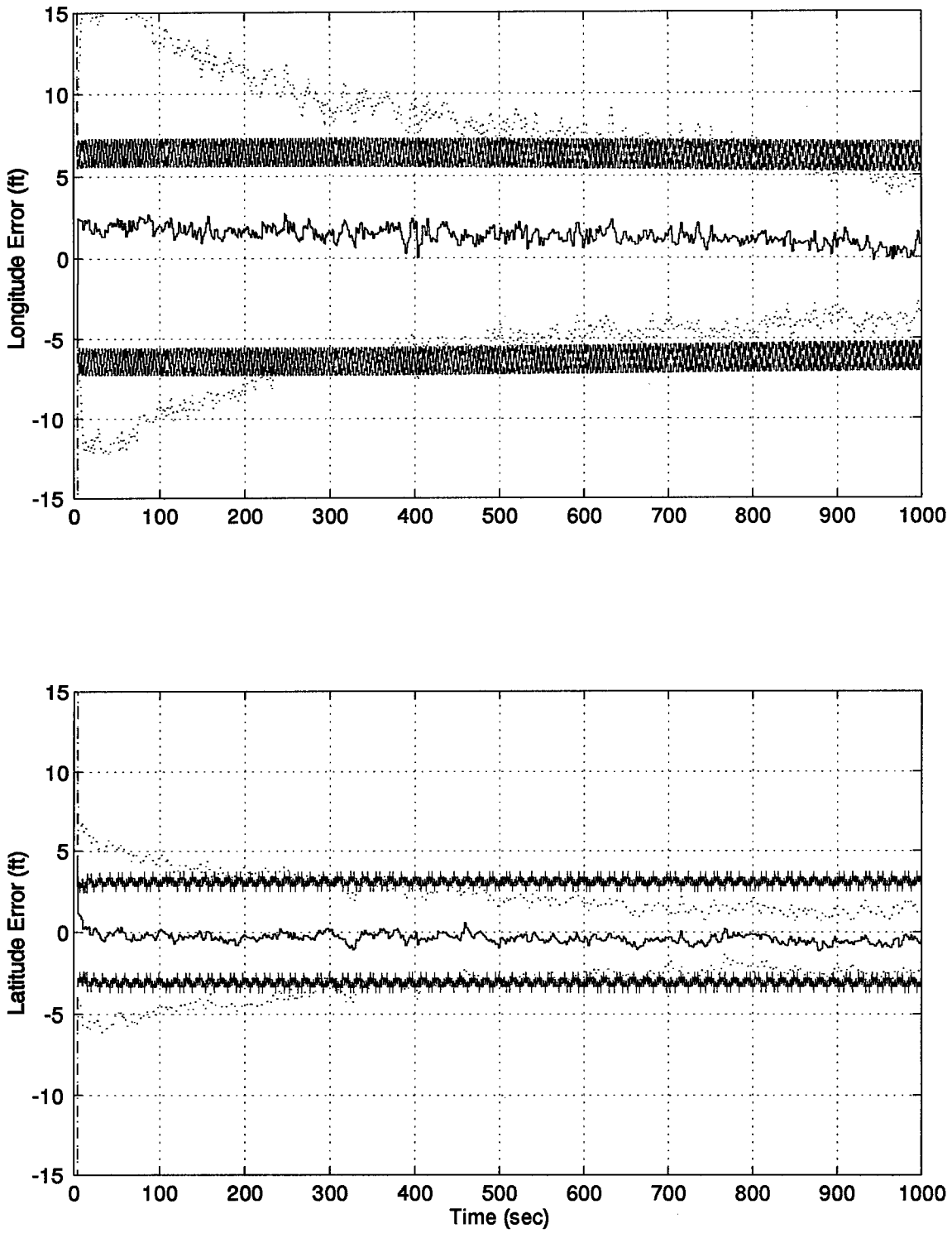

Figure H.1 Longitude and Latitude Error Plots

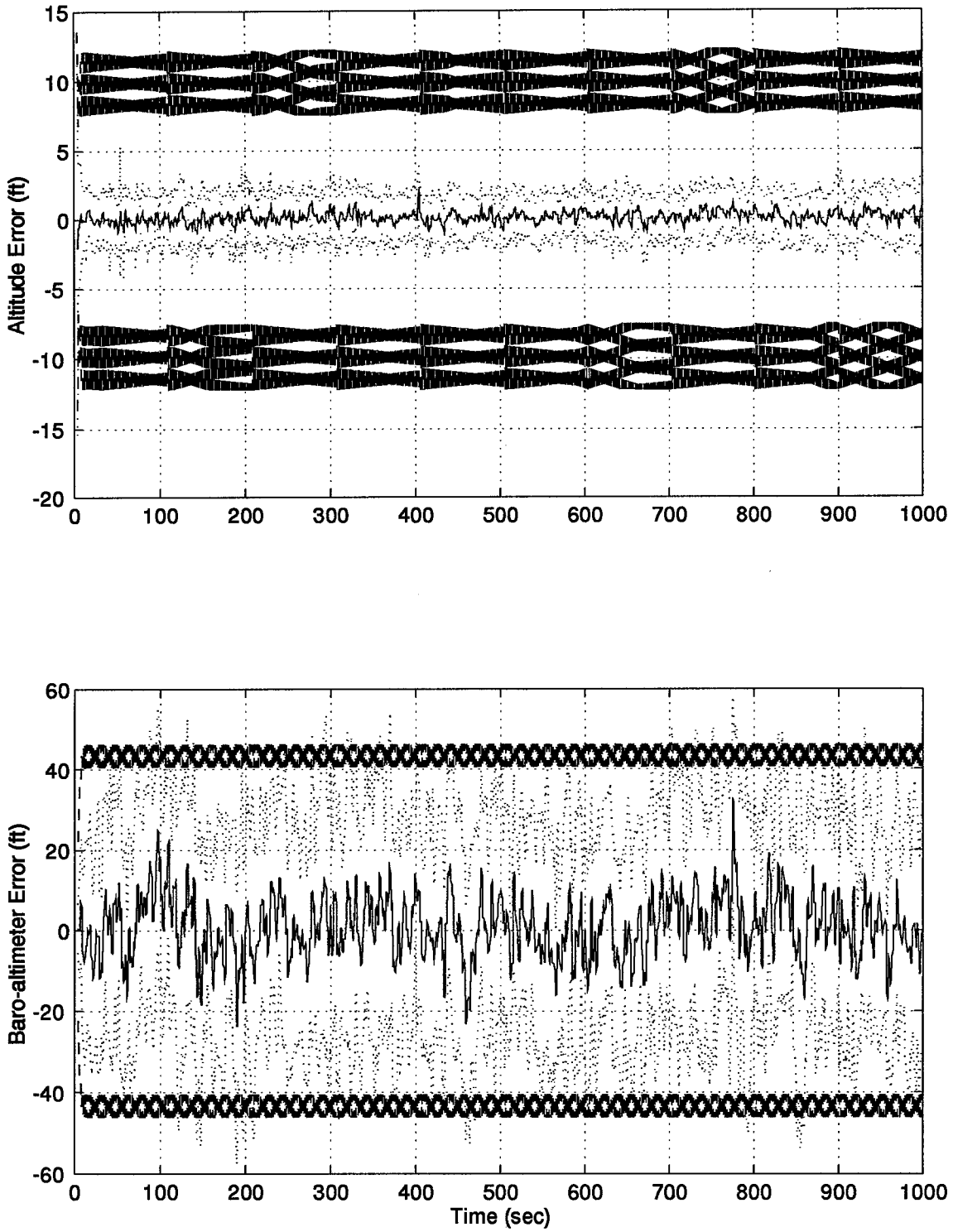

Figure H.2 Altitude and Barometric Altimeter Error Plots

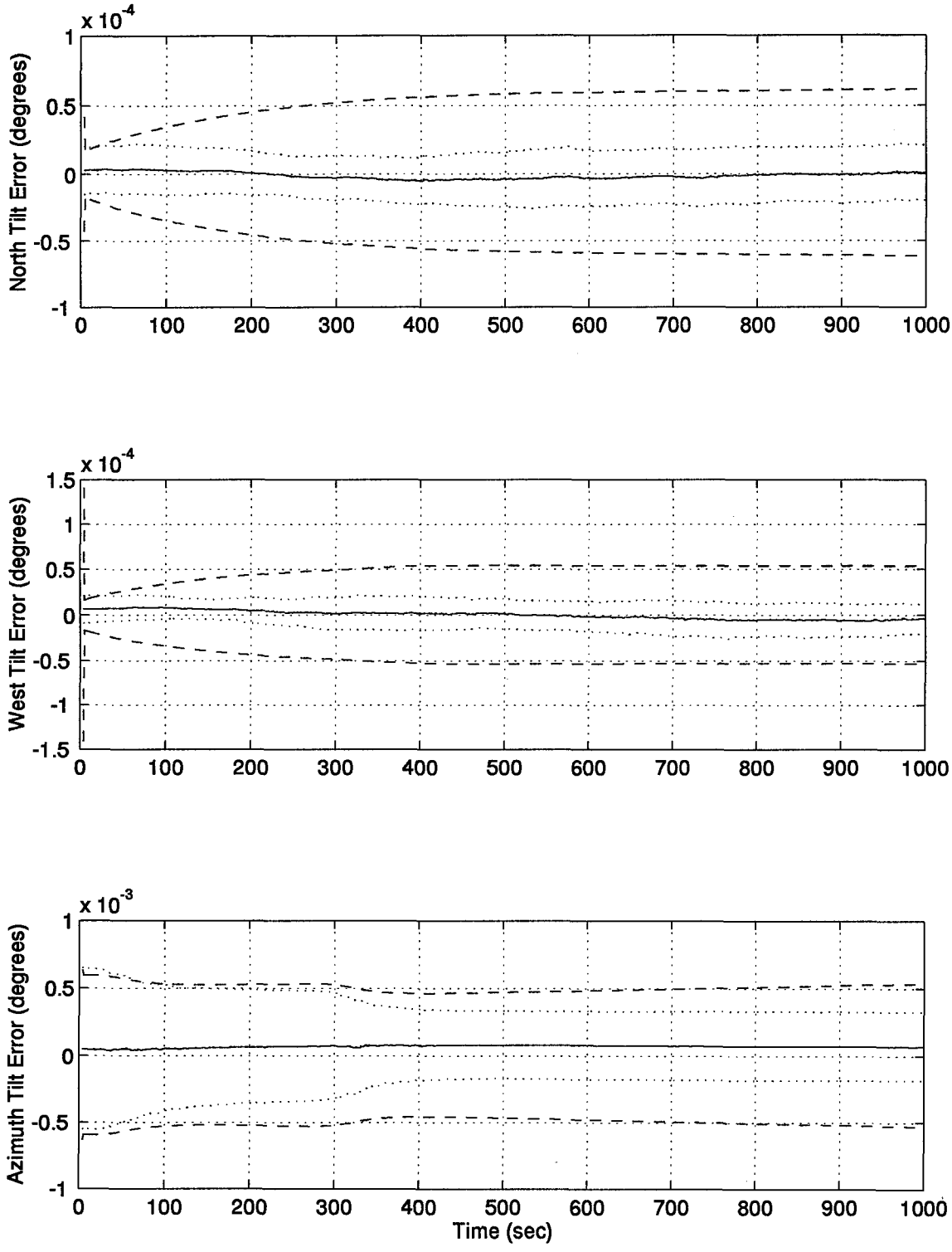

Figure H.3 North, West, and Azimuth Tilt Error Plots

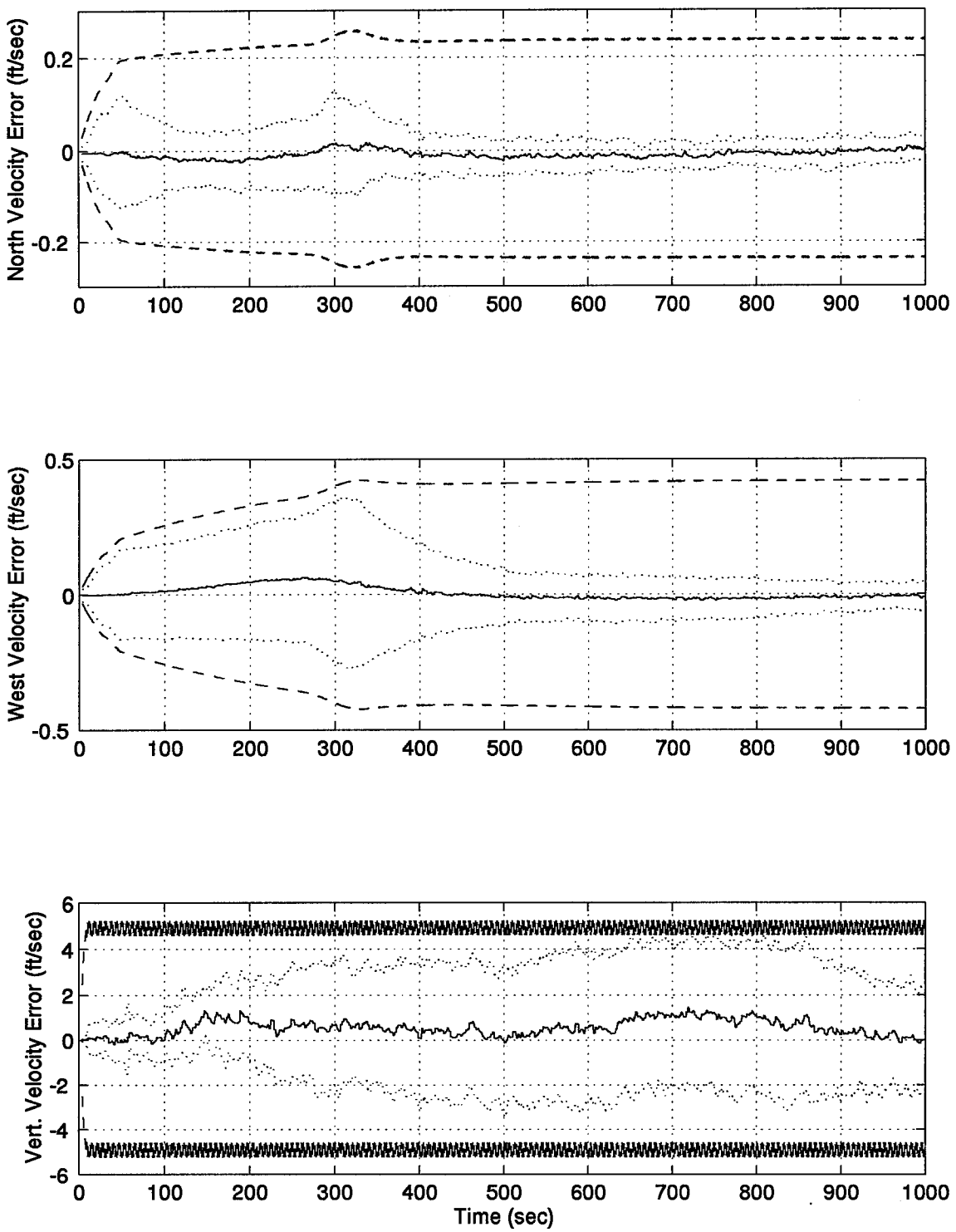

Figure H.4 North, West, and Vertical Velocity Error Plots

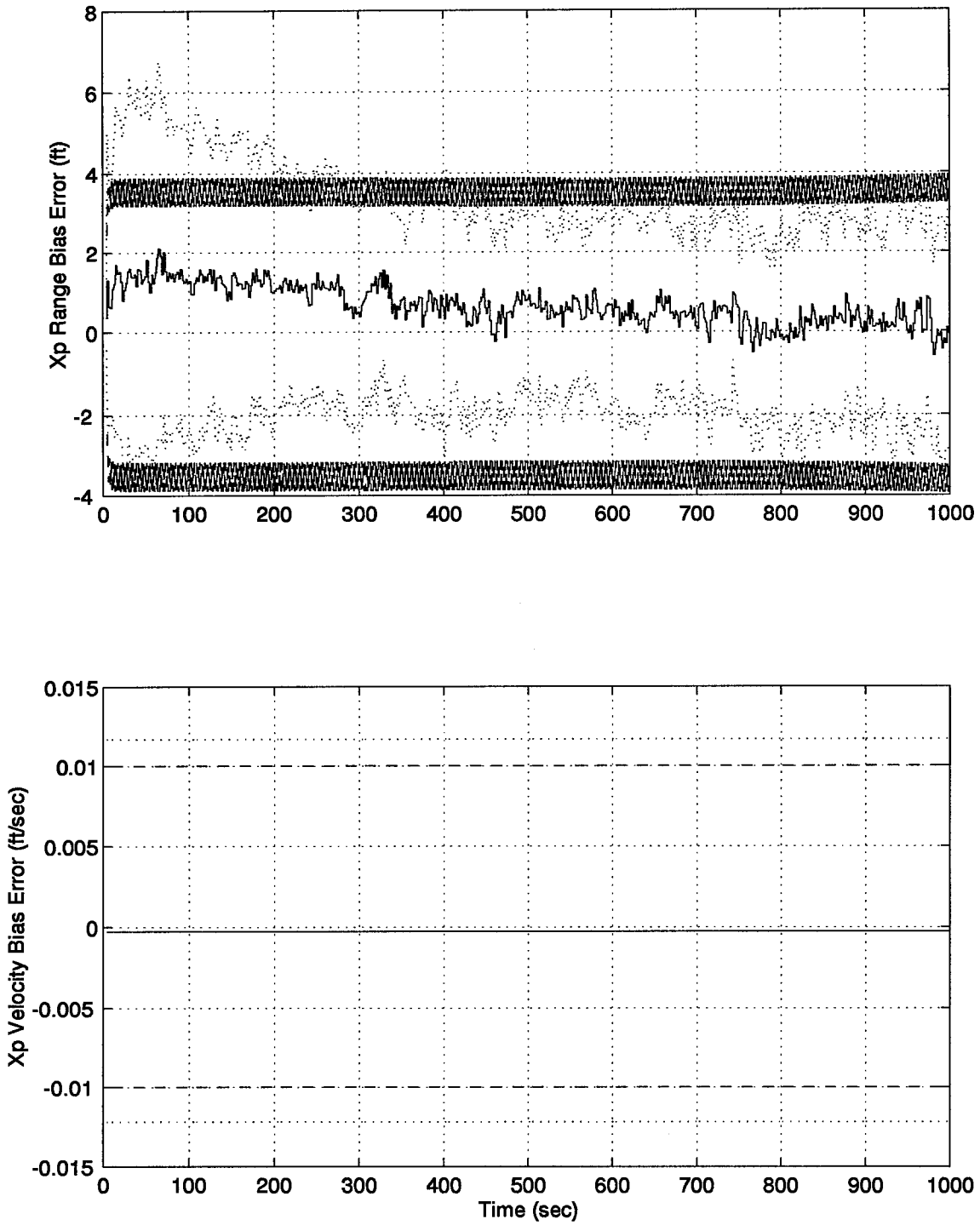

Figure H.5 RRS Range Bias, Range Velocity, and Atmospheric Propagation Delay Error Plots

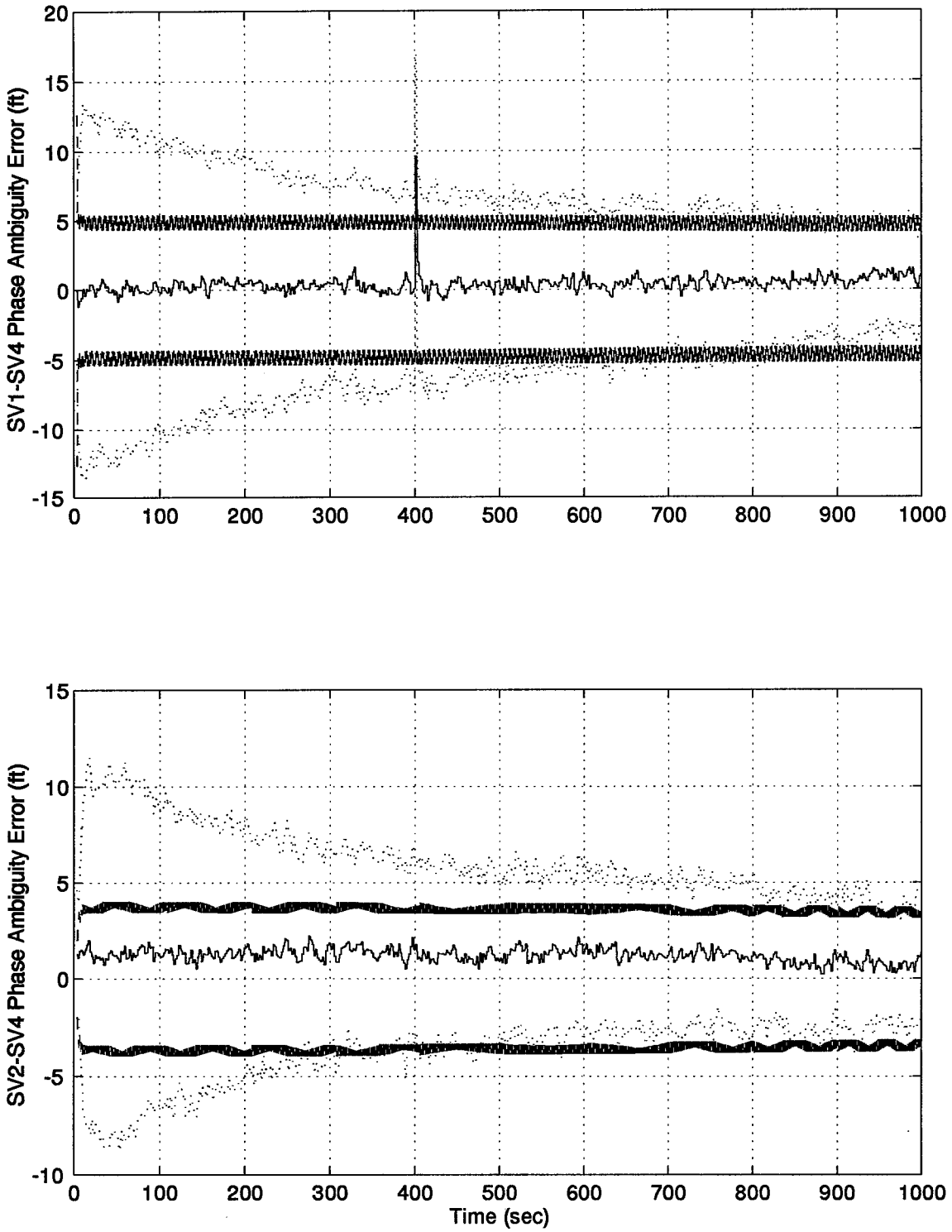

Figure H.6 GPS Satellites 1 and 2 Phase Ambiguity Error Plots

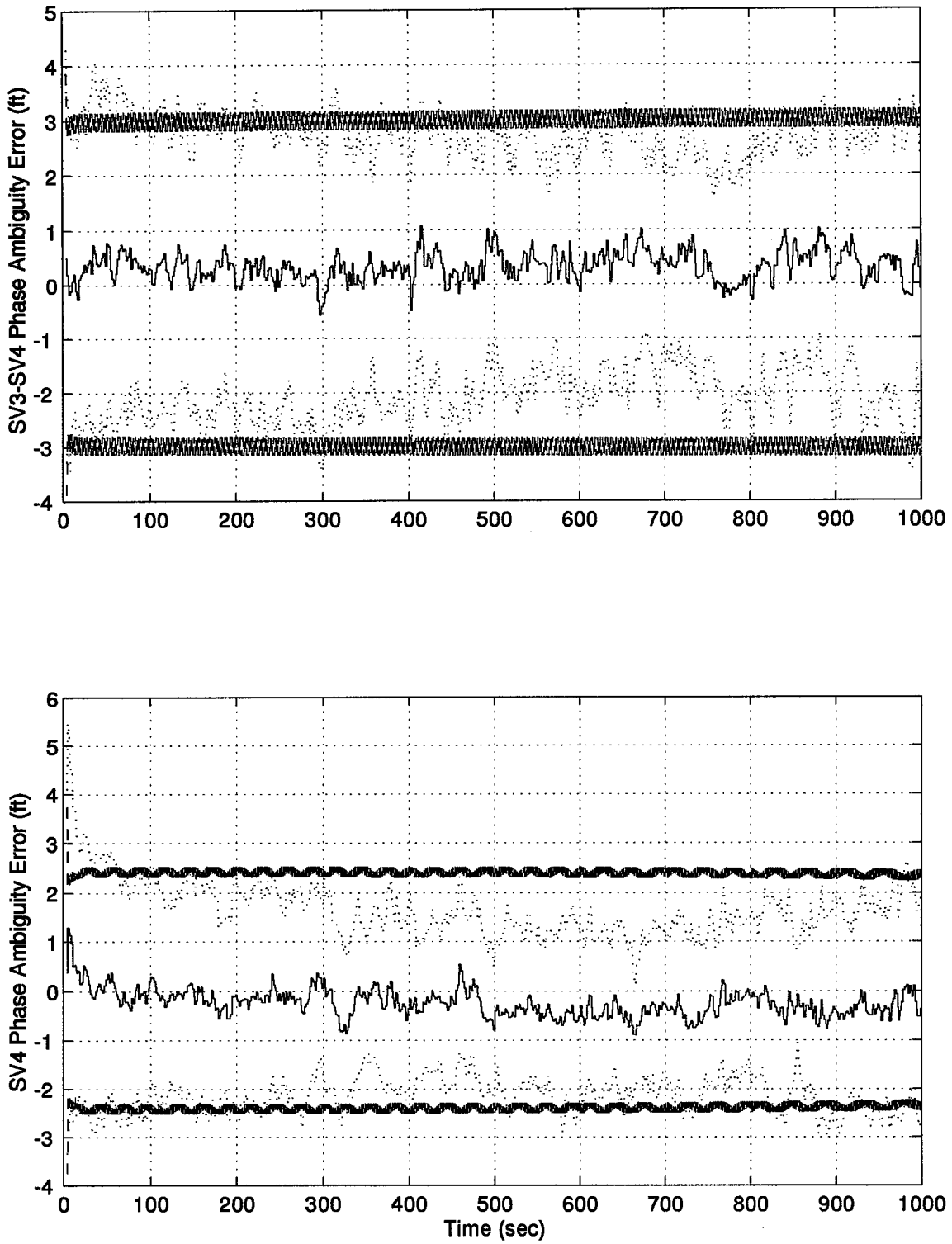

Figure H.7 GPS Satellites 3 and 4 Phase Ambiguity Error Plots

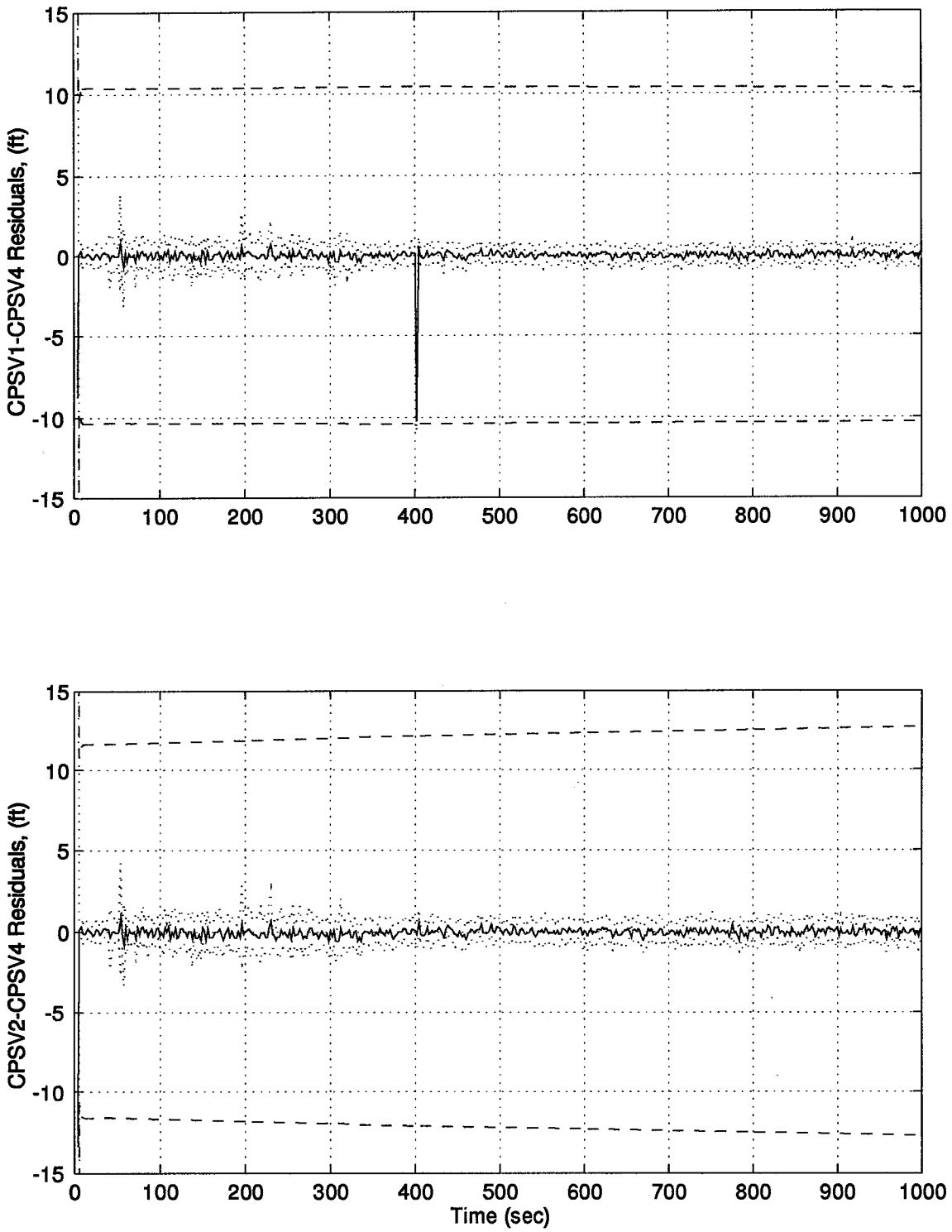

Figure H.8 GPS Satellites 1 and 2 Residual Plots

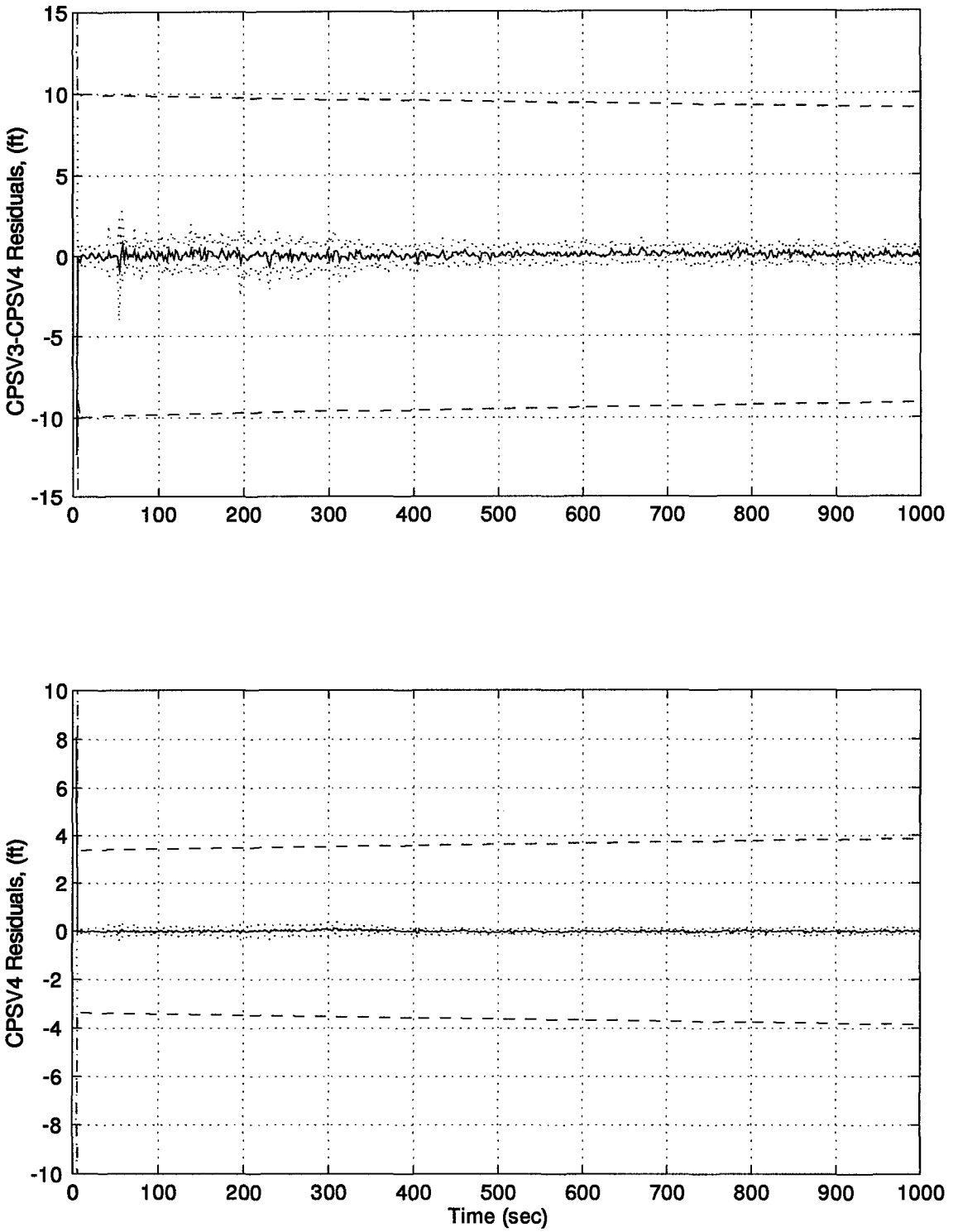

Figure H.9 GPS Satellites 3 and 4 Residual Plots

Appendix I. Double Difference PNRS Satellite #1 Loss Results

This appendix contains the results of the 1000 second simulation run of the Double Difference PNRS filter with a GPS satellite loss on satellite #1. The plots are in the same order of Appendix G for direct comparison.

A legend for the presented figures is given below.

Table I.1 Legend for Filter Tuning Plots

Symbol	Definition
— Solid Line	Mean Error
··· Dotted Line	Mean Error ± True Sigma
– – Dashed Line	± Filter Predicted Sigma

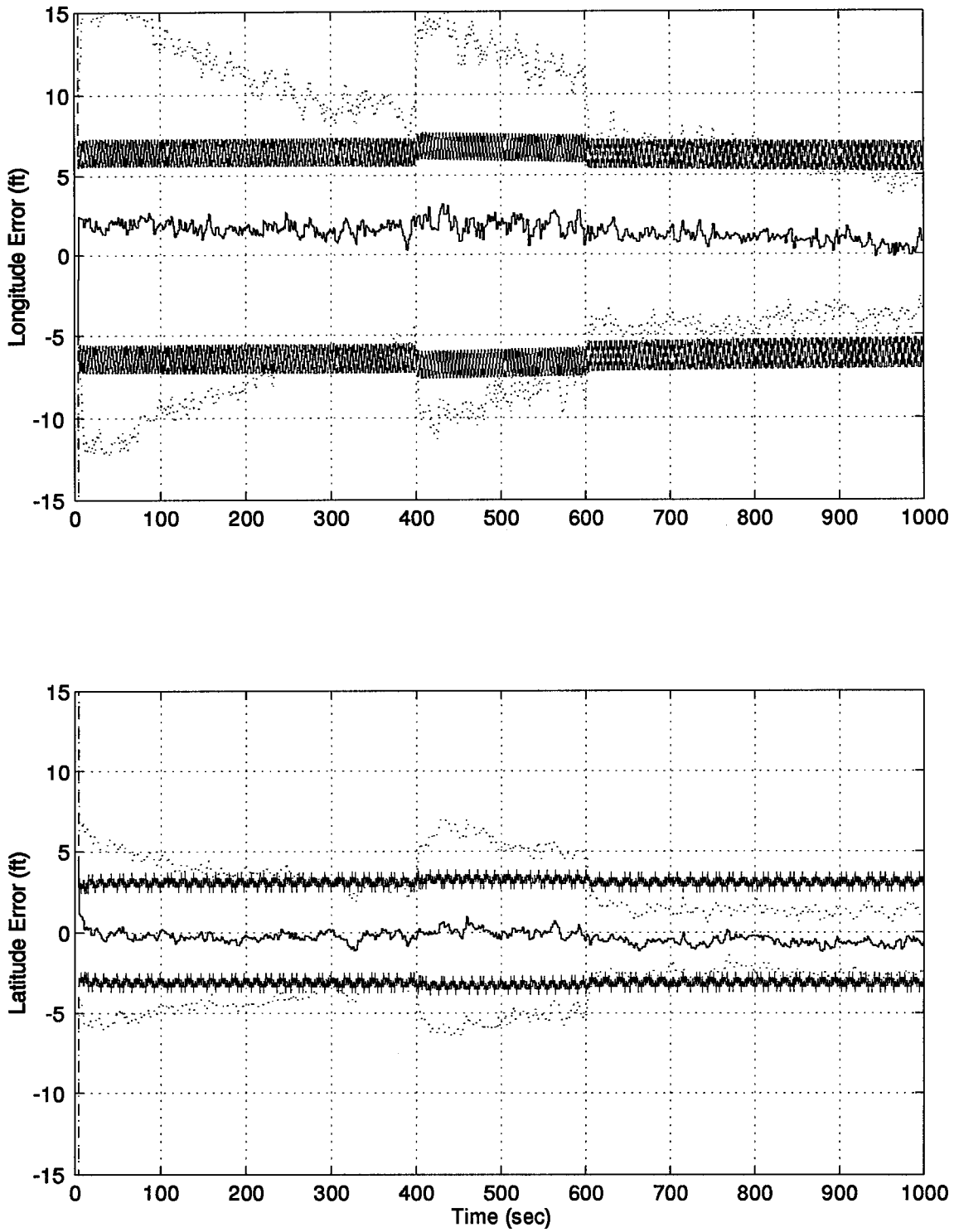

Figure I.1 Longitude and Latitude Error Plots

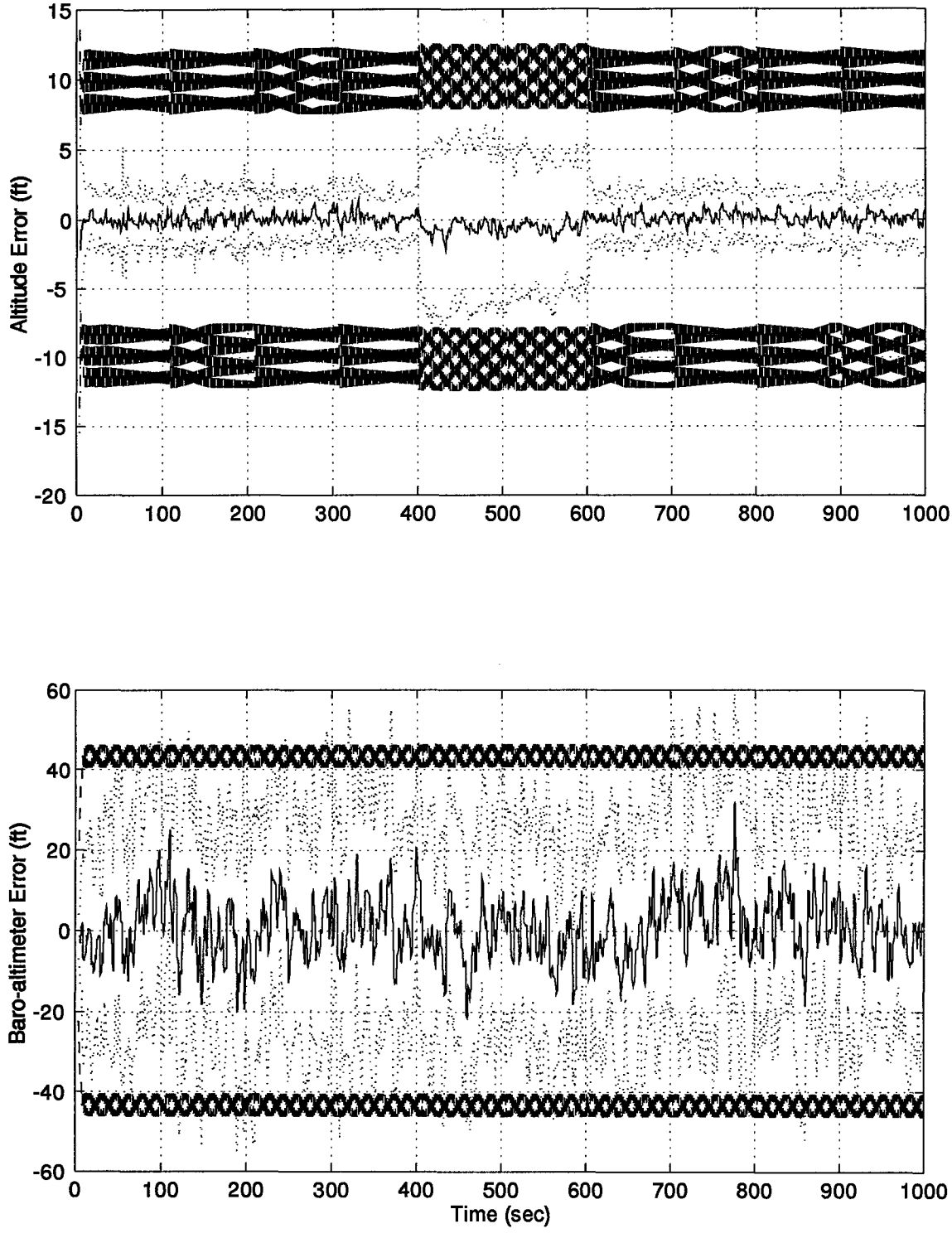

Figure I.2 Altitude and Barometric Altimeter Error Plots

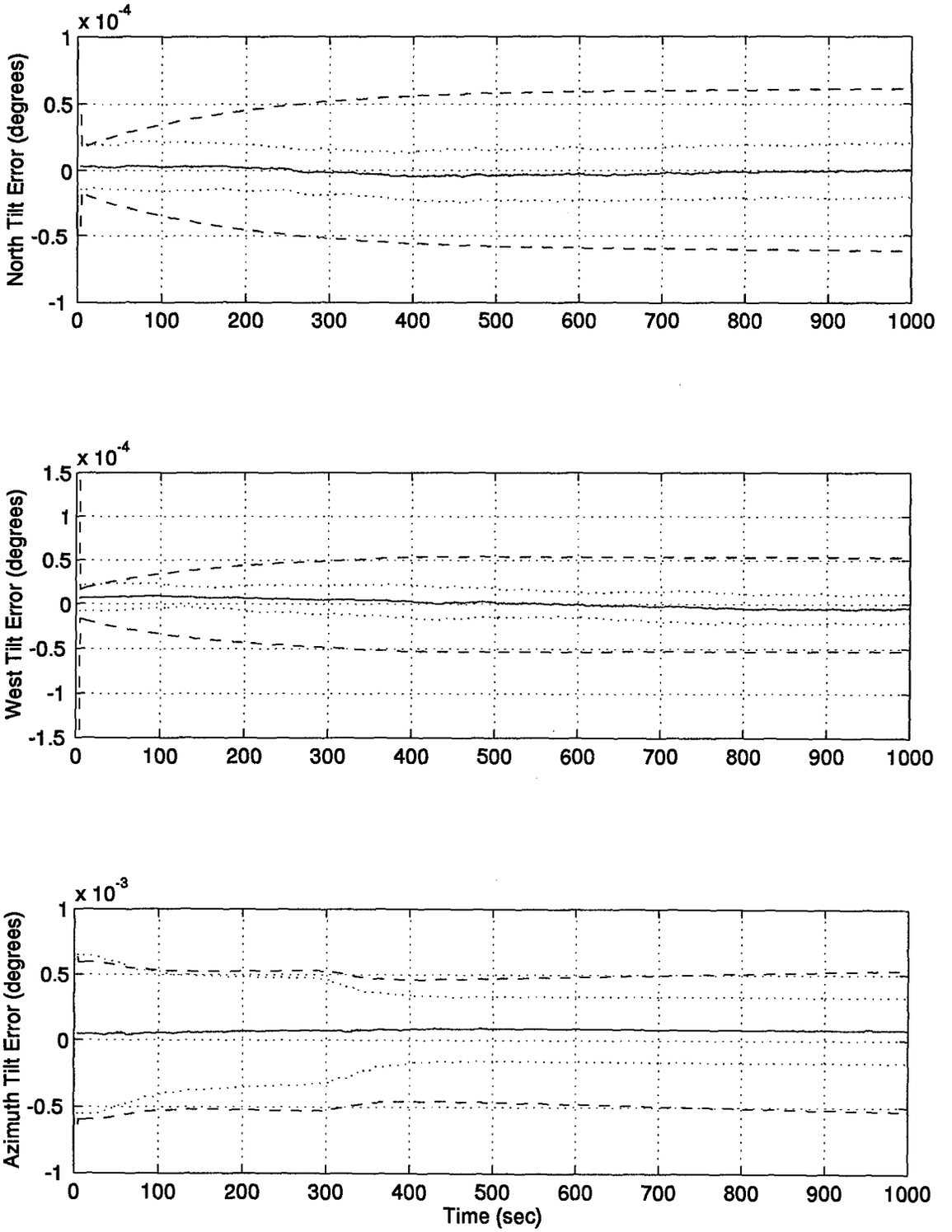

Figure I.3 North, West, and Azimuth Tilt Error Plots

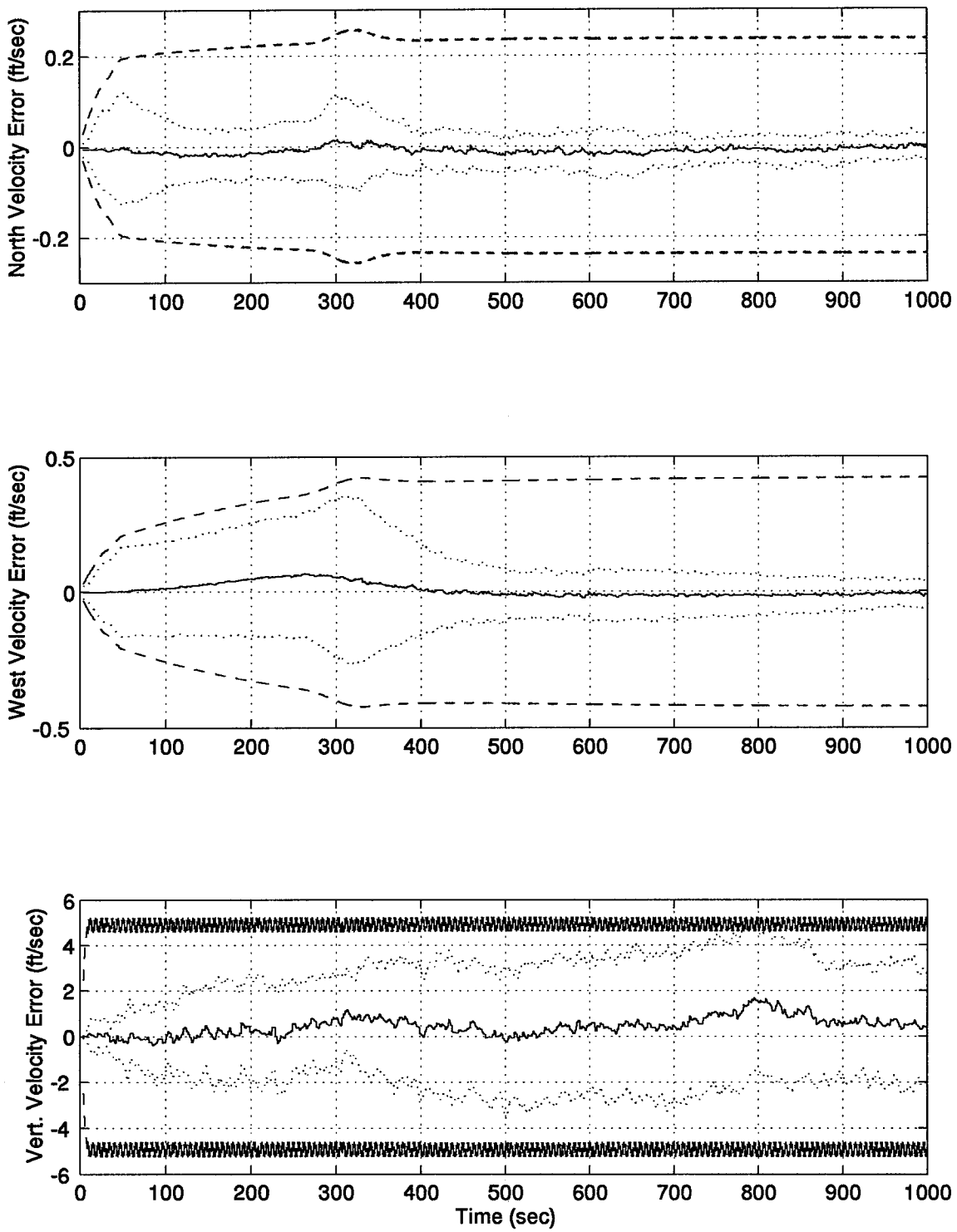

Figure I.4 North, West, and Vertical Velocity Error Plots

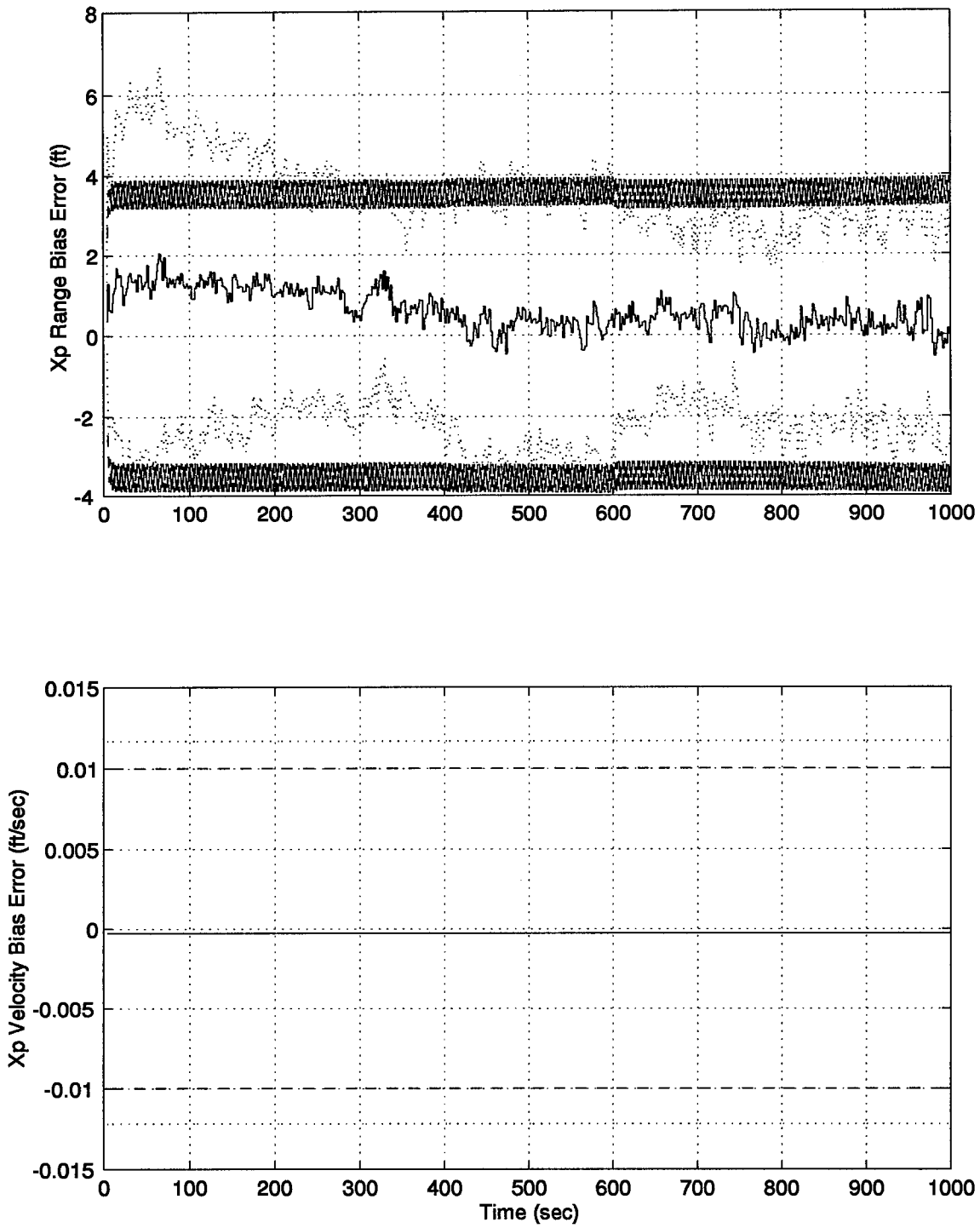

Figure I.5 RRS Range Bias, Range Velocity, and Atmospheric Propagation Delay Error Plots

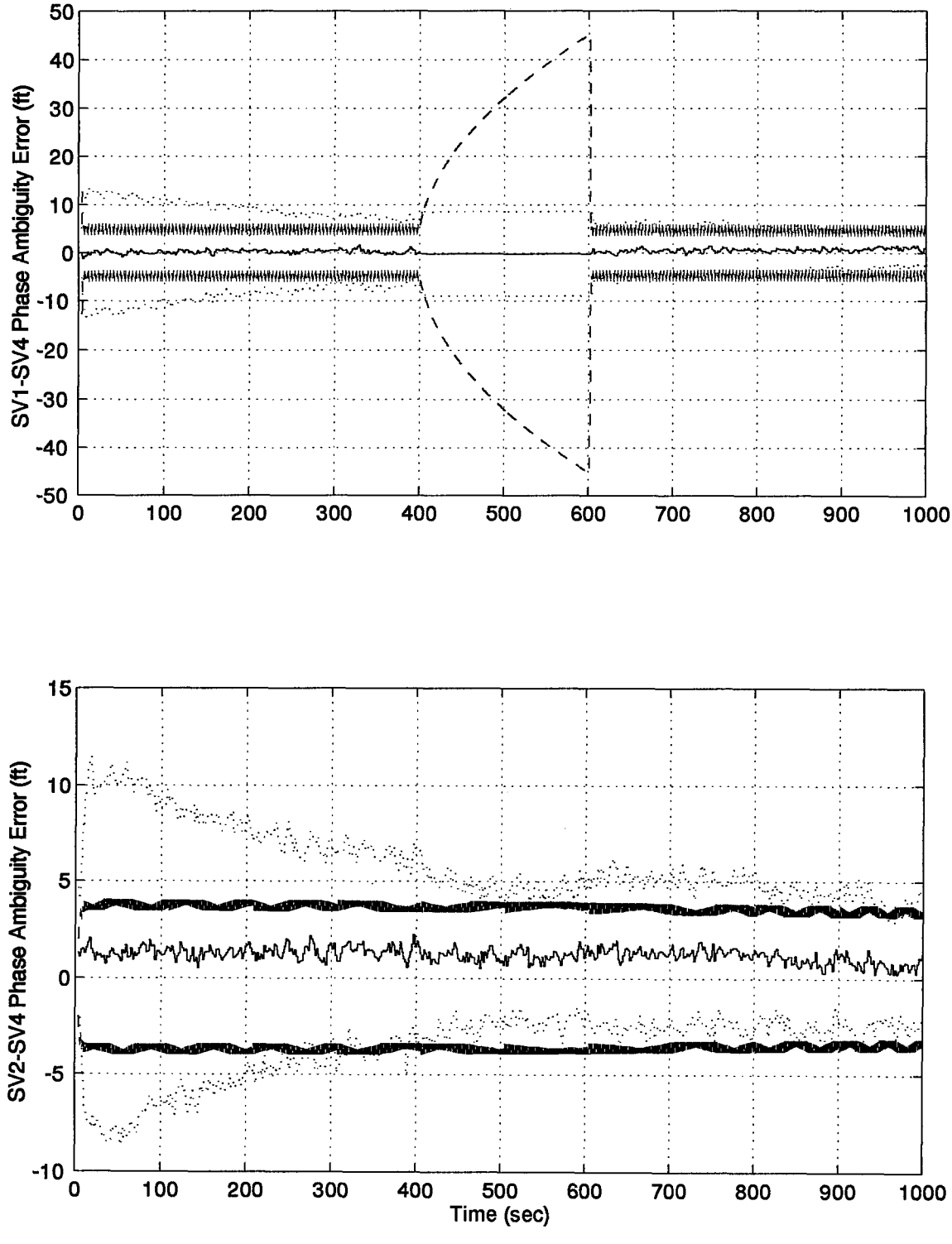

Figure I.6 GPS Satellites 1 and 2 Phase Ambiguity Error Plots

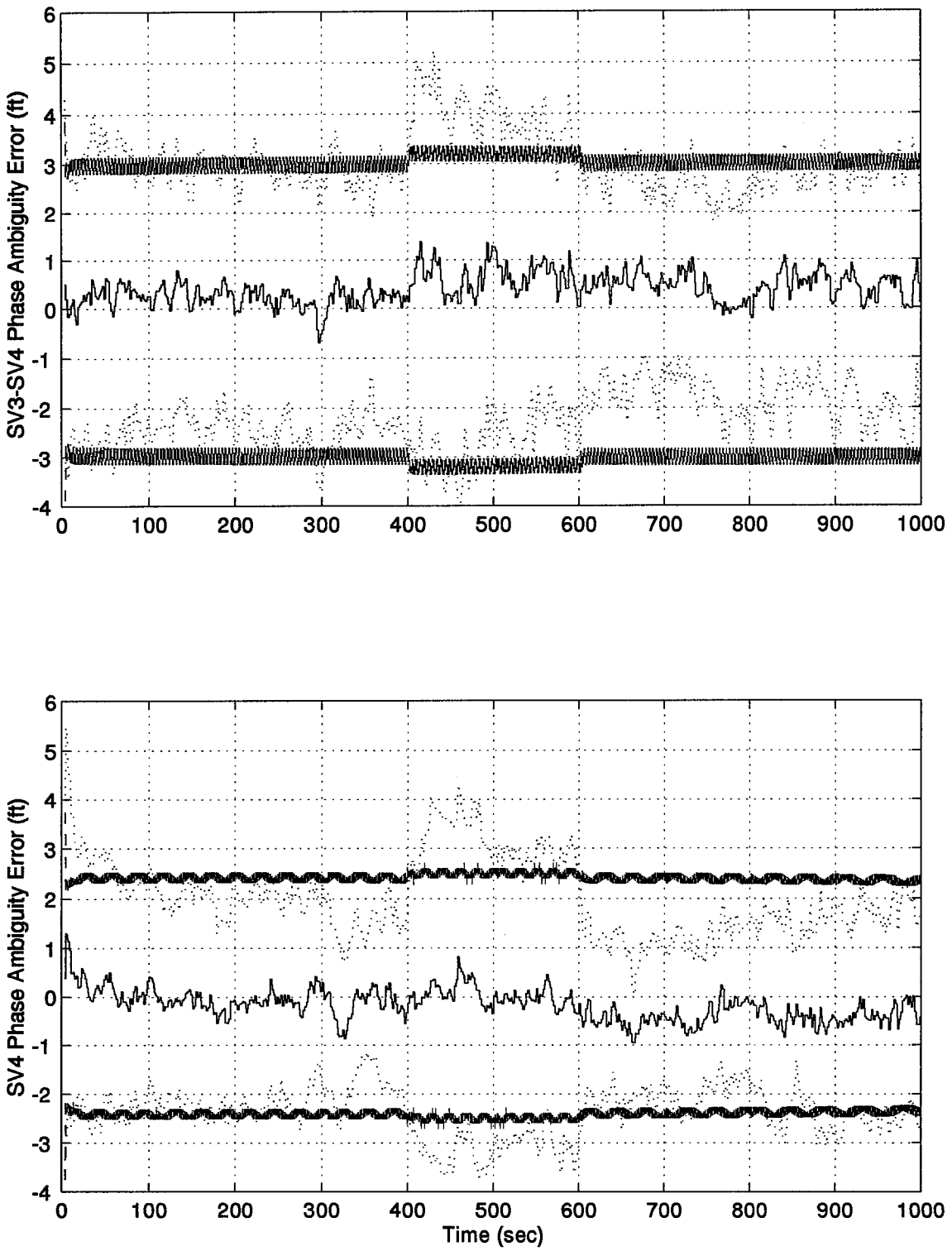

Figure I.7 GPS Satellites 3 and 4 Phase Ambiguity Error Plots

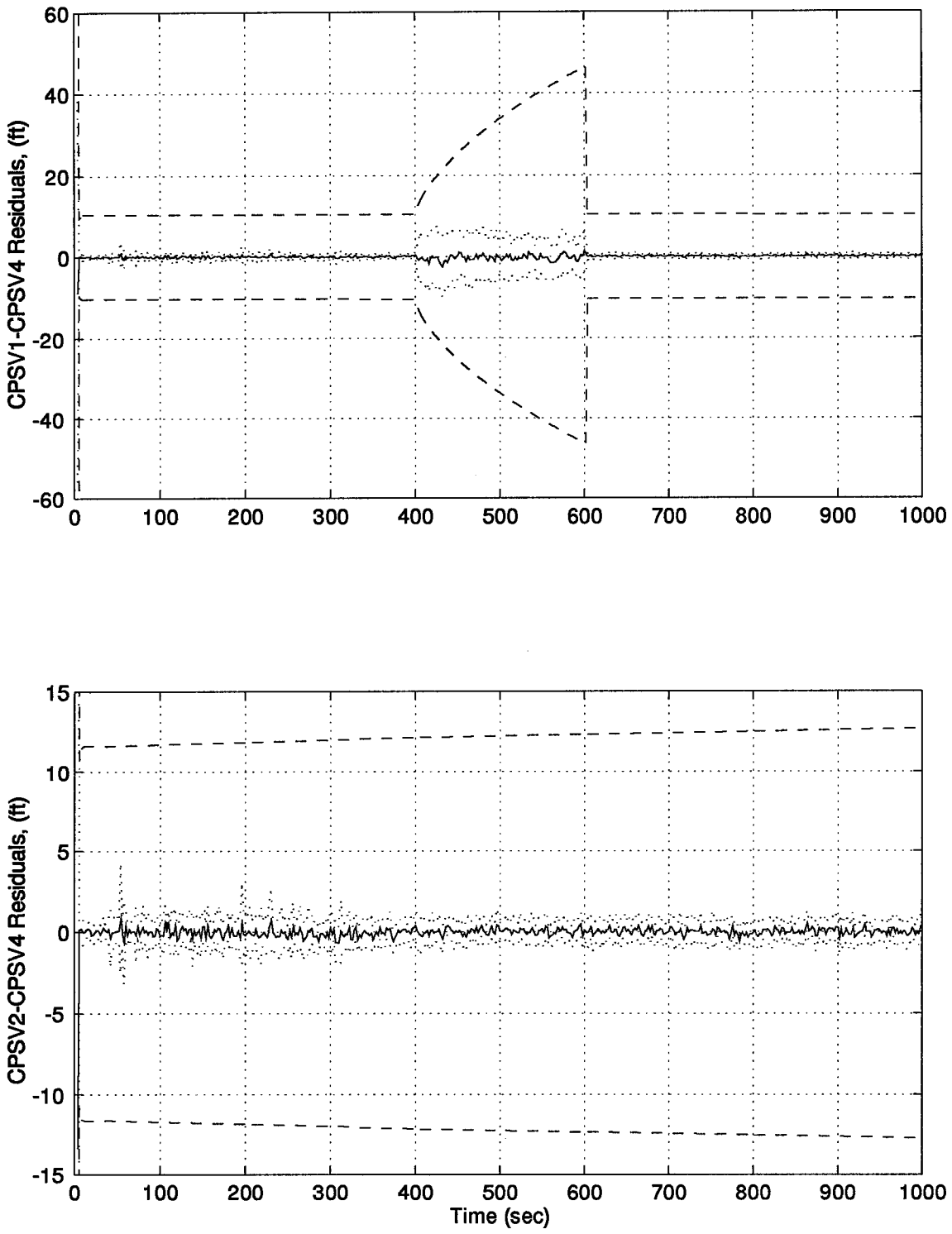

Figure I.8 GPS Satellites 1 and 2 Residual Plots

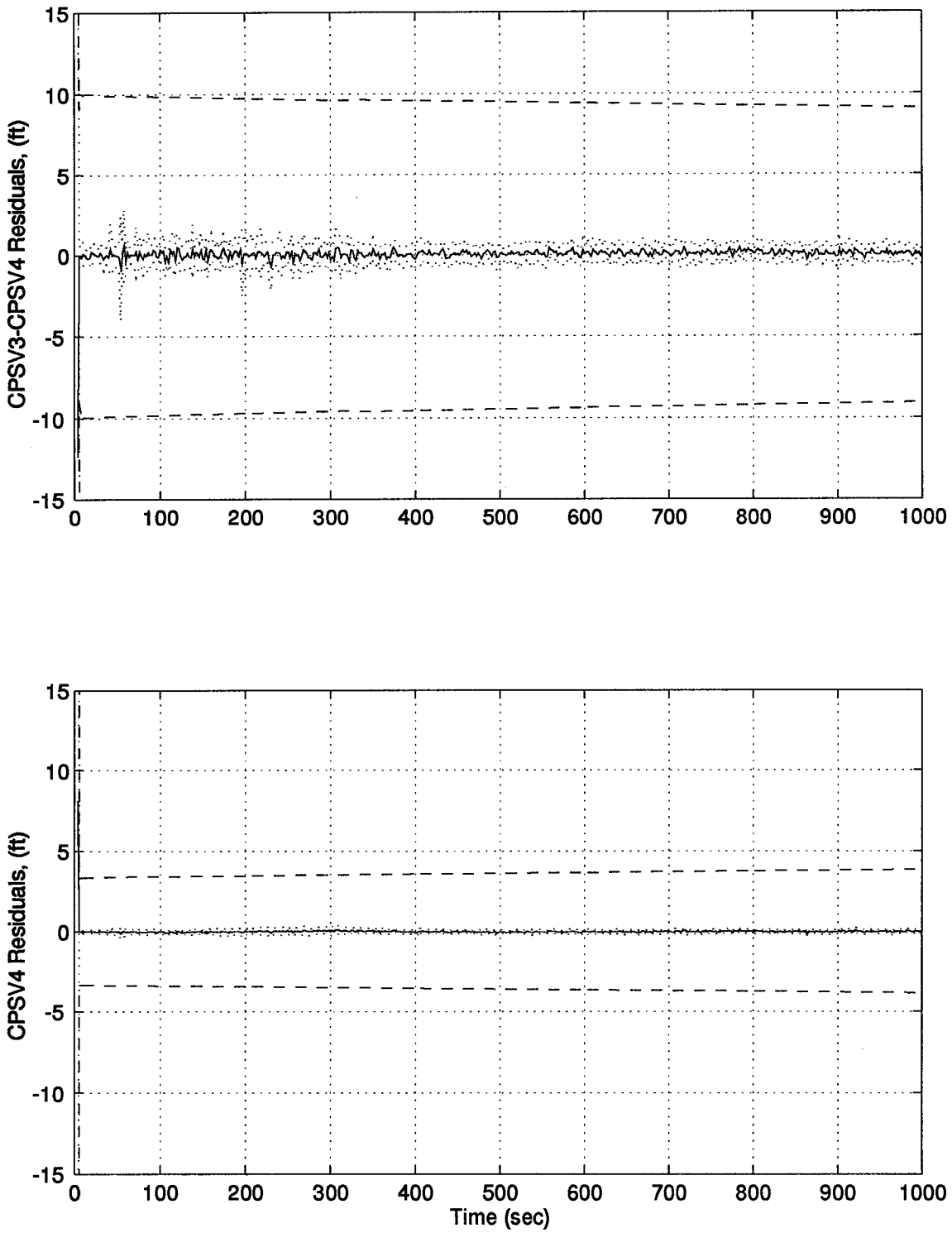

Figure I.9 GPS Satellites 3 and 4 Residual Plots

Appendix J. Double Difference PNRS Large Cycle Slip on Satellite #1 Results

This appendix contains the results of the 1000 second simulation run of the Double Difference PNRS filter with a large cycle slip on satellite #1. The plots are in the same order of Appendix G for direct comparison.

A legend for the presented figures is given below.

Table J.1 Legend for Filter Tuning Plots

Symbol	Definition
— Solid Line	Mean Error
··· Dotted Line	Mean Error ± True Sigma
– – Dashed Line	± Filter Predicted Sigma

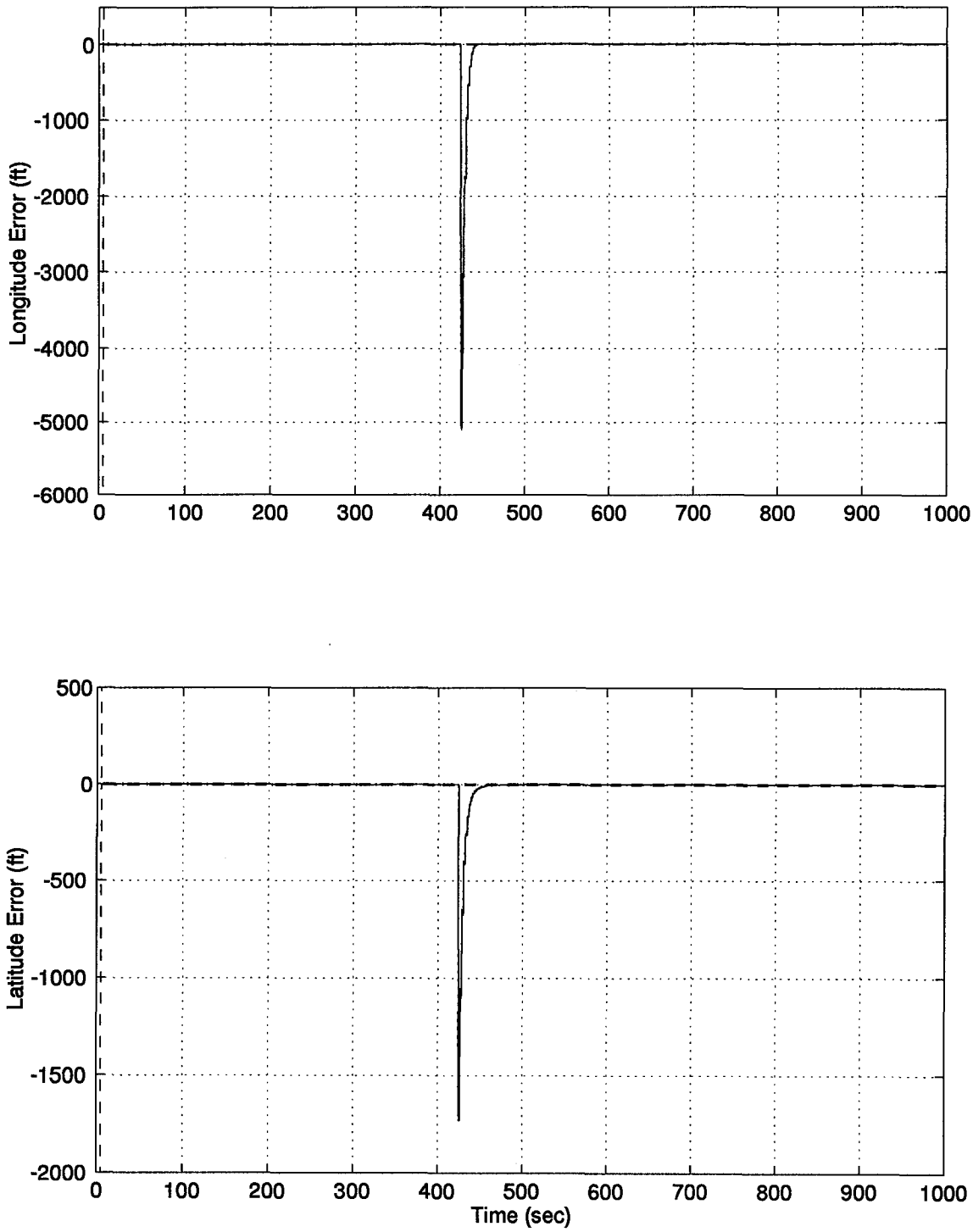

Figure J.1 Longitude and Latitude Error Plots

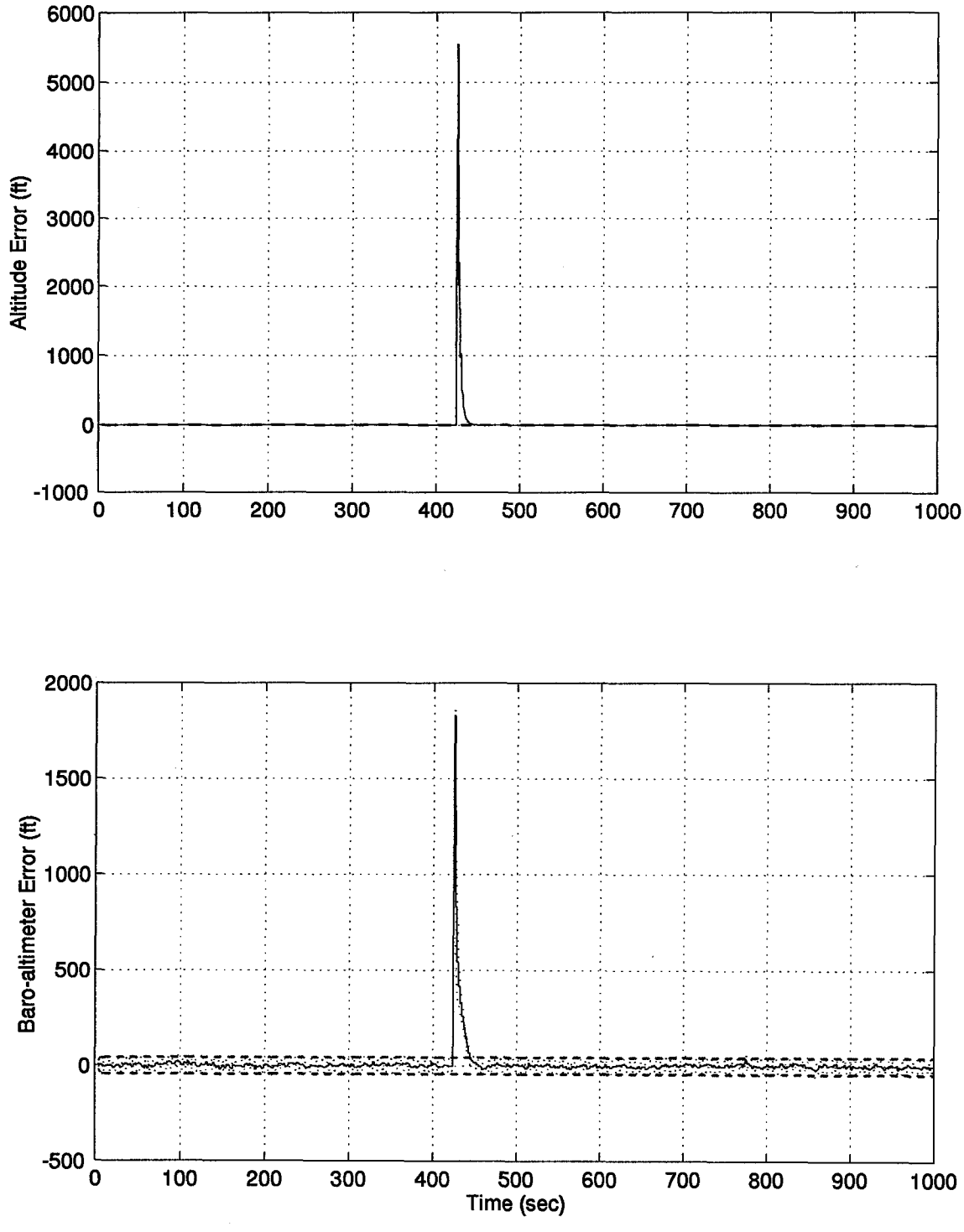

Figure J.2 Altitude and Barometric Altimeter Error Plots

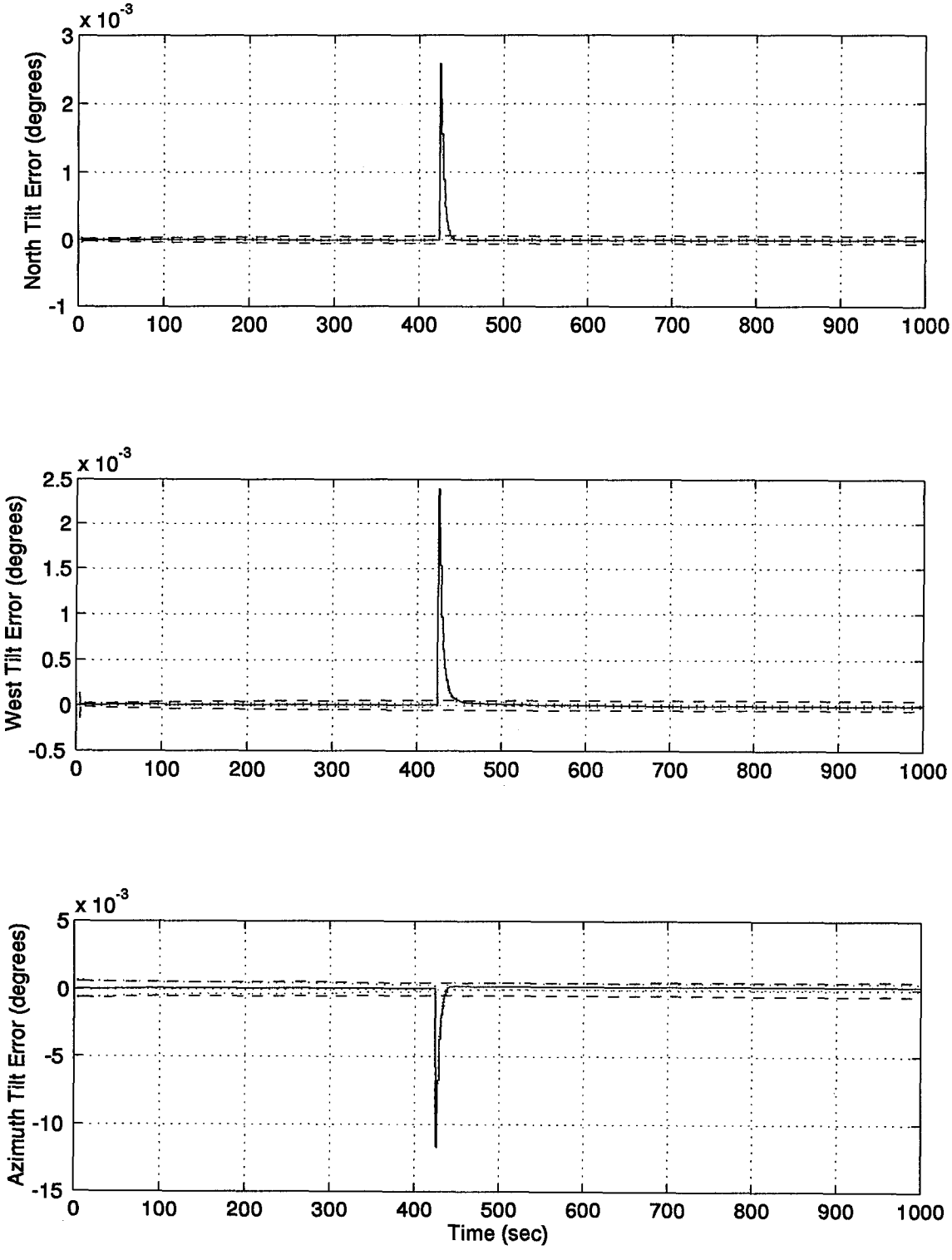

Figure J.3 North, West, and Azimuth Tilt Error Plots

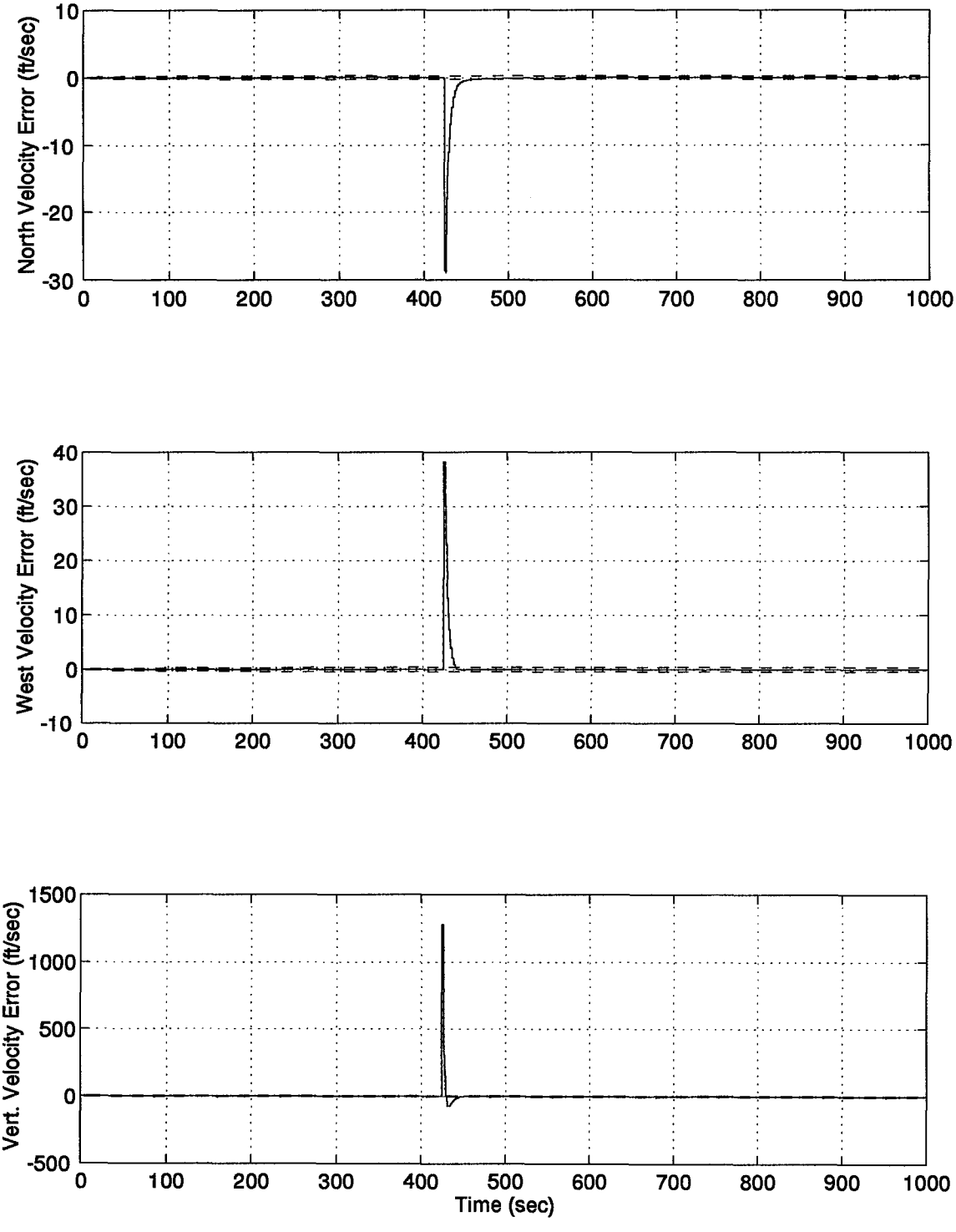

Figure J.4 North, West, and Vertical Velocity Error Plots

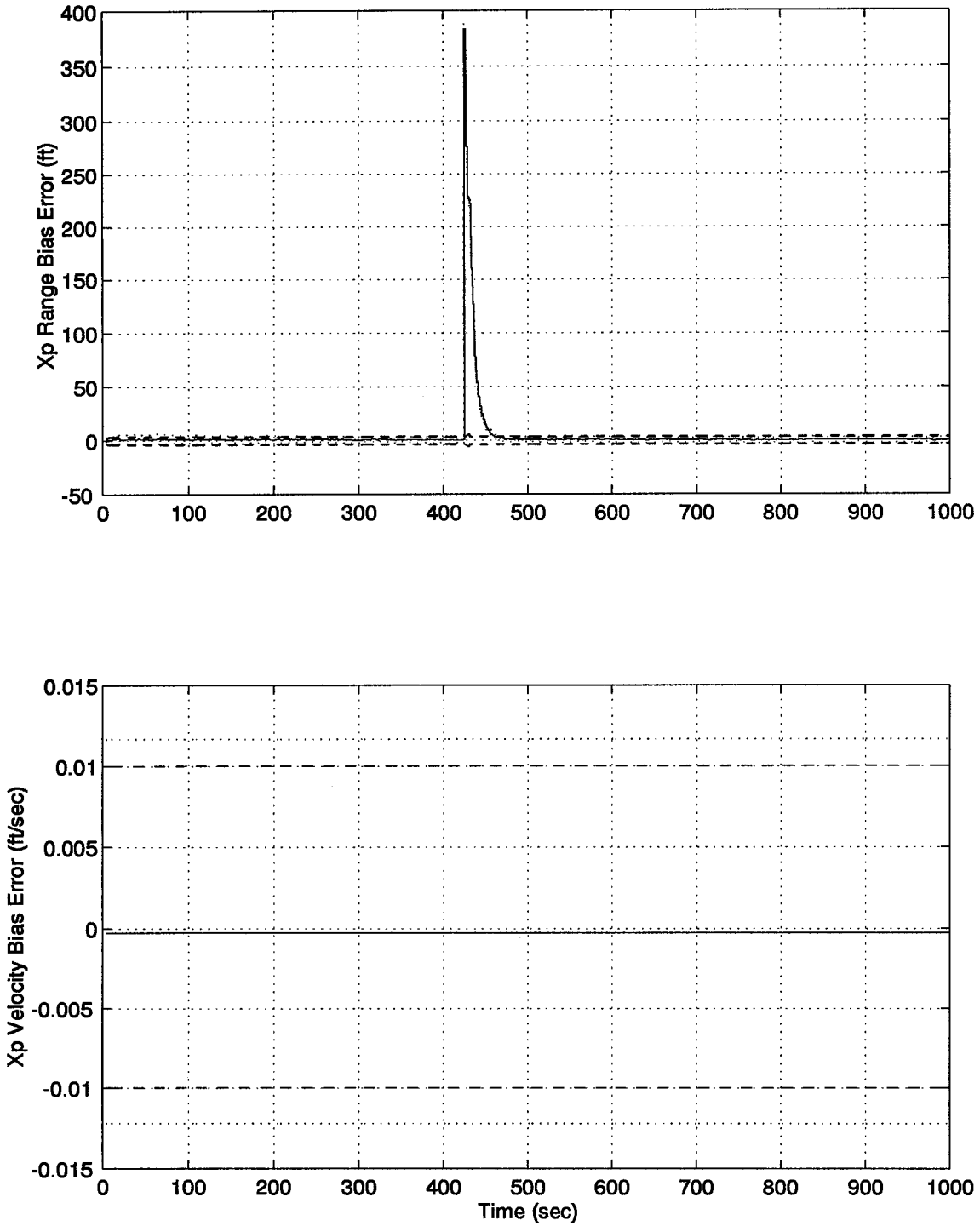

Figure J.5 RRS Range Bias, Range Velocity, and Atmospheric Propagation Delay Error Plots

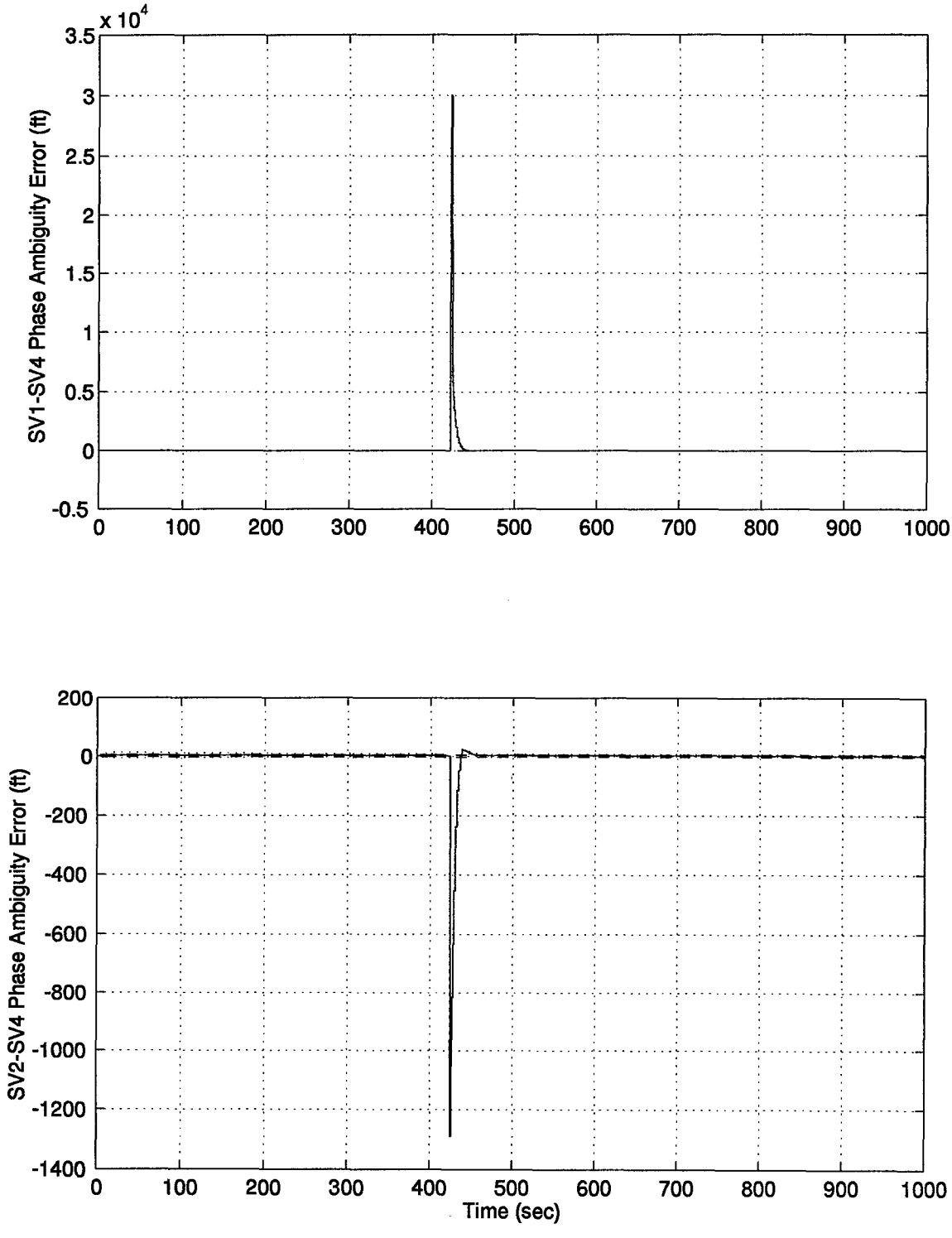

Figure J.6 GPS Satellites 1 and 2 Phase Ambiguity Error Plots

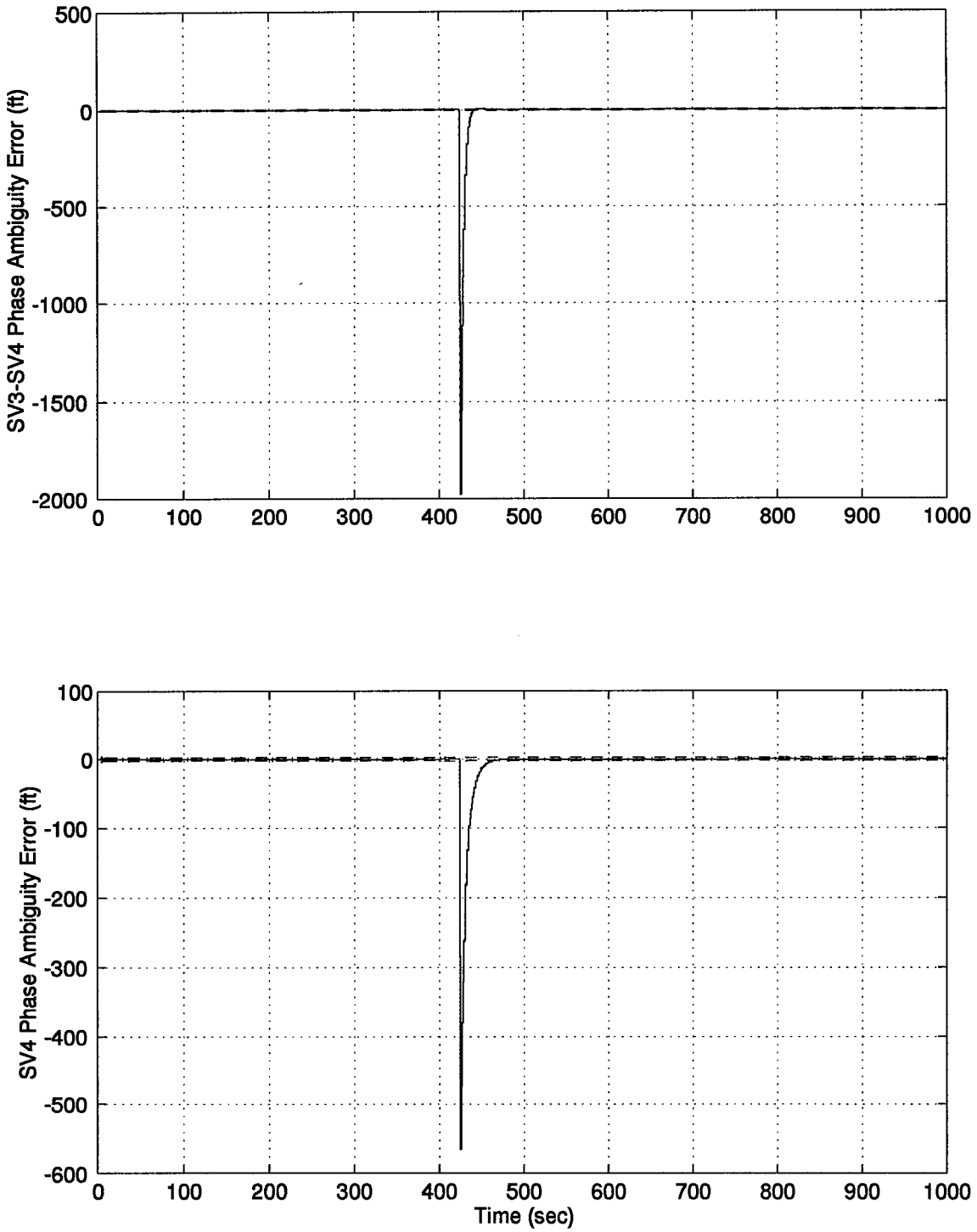

Figure J.7 GPS Satellites 3 and 4 Phase Ambiguity Error Plots

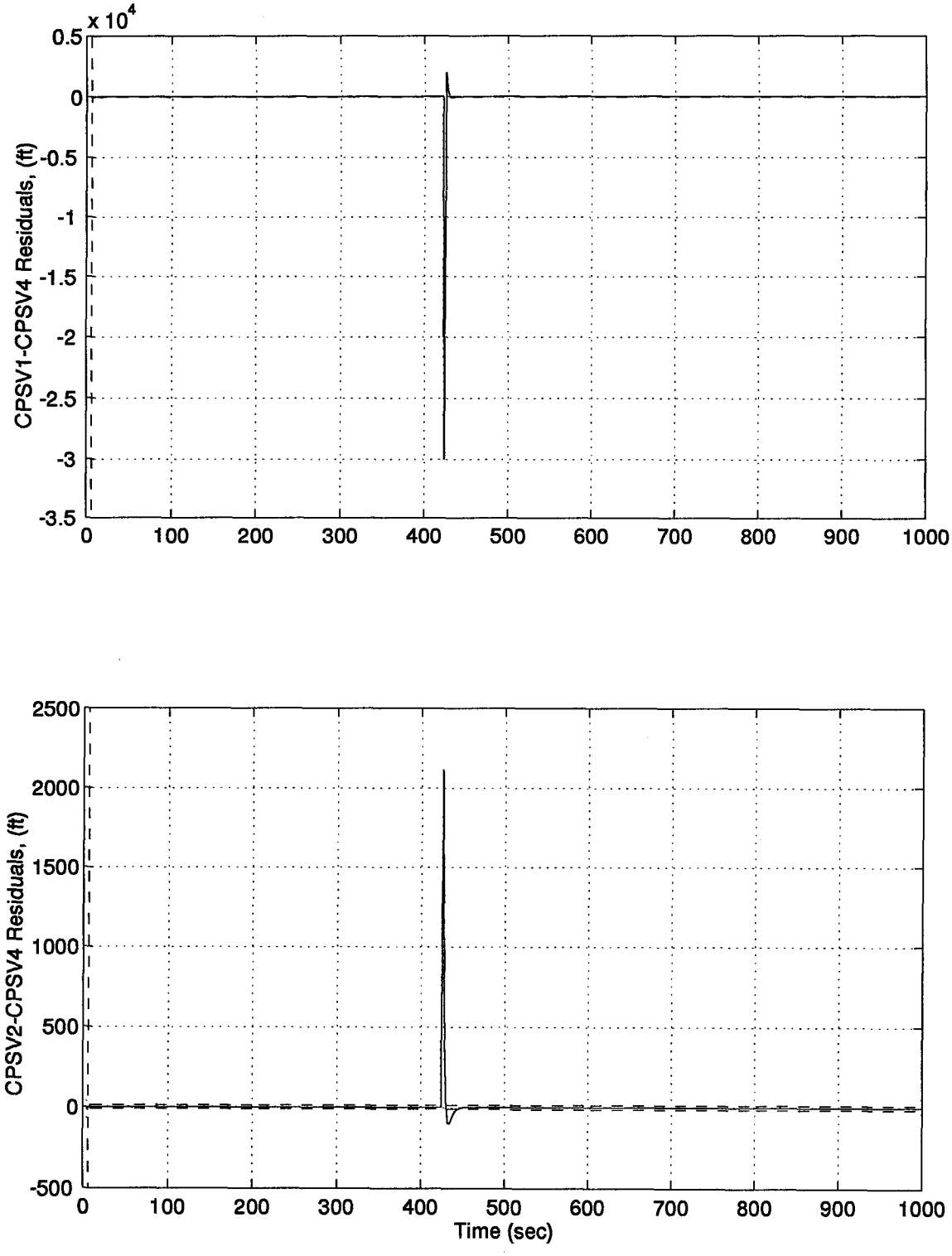

Figure J.8 GPS Satellites 1 and 2 Residual Plots

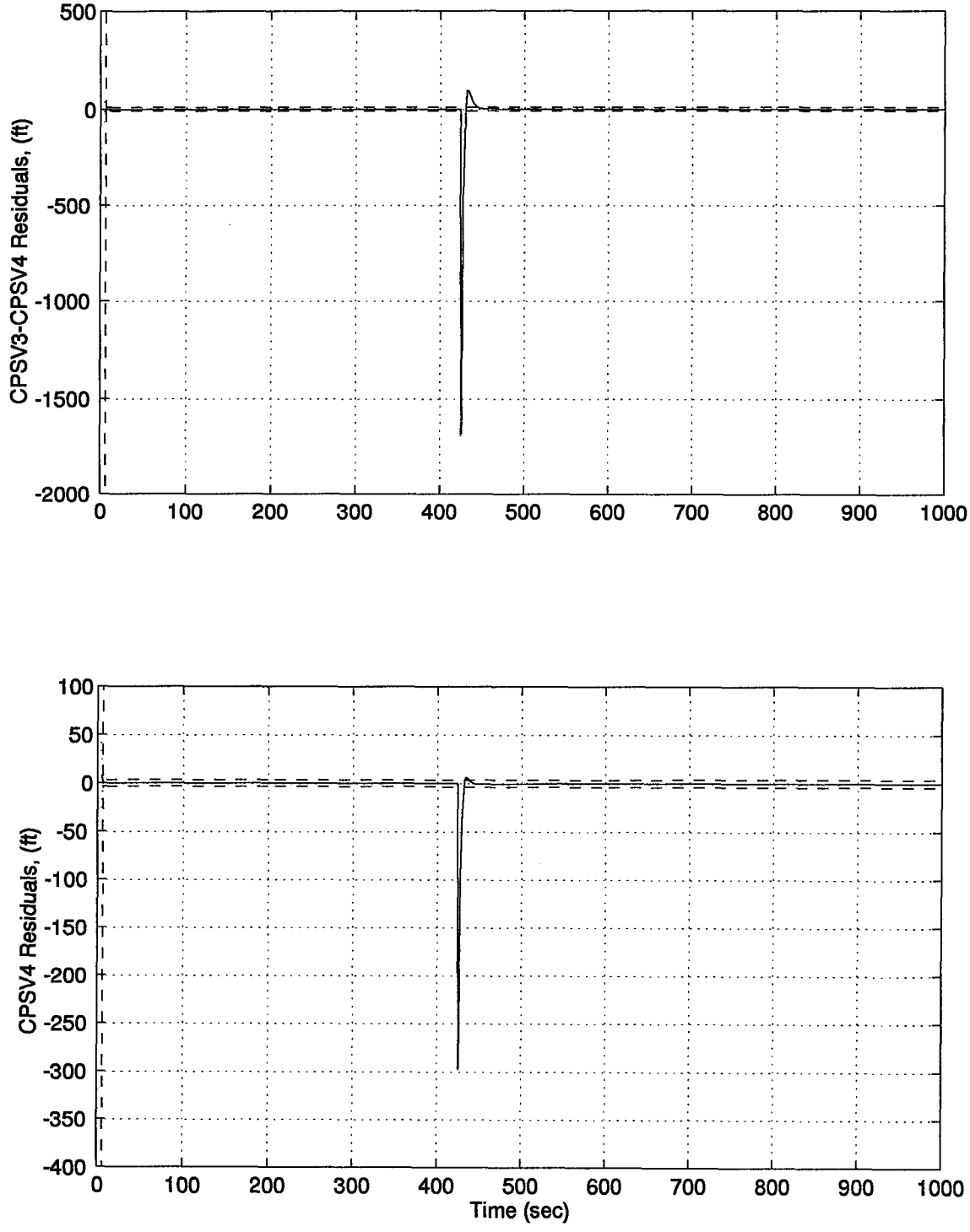

Figure J.9 GPS Satellites 3 and 4 Residual Plots

Appendix K. Double Difference PNRS Large Cycle Slip on Satellite #4 Results

This appendix contains the results of the 1000 second simulation run of the Double Difference PNRS filter with a large cycle slip on satellite 4. The plots are in the same order of Appendix G for direct comparison.

A legend for the presented figures is given below.

Table K.1 Legend for Filter Tuning Plots

Symbol	Definition
—- Solid Line	Mean Error
$\cdots$ Dotted Line	Mean Error $\pm$ True Sigma
$--$ Dashed Line	$\pm$ Filter Predicted Sigma

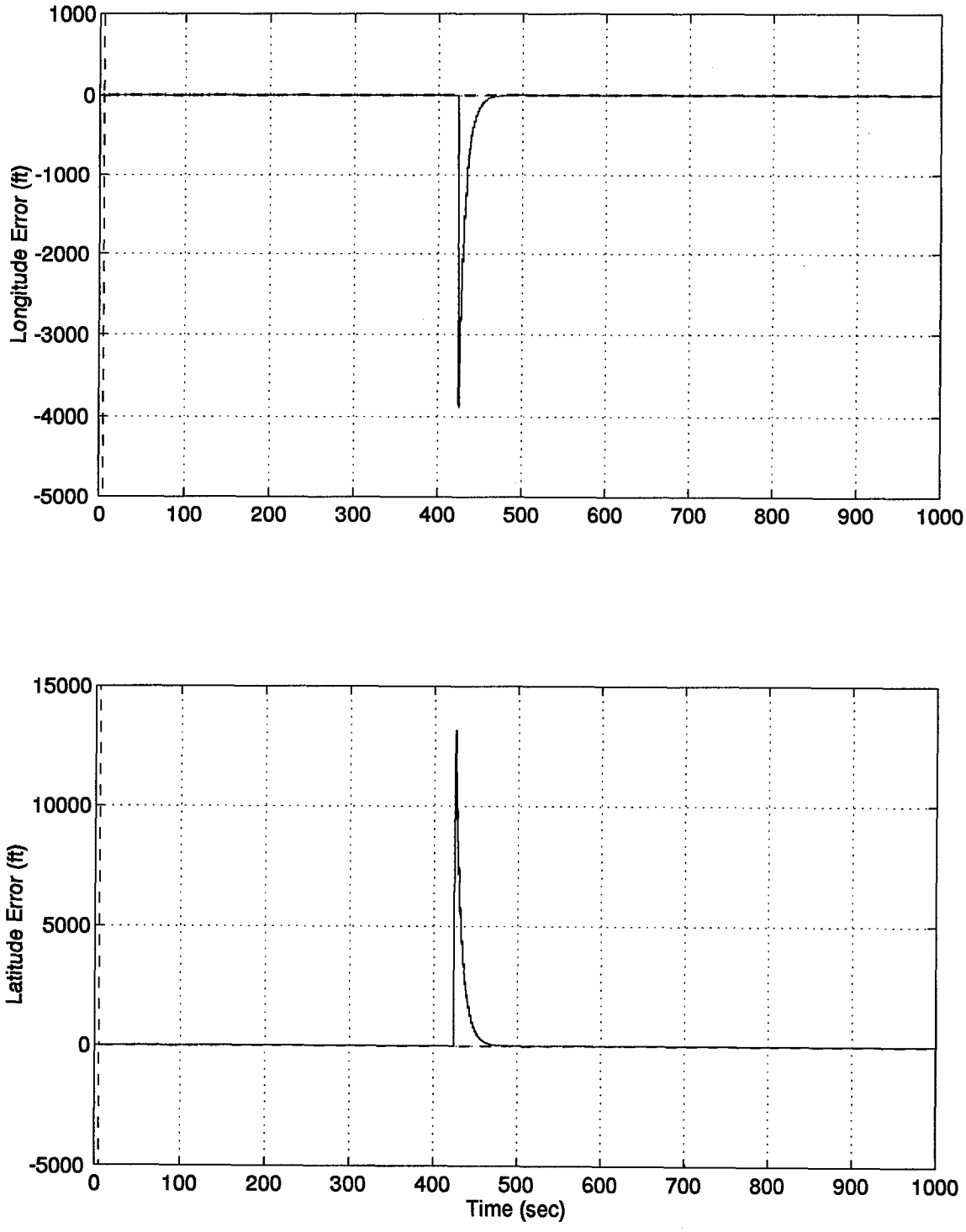

Figure K.1 Longitude and Latitude Error Plots

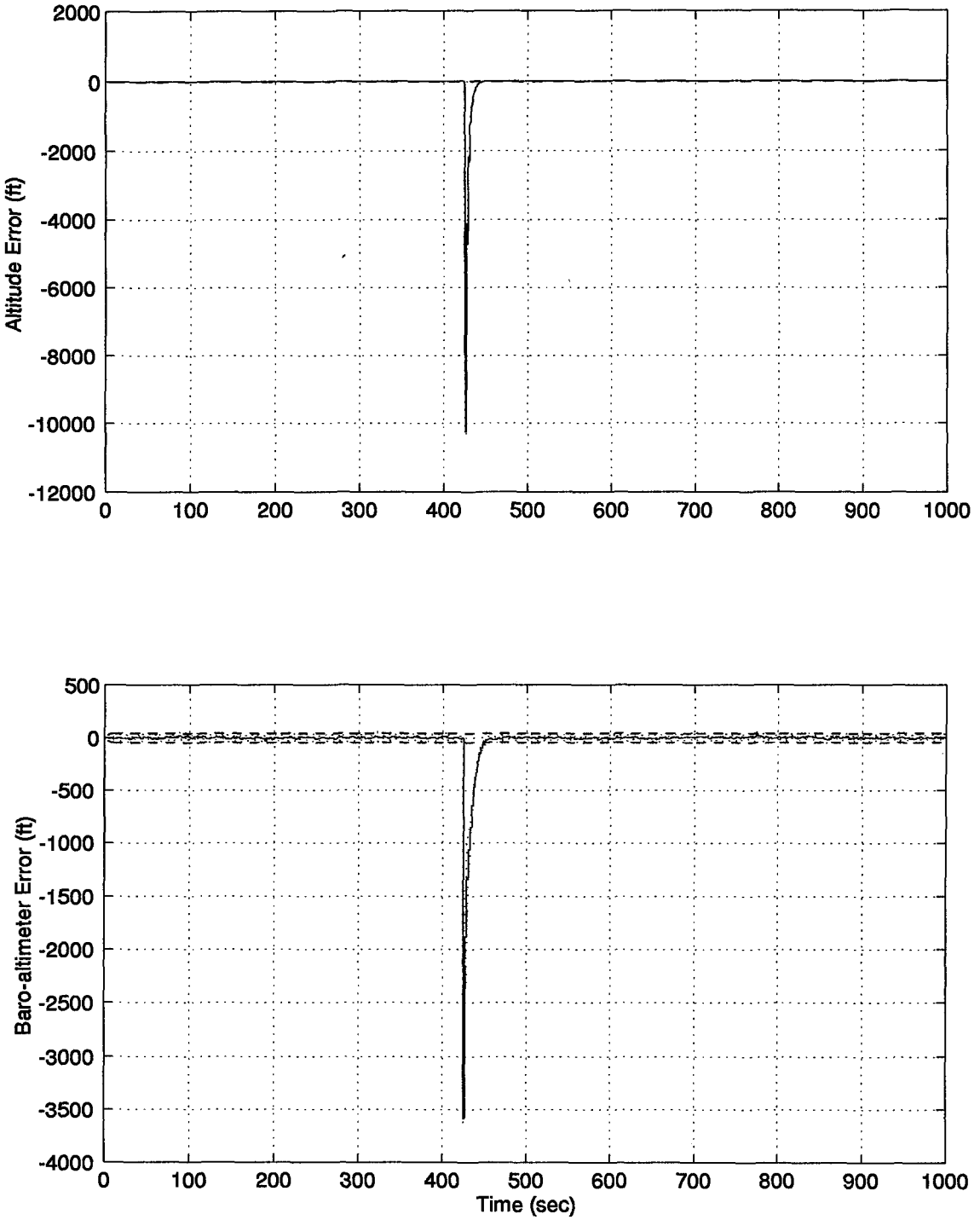

Figure K.2 Altitude and Barometric Altimeter Error Plots

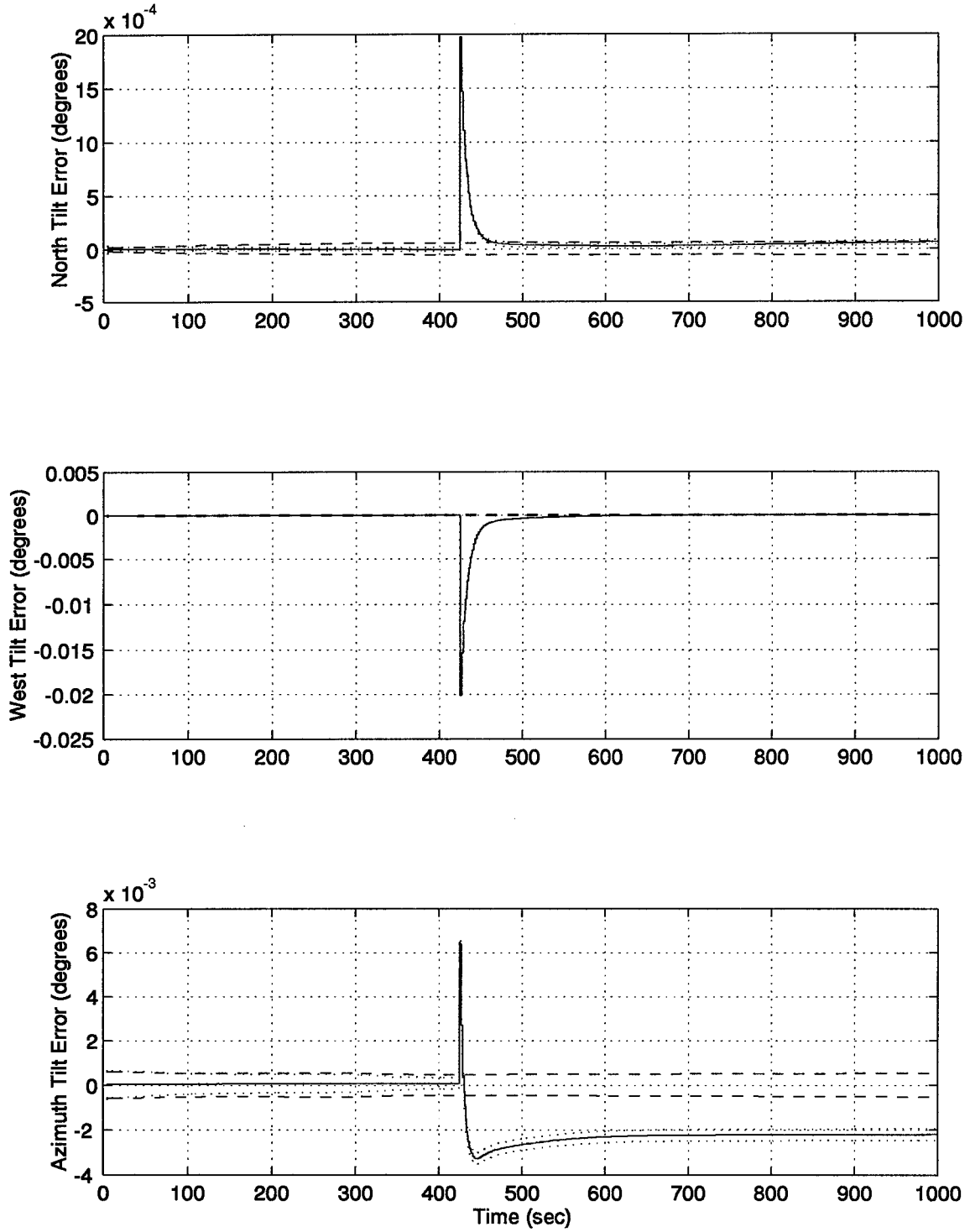

Figure K.3 North, West, and Azimuth Tilt Error Plots

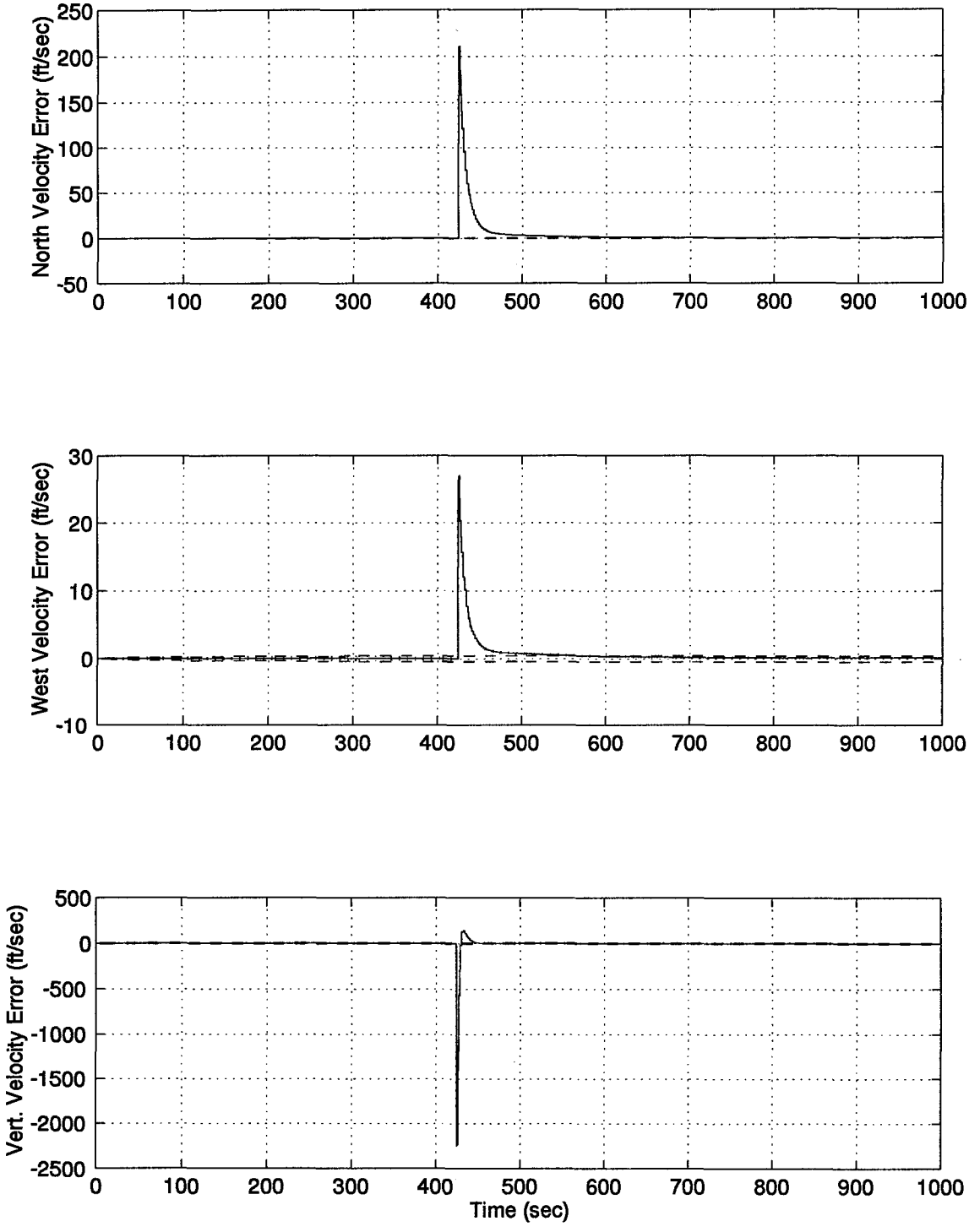

Figure K.4 North, West, and Vertical Velocity Error Plots

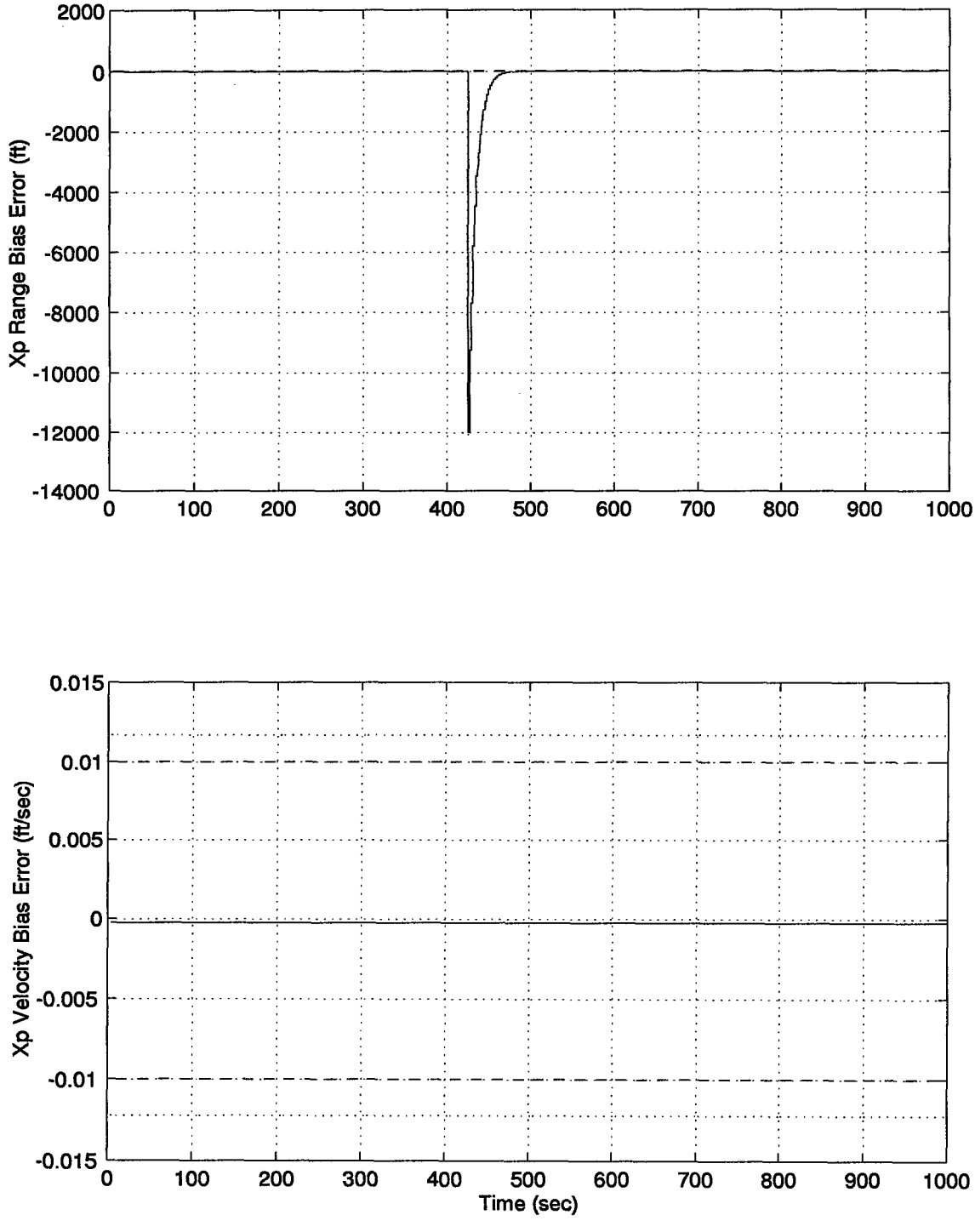

Figure K.5 RRS Range Bias, Range Velocity, and Atmospheric Propagation Delay Error Plots

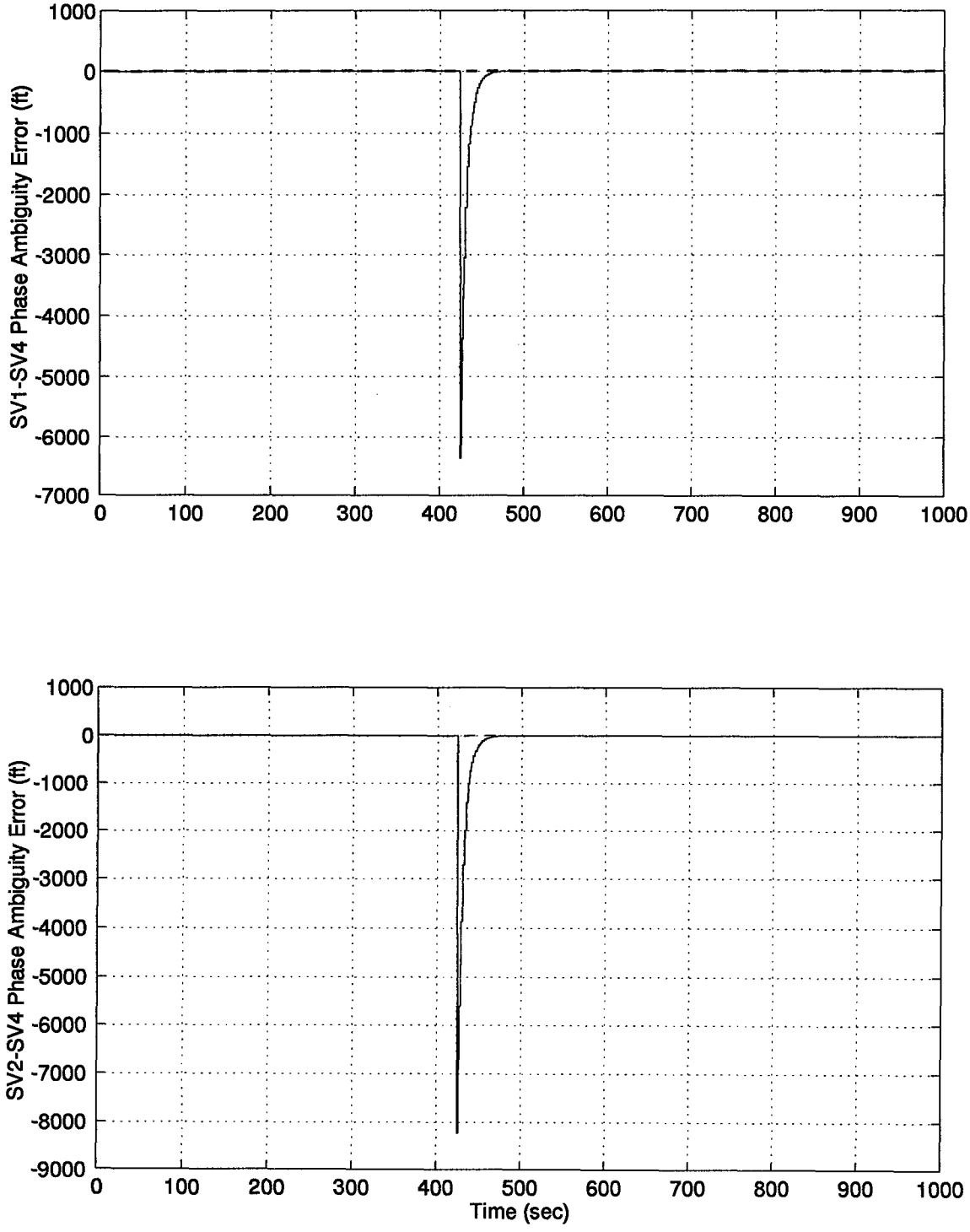

Figure K.6 GPS Satellites 1 and 2 Phase Ambiguity Error Plots

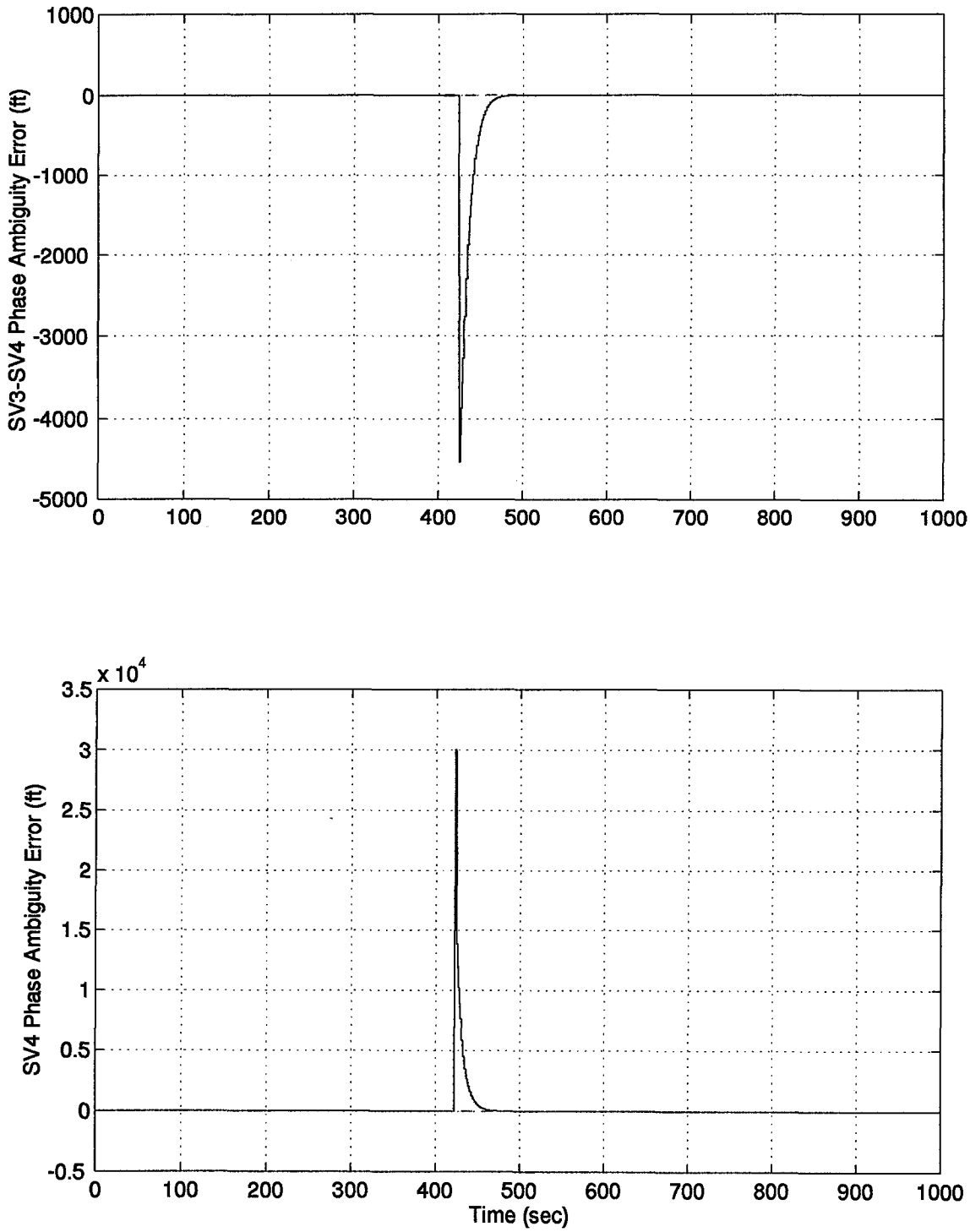

Figure K.7 GPS Satellites 3 and 4 Phase Ambiguity Error Plots

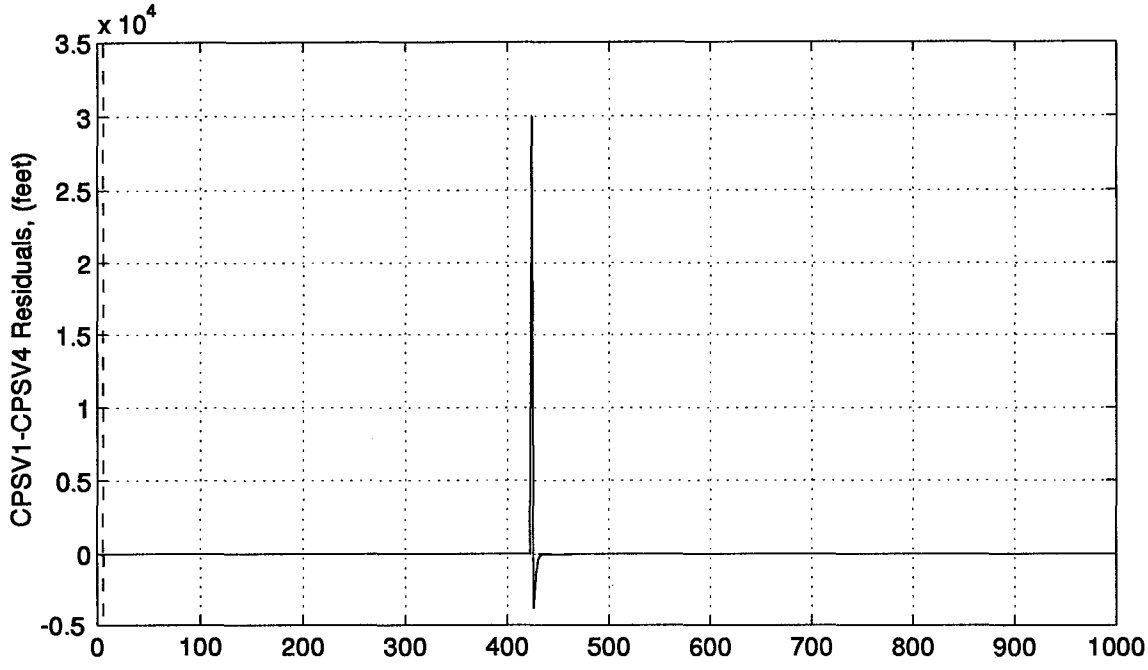

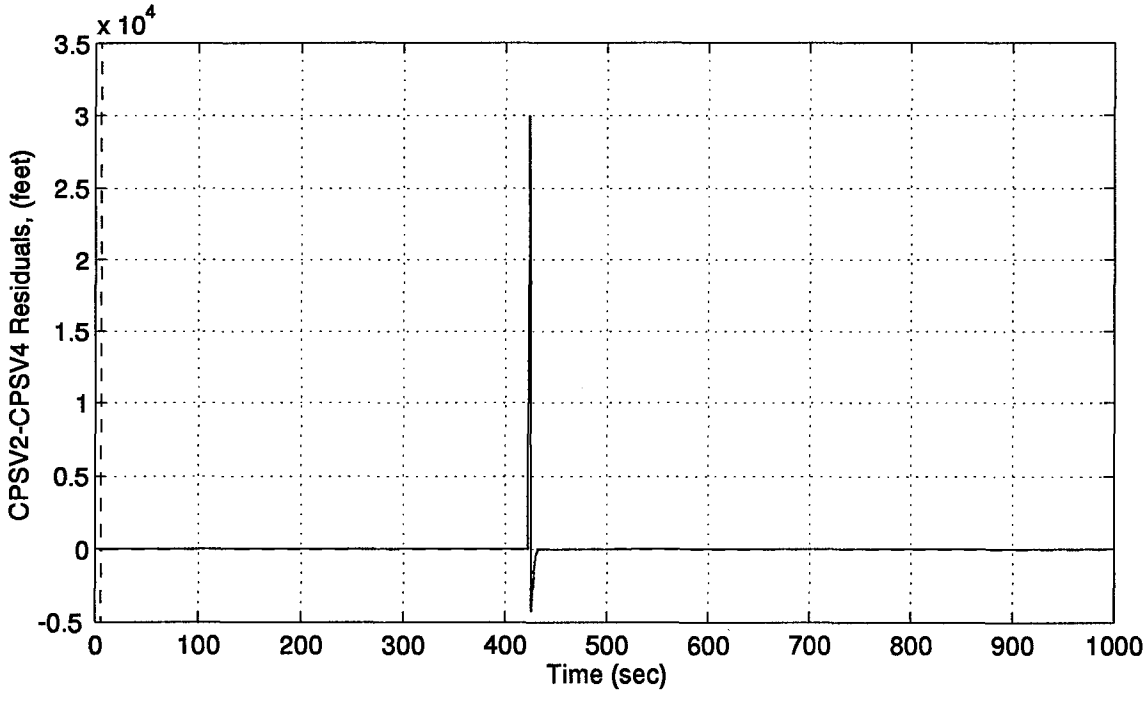

Figure K.8 GPS Satellites 1 and 2 Residual Plots

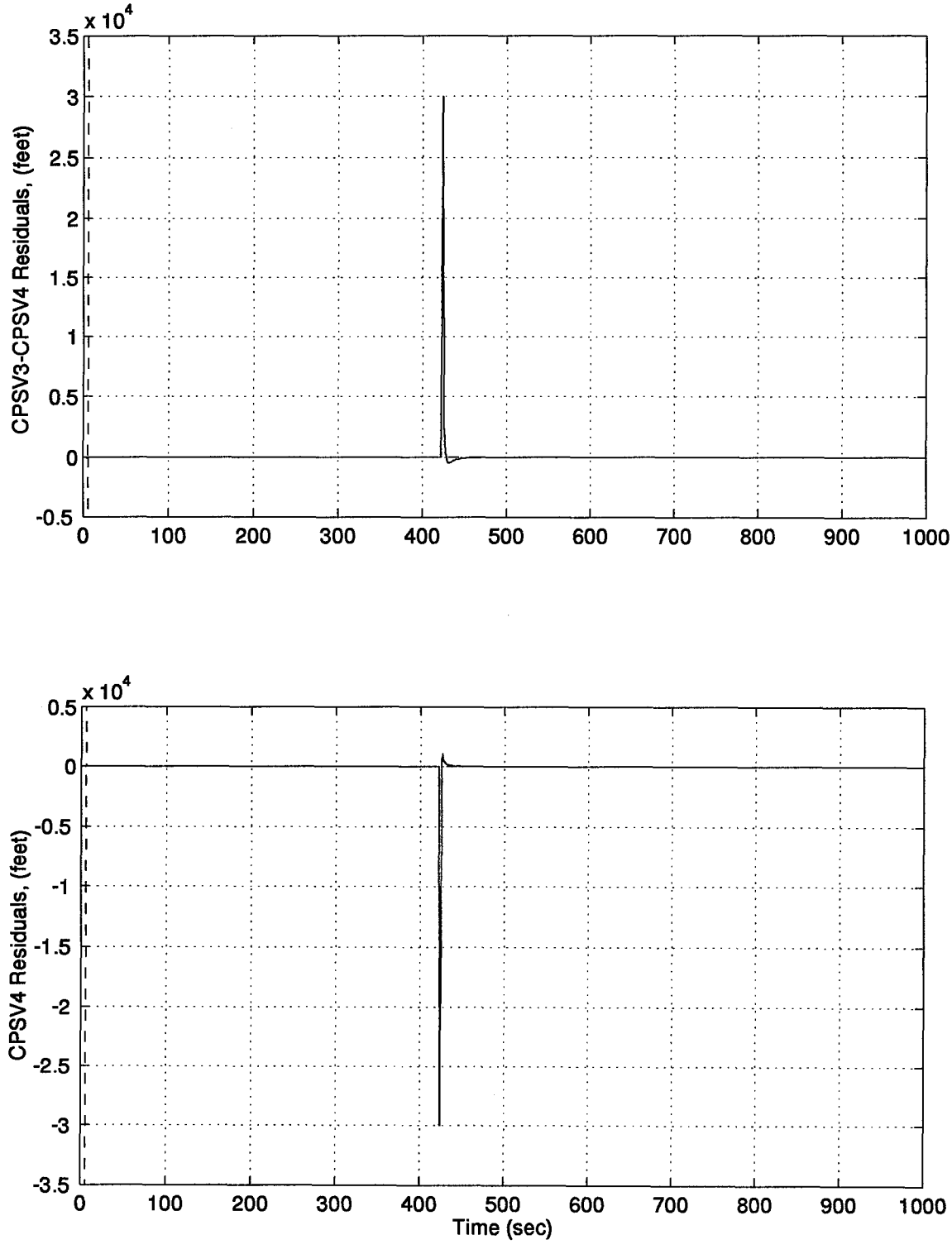

Figure K.9 GPS Satellites 3 and 4 Residual Plots

Appendix L. FDIR Results from Chi-Square Analysis

This appendix contains the plots of the Chi-Square test conducted for Cycle Slip detection, isolation, and recovery analysis. The results from simulations of the ROPNRS and DDPNRS filters are presented.

L.1 Chi-Square Test from the ROPNRS Filter

The figures presented consist of the single cycle slip simulation on each of the four simulated satellites and the final figure depicts the multiple cycle slip scenario analyzed for the ROPNRS filter.

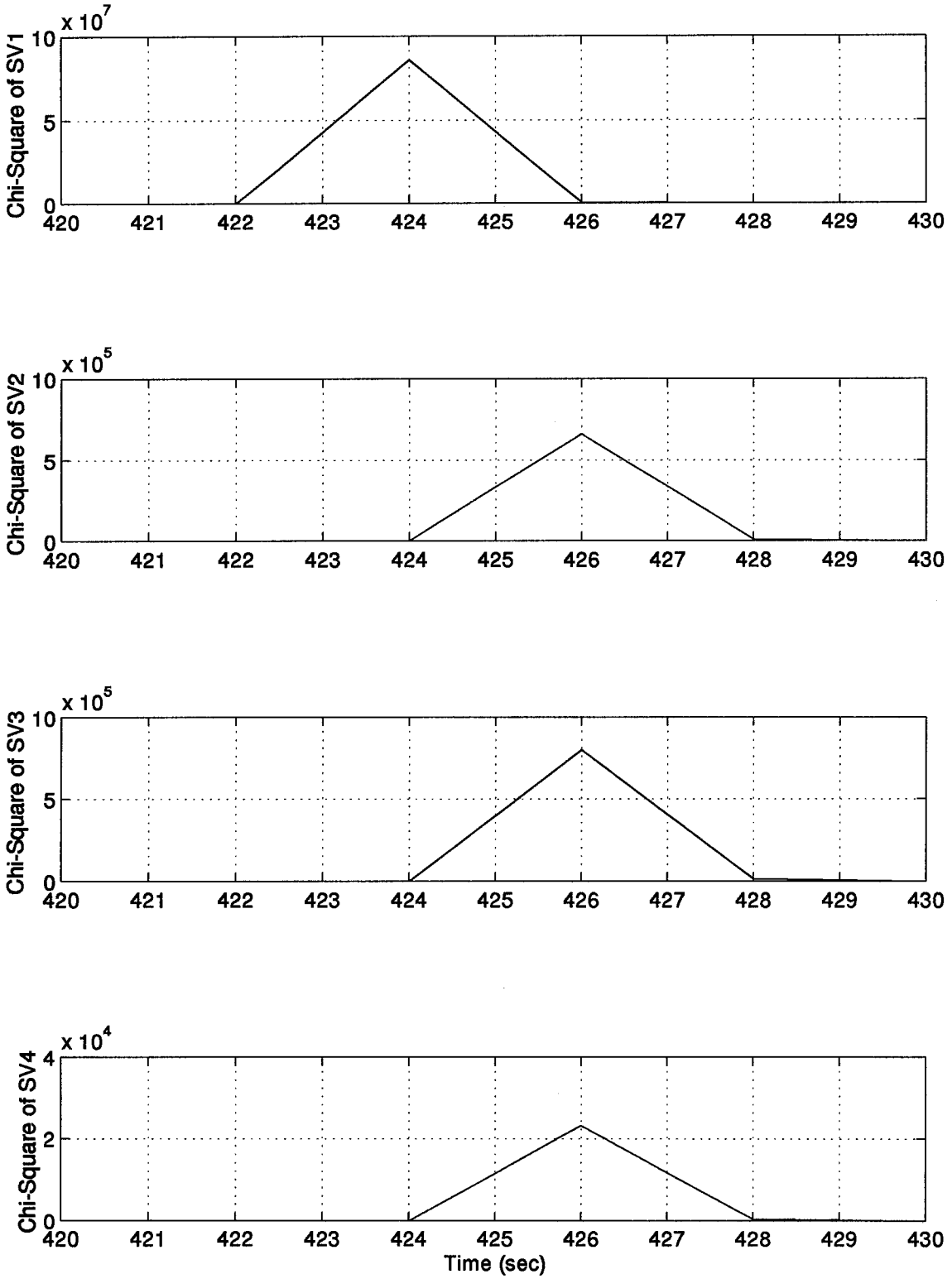

Figure L.1 Chi-Square Plots of Individual Residuals for Cycle Slip on Satellite #1

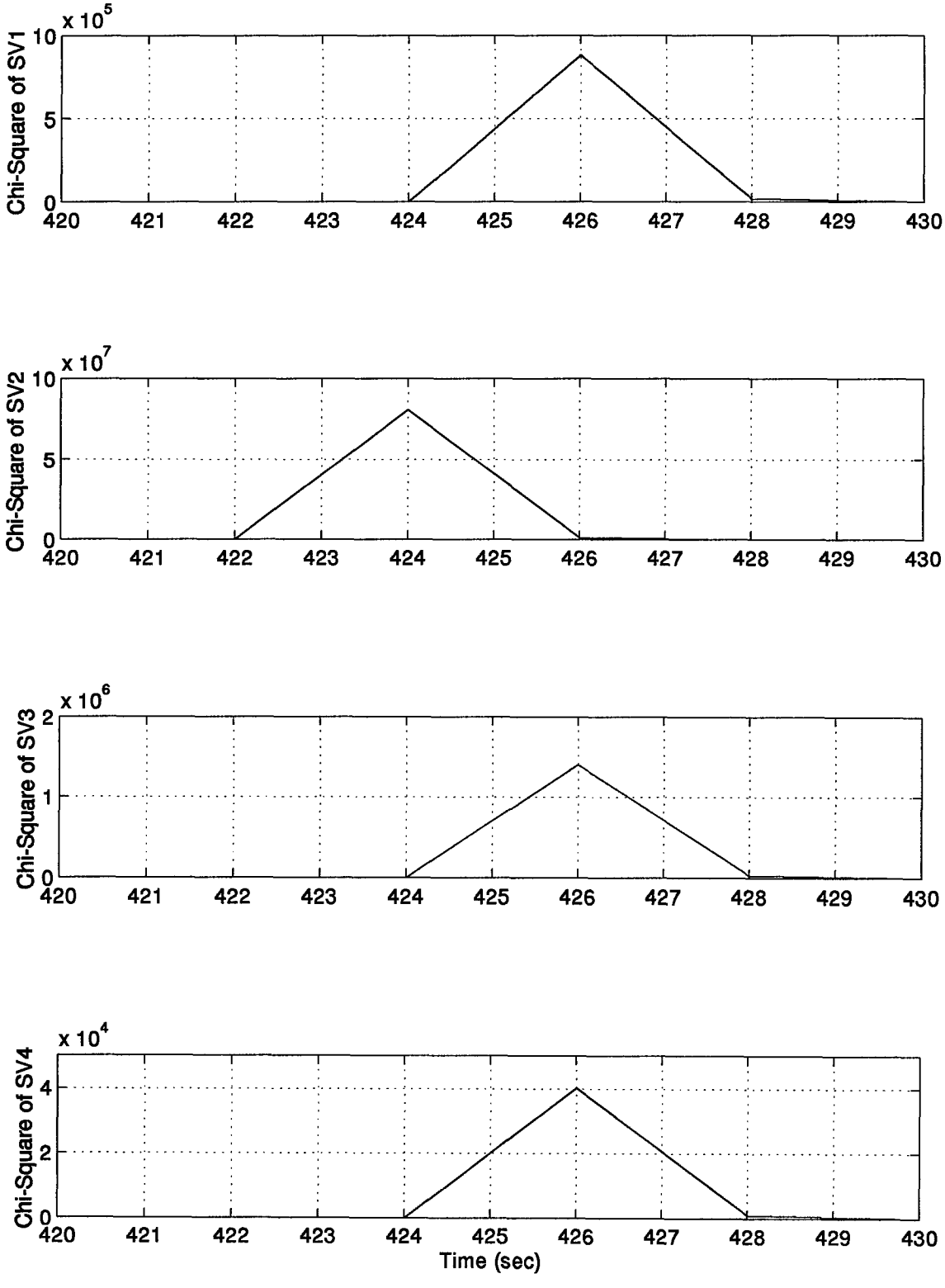

Figure L.2 Chi-Square Plots of Individual Residuals for Cycle Slip on Satellite #2

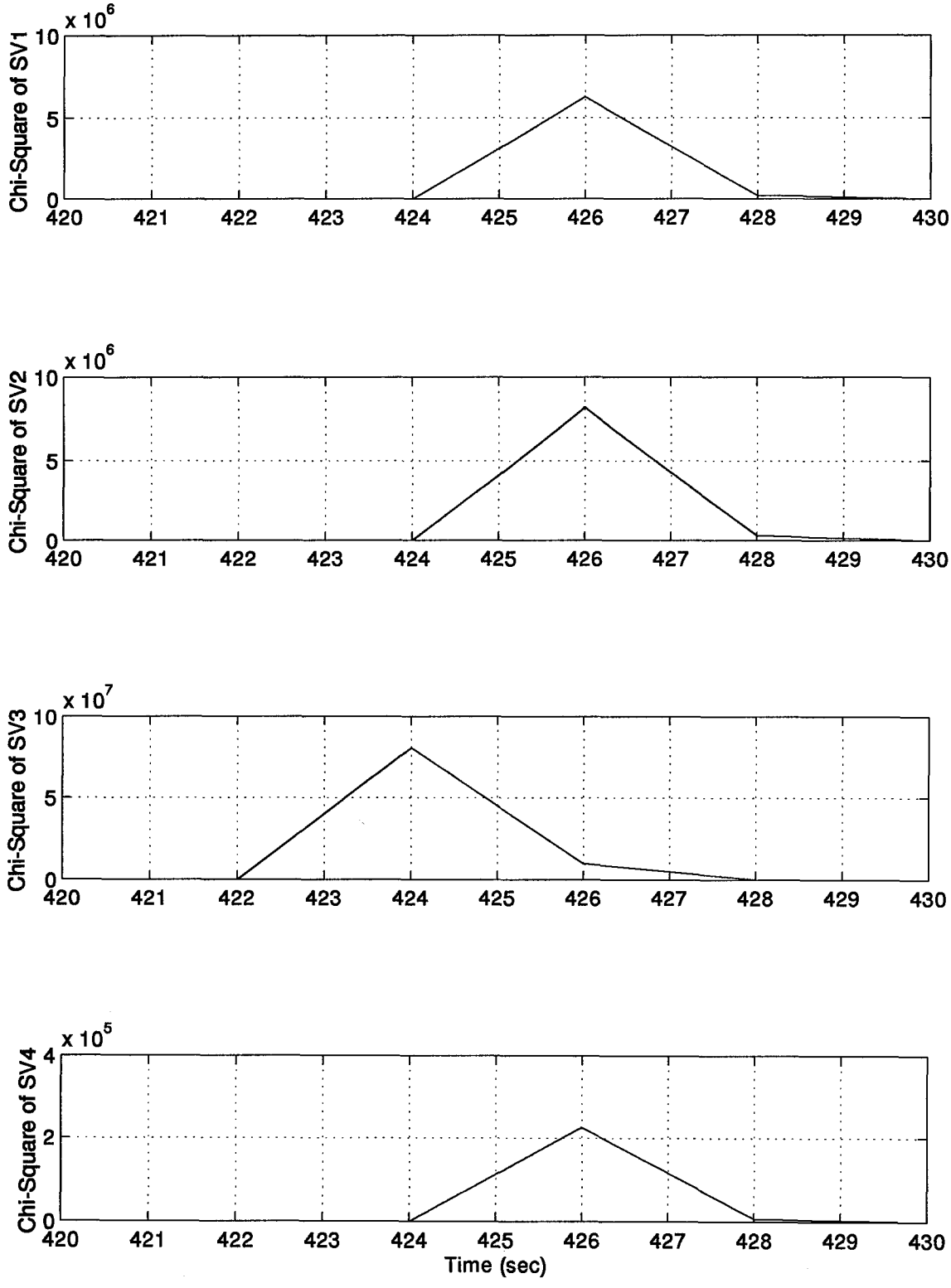

Figure L.3 Chi-Square Plots of Individual Residuals for Cycle Slip on Satellite #3

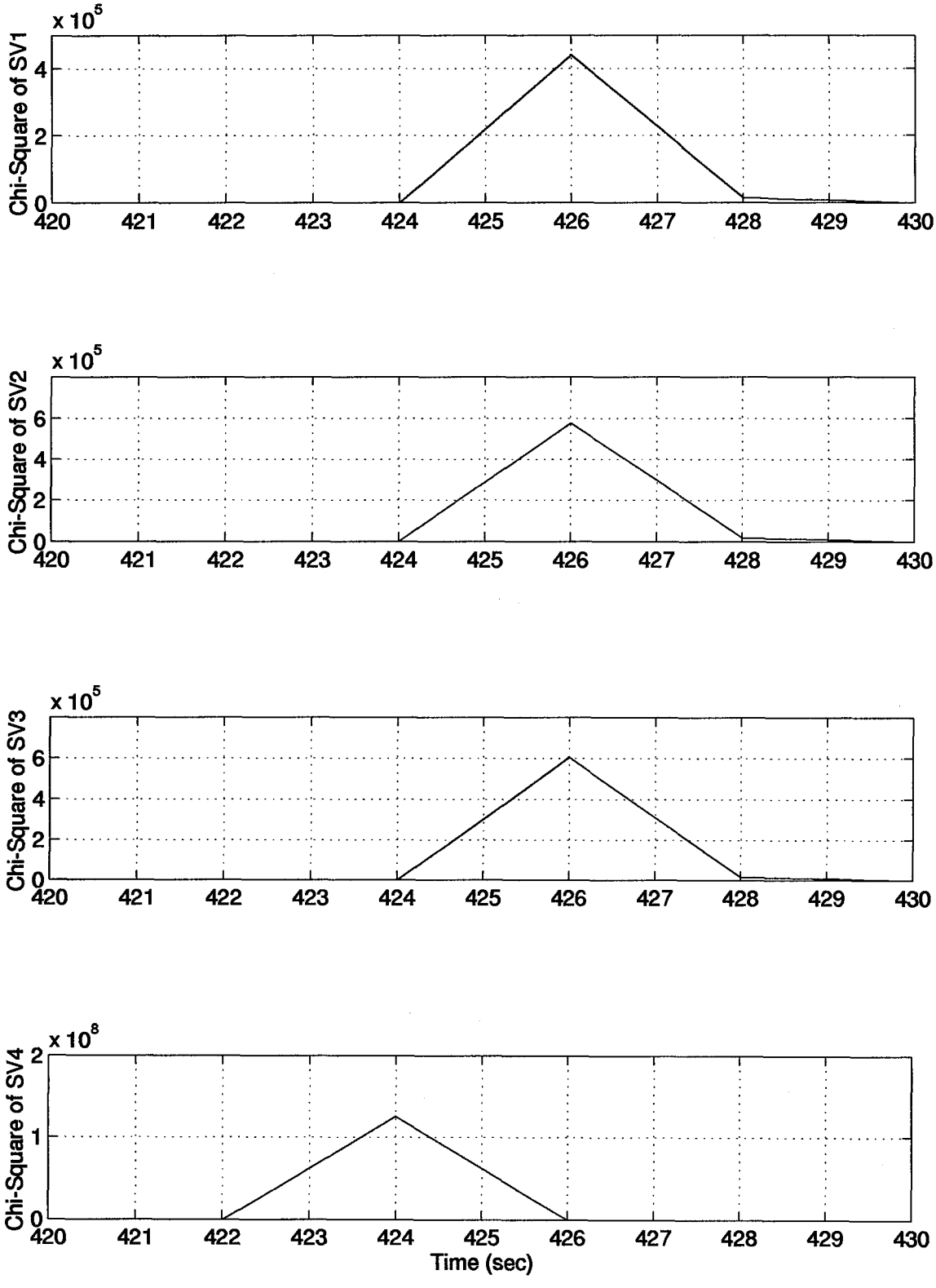

Figure L.4 Chi-Square Plots of Individual Residuals for Cycle Slip on Satellite #4

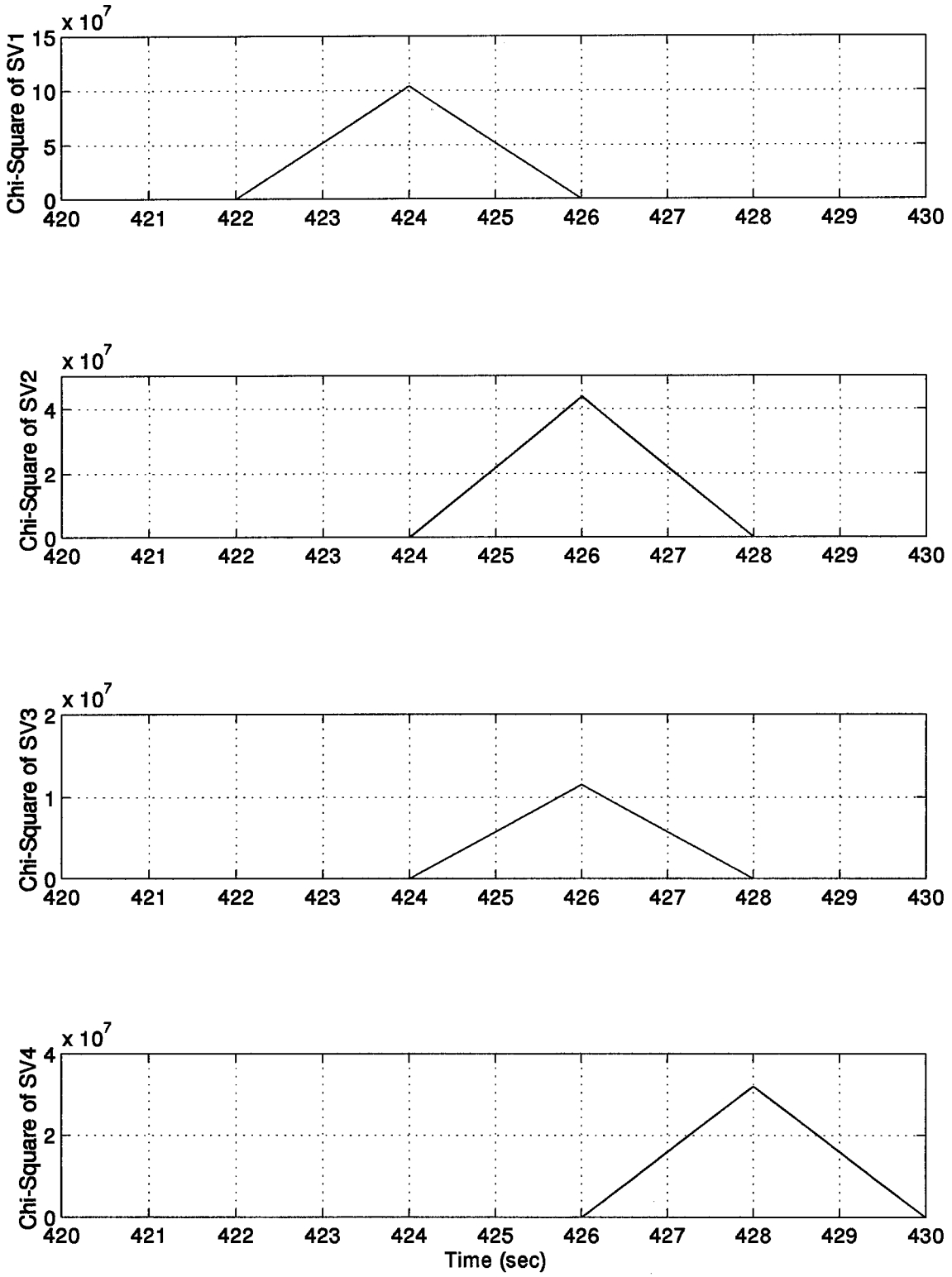

Figure L.5 Chi-Square Plots of Individual Residuals for Multiple Cycle Slip Scenario

L.2 Chi-Square Test from the DDPNRS Filter

The figures presented consist of the single cycle slip simulation on each of the four simulated satellites and the final figure depicts the multiple cycle slip scenario analyzed for the DDPNRS filter.

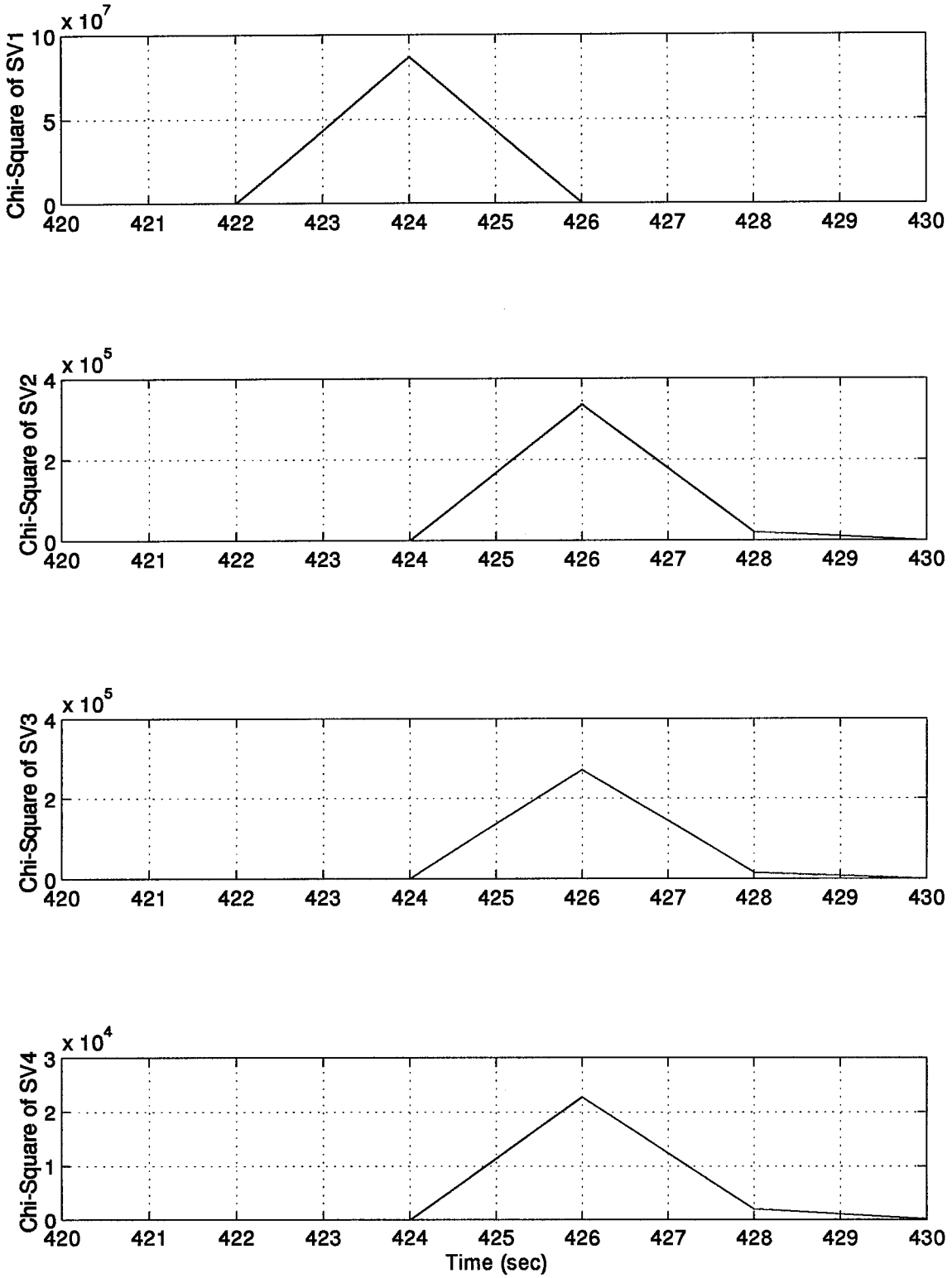

Figure L.6 Chi-Square Plots of Individual Residuals for Cycle Slip on Satellite #1

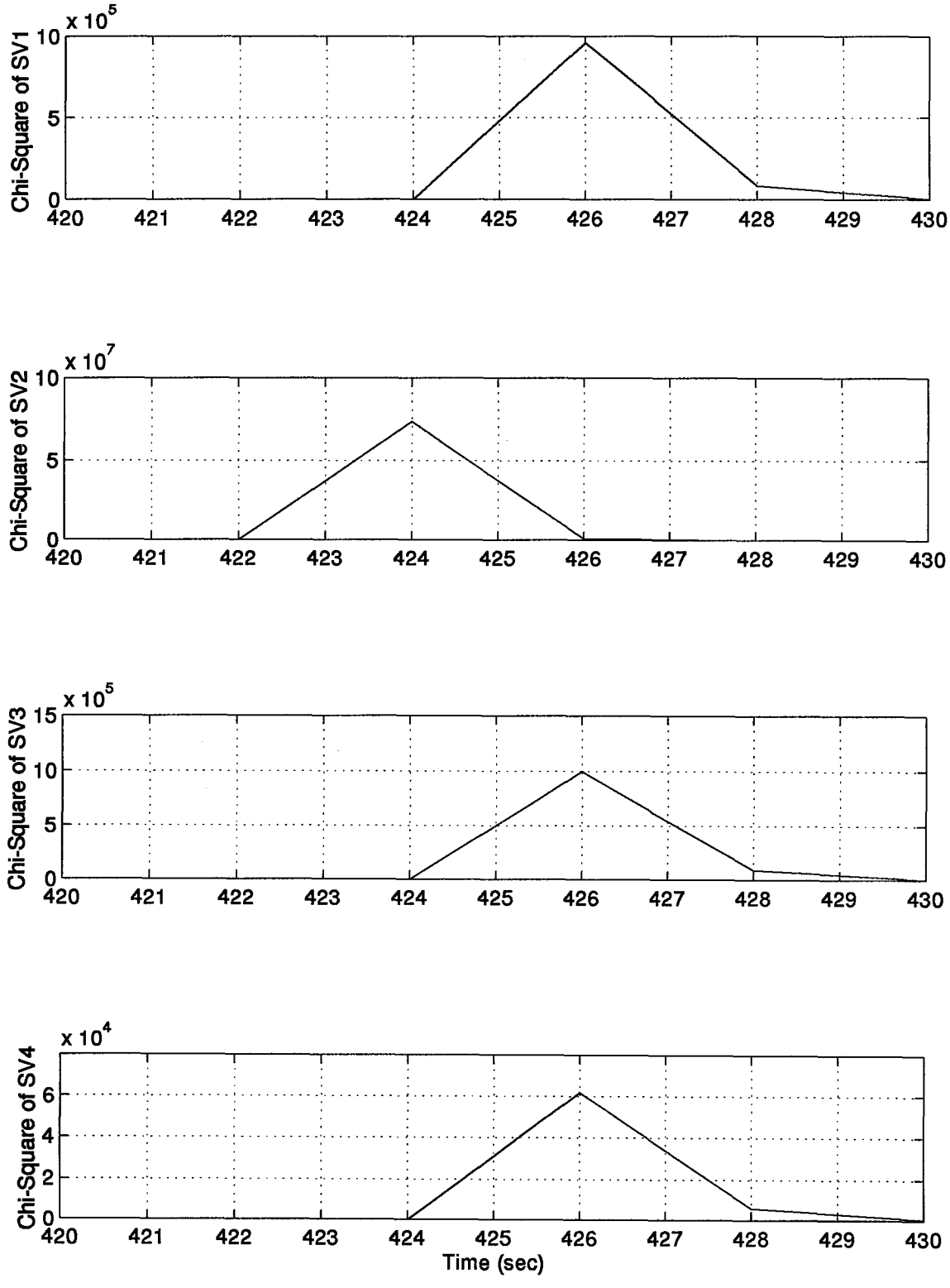

Figure L.7 Chi-Square Plots of Individual Residuals for Cycle Slip on Satellite #2

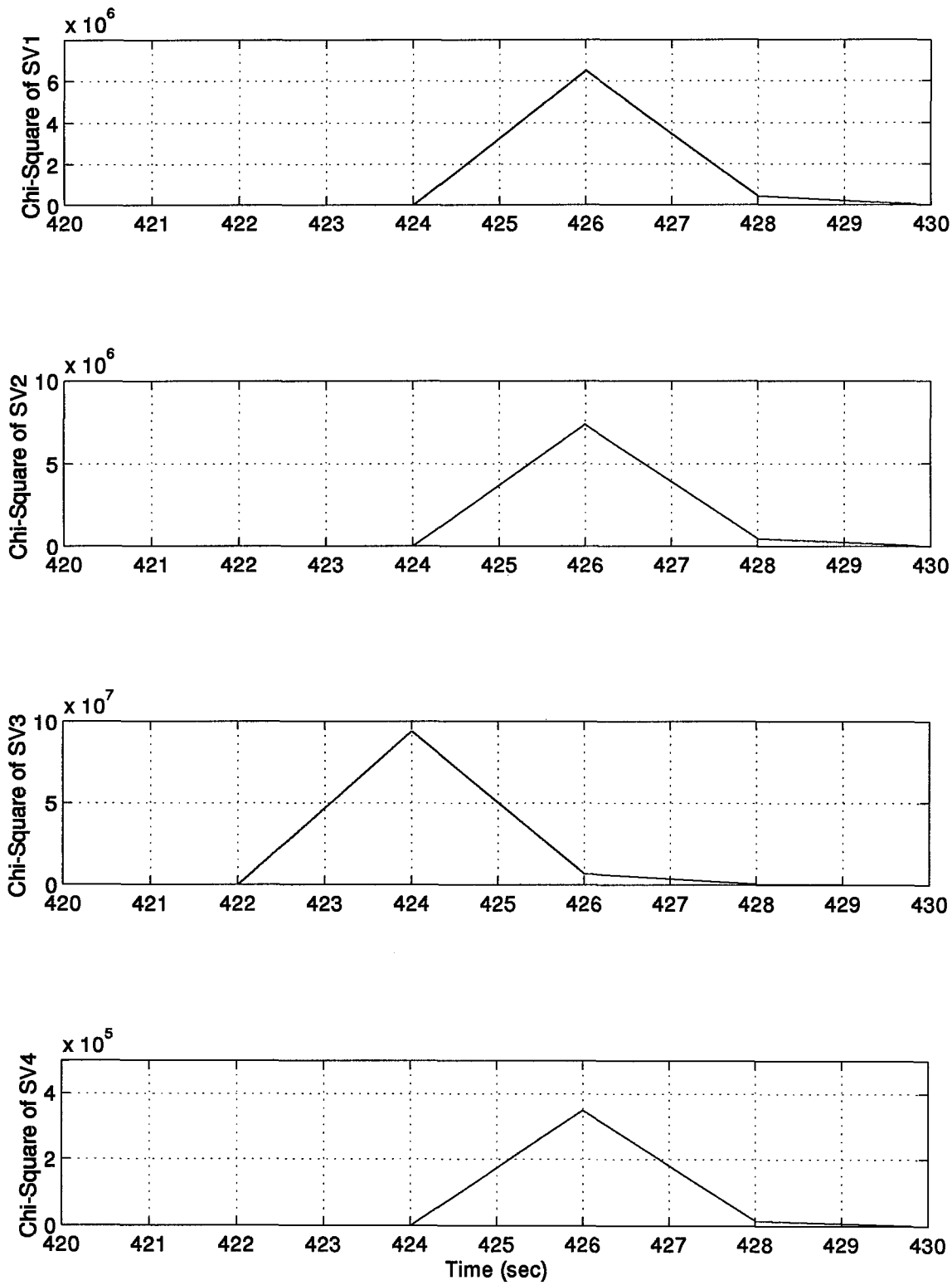

Figure L.8 Chi-Square Plots of Individual Residuals for Cycle Slip on Satellite #3

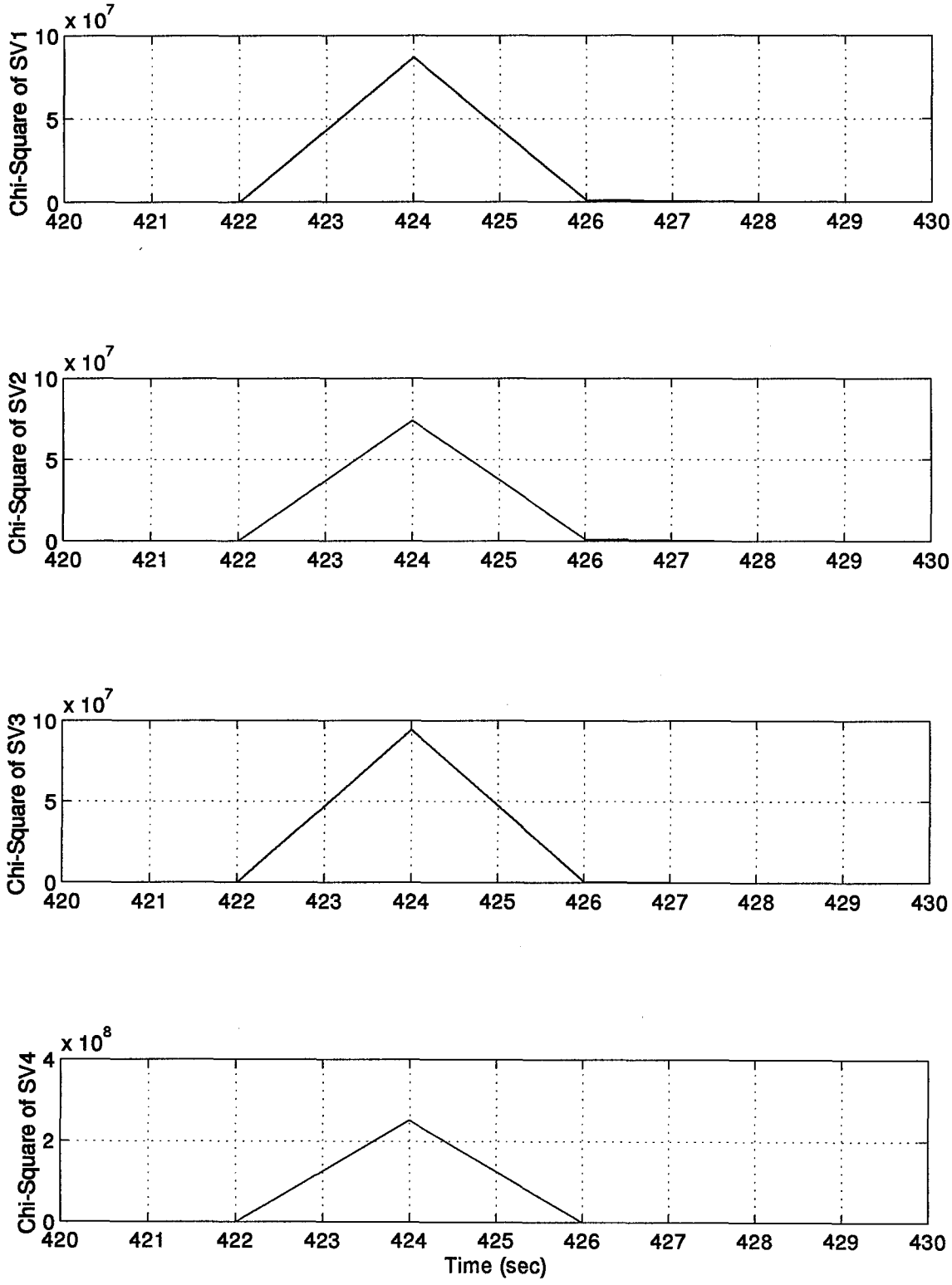

Figure L.9 Chi-Square Plots of Individual Residuals for Cycle Slip on Satellite #4

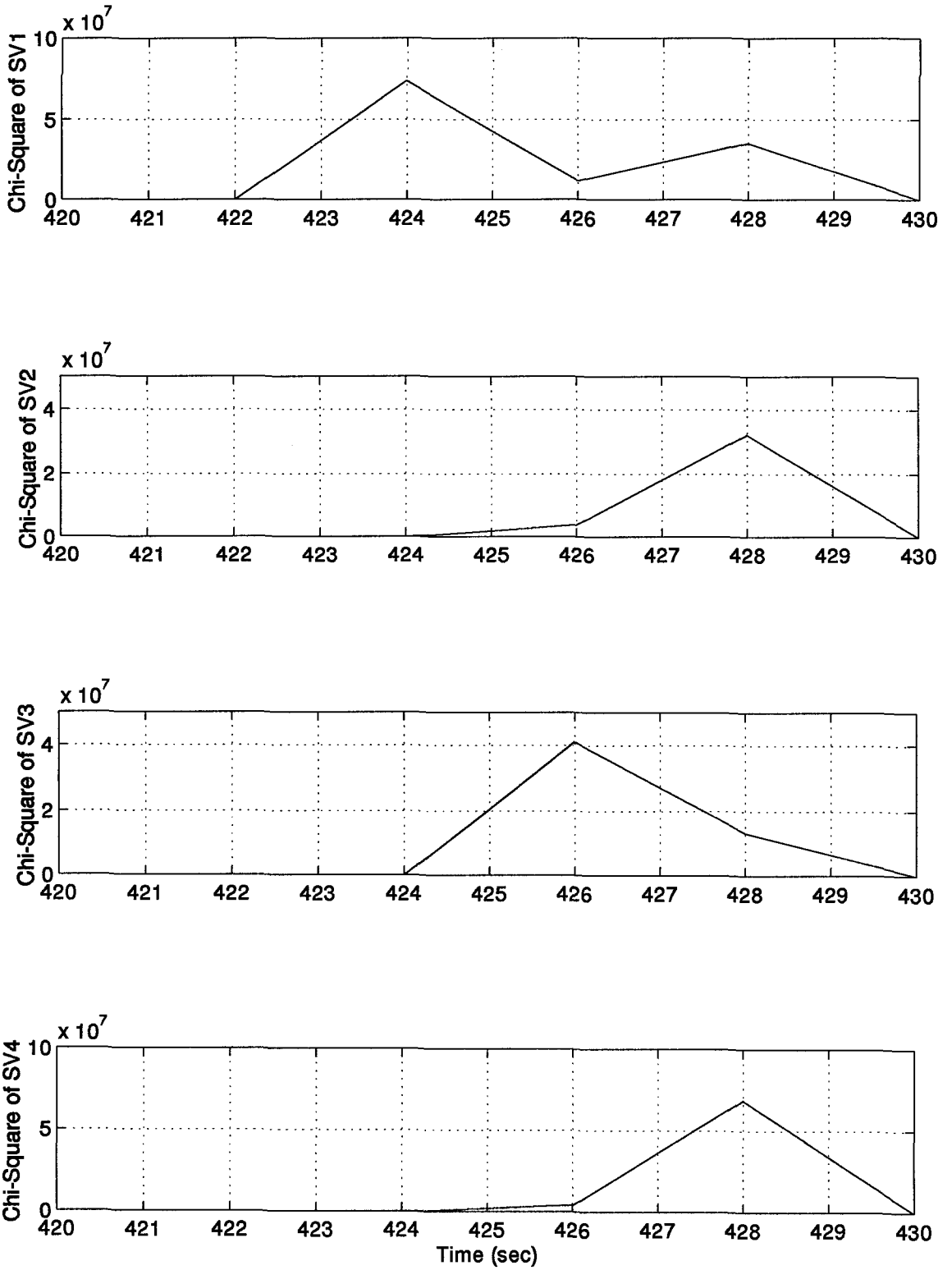

Figure L.10 Chi-Square Plots of Individual Residuals for Multiple Cycle Slip Scenario

Appendix M. Lack of Independence of GPS Satellite Differencing Proof

This proof will show, for the case of using GPS satellite combinations of $SV1 - SV4$, $SV2 - SV4$, and $SV3 - SV4$, where SV stands for Space Vehicle, that independence between these measurement combinations does not exist.

First, we assume that each measurement error can be represented by a Gaussian random variable, m, with the following statistics:

$$E[m_x] = 0 \tag{M.1}$$

and

$$E[m_x^2] = M_x \tag{M.2}$$

where x represents the number of the satellite measurement. It is assumed that the noises in all original (undifferenced) measurements are independent of each other. With this assumption, the following is true:

$$E[m_x m_y m_z] = \begin{cases} E[m_x^3] & \text{if x = y = z} \\ 0 & \text{otherwise} \end{cases} \tag{M.3}$$

Taking the fourth satellite measurement, m_4, as a base measurement, the following difference pairs are available: $m_1 - m_4$, $m_2 - m_4$, $m_3 - m_4$. For independence between measurements to be proven, the following relation must be true:

$$E[(m_1 - m_4)(m_2 - m_4)(m_3 - m_4)] \equiv E[m_1 - m_4]E[m_2 - m_4]E[m_3 - m_4] \tag{M.4}$$

Combining the different quantities on the left hand side of Equation (M.4) produces:

$$E[m_1 m_2 m_3 - m_1 m_3 m_4 - m_2 m_3 m_4 + m_3 m_4^2 - m_1 m_2 m_4 + m_1 m_4^2 + m_2 m_4^2 - m_4^3] \tag{M.5}$$

Using the distributive property of expected values, Equation (M.5) becomes:

$$E[m_1 m_2 m_3] - E[m_1 m_3 m_4] - E[m_2 m_3 m_4] + E[m_3 m_4^2]$$
$$-E[m_1 m_2 m_4] + E[m_1 m_4^2] + E[m_2 m_4^2] - E[m_4^3] \quad \text{(M.6)}$$

Invoking the independence assumption of Equation (M.3) changes Equation (M.6) to become:

$$- E[m_4^3] \quad \text{(M.7)}$$

Using the distributive property of expected values on the right hand side of Equation (M.4) produces:

$$[E[m_1] - E[m_4]]\,[E[m_2] - E[m_4]]\,[E[m_3] - E[m_4]] \quad \text{(M.8)}$$

From the zero mean assumption of Equation (M.1), Equation (M.8) becomes zero. Because of the conditions set forth in Equation (M.4) were not met, the independence of the three satellite measurement combinations does not exist.

Bibliography

1. Britting, Kenneth R. *Inertial Navigation Systems Analysis.* New York: Wiley-Interscience, 1971.
2. Canadian GPS Associates. *Guide to GPS Positioning* . ISBN: 0-920-114-73-3, Fredericton, New Brunswick: University of New Brunswick Graphic Services, May 1987.
3. Carlson, Neal and Stanton Musick. *User's Manual for a Multimode Simulation for Optimal Filter Evaluation (MSOFE).* AFWAL-TR-88-1138, Wright-Patterson AFB OH: Avionics Lab, AFWAL/AARN-2, April 1990.
4. Cox, D. B. "Integration of GPS with Inertial Navigation Systems," *Global Positioning System.* Papers Published in *Navigation*, Volume I:144-153, The Institute of Navigation, Alexandria, VA 22314, 1980.
5. Knudsen, L. *Performance Accuracy (Truth Model/Error Budget) Analysis for the LN-93 Inertial Navigation Unit.* Technical Report, Litton Guidance and Control Systems, January 1985. DID No. DI-S-21433 B/T:CDRL No. 1002.
6. Lachapelle, Gerard, M. E. Cannon and G. Lu. "High-Precision GPS Navigation with Emphasis on Carrier Phase Ambiguity Resolution," *Marine Geodesy, 15*: 253-269 (1992)
7. Lachapelle, Gerard and M Casey. "Use of Phase Data for Accurate Differential GPS Kinematic Positioning," *Proceedings of Position, Location, and Navigation Symposium.* 393-398. New York: IEEE Press, 1986.
8. Hansen, Neil P. *Incorporating Carrier Phase GPS Measurements into the CHAPS Extended Kalman Filter.* Unpublished Report to 46th GTS/TGFGXR, Holloman AFB, New Mexico. 03 May 1994.
9. Hansen, Neil P. *Incorporation of Carrier Phase Global Positioning System Measurements into the Navigation Reference System for Improved Performance.* MS Degree Thesis, AFIT/GE/ENG/93D-40. School of Engineering, Air Force Institute of Technology (AU), Wright-Patterson AFB OH, December 1993 (AD-A274136).
10. Hooser, Michael. Director Research and Development, Central Inertial Guidance Test Facility, Holloman AFB, NM. Telephone Interview. 20 July 1994.
11. Johnson, Gregory B. *Closed-Loop Performance of GPS Aided INS.* MS Degree Thesis, AFIT/GE/ENG/89D-19. School of Engineering, Air Force Institute of Technology (AU), Wright-Patterson AFB OH, December 1989 (AD-B139003).
12. Lewantowicz, Zdzislaw H. and Danny W. Keen. "Graceful Degradation of GPS/INS Performance With Fewer Than Four Satellites," *The Institute of Navigation, National Technical Meeting* (January 1991).
13. Mader, Gerald L. "Dynamic Positioning Using GPS Carrier Phase Measurements," *Manuscripta Geodaetica, 11*: 272-277 (1986).
14. *Matlab.* Version 4.1. Computer software. The MathWorks, Inc. 24 Prime Park Way, Natick, MA 01760. June 1993.
15. Maybeck, Peter S. *Stochastic Models, Estimation, and Control.* Volume 1. New York: Academic Press, Inc., 1979.
16. Maybeck, Peter S. *Stochastic Models, Estimation, and Control.* Volume 2. New York: Academic Press, Inc., 1982.
17. Maybeck, Peter S. *Stochastic Models, Estimation, and Control.* Volume 3. New York: Academic Press, Inc., 1982.

18. Maybeck, Peter S. Professor of Electrical Engineering, Air Force Institute of Technology, Wright-Patterson AFB, NM. Personal Interview. 12 September 1994.

19. Menke, Timothy E. and Peter S. Maybeck. "Sensor/Actuator Failure Detection in the VISTA F-16 by Multiple Model Adaptive Estimation," *Proceedings of the American Control Conference, San Francisco, June 1993* (1993).

20. Mosle, William B. *Detection, Isolation, and Recovery of Failures in an Integrated Navigation System.* MS Degree Thesis, AFIT/GE/ENG/93D-28. School of Engineering, Air Force Institute of Technology (AU), Wright-Patterson AFB OH, December 1993 (AD-A274056).

21. Mosle, 1Lt William B. Aircraft GPS Integration Element Officer, 46th Guidance Test Squadron, Holloman AFB, NM. Telephone Interview. 18 July 1994.

22. Musick, Stanton H. *PROFGEN - A Computer Program for Generating Flight Profiles.* Technical Report, Air Force Avionics Laboratory, WPAFB, Ohio, November 1976. AFAL-TR-76-247, DTIC ADA034993.

23. Negast, William Joseph. *Incorporation of Differential Global Positioning System Measurements Using an Extended Kalman Filter for Improved Reference System Performance.* MS Degree Thesis, AFIT/GE/ENG/91D-41. School of Engineering, Air Force Institute of Technology (AU), Wright-Patterson AFB OH, December 1991 (AD-A243742).

24. Nielsen, Robert L. *Development of a Performance Evaluation Tool (MMSOFE) for the Detection of Failures with Multiple Model Adaptive Estimation (MMAE).* MS Degree Thesis, AFIT/GE/ENG/93S-37. School of Engineering, Air Force Institute of Technology (AU), Wright-Patterson AFB OH, September 1993 (AD-A274218).

25. Riggins, Lt Col Robert N. Assistant Professor of Electrical Engineering, Air Force Institute of Technology, Wright-Patterson AFB, OH. Personal Interview. 2 May 1994.

26. Snodgrass, Faron Britt. *Continued Development and Analysis of an New Extended Kalman Filter for the Completely Integrated Reference Instrumentation System (CIRIS).* MS Thesis, AFIT/GE/ENG/90M-5. School of Engineering, Air Force Institute of Technology (AU), Wright-Patterson AFB OH, March 1990 (AD-A220106).

27. Snodgrass, Capt Britt and Capt John Raquet. Project Officers of The CIGTF High Accuracy Post-processing Reference System, 46th Guidance Test Squadron, Holloman AFB, NM. Personal Interview. 17 March 1994.

28. Solomon, Joseph K. *Development of the Extended Kalman Filter for the Advanced Completely Integrated Reference Instrumentation System (CIRIS).* MS Degree Thesis, AFIT/GE/ENG/89M-08. School of Engineering, Air Force Institute of Technology (AU), Wright-Patterson AFB OH, March 1989 (AD-A206083).

29. Stacey, Richard D. *A Navigation Reference System (NRS) Using Global Positioning System (GPS) and Transponder Aiding.* MS Degree Thesis, AFIT/GE/ENG/91M-04. School of Engineering, Air Force Institute of Technology (AU), Wright-Patterson AFB OH, March 1991 (AD-A238890).

30. Talbot, Nicholas C. "High-Precision Real-Time GPS Positioning Concepts: Modeling and Results," *Global Positioning System.* Papers Published in *Navigation*, Volume IV:221-235, The Institute of Navigation, Alexandria, VA 22314, 1993.

31. Vasquez, Juan R. *Detection of Spoofing, Jamming, or Failure of a Global Positioning System (GPS).* MS Degree Thesis, AFIT/GE/ENG/92D-37. School of Engineering, Air Force Institute of Technology (AU), Wright-Patterson AFB OH, December 1992 (AD-A259023).

32. Wong, R. V. C., K. P. Schwarz, and M. E. Cannon. "High-Accuracy Kinematic Positioning by GPS-INS," *Global Positioning System.* Papers Published in *Navigation*, Volume IV:237-250, The Institute of Navigation, Alexandria, VA 22314, 1993.

Vita

Second Lieutenant Brian J. Bohenek was born to Mr. and Mrs. Joseph Bohenek on 9 December 1971 in Scranton, Pennsylvania. Upon graduation from Scranton Central High School in 1989, Brian began his undergraduate studies in Electrical Engineering at Wilkes University in Wilkes-Barre, Pennsylvania. While at Wilkes, he enrolled in the Air Force Reserve Officer Training Corps (ROTC) to pursue his dream of becoming an Air Force Officer. Wilkes also provided Brian the opportunity to meet his fiancé, Miss Linda Wiernusz of Wilkes-Barre Township, Pennsylvania. Upon graduation from Wilkes in May 1993, Brian was commissioned as a Second Lieutenant in the United States Air Force and recognized as a Distinguished Graduate from Air Force ROTC. In June 1993, Brian was called onto active duty in the Air Force to continue his previous career as a student at the Air Force Institute of Technology (AFIT) Wright-Patterson AFB, Ohio. While at AFIT, he earned a Masters of Science Degree in Electrical Engineering with a concentration in navigation systems. Following graduation from AFIT in December 1994, the seemingly endless academic career of Brian's was temporarily put on hold so he could become a member of the 746th Test Squadron, Holloman AFB, New Mexico. While working at Holloman, Brian worked as a Flight Test Engineer and prepared for his wedding to his fiancé, Linda.

Permanent address: 906 Monroe Avenue
Scranton, PA 18510

REPORT DOCUMENTATION PAGE

Form Approved
OMB No. 0704-0188

1. AGENCY USE ONLY (Leave blank)	2. REPORT DATE	3. REPORT TYPE AND DATES COVERED
	December 1994	Master's Thesis

4. TITLE AND SUBTITLE
THE ENHANCED PERFORMANCE OF AN INTEGRATED NAVIGATION SYSTEM IN A HIGHLY DYNAMIC ENVIRONMENT

5. FUNDING NUMBERS

6. AUTHOR(S)
Brian J. Bohenek

7. PERFORMING ORGANIZATION NAME(S) AND ADDRESS(ES)
Air Force Institute of Technology, WPAFB OH 45433-6583

8. PERFORMING ORGANIZATION REPORT NUMBER
AFIT/GE/ENG/94D-01

9. SPONSORING / MONITORING AGENCY NAME(S) AND ADDRESS(ES)
746th Test Squadron
1644 Vandergrift Rd.
Holloman AFB, NM 88330-7850

10. SPONSORING / MONITORING AGENCY REPORT NUMBER

11. SUPPLEMENTARY NOTES

12a. DISTRIBUTION / AVAILABILITY STATEMENT
Distribution Unlimited

12b. DISTRIBUTION CODE

13. ABSTRACT (Maximum 200 words)

For the U. S. Air Force to maintain an accurate and reliable Navigation Reference System (NRS) with Carrier-Phase Global Positioning System (CPGPS) measurements, it must develop an accurate and robust NRS in the face of cycle slips caused by highly dynamic maneuvers. This research investigates the implementation of a double differencing between receivers/satellites scheme to improve the accuracy of current NRS models. The removal of the "perfect Doppler velocity aiding measurements" (a very poor assumption of past research) was completed with stable and accurate results. The double differencing implemented showed improvement in the accuracy of the NRS. An investigation of two Failure Detection, Isolation, and Recovery (FDIR) algorithms for large cycle slip failures is conducted. The two FDIR techniques are the Chi-Square test and a Multiple Model Adaptive Estimator (MMAE). The FDIR results show that a Chi-Square test as a stand-alone algorithm can work accurately for detection and isolation of failures with an accurate and reliable recovery algorithm. The MMAE algorithm as conjectured seems to be the best FDIR technique to handle single and multiple cycle slips accurately and reliably.

14. SUBJECT TERMS	15. NUMBER OF PAGES
Carrier-Phase GPS, Cycle Slip, Global Positioning System, GPS, Extended Kalman Filter, Navigation Reference System, MSOFE	245
	16. PRICE CODE

17. SECURITY CLASSIFICATION OF REPORT	18. SECURITY CLASSIFICATION OF THIS PAGE	19. SECURITY CLASSIFICATION OF ABSTRACT	20. LIMITATION OF ABSTRACT
UNCLASSIFIED	UNCLASSIFIED	UNCLASSIFIED	UL